

UNIVERSIDADE DE SÃO PAULO
INSTITUTO DE FÍSICA DE SÃO CARLOS

ÍTALO AUGUSTO CAVINI

Monomeric states of the beta-amyloid peptide investigated under high pressure
by nuclear magnetic resonance spectroscopy

São Carlos
2018

ÍTALO AUGUSTO CAVINI

Monomeric states of the beta-amyloid peptide investigated under high pressure
by nuclear magnetic resonance spectroscopy

Thesis presented to the Graduate Program in
Physics at the Instituto de Física de São
Carlos, Universidade de São Paulo to obtain
the degree of Doctor of Science.

Concentration area: Applied Physics
Option: Biomolecular Physics
Advisor: Prof. Dr. Richard Charles Garratt

Corrected Version

(Original version available on the Program Unit)

São Carlos

2018

I AUTHORIZE THE REPRODUCTION AND DISSEMINATION OF TOTAL OR PARTIAL COPIES OF THIS DOCUMENT, BY CONVENCIONAL OR ELECTRONIC MEDIA FOR STUDY OR RESEARCH PURPOSE, SINCE IT IS REFERENCED.

Cavini, Ítalo Augusto

Monomeric states of the beta-amyloid peptide investigated under high pressure by nuclear magnetic resonance spectroscopy / Ítalo Augusto Cavini; advisor Richard Charles Garratt - revised version -- São Carlos 2018.

202 p.

Thesis (Doctorate - Graduate Program in Física Aplicada Biomolecular) -- Instituto de Física de São Carlos, Universidade de São Paulo - Brasil , 2018.

1. Alzheimer's disease. 2. Beta-amyloid peptide. 3. Nuclear magnetic resonance. 4. Septin. 5. Coiled-coil. I. Garratt, Richard Charles, advisor. II. Title.

Dedicated to my family and
especially to Gabriela Rossi Albino
whose soul rests in peace.

ACKNOWLEDGEMENTS

I wish to deeply thank Prof. Dr. Claudia Elisabeth Munte, the advisor in my scientific initiation and in the first part of this PhD. She is not only my science life-coach but a friend! I would like to express my gratitude to all the regard and assistance provided during these years. I am also grateful to my current advisor Prof. Dr. Richard Charles Garratt that, despite all his appointments and tight schedule, is always ready to give some help or advice. I also appreciate his solicitude and readiness in provide feedback on my work.

A very special thanks to Prof. Dr. Dr. Hans Robert Kalbitzer (Universität Regensburg) for receiving me in his research group so many times and for trusting me as a member of his project. It was fantastic to have the opportunity to work majority of my research in your facilities. I thank him also for the coaching tips on weekend days at the spectrometer. Part of the content of this thesis is due to Dr. Markus Beck Erlach which I am grateful. I also would like to thank Prof. Dr. Werner Kremer and all members of Kalbitzer's group for the support in foreign lands.

I am really grateful to my parents, Domingos and Ana Lúcia, and my sister, Izis, who have provided me moral and emotional guidance over my entire life. I am also grateful to my girlfriend, Naiara Torres, and my roommate, Bruno Ono ("Kuririn"), for their constant encouragement and patience along the way. A special thanks to my office colleagues, Francesco Brugnera and Edson Crusca, for the sincere friendship.

Thanks to the staff of the Group of Molecular Biophysics "Sérgio Mascarenhas": Derminda Isabel ("Bel"), Andressa Alves ("Drê"), Rafael Spadaccia and José Fernando de Lima for the unfailing and handy support. I would like to thank all members of our septinologist group, especially Diego Cabrejos and Patrícia Kumagai, which directly collaborated to this project.

To Instituto de Física de São Carlos (IFSC) of the Universidade de São Paulo (USP), their excelent professors and employees.

To Fundação de Amparo à Pesquisa do Estado de São Paulo (FAPESP), Deutsche Forschungsgemeinschaft (DFG) and Coordenação de Aperfeiçoamento de Pessoal de Nível Superior (CAPES) scholarship agencies for providing the funding for the present work.

"If I have seen further it is by standing
on the shoulders of giants."

Isaac Newton (1643-1727)

ABSTRACT

CAVINI, Í. A. **Monomeric states of the beta-amyloid peptide investigated under high pressure by nuclear magnetic resonance spectroscopy**. 2018. 202 p. Thesis (Doctor in Science) - Instituto de Física de São Carlos, Universidade de São Paulo, São Carlos, 2018.

The main histological feature of Alzheimer's disease is the presence of amyloid plaques in the patient's brain. The most abundant element of these plaques is the β -amyloid peptide ($A\beta$). Initially soluble, the peptide exhibits in solution an intricate equilibrium among monomeric, oligomeric (some of which are regarded as the toxic species) and fibrillar states, which prevents its crystallization and subsequent structural determination by X-ray diffraction. High-pressure nuclear magnetic resonance (NMR) spectroscopy has been used by our group to detect rare, high-energy monomeric $A\beta(1-40)$ states, coexisting in equilibrium with oligomers and fibrils. This work aims to characterize the thermodynamics and the structure of the rare "excited" states of the $A\beta$ peptide through the use of high pressure NMR. A large collection of NMR spectra of the $A\beta(1-40)$ peptide as a function of pressure was recorded and analyzed. Secondary structure predictions revealed that the $A\beta$ peptide adopts extended β -strand-like structures, similar to those found in amyloid-fibril structures. From the pressure curves of chemical shifts and cross-peak volumes, at least three monomeric states could be detected, which were thermodynamically characterized by the calculation of the variation of their Gibbs free energy (ΔG_{ij}) and molar partial volumes (ΔV_{ij}). The study of nuclear Overhauser effects (NOEs) and $^3J_{H\alpha-HN}$ NMR couplings reinforces the existence of extended structures with β -strand propensity, both at ambient (0.1 MPa) and high (275 MPa) pressures. The interaction between the $A\beta$ peptide and the D-peptides RD2 and RD2D3, D-enantiomeric fibril inhibitors, was also characterized. Our results indicate that the D-peptides recognize and bind to a more compact conformation of $A\beta$. The formation of the $A\beta$ -D-peptide heterodimers ultimately prevents the formation of toxic oligomers, therefore representing a potential therapy against Alzheimer's disease. Additionally, in the second chapter, we present results on the coiled-coils (CC) from group-III human septins (SEPT1, SEPT2, SEPT4 and SEPT5) also studied by NMR spectroscopy. Septins are GTP-binding proteins present in most eukaryotic organisms and capable of forming filaments, which are essential in cell division. In this study, we used 1H - 1H -NOESY spectra to detect the orientation and helix pairings adopted by the C-terminal coiled-coils in solution. The NOE analysis, aided by back-calculated

spectra, showed that the only sequence to show an antiparallel structure was SEPT2CC; all the others are parallel. However, the disappearance of specific peaks in the NMR spectrum of SEPT5CC caused by the attachment of a paramagnetic spin label indicates an antiparallel orientation, contrary to our other NMR result. A simple evaluation of the coiled-coil heptameric positions, based on the occurrence of each amino acid residue occupying each position, revealed that both orientations are equally stable. Despite being far less stable compared to other coiled-coils, both could exist physiologically. Other results from the group also suggest that these peptides could have the ability to form both parallel and antiparallel coiled-coils. We speculate that the antiparallel conformation might be related to cross-linking between filaments.

Keywords: Alzheimer's disease. Beta-amyloid peptide. Nuclear magnetic resonance. Septin. Coiled-coil.

RESUMO

CAVINI, Í. A. **Estados monoméricos do peptídeo beta-amiloide investigados sob alta pressão por espectroscopia de ressonância magnética nuclear.** 2018. 202 p. Tese (Doutorado em Ciências) - Instituto de Física de São Carlos, Universidade de São Paulo, São Carlos, 2018.

A principal característica histológica da doença de Alzheimer é a presença de placas amiloides no cérebro de pacientes. O constituinte mais abundante dessas placas é o peptídeo β -amiloide ($A\beta$). Inicialmente solúvel, o peptídeo exhibe em solução um intrincado equilíbrio entre estados monoméricos, oligoméricos (alguns deles tidos como as espécies tóxicas) e fibrilares, o que impossibilita sua cristalização e posterior determinação estrutural por difração de raios-X. A espectroscopia de ressonância magnética nuclear (RMN) de alta pressão foi utilizada por nosso grupo para detectar estados monoméricos raros e de alta energia do $A\beta(1-40)$, coexistindo em equilíbrio com oligômeros e fibras. Esse trabalho visa caracterizar a termodinâmica e a estrutura dos estados “excitados” raros do peptídeo $A\beta$ através do uso da RMN de alta pressão. Uma grande coleção de espectros de RMN do peptídeo $A\beta(1-40)$ em função da pressão foi coletada e analisada. Predições de estrutura secundária revelaram que o peptídeo $A\beta$ adota estruturas estendidas do tipo fitas- β , similares àquelas encontradas em estruturas de fibras amiloides. A partir das curvas de deslocamento químico e volume de pico pela pressão, ao menos três estados monoméricos puderam ser detectados, os quais foram termodinamicamente caracterizados através do cálculo da variação das suas energias livres de Gibbs (ΔG_{ij}) e volumes parciais molares (ΔV_{ij}). O estudo de efeitos Overhauser nucleares (NOEs) e de acoplamentos $^3J_{H\alpha-HN}$ de RMN reforçam a existência de estruturas estendidas com propensão a fitas- β , tanto a pressão ambiente (0,1 MPa) quanto em alta pressão (275 MPa). A interação entre o peptídeo $A\beta$ e os D-peptídeos RD2 e RD2D3, inibidores D-enantioméricos de fibras, também foi caracterizada. Nossos resultados indicam que os D-peptídeos reconhecem e se ligam a uma conformação mais compacta de $A\beta$. A formação dos heterodímeros $A\beta$ -D-peptídeo previne, por fim, a formação dos oligômeros tóxicos, representando uma potencial terapia contra a doença de Alzheimer. Adicionalmente, no segundo capítulo, apresentamos resultados sobre os *coiled-coils* (CC) das septinas humanas do grupo III (SEPT1, SEPT2, SEPT4 e SEPT5) também estudados por espectroscopia de RMN. Septinas são proteínas ligantes de GTP presentes na maioria dos

organismos eucarióticos e capazes de formar filamentos, os quais são essenciais à divisão celular. Nesse estudo, utilizamos espectros ^1H - ^1H -NOESY a fim de detectar a orientação e o pareamento de hélices adotados pelos *coiled-coils* em solução. A análise dos NOEs, auxiliada por espectros retrocalculados, mostrou que a única sequência a mostrar uma estrutura antiparalela foi SEPT2CC; todas as outras são paralelas. Entretanto, o desaparecimento de picos específicos no espectro de RMN de SEPT5CC causado pela presença de um marcador paramagnético de spin indica uma orientação antiparalela, contrário ao nosso outro resultado de RMN. Uma avaliação simples das posições heptaméricas dos *coiled-coils*, baseada na ocorrência de cada resíduo de aminoácido em ocupar cada posição, revelou que ambas as orientações são igualmente estáveis. Apesar de serem bem menos estáveis comparadas a outros *coiled-coils*, ambas poderiam existir fisiologicamente. Outros resultados do grupo também sugerem que esses peptídeos poderiam formar tanto *coiled-coils* paralelos quanto antiparalelos. Nós especulamos que a conformação antiparalela pode estar relacionada a ligações cruzadas entre filamentos.

Palavras-chave: Doença de Alzheimer. Peptídeo beta-amiloide. Ressonância magnética nuclear. Septina. Coiled-coil.

LIST OF FIGURES

| | |
|---|----|
| Figure 1.1 – Hallmarks of Alzheimer’s disease (AD) and amyloid cascade hypothesis | 32 |
| Figure 1.2 – Amyloidogenic and non-amyloidogenic processing of APP | 33 |
| Figure 1.3 – Most important mutations in APP protein | 34 |
| Figure 1.4 – A β oligomerization and fibrilization | 35 |
| Figure 1.5 – NMR-based atomic models of amyloid- β peptide (A β) | 36 |
| Figure 1.6 – Structural model for A β in solution reported by DANIELSSON | 37 |
| Figure 1.7 – High pressure NMR study on A β 40 | 38 |
| Figure 1.8 – D3, RD2 and RD2D3 D-enantiomeric peptides | 40 |
| Figure 1.9 – The NMR experiment for spin-1/2 nuclei | 42 |
| Figure 1.10 – Intraresidual (red) and interresidual (blue) couplings in two sequential amino acid residues (i and $i+1$) in a protein | 44 |
| Figure 1.11 – Scalar couplings in protein NMR | 45 |
| Figure 1.12 – Example of HNCA (blue) and CBCA(CO)NH (green) NMR spectra from a generic protein and the magnetization transfer involved in the respective experiments (upper right insert) | 46 |
| Figure 1.13 – Effects of high pressure on soluble proteins | 47 |
| Figure 1.14 – Simulations of ^1H NMR chemical exchange for a two-spin system (states A and B) under pressure | 48 |
| Figure 1.15 – Sephadex column was able to remove some small contaminant molecules present in A β samples | 51 |
| Figure 1.16 – High pressure NMR sample cell apparatus | 54 |
| Figure 1.17 – ^1H - ^1H -TOCSY <i>mlevgpph19</i> pulse sequence | 56 |
| Figure 1.18 – ^1H - ^1H -NOESY <i>noesyphpr</i> (A) and <i>noesygpph19</i> (B) pulse sequences | 57 |
| Figure 1.19 – Example of a ^1H - ^{13}C -HSQC <i>hsqcetgpsi</i> NMR pulse sequence | 58 |
| Figure 1.20 – Triple resonance <i>hncogpww3d</i> pulse sequence for HNC(O) experiment | 58 |
| Figure 1.21 – NOE patterns and $^3J_{\text{HN-H}\alpha}$ scalar couplings expected for different types of secondary structures in proteins | 67 |
| Figure 1.22 – Simple model to describe the polymerization of globular proteins | 69 |

| | |
|--|----|
| Figure 1.23 – Different aggregation behavior shown by fluorescence assays for chemically synthetic (left, red) and recombinant (right, blue) A β peptide | 71 |
| Figure 1.24 – Expression test of A β attached to fusion protein in LB medium using (A) pRSET_A construct and (B) pET28a construct..... | 72 |
| Figure 1.25 – Tricine/polyacrilamide (16%) SDS-PAGE of A β 40 peptide purification..... | 73 |
| Figure 1.26 – HPLC purifications of A β 40 after tag removal | 74 |
| Figure 1.27 – Depolymerization of a 750 μ M A β sample followed by 1D- 1 H NMR spectra at 283 K..... | 75 |
| Figure 1.28 – Simulation of protein depolymerization curves by high hydrostatic pressures up to 300 MPa | 76 |
| Figure 1.29 – Pressure induced depolymerization of A β | 77 |
| Figure 1.30 – Temperature dependence of ΔG^0 , ΔV^0 and $\Delta \beta'^0$ for A β polymerization | 78 |
| Figure 1.31 – A β maximum depolymerization obtained for different total sample concentrations at different temperatures | 78 |
| Figure 1.32 – A β shows repolymerization at high pressures | 79 |
| Figure 1.33 – High pressure NMR 1 H- 15 N-HSQC spectra at 277 K | 82 |
| Figure 1.34 – 1 H $^\alpha$ - 13 C $^\alpha$ section of high pressure 1 H- 13 C-HSQC spectra at 277 K..... | 83 |
| Figure 1.35 – Superposition of high pressure 2D-HNCO spectra at 277 K..... | 83 |
| Figure 1.36 – Manual treatment effects on the data | 84 |
| Figure 1.37 – Pressure dependence of 1 H N and 15 N H NMR chemical shifts before (gray) and after (color) pressure correction | 85 |
| Figure 1.38 – Corrected chemical shift (δ^*) pressure curves for residue Val-12 of A β (1-40) | 86 |
| Figure 1.39 – Correlation between B_1^* (horizontal axis) and B_2^* (vertical axis) pressure coefficients..... | 87 |
| Figure 1.40 – First (B_1^*) and second order (B_2^*) pressure coefficients of A β (1-40) from combined chemical shifts | 88 |
| Figure 1.41 – Distribution of B_2^*/B_1^* values for all atoms in A β peptide compared to random coil peptide data | 89 |
| Figure 1.42 – Sequence dependence of the mean B_2^*/B_1^* ratio for A β (1-40) at different temperatures..... | 91 |
| Figure 1.43 – Parameters evolution of chemical shifts fitting | 93 |

| | |
|---|-----|
| Figure 1.44 – Distribution of the largest absolute difference among final δ_1 , δ_2 and δ_3 plateau values ($\Delta\delta_i^{\max}$) in the chemical shifts fit routine | 94 |
| Figure 1.45 – Statistics of chemical shifts fitting using a three-state model..... | 95 |
| Figure 1.46 – Cross-peak volume changes are different in different structural portions of A β | 96 |
| Figure 1.47 – Different behavior of cross-peak volumes (green) and intensities (red) | 97 |
| Figure 1.48 – Monomeric A β populations of different conformations at 277 K | 99 |
| Figure 1.49 – A β (1-40) secondary chemical shifts at 277 K and at 3, 80 and 160 MPa | 101 |
| Figure 1.50 – A β secondary structure propensities calculated by TALOS+..... | 102 |
| Figure 1.51 – Aromatic-aliphatic cross-peaks in ^1H - ^1H -NOESY spectra of A β (1-40)..... | 104 |
| Figure 1.52 – NOE patterns for the A β peptide at 0.1 MPa (blue bars) and 275 MPa (red bars)..... | 105 |
| Figure 1.53 – $^3J_{\text{HN-H}\alpha}$ coupling constants for A β (1-40) at 277 K..... | 106 |
| Figure 1.54 – Pressure dependence of $^3J_{\text{HN-H}\alpha}$ NMR couplings | 107 |
| Figure 1.55 – ^1H NMR spectra of titration experiments with A β (1-40) in the presence of RD2 (A) and RD2D3 (B) | 109 |
| Figure 1.56 – Calculated concentrations of relevant species in A β titration with (A) RD2 and (B) RD2D3 | 109 |
| Figure 1.57 – A β -RD2 and A β -RD2D3 heterocomplexes have a reduced hydrodynamic radius | 110 |
| Figure 1.58 – Selected region of ^1H - ^{15}N -HSQC spectra showing the possible formation of A β -RD2D3 complexes | 111 |
| Figure 1.59 – Time dependence of 1:4 A β :RD2 (A) and 1:4 A β :RD2D3 (B) samples | 111 |
| Figure 1.60 – Chemical shifts and peak volumes changes caused by A β interaction with RD2D3 peptide at 1:0.2 molar (concentrations of A β and RD2D3 are 60 μM and 12 μM , respectively) | 112 |
| Figure 1.61 – Interaction sites of RD2D3 plotted on different A β three dimensional structures..... | 113 |
| Figure 1.62 –A β secondary chemical shift comparison ($\Delta\delta$) between the present study and ROCHE | 116 |
| Figure 1.63 – A β (1-40) amide pressure coefficients comparison among the present and previous studies..... | 118 |

| | |
|---|-----|
| Figure 1.64 – Comparison of $^3J_{\text{HN-H}\alpha}$ A β couplings between the present work (horizontal axis) and data reported by ROCHE..... | 120 |
| Figure 1.65 – Correlation between monomeric A β states calculated here and reported by MUNTE..... | 122 |
| Figure 1.66 – Proposed mode of action of D-peptides | 124 |
| Figure 2.1 – Human septins architecture and homology clustering | 130 |
| Figure 2.2 – Septins can form heterofilaments..... | 131 |
| Figure 2.3 – Helical wheel diagram and side view of a parallel (panel a) and an antiparallel (panel b) dimeric coiled-coils..... | 132 |
| Figure 2.4 – Multiple sequence alignment of C-terminal domain of group-III septins..... | 133 |
| Figure 2.5 – Coiled-coil crystallography structures of human septins | 134 |
| Figure 2.6 – Different helical pairings for septin coiled-coil peptides | 135 |
| Figure 2.7 – Structure of antiparallel SEPT4CC in detail..... | 135 |
| Figure 2.8 – Structural alignment of simulated SEPTCC structures with their respective crystallographic models | 136 |
| Figure 2.9 – Approach used to investigate the relative orientation of septins coiled-coils by NOESY NMR spectra | 139 |
| Figure 2.10 – Methanethiosulfonate spin labeling (MTSL) in proteins | 140 |
| Figure 2.11 – SEPT1CC presents no antiparallel contacts | 143 |
| Figure 2.12 – Assigned fingerprint region of SEPT4CC spectra | 145 |
| Figure 2.13 – SEPT4CC presents no antiparallel contacts | 146 |
| Figure 2.14 – SEPT5CC presents no antiparallel contacts | 147 |
| Figure 2.15 – SEPT2CC, differently from 1CC, 4CC and 5CC, presents characteristic antiparallel contacts | 149 |
| Figure 2.16 – Interaction contacts for SEPT2CC..... | 149 |
| Figure 2.17 – I6 H $^{\delta 2}$ /K9 H $^{\epsilon 2,3}$ contacts are potential intermolecular NOEs in parallel SEPT1CC, 4CC and 5CC structures | 150 |
| Figure 2.18 – Intensity changes caused by the presence of MTSL | 152 |
| Figure 2.19 – MTS label selectively affects SEPT5CC residues..... | 152 |
| Figure 2.20 – SEPTCC peptides are dimers in different buffer systems according to SEC-MALS experiments..... | 155 |

| | |
|--|-----|
| Figure 2.21 – SEC-MALS chromatograms and calculated masses for SEPTCC peptides.... | 156 |
| Figure 2.22 – Correspondence of amino acid residues between parallel and antiparallel coiled-coils of group-III septins..... | 159 |
| Figure 2.23 – Importance of ‘chameleon’-like behavior of group-III septin coiled-coils in the formation and cross-linking of filaments..... | 160 |
| Figure S1 – Mixed exchanging-states system with three conformers in fast exchange (states 1, 2 and 3) and three conformers in slow exchange (1, II and III)..... | 196 |

LIST OF TABLES

| | |
|---|-----|
| Table 1.1 – Starting values and restriction of parameters used in chemical shifts fitting (transitions 1-2 and 1-3)..... | 65 |
| Table 1.2 – Starting values and restriction of parameters used in peak intensity fitting..... | 65 |
| Table 1.3 – NOE classification based on distance ranges | 67 |
| Table 1.4 – Thermodynamic data of A β polymerization..... | 77 |
| Table 1.5 – Features of the recorded data set of high pressure NMR spectra | 81 |
| Table 1.6 – Average values for inverse-variance weighted B_2^*/B_1^* ratios at two different temperatures (277 and 288 K) | 90 |
| Table 1.7 – Thermodynamic parameters of monomeric A β (1-40) conformational transitions at 277 K | 94 |
| Table 1.8 – Possible transition in slow exchange is ambiguous and is probably the same as transition 3-2 but for residues in slow exchange | 98 |
| Table 1.9 – Comparison between two data sets of A β depolymerization at 277 K | 115 |
| Table 1.10 – Pearson correlation coefficients (r) between B_1^* and B_2^* pressure coefficients..... | 118 |
| Table 1.11 – Comparison between thermodynamic parameters calculated by the present study and by MUNTE | 123 |
| Table 2.1 – Comparison between expected NOEs and backcalculated NOEs in antiparallel SEPT1CC | 144 |
| Table 2.2 – Comparison between expected NOEs and backcalculated NOEs in antiparallel SEPT4CC | 145 |
| Table 2.3 – Comparison between expected NOEs and backcalculated NOEs in antiparallel SEPT5CC | 148 |
| Table 2.4 – Scores based on residue occurrence profiles for coiled-coil positions a , d , a,d -combined and for all heptameric positions..... | 154 |
| Table 2.5 – Hydrodynamic radius (R_h) measured by diffusion NMR experiments for different coiled-coil septins in different conditions | 157 |

LIST OF ABBREVIATIONS AND ACRONYMS

| | |
|-------------|--|
| A β | beta-amyloid peptide |
| AChe | acetylcholinesterase |
| ACN | acetonitrile |
| AD | Alzheimer's disease |
| AICD | amyloid intracellular domain |
| <i>APOE</i> | apolipoprotein E gene |
| apoE | apolipoprotein E |
| APP | amyloid precursor protein |
| BMRB | biological magnetic resonance data bank |
| CC | coiled-coil |
| CHC | central hydrophobic cluster |
| CSF | cerebrospinal fluid |
| COSY | correlation spectroscopy |
| DSS | 4,4-dimethyl-4-silapentane-1-sulfonic acid |
| DOSY | diffusion-ordered spectroscopy |
| EDTA | 2,2',2'',2'''-(ethane-1,2-diyldinitrilo)tetraacetic acid |
| EM | exponential multiplication |
| EPR | electron paramagnetic resonance |
| FID | free induction decay |
| FT | Fourier transform |
| GM | gaussian multiplication |
| GDP | guanosine-5'-diphosphate |
| GTP | guanosine-5'-triphosphate |
| HFIP | 1,1,1,3,3,3-hexafluoro-2-propanol |
| HP | high pressure |
| HPLC | high performance liquid chromatography |
| HSQC | heteronuclear single quantum coherence |

| | |
|--------|--|
| INEPT | insensitive nuclei enhanced by polarization transfer |
| IPTG | isopropyl β -D-1-thiogalactopyranoside |
| LB | line broadening |
| MALS | multi-angle light scattering |
| MTSL | methyl methanesulfonylthioate spin label |
| MW | molecular weight |
| NMR | nuclear magnetic resonance |
| NMDA | N-methyl D-aspartate |
| NOE | nuclear Overhauser effect |
| NOESY | nuclear Overhauser effect spectroscopy |
| PAGE | polyacrylamide gel electrophoresis |
| PDB | protein data bank |
| PFGSTE | pulsed-field gradient stimulated-echo |
| PII | polyproline helix type-II |
| PrP | prion protein |
| RF | radio frequency |
| RMSD | root-mean-square deviation |
| SDS | sodium dodecyl sulfate |
| SEC | size exclusion chromatography |
| SNR | signal-to-noise ratio |
| SS | secondary structure |
| SUE | septin unique element |
| SW | spectral window |
| TEV | tobacco etch virus |
| TOCSY | total correlation spectroscopy |

CONTENTS

| | | |
|-----------|--|----|
| Chapter 1 | AMYLOID-BETA PEPTIDE | 29 |
| 1.1 | INTRODUCTION..... | 31 |
| 1.1.1 | Dementia and Alzheimer's disease..... | 31 |
| 1.1.2 | APP processing and genetics of AD | 32 |
| 1.1.3 | β -amyloid peptide | 35 |
| 1.1.4 | D3 peptides..... | 38 |
| 1.1.5 | Nuclear magnetic resonance spectroscopy..... | 40 |
| 1.1.5.1 | NMR assignment | 43 |
| 1.1.5.2 | High pressure NMR | 46 |
| 1.2 | RESEARCH OBJECTIVES | 49 |
| 1.3 | MATERIALS AND METHODS | 49 |
| 1.3.1 | Sample preparation | 49 |
| 1.3.1.1 | A β (1-40) peptide..... | 49 |
| 1.3.1.2 | D3 peptide analogs | 51 |
| 1.3.2 | NMR spectroscopy | 52 |
| 1.3.2.1 | High pressure NMR instrumentation..... | 53 |
| 1.3.3 | NMR parameters and pulse programs | 55 |
| 1.3.3.1 | One-dimensional ^1H spectra | 55 |
| 1.3.3.2 | Translational diffusion ^1H spectra | 55 |
| 1.3.3.3 | ^1H - ^1H -TOCSY | 56 |
| 1.3.3.4 | ^1H - ^1H -NOESY..... | 56 |
| 1.3.3.5 | ^1H - ^{13}C -, ^{15}N -HSQCs | 57 |
| 1.3.3.6 | Three-dimensional spectra..... | 58 |
| 1.3.4 | NMR assignment | 59 |
| 1.3.5 | NMR data pretreatment..... | 60 |
| 1.3.5.1 | Normalization and combination of chemical shifts | 60 |
| 1.3.5.2 | Pressure corrections | 61 |
| 1.3.6 | NMR data analysis..... | 61 |
| 1.3.6.1 | Monomeric thermodynamic characterization..... | 62 |
| 1.3.6.1.1 | Models and equations | 62 |
| 1.3.6.1.2 | Fitting methodology..... | 64 |

| | | |
|-----------|---|-----|
| 1.3.6.2 | Monomeric structural characterization | 66 |
| 1.3.6.2.1 | Prediction of secondary structures..... | 66 |
| 1.3.6.2.2 | NOEs and $^3J_{\text{HN-H}\alpha}$ couplings..... | 66 |
| 1.3.6.3 | Diffusion NMR experiments | 68 |
| 1.3.6.4 | A β depolymerization model..... | 69 |
| 1.4 | RESULTS | 70 |
| 1.4.1 | Attempts to obtain recombinant β -amyloid peptides..... | 70 |
| 1.4.2 | Depolymerization of A β by high pressure | 74 |
| 1.4.3 | Characterization of A β monomer | 80 |
| 1.4.3.1 | High pressure NMR data set | 80 |
| 1.4.3.2 | Pressure coefficients | 87 |
| 1.4.3.3 | Thermodynamic analysis | 91 |
| 1.4.3.3.1 | Fast exchange: Chemical shifts | 91 |
| 1.4.3.3.2 | Slow exchange: Peak intensities and volumes | 95 |
| 1.4.3.3.3 | State populations..... | 98 |
| 1.4.3.4 | Structural analysis..... | 99 |
| 1.4.3.4.1 | Secondary structure propensities | 99 |
| 1.4.3.4.2 | NOEs and NMR coupling constant | 103 |
| 1.4.4 | A β interaction with D3 peptide analogs..... | 108 |
| 1.4.4.1 | Titration experiments | 108 |
| 1.4.4.2 | Investigation of interaction sites..... | 112 |
| 1.5 | DISCUSSION | 114 |
| 1.5.1 | Depolymerization of A β by high pressure | 114 |
| 1.5.2 | Characterization of monomeric A β states..... | 115 |
| 1.5.3 | A β interaction with D3 peptide analogs..... | 123 |
| 1.6 | CONCLUSIONS..... | 124 |
| Chapter 2 | ORIENTATION OF DIMERIC COILED-COIL HUMAN SEPTINS | 127 |
| 2.1 | INTRODUCTION..... | 129 |
| 2.1.1 | Septins | 129 |
| 2.1.2 | Coiled-coils | 132 |
| 2.1.3 | Structures of septin coiled-coils | 133 |
| 2.2 | RESEARCH OBJECTIVES | 137 |
| 2.3 | MATERIALS AND METHODS | 137 |
| 2.3.1 | Sample preparation | 137 |

| | | |
|-----------|---|-----|
| 2.3.2 | NMR spectroscopy | 138 |
| 2.3.2.1 | Back-calculation of NOESY NMR spectra..... | 138 |
| 2.3.2.2 | NMR paramagnetic relaxation enhancement | 139 |
| 2.3.3 | Oligomeric state investigation..... | 140 |
| 2.3.3.1 | SEC-MALS experiments | 140 |
| 2.3.3.2 | Diffusion NMR experiments | 140 |
| 2.3.4 | SEPTCC heptameric position analysis | 141 |
| 2.4 | RESULTS | 141 |
| 2.4.1 | Relative coiled-coil orientation by NMR..... | 141 |
| 2.4.1.1 | NOEs analysis | 141 |
| 2.4.1.1.1 | SEPT1CC | 142 |
| 2.4.1.1.2 | SEPT4CC | 144 |
| 2.4.1.1.3 | SEPT5CC | 147 |
| 2.4.1.1.4 | SEPT2CC | 148 |
| 2.4.1.1.5 | Potential intermolecular NOE in parallel conformations..... | 150 |
| 2.4.1.2 | Paramagnetic relaxation enhancement (PRE) NMR | 151 |
| 2.4.2 | Analysis of SEPTCC heptameric positions..... | 153 |
| 2.4.3 | Oligomeric studies | 155 |
| 2.4.3.1 | SEC-MALS experiments | 155 |
| 2.4.3.2 | Diffusion NMR experiments | 156 |
| 2.5 | DISCUSSION | 157 |
| 2.6 | CONCLUSIONS..... | 161 |
| | REFERENCES | 163 |
| | APPENDIX | 179 |
| | ANNEX..... | 201 |

CHAPTER 1 AMYLOID-BETA PEPTIDE

1.1 INTRODUCTION

Chapter 1 reports the study of the amyloid-beta peptide ($A\beta$) of Alzheimer's disease by conventional and high-pressure nuclear magnetic resonance spectroscopy. This study was done in collaboration with Prof. Dr. Dr. Hans Robert Kalbitzer at Universität Regensburg, Germany and Prof. Dr. Claudia Elisabeth Munte (former advisor and professor at University of São Paulo). A collaboration with Prof. Dr. Dieter Willbold at Heinrich-Heine Universität Düsseldorf/Forschungszentrum Jülich enabled the investigation of $A\beta$ interaction with fibrillization inhibitor D-peptides.

1.1.1 Dementia and Alzheimer's disease

Alzheimer's disease (AD) is an amyloidogenic, neurodegenerative disease and the most common cause of dementia (60-80%).¹ It is believed that more than 47 million people worldwide suffer from dementia.² Like other types of dementia, AD is characterized by the deterioration of memory and abilities such as learning, language, guidance and judgment. The progression of the disease seems to begin before the emergence of clinical symptoms. However it usually starts with the difficulty of remembering recent events as well as apathy and depression. Later symptoms can include impaired communication, disorientation, confusion, poor judgment and behavior changes. Ultimately, AD patients can face difficulty speaking, swallowing and walking.¹

The disease is officially the sixth-leading cause of death in United States although it may cause even more deaths than official sources recognize. According to Alzheimer's Association, AD caused 123% more deaths in 2015 than 2000, killing more people than breast and prostate cancer together.¹ Despite being first described by Alois Alzheimer in 1906,³ several decades passed before it started to be recognized as a major cause of death⁴ and, even nowadays, the cause and progression of AD are still incompletely understood.⁵

As Alzheimer's disease progresses, brain tissue shrinks due to the significant loss of neuron cells. Besides, the main histological hallmark of AD is the presence of amyloid plaques, i.e., extracellular deposit of protein aggregates, between neurons in the patient's

brain. Those plaques are mainly constituted of precipitated fibers of amyloid-beta peptide, or $A\beta$.^{6, 7} Another AD's hallmark are neurofibrillary tangles found intracellularly which are primarily composed of hyperphosphorylated tau protein.^{8, 9} Despite some debate and modifications to the initial proposal,¹⁰⁻¹⁴ the 'amyloid hypothesis' is now reasonably accepted due to several experimental evidence. The 'amyloid hypothesis' states that the imbalance between production and consumption of the $A\beta$ peptide in the brain is the starting point of the pathogenesis of AD and the tangles formation is merely a downstream event.¹⁰

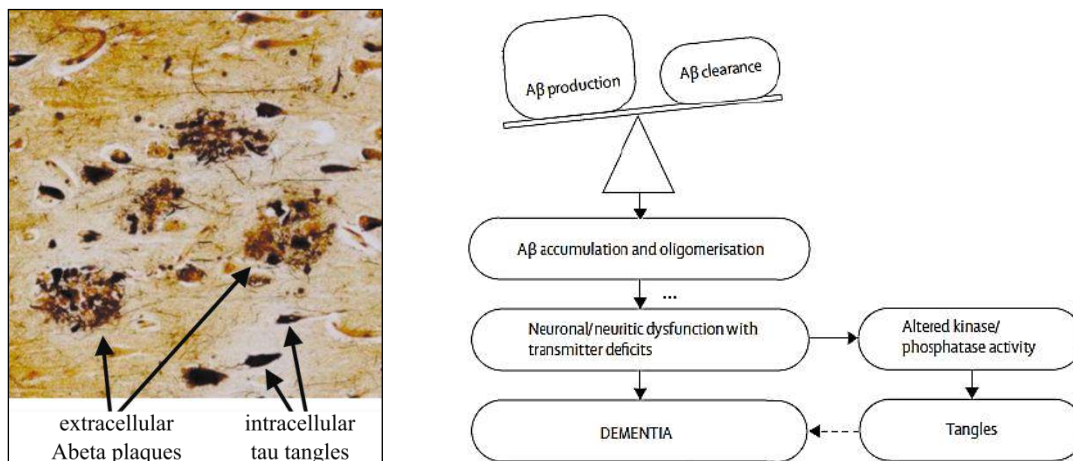


Figure 1.1 – Hallmarks of Alzheimer's disease (AD) and amyloid cascade hypothesis. Insert on the left presents the histological indication of AD, presence of plaques and tangles in the brain. The amyloid hypothesis says that the central event in the pathogenesis of AD is the imbalance of production and clearance of the amyloid- β ($A\beta$) peptide. Tau pathology is believed to be only a result of the cascade effects derived from that imbalance.

Source: Adapted from BLENNOW⁵

1.1.2 APP processing and genetics of AD

The amyloid- β peptide is physiologically produced through a proteolytic cleavage of the amyloid precursor protein (APP), a transmembrane glycoprotein found on the neuron's membrane, by β - and γ -secretases.^{15, 16} Due to the unspecificity of the γ -secretases, different forms of $A\beta$ may result from cleavage, resulting predominantly in the $A\beta(1-40)$ and $A\beta(1-42)$ (or $A\beta_{40}$ and $A\beta_{42}$) forms. In case α -secretase cleaves APP first, a non-amyloid form of $A\beta$ called P3 peptide, which is $A\beta(17-40/42)$, is released instead. Other APP fragments are generated in the processing pathway like the soluble APP β or APP α domains (sAPP β , sAPP α) and the amyloid intracellular domain (AICD) (Figure 1.2).

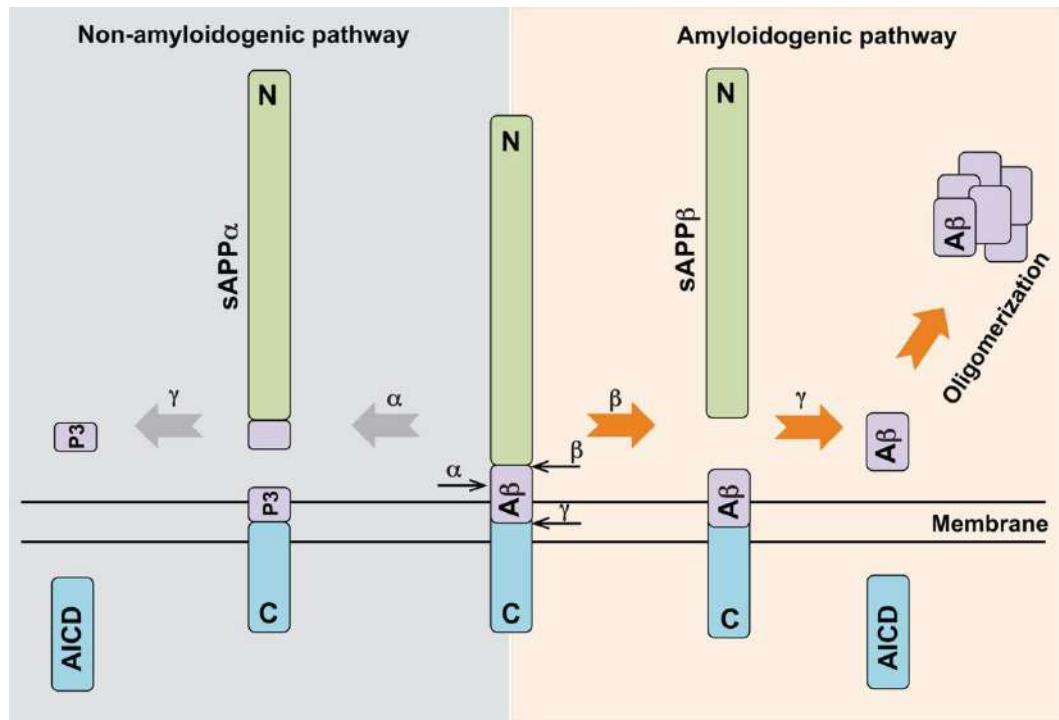


Figure 1.2 – Amyloidogenic and non-amyloidogenic processing of APP. Amyloid precursor protein (APP) is represented in the center of the figure and contains the A β sequence, which is released through proteolytic cleavage by β - and γ -secretases (right, amyloidogenic pathway). Two APP fragments are generated, soluble APP β (sAPP β) and the amyloid intracellular domain (AICD). The cleavage by α -secretase prevents the formation of full A β (left, non-amyloidogenic pathway) and, after full processing, releases the P3 peptide (A β 17-40/42), soluble APP α and also AICD.

Source: NICOLAS; HASSAN¹⁷

Although differing by two residues only, A β 40 and A β 42 present different behaviour. The former is the most common (around 10x more abundant than A β 42¹⁸) and the latter is the most toxic and amyloidogenic. Literature data on the β -amyloid peptide level in plasma and different parts of the brain is quite inconsistent. This difficulty is probably due to two reasons: the A β binding to several plasma and membrane proteins; and the high degree of variance among subjects. Recent studies have shown that the ratio A β 42/A β 40 is a better diagnostic biomarker of AD than the levels of A β 40 and A β 42 individually.^{19, 20} A β 42/A β 40 levels ratio decreases in AD patients compared to non-AD subjects probably due to the higher propensity of A β 42 deposition.^{18, 20, 21}

From a genetic point of view, there are two types of Alzheimer's disease: early-onset or familiar AD and late-onset or sporadic AD. Early-onset AD occurs in young patients aged from 30 to mid-60 years and represents a small percentage of the total number of cases (less than 10%). This type of AD is mostly caused by missense mutations in one of three genes, two of them encoding for presenilins (presenilin 1, PS-1 and presenilin 2, PS-2) and the other

encoding for APP. Presenilins constitute the catalytic subunit of the γ -secretases complex and the mutations appear to increase their activity and hence the production of A β .²² Several mutations within APP are also related to early-onset familial AD which commonly does not occur in sporadic cases.^{23, 24} Most mutations are clustered in the vicinity of secretase cleavage sites, thereby influencing APP processing, and are named after the location of the first family in which that specific mutation was found.²⁵ It was also reported a rare mutation in the APP gene (A673T) that protects against AD (Figure 1.3).²⁶

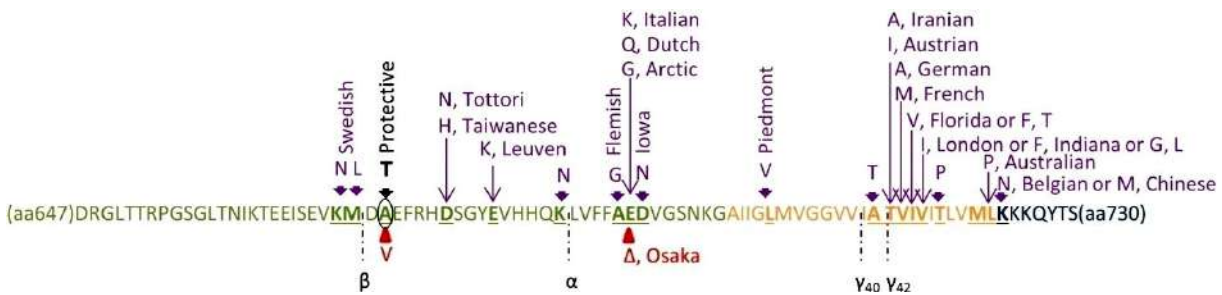


Figure 1.3 – Most important mutations in APP protein. Different colors representing APP domains are shown: green, extracellular domain; orange, transmembrane domain; blue, intracellular domain. Pathogenic mutations are colored in purple. In red are the two recessive pathogenic mutations. A delta (Δ) indicates a deletion in the Osaka mutation. The cleavage sites of α , β , and γ secretases are marked with black dotted lines.

Source: Adapted from CACACE²⁴

Most people with Alzheimer's have the late-onset form of the disease, in which symptoms start appearing in the mid-60s. Researchers have not found a specific reason that directly causes the late-onset form, but it is likely to include a combination of genetic, environmental, and lifestyle factors. However, the apolipoprotein E gene (APOE) has been considered the strongest genetic risk factor for sporadic AD.²⁷ APOE comes with three major forms or alleles, $\epsilon 2$, $\epsilon 3$ and $\epsilon 4$. APOE- $\epsilon 2$ may provide some protection against the disease whereas APOE- $\epsilon 4$ frequency is dramatically increased in patients with AD, being around 40% more common.²⁸ The apolipoprotein E (apoE) originally mediates the transport and delivery of cholesterol and other lipids throughout the cell but also binds A β with high affinity, affecting its removal and consequently its aggregation and deposition.²⁹

1.1.3 β -amyloid peptide

After being released by the APP cleavage, monomeric $A\beta$ accumulates mostly in the extracellular region. However, it is possible to find $A\beta$ aggregates in neuron's cytoplasm as well.³⁰⁻³² Some believe that intraneuronal $A\beta$ might be an important trigger of the pathological cascade of events which leads to neurodegeneration.^{11, 32} Initially soluble, the peptide assembles into small oligomers and, ultimately, insoluble cross- β amyloid fibrils and plaques.^{33, 34} Initially, it was thought that extracellular amyloid plaques would cause the massive neuronal damage typical of AD. However, the existence of patients presenting brains almost completely taken by plaques which did not have dementia (and *vice versa*) suggested that the assumption was not truly correct. In the last couple of decades, evidence indicating oligomers as the most toxic form of $A\beta$ has increased.

The kinetics of $A\beta$ has been well studied and requires at least two stages: nucleation phase and growth or elongation phase.³⁵ Fibrils or protofibrils may also break during oligomerization and thereby provide 'seeds' and new ends for elongation (Figure 1.4).

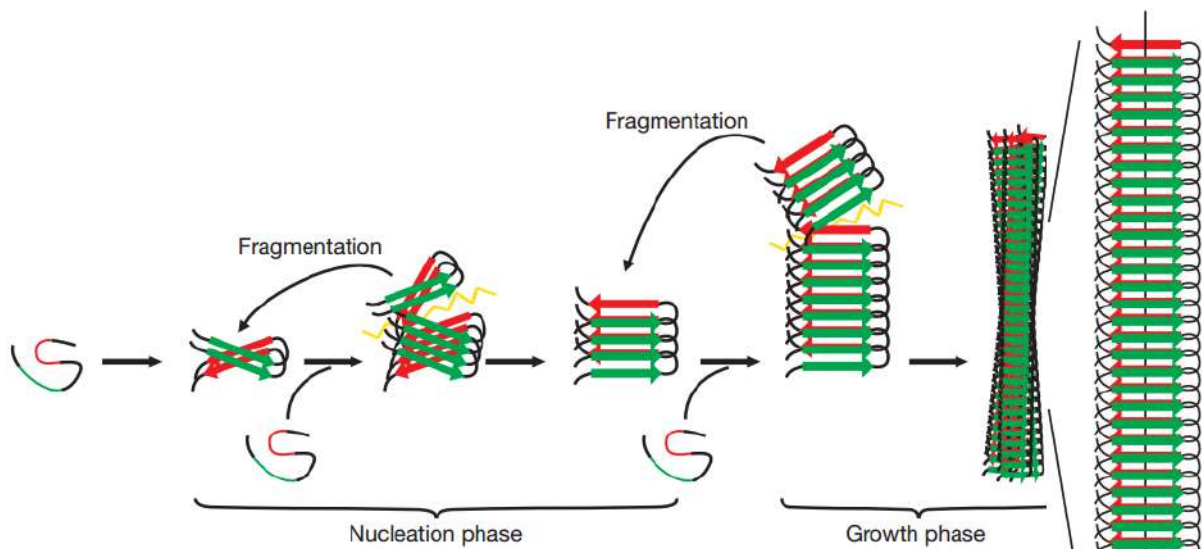


Figure 1.4 – $A\beta$ oligomerization and fibrilization. Soluble $A\beta$ peptides are able to aggregate into oligomeric assemblies and ultimately amyloid plaques. Nucleation phase (or lag phase) generates nuclei which will be extended in the growth phase. Fragments might act as seeds, enhancing kinetic fibrilization properties.

Source: Adapted from JUCKER; WALKER³⁶

$A\beta$ is commonly thought to be intrinsically unstructured and hence cannot be crystallized and studied by the most used structural method nowadays, X-ray crystallography.

An A β structural model in solution based on information collected by ^{15}N NMR relaxation experiments was reported.⁴⁶ Six different regions of secondary structure propensities could be detected by the relaxation rates of A β amide groups. Two regions in the N-terminus (Asp-1 to Arg-5 and Glu-11 to Gln-15) were recognized as having a high propensity to adopt polyproline type-II (PII) helices. The A β peptide has two regions with extended (E) conformation propensity (Lys-16 to Val-24 and Ile-31 to Val-40), which correlate well with the suggested β -sheet regions to be present in the fibrils. The other regions (His-6 to Tyr-10 and Gly-25 to Ala-30) have a higher mobility and are unstructured turn (T) regions connecting the structural elements.



Figure 1.6 – Structural model for A β in solution reported by DANIELSSON.⁴⁶ The A β sequence was divided into six portions, according to the secondary structure propensity reported by the ^{15}N NMR relaxation rates. PII, polyproline type-II helix; T, turn; E, extended region.

Source: By the author.

The conformational transition of the A β peptide to a β -sheet-rich state, resulting in its aggregation into water-soluble oligomers, is believed to be crucial in the development of AD symptoms.^{47, 48} Despite most A β oligomers exhibit some synapse toxic effect,⁴⁹ annular assemblies formed on the amyloid pathway (more likely than the mature fibrils) are believed to represent the most toxic species of A β , possibly by inactivating synaptic transmissions between neurons. The intermediate steps in this conformational change must involve intermediate states, including the toxic species, and those have been the major current focus on structural studies.⁴⁹⁻⁵¹

Very little is known about the function the β -amyloid peptide might exert physiologically. It is believed that the monomeric A β assists the synaptic activity regulation and play an important role as a neuroprotective agent *in vivo*.^{52, 53} In AD, it is possible that part of the symptoms comes from the loss of A β , which is aggregated as the disease progresses. Interestingly, several neurodegenerative disorders that occur without A β deposition, exhibit reduced cerebrospinal fluid (CSF) levels of A β peptide.⁵⁴⁻⁵⁶

Studies targeting monomeric A β have contributed to a better understanding on how the initiation of amyloid aggregation takes place.^{38, 57-61} The stabilization of a turn at positions

Asp-23 to Ala-30 in the monomer, around the same turn region in fibril structures, would configure a ‘nucleus’ for amyloid fibril formation.³⁸ It is noteworthy a study using high pressure (HP) nuclear magnetic resonance (NMR) spectroscopy performed by our group that detected different A β monomeric conformers in solution, a compactly folded state and partially folded states, coexisting with oligomers and fibrillary structures in a complex, dynamic equilibrium (Figure 1.7).⁵⁹

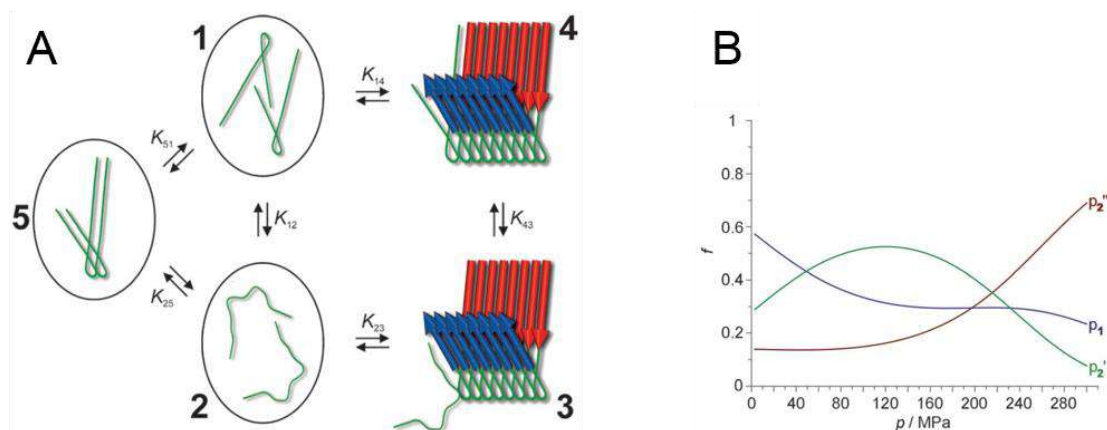


Figure 1.7 – High pressure NMR study on A β 40. A) Different monomeric conformational states were detected (1 and 2 in panel A) that might have different affinities by crescent fibrils. B) Pressure dependence of populations calculated by MUNTE and coworkers.⁵⁹ A compactly folded state 1, a partially folded state 2' and a random-coil-like state 2'' were detected by high pressure NMR spectroscopy.

Source: MUNTE⁵⁹

1.1.4 D3 peptides

Nowadays, all approved drugs for AD consist of symptomatic treatment. In other words, they do not affect AD's cause, which is believed to be related to A β peptide. An example of medication for AD are acetylcholinesterase (AChE) inhibitors⁶² such as donepezil,⁶³ rivastigmine⁶⁴ and galantamine⁶⁵. AChE is an enzyme that plays an essential role on synapses functioning and hinders cholinergic pathways in the brain,⁶⁶ which are impaired in a patient with AD. Another drug used to treat AD is memantine, an antagonist of N-methyl D-aspartate (NMDA) receptors.⁶⁷ Even after much scientific effort, there is no treatment available which is capable of curing AD.

Regardless, therapies that have A β as main target have been recently developed,⁶⁸ which includes anti-A β immunization, β - and γ -secretase inhibitors, metal chelators and aggregation inhibitors. Several A β -targeting peptides have been already reported (for an extensive list, see Ryan et al.⁶⁹). Some peptides are designed to mimic the sequence of A β to make use of its self-recognition properties, while others were found via high throughput approaches.

Identified by the mirror image phage display technique using a large 12-mer (12-residues long peptides) library, a D-enantiomeric peptide called D3 has been reported as a promising drug candidate against AD.⁷⁰ Because of its unusual enantiomerism, the D3 peptide enables oral ingestion and has a high stability against *in vivo* proteolysis. D3 possibly acts on changing the equilibrium balance between various conformations of A β , stabilizing A β monomers in an aggregation-incompetent conformation and turn toxic species into innocuous and nonamyloidogenic species.^{71, 72} *In vivo* tests on transgenic AD mouse models have shown that D3 is able to reduce plaque load and enhance cognition in rodents.^{71, 73}

D3 is a polybasic sequence, containing a large number of arginines. The sequence of D3 was used as a template to derive other D-peptides, as RD2. RD2 is a scrambled version of D3 and displays all five arginines sequentially in the C-terminus (Figure 1.8). The role played by those positively charged residues at physiological pH is not very well understood. Simulation studies on an A β nonamer complex interacting with D3 peptide tried to explain the D-enantiomeric peptide mode of action. It was shown that D3 establishes interactions with negatively charged residues of A β , namely Asp-7, Glu-11, Glu-22 and Asp-23. Those interactions were maintained all over the simulation and are responsible for neutralizing A β charges which helps its aggregation and inactivation.⁷⁴

Many studies with analogs of D3 have been performed lately.^{72, 75-80} It was shown that RD2 has a strong binding to A β .⁷⁵ *In tandem* versions of D3 (D3D3) and RD2 (RD2RD2 and RD2D3) were tested in mice bearing the Swedish and London APP mutations.⁷⁹ RD2D3 was reported to interfere with A β -PrP complexes.⁸⁰ PrP is a membrane-associated prion protein and a receptor which binds oligomeric A β , possibly triggering toxic events inside the cell.^{80, 81} New variants were designed from D3, showing improved properties (it is worth mentioning DB3, rpitrlrthqnr* and ANK6, rkrirlvtkkkr*).^{77, 78}

* D-enantiomeric peptide amino acid sequences are written in lowercase letters.

response of oscillating magnetic fields that can provide valuable information about matter. Neutrons and protons compose all atomic nuclei and have an intrinsic quantum property of spin (S). The nuclear spin is quantized and can only adopt specific orientations. However, in the absence of an external magnetic field (B_0) all orientations are equally probable since their energy levels are degenerated. The magnetic field breaks the energy degeneracy between spin states creating transition levels. For a nuclear spin $S = 1/2$ (which is the most common spin used in NMR like ^1H , ^{13}C , ^{15}N , ^{19}F and ^{31}P atoms; ^{12}C and ^{16}O have zero spin; ^{14}N has $S = 1$), two possible orientations of the nuclear spin exist. The state of lower energy and therefore more populated orientation is parallel to B_0 (spin-‘up’). On the other side, the antiparallel orientation (spin-‘down’) is energetically higher and thus less populated.

Upon irradiation, in the form of an oscillating pulse of electromagnetic field, the resonance condition is fulfilled and a spin transition takes place. The angular frequency required for the transition must match the energy gap between states for the resonance to occur. In practical applications, the resonance frequency is in the megahertz (MHz) radio frequency (RF) range. In the early days of NMR, measurements were made using the continuous wave (CW) method, in which the magnetic field B_0 is swept until a resonance is obtained. Nowadays, spectrometers have a constant B_0 and work with pulsed techniques where the radiation emitted by nuclear spins are monitored as they return to the ground state after the appropriate stimulation. The signal analysis into harmonic components is achieved by the mathematical technique of Fourier transformation (FT).

The NMR phenomenon is usually described by a simple vectorial analysis of the physical quantities involved. Although, this description is insufficient in some cases and only quantum mechanics can fully explain NMR. By this semi-classical approach, the sample gains a vertical magnetization (M) when B_0 is applied. The magnetization is created because the spins have a higher probability in occupying the lower energy state, according to the Boltzmann-Gibbs distribution. Because of the thermal energy is usually much higher compared to the magnetic energy, the population difference between states is only one in one million ($\sim 10^{-6}$). Another effect that occurs is, due to the presence of magnetic field, the spins start to precess around the direction of this field. The frequency of the precessional motion is called the Larmor frequency. For ^1H , as an example, the Larmor frequency is around 800 MHz for an 18.8 T high-field magnet. Once the sample is magnetized, an oscillating pulse with frequencies equal to the Larmor frequencies of the nuclei in the sample is switched on. Because of the torque caused by

the RF pulse, the magnetization starts to rotate around horizontal B_1 . The RF pulse length and/or power are chosen so that macroscopic magnetization is deflected by a determined angle, saying 90-degrees. The transversal (xy -plane) magnetization created, which rotates around B_0 , is then measured by detection coils through induced electric currents. The NMR signal is amplified and sent to a computer (Figure 1.9A).

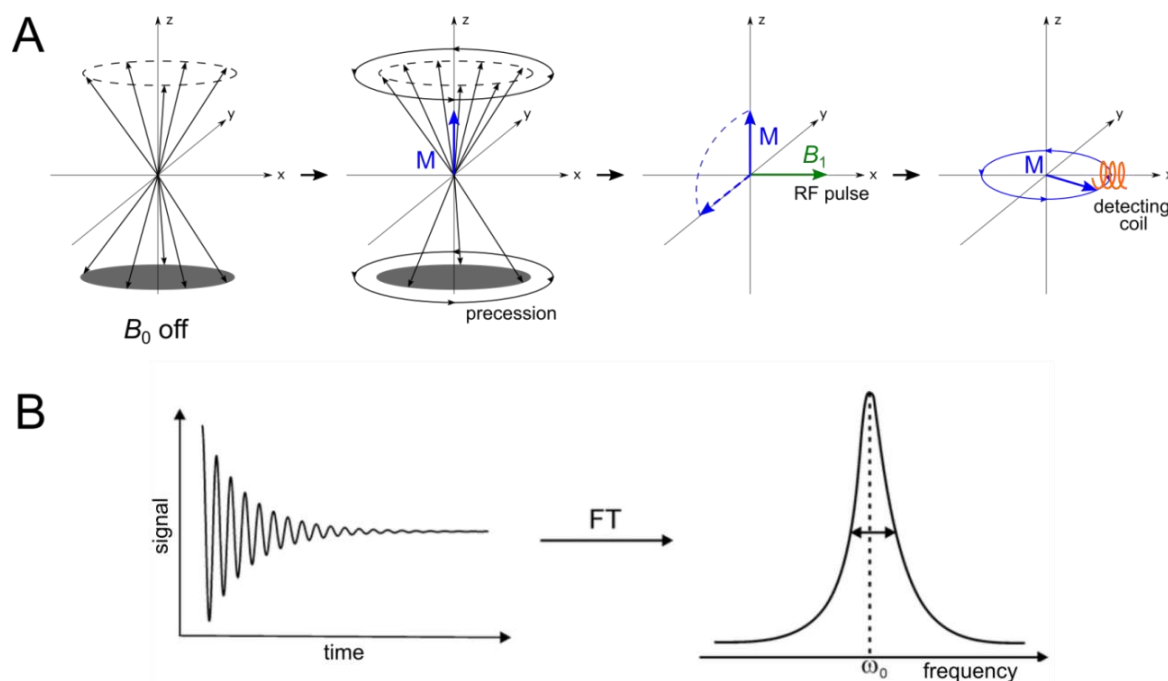


Figure 1.9 – The NMR experiment for spin-1/2 nuclei. A) In the absence of an external B_0 field, there are equal numbers of ‘up’ and ‘down’ spins. When B_0 (in the z direction) is applied, a net magnetization (M , blue) appears. If a radio frequency magnetic field (B_1 , green) is applied in the xy -plane by a certain period of time, the magnetization M is rotated into the xy -plane. This magnetization can then be detected by inducing coils (orange). B) The NMR spectrum is generated by the Fourier transform of the signal (free induction decay, FID).

Source: By the author.

According to our description, after the RF pulse is turned off the magnetization should persist indefinitely. In reality, transversal magnetization is a non-equilibrium state and the system returns to the initial state within short time using different relaxation pathways. The longitudinal or spin-lattice relaxation with time constant T_1 is the mechanism by which M_z reaches thermodynamic equilibrium with its surroundings, returning to the initial populational equilibrium. The transversal or spin-spin relaxation with time constant T_2 describes the decay of M_{xy} towards its equilibrium value, losing the spin coherence. Because of the latter, the detected NMR signal is not a sinusoid over time but it is modulated by an exponential function. This response is called FID (free induction decay). NMR data is usually analyzed not in the time domain but in the frequency domain. To convert the FID into a NMR

spectrum, a Fourier transform is employed. Peaks in form of Lorentzian functions appear in each frequency present in the FID (Figure 1.9B).

Electrons create a small magnetic field which modifies the magnetic field sensed by the surrounding nuclei, an effect known as chemical shielding. Therefore, the Larmor frequency varies based on different chemical environments. This effect is called chemical shift (δ) and it is one of the major parameters used in NMR spectroscopy. δ is calculated relatively to the standard reference frequency ν_0 and is measured in parts per million (ppm). One advantage of using chemical shifts instead of resonance frequencies is that the δ scale remains the same in different spectrometers using different B_0 intensity.

Historically, NMR was discovered by Felix Bloch and Edward Purcell in 1946.^{84, 85} Both researchers were awarded the Nobel Prize in Physics in 1952. High-field magnets and cryogenic probes development have reduced the measurement time and added powerful tools for increasing sensitivity and spectral resolution in NMR studies of biomolecules. The implementation of Fourier transform (FT-NMR) to higher dimensions originally proposed by Jean Jeener,⁸⁶ and later developed by the Nobel laureate in 1991 Richard R. Ernst,⁸⁷ made studies of nucleic acids and proteins in solution feasible. Later, Kurt Wüthrich shared the Nobel Prize in Chemistry 2002 for being the pioneer to determine the three-dimensional structure of biological macromolecules in solution by NMR.⁸⁸

1.1.5.1 NMR assignment

The initial stage of investigation by NMR spectroscopy is to associate each resonance peak present in the spectrum with a specific nucleus of the investigated molecule, a process called assignment. In general, the assignment can be divided in two stages: the sequential assignment of the amino acid residues in the backbone and the assignment of the side chains. Assignment strategy depends whether the molecule is unlabeled, ^{15}N labeled or $^{15}\text{N}/^{13}\text{C}$ doubly labeled. In the case of proteins up to 10 kDa (10,000 g/mol), homonuclear 2D spectra can be used and no labeling is required. For larger proteins, it is advisable to use $^{15}\text{N}/^{13}\text{C}$ uniformly labeled proteins and record triple resonance spectra for its assignment.

The principle process of homonuclear sequential assignment was developed and proposed by Kurt Wüthrich and coworkers in the early 1980s.⁸⁸ The spectra needed for this approach are largely utilized in NMR, which are NOESY (Nuclear Overhauser Effect Spectroscopy), COSY (COrrrelation Spectroscopy) and TOCSY (TOtal Correlation Spectroscopy). Figure 1.10 depicts the magnetization transfer which occurs in these experiments in protein NMR.

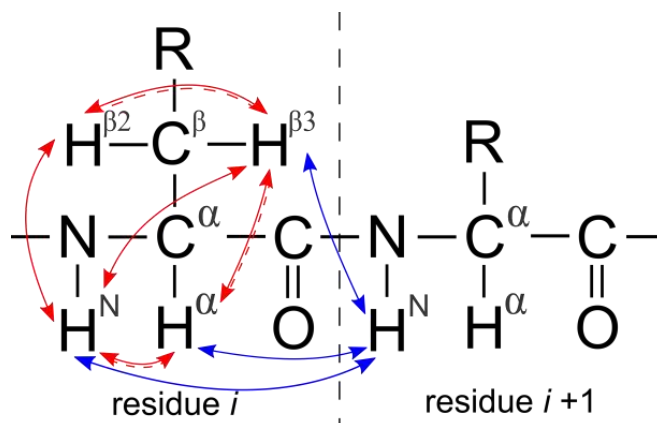


Figure 1.10 – Intraresidual (red) and interresidual (blue) couplings in two sequential amino acid residues (i and $i+1$) in a protein. TOCSY correlates all protons in an amino acid residue (solid red arrows) through scalar couplings. Only protons signals which are two or three bonds apart are visible in a COSY spectrum (dashed red arrows), coupled by $^2J_{\text{HH}}$ and $^3J_{\text{HH}}$ scalar couplings. NOESY uses dipolar couplings to connect not only intra- (omitted for clarity) but also interresidual protons up to 5 Å distance apart (blue arrows).

Source: By the author.

Experiments as COSY and TOCSY are employed for the identification of amino acid spin systems, using $^2J_{\text{HH}}$ and $^3J_{\text{HH}}$ scalar couplings. A 2D-COSY spectrum gives correlations between protons that are two or three bonds apart. A 2D-TOCSY, on the other hand, uses spin lock pulses to give correlations between all protons of a given spin system (except for aromatic protons, which appear as a second spin system). Most of the time, because of its completeness, TOCSY is preferred over COSY even that the magnetic transfer becomes ineffective between backbone protons and the most distant protons.

2D-NOESY experiment correlates protons that are up to 5 Å (0.5 nm) distant from each other. It uses dipolar couplings, which does not need covalent bonds to work, transferring magnetization through 'space'. It is used to sequentially connect spin systems and also provides distance restraints for the solution of three-dimensional structure of proteins and peptides by NMR.

Triple resonance assignment methodology offers another way to assign NMR resonances. No previous knowledge about spin systems is needed and can be applied to proteins up to 30 kDa. It uses three dimensional spectra, which reduce the overlap seen in homonuclear experiments. Sequential correlations involving ^1H , ^{13}C and ^{15}N nuclei via 1J and 2J couplings are used to establish connectivities between amino acids residues. In 3D-NMR spectra, the magnetization can be selectively transferred towards a specific chemical group. Sequences make use of different coupling constants for that (Figure 1.11). Passive nuclei are normally represented between parentheses in the name of the spectrum. There is several spectra combination that allows the backbone assignment of proteins. HNCA and CBCA(CO)NH spectra⁸⁹ were used for the backbone assignment of A β (1-40).

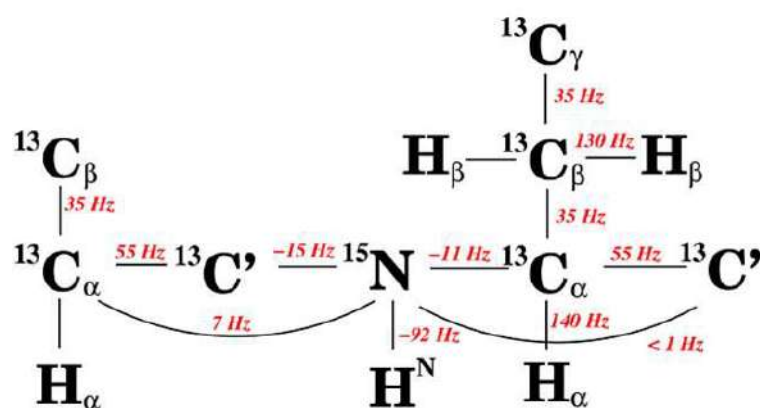


Figure 1.11 – Scalar couplings in protein NMR. Values can be negative when spins of the involved nuclei are parallel (and positive if they are opposite).
Source: NMR experiments and sequences webpage⁹⁰

The HNCA spectrum has three frequency axes (^1H , ^{15}N and ^{13}C) and correlates the amide group of a residue with the alpha carbon ($^{13}\text{C}_\alpha$) of this residue i and also with the previous one ($i-1$). This happens because $^1J_{\text{N-C}_\alpha}$ and $^1J_{\text{N-C}'}$ have similar magnitude (Figure 1.11). Signal of both intra- and interresidual correlations are seen on the spectrum at the same $^{15}\text{N}^{\text{H}}$ plane and in the same $^1\text{H}^{\text{N}}$ line. Because of the more efficient magnetization transfer, the intraresidual peak is more intense (Figure 1.12). A $^1\text{H}/^{15}\text{N}$ projection of a HNCA looks like an HSQC, and each signal represents a single amino acid residue.

The experiment CBCA(CO)NH connects $^{13}\text{C}_\alpha$ and $^{13}\text{C}_\beta$ carbons of residue $i-1$ with $^1\text{H}^{\text{N}}$ and $^{15}\text{N}^{\text{H}}$ nuclei of the residue i , selectly through the carbonyl carbon, $^{13}\text{C}'(i-1)$. Note that the correlation $^{13}\text{C}_\alpha(i-1)$ - $^{15}\text{N}^{\text{H}}(i)$ - $^1\text{H}^{\text{N}}(i)$ is the same correlation as in the HNCA experiment (Figure 1.12), allowing to reveal which of the peaks in the HNCA is interresidual, in case of doubt. In this way, the backbone assignment is performed sequentially through the

conjunction of the HNCA and CBCA(CO)NH spectra. HNCO spectrum can be acquired to help this process and also used to provide $^{13}\text{C}'$ chemical shifts, which is useful to predict backbone torsion angles and secondary structures.

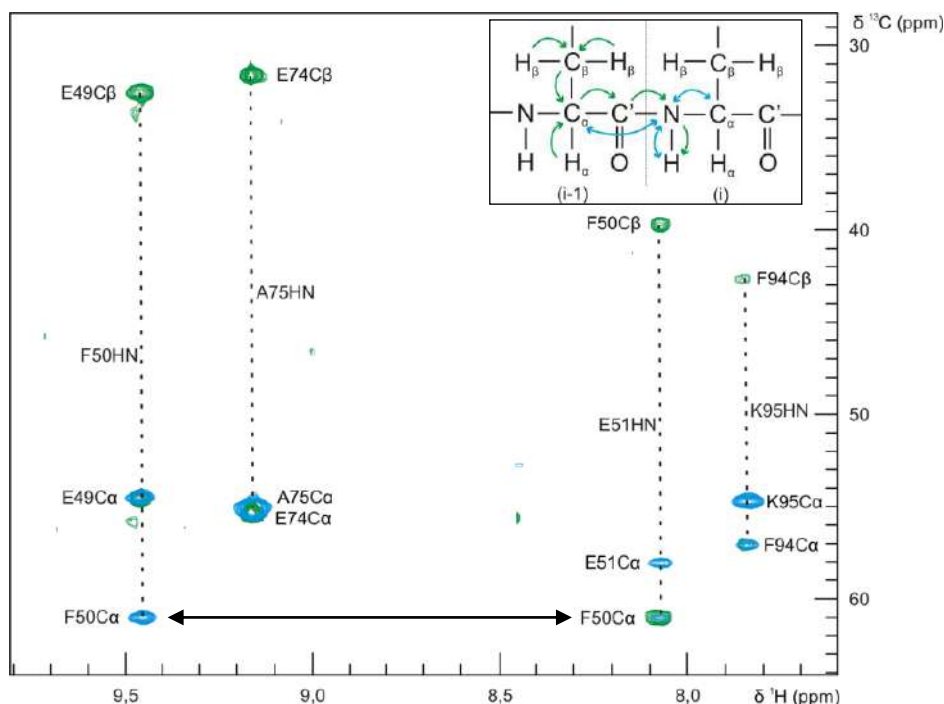


Figure 1.12 – Example of HNCA (blue) and CBCA(CO)NH (green) NMR spectra from a generic protein and the magnetization transfer involved in the respective experiments (upper right insert). The arrow indicates a connection between spin systems (chemical shift of the $^{13}\text{C}\alpha$ from Phe-50 residue), which allows the sequential assignment of the chemical shifts of backbone nuclei.

Source: By the author.

Once the sequential assignment by triple resonance experiments is done, the side chain assignment can be started with information from the H(C)CH-TOCSY experiment. The H(C)CH-TOCSY spectrum is a ^1H - ^1H -TOCSY spectrum resolved in the ^{13}C dimension, decreasing the overlapping of peaks and assisting in their identification.

1.1.5.2 High pressure NMR

High-pressure biochemistry started to emerge in the 1960s focused on the effects of pressure on macromolecules.⁹¹ The idea to combine high hydrostatic pressures to NMR spectroscopy is also rather recent and two basic methods were independently developed to pressurize samples in an NMR spectrometer.^{92, 93} There is the method developed by Jonas and

collaborators, where the whole probe head is pressurized.⁹⁴ This kind of pressurization allows very high pressures to be obtained but results in severe problems, mainly related to the space limitation inside high-field NMR spectrometers. On the other hand, Yamada developed a more convenient method that only the sample tube is pressurized,⁹³ the pressure is generated outside the spectrometer and carried to the sample by pressure lines. However, this method had a low sensitivity since the volume of capillaries used at the time was relatively small (~50 μl). In the last decades, the emergence of high active volume cells (higher than 300 μl) has enabled state-of-the-art NMR based studies of pressure-dependent phenomena on biological macromolecules up to 300 MPa.^{95, 96}

Proteins are thought to fold into a single conformation which is the most stable and dominant under physiological conditions, called the ‘native’ structure. Although, in solution proteins exist in a constant thermodynamic equilibrium among different conformational states, some of them with low abundance at normal conditions of temperature and pressure. The study of ‘rare’ conformers can offer relevant information on protein folding and dynamics.^{59, 97, 98} Specially, investigating misfolding pathways of proteins involved in neurodegenerative diseases by high hydrostatic pressure is an alternative to irreversible methods that use denaturing agents or temperature variation.

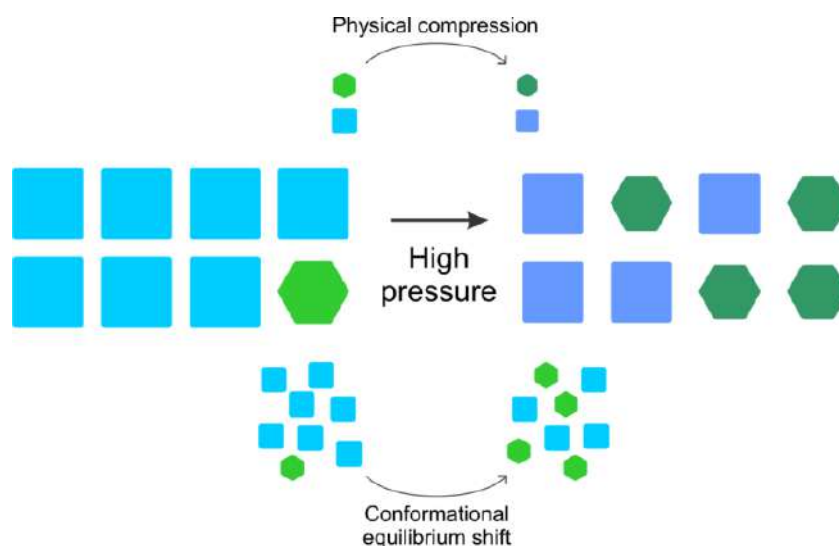


Figure 1.13 – Effects of high pressure on soluble proteins. Pressure physically compresses the sample and shifts the conformational equilibrium generally towards more compact states, represented by the green hexagons.

Source: By the author.

Pressure generally causes two effects on proteins: (i) it compresses molecules and also (ii) shifts their conformational equilibria (Figure 1.13). This shift is usually towards species

with lower partial molar volumes (V^0). With high pressures, those ‘rare’, low-lying ‘excited’ conformations can potentially increase their concentration relative to other states, becoming detectable under physiological conditions by high-resolution multidimensional NMR spectroscopy.

NMR chemical shifts and peak intensities have been used in a number of proteins to report conformational changes under pressure.^{59, 97-99} The rate of exchange (compared to the frequency difference between exchanging states, $\Delta\omega_{ij}$) has a great impact on the NMR spectrum if pressure changes the states populations (Figure 1.14). Fast exchange processes (Figure 1.14A) are completely averaged out on the NMR timescale and yield a spectrum that is an average of the individual spectra of each state. The position of the averaged peaks will shift and the pressure curve will look like a sigmoid (for a two-state system). The analysis of these high pressure chemical shift curves can yield important thermodynamic parameters about exchanging conformations. Peak intensity and/or volume changes, on the other side, can monitor intermediate and slow exchange processes (Figure 1.14B and Figure 1.14C).

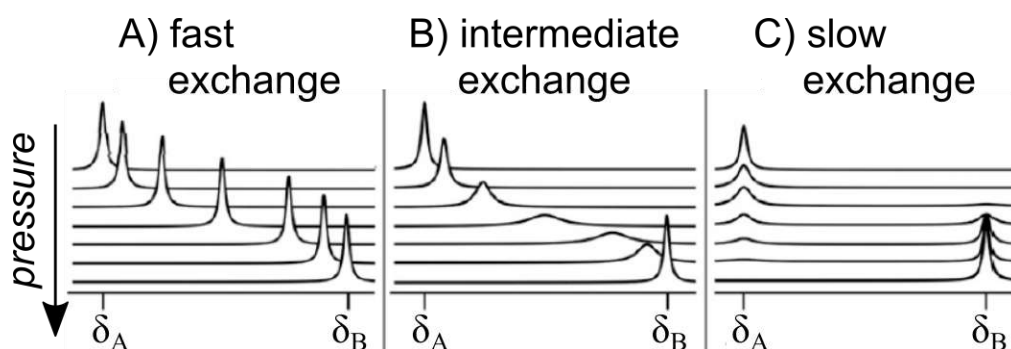


Figure 1.14 – Simulations of ^1H NMR chemical exchange for a two-spin system (states A and B) under pressure. If populations exchange in fast regime (A), the peak does not change intensity and shifts towards the frequency of the most abundant state. If intermediate rate of exchange is present (B), only one peak with reduced intensity is visible. If the exchange is slow (C) compared to the NMR timescale, both peaks can potentially be observed changing intensity according to the state populations. Plots do not represent the intensity increase due to pressure-induced solvent compression.

Source: Adapted from WAUDBY¹⁰⁰

The high pressure NMR technique allowed the detection of different monomeric conformers of the A β peptide using backbone ^1H and ^{15}N data.⁵⁹ By characterizing thermodynamically the equilibrium of these monomeric states and collecting information about the structure of them using high pressure NMR, their role for polymerization can be explored and the findings may be helpful in drug-design for preventing the amyloid formation. It is also desirable to expand the characterization initiated by Munte and

coworkers⁵⁹ in order to obtain a more representative data set, including also ^{13}C and side chain nuclei.

1.2 RESEARCH OBJECTIVES

The present work aims to detect and thermodynamically and structurally study rare, ‘excited’ monomeric states of $\text{A}\beta(1-40)$ peptide involved in Alzheimer’s disease. Some of the monomeric conformers might play an important role in the formation and stability of pathogenic aggregates and, ultimately, the fibrillization of β -amyloid. More specifically, monomeric states will be characterized by the use of high pressure nuclear magnetic resonance (NMR) spectroscopy in order to obtain a pressure and temperature dependence of the different conformational states. Structural information on monomeric $\text{A}\beta(1-40)$ will be obtained from NMR data analyses at atomic level, including chemical shifts, peak intensities, couplings and proton distances.

Additionally, the work will characterize, also through NMR spectroscopy, the interaction of $\text{A}\beta(1-40)$ with D3 peptide analogs, namely RD2 and RD2D3, D-enantiomeric peptides reported as oligomeric inhibitors and promising drug candidates.

1.3 MATERIALS AND METHODS

1.3.1 Sample preparation

1.3.1.1 $\text{A}\beta(1-40)$ peptide

^1H , uniformly $^{13}\text{C}/^{15}\text{N}$ and ^{15}N -labelled recombinant $\text{A}\beta(1-40)$ were purchased from rPeptide (Bogard, Georgia, USA). Amino acid residues 1-40 of $\text{A}\beta(1-40)$ correspond to residues 672-711 of βAPP770 (UniProtKB entry P05067, sequence DAEFRHDSGY EVHHQKLVFF AEDVGSNKG A IIGLMVGGVV; molecular weight of 4329.86 Da).

Sample preparation was done as described by Munte et al. 2013.⁵⁹ To eliminate the so called ‘conformational memory’ of A β , samples were pre-treated with hexafluoro-2-propanol (HFIP) to produce an uniform, unaggregated A β (1-40) peptide solution. The lyophilized peptide was diluted in HFIP (Sigma-Aldrich, St. Louis, Missouri, USA) and sonicated. The resulting solution was first evaporated in a rotary evaporator during one hour, frozen in liquid nitrogen and dried under vacuum overnight. Typically, at this stage, the resulting film was stored into -80 °C freezer for further use. The pre-treated peptide was resuspended in 100 mM NaOH solution first, then concentrated NMR buffer was added and the pH adjusted to 7.0 with 25 or 50 mM HCl solutions. A 3 M KCl electrolyte spinrode pH sensor (Hamilton, Reno, Nevada, USA) attached to a pHmeter (Beckman Coulter, Pasadena, California, USA) was used for pH measurements.

We verified in the NMR spectra the presence of low contents of guanidinium hydrochloride (Gnd-HCl) and HFIP in some samples (Figure 1.15A). Guanidinium is probably coming from the purification process, in which many protocols use to solubilize A β after tag cleavage. In order to remove those contaminants, we applied A β samples in a Sephadex-G25 PD Mini- or MidiTrap desalting column (GE Healthcare, Chicago, Illinois, USA). Eluent buffer used was 50 mM ammonium bicarbonate (pH 7.6) which allowed posterior freeze-drying, re-dissolving the powder (same procedure as described before) to maintain the original sample volume. NMR spectra (Figure 1.15) show that the purification protocol was successful.

Generally, the final NMR buffer was composed of 50 mM Tris-d₁₁, pH 7.0, 100 mM NaCl, 0.5 mM EDTA-d₁₆, 1 mM sodium azide in 8% D₂O (P4H buffer). For deuterated samples, DCl, NaOD, and 99.5% (v/v) D₂O (Cambridge Isotopes Laboratories, Andover, Massachusetts, USA) was used instead (which we called P4D buffer). Tris buffer was chosen for high pressure experiments because of its low pK_a (logarithmic acid dissociation constant), being considered almost pH insensitive with pressure.¹⁰¹ In some samples, 5 μ M DSS was used as internal reference. To remove high order aggregates, the produced samples were centrifuged at 50,000 g for 2 h at 4 °C before being subjected to NMR measurements.

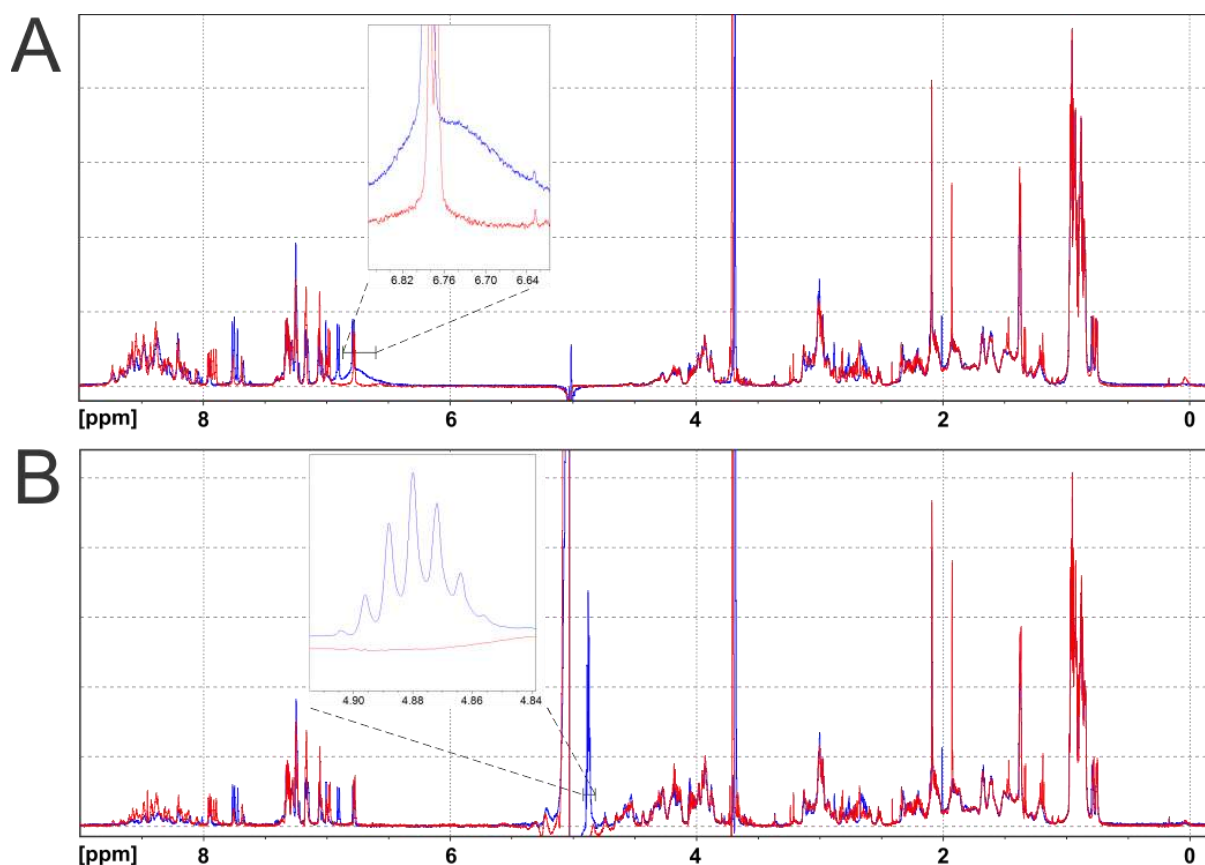


Figure 1.15 – Sephadex column was able to remove some small contaminant molecules present in A β samples. ^1H 1D-spectra comparison between hexafluoro-2-propanol (HFIP) pre-treated sample before (blue) and after subjected to desalting (red). (A) Gnd-HCl was detected as a broad peak in spectra using pulsed field gradient-based water suppression and (B) multiplet from HFIP visualized by spectra using water presaturation.

Source: By the author.

1.3.1.2 D3 peptide analogs

Two different D3 analogs (RD2 and RD2D3) were kindly provided by Prof. Dieter Willbold (Forschungszentrum Jülich, Germany). RD2 and RD2D3 are D-enantiomeric peptides with the amino acid sequences $\text{ptlht hnrrr rr}^*\text{-NH}_2$ (molecular weight of 1598.83 kDa) and $\text{ptlht hnrrr rrrpr trlht hnr}^*\text{-NH}_2$ (molecular weight of 3180.63 kDa), respectively. The peptides were obtained as reversed phase high performance liquid chromatography purified products (P&E, Potsdam, Germany). The purified and lyophilized D-peptides were dissolved in 99.5% D_2O and stored at $-20\text{ }^\circ\text{C}$ at 10 mM concentration.

* D-enantiomeric peptide amino acid sequences are written in lowercase letters.

Interaction studies of RD2 and RD2D3 D3 analogs with A β were conducted by NMR. A β (1-40) sample was prepared as usual and the respective concentrated D3 analog peptide was added just before the pH sample adjustment. The same amount of D₂O was added in A β control samples containing no D3 peptide. At the end of sample preparation, the pH was measured again and carefully adjusted by comparing the proton chemical shift of Tris located at 3.7 ppm. The tris peak of an A β (1-40) sample without D3 peptide was taken as standard.

In the titration experiments, a 1:4 A β :D3-analog sample, prepared as mentioned before, was used to obtain a 1:2 sample by simply mixing it with 50% of an A β sample with no D3 peptides (1:0 sample). The dilution step was repeated to obtain the following concentrations: 1:0, 1:0.2, 1:0.4, 1:0.6, 1:0.8, 1:1, 1:2 and 1:4 A β :RD2 or A β :RD2D3. This mixing method ensures that the A β concentration is constant through the titration series. Otherwise, in ‘classic’ titration experiments (where titrant is added to the sample), A β concentration has to be corrected for the respective dilution factor. Since the initial samples were used throughout the titration series, they were kept inside a heating electric stove set at the same temperature 283 K during the measurements.

1.3.2 NMR spectroscopy

Unless stated otherwise, NMR spectra were recorded with a Bruker Avance 800 NMR (Bruker Biospin, Karlsruhe, Germany) spectrometer operating at a proton frequency of 800.20 MHz (magnetic field equal to 18.8 T) equipped with a 5 mm TCI cryoprobe. Temperature was calibrated as described by Raiford et al.,¹⁰² measuring the difference of the proton resonance of the hydroxyl and the methyl groups in 100% methanol in a sealed capillary inside the NMR tube, which contained 99.5% D₂O for locking purposes.

NMR data were processed using TopSpin 3.5 software (Bruker, Billerica, Massachusetts, USA) and analyzed with AUREMOL.¹⁰³ ¹H-NMR shifts were referenced to DSS used as internal standard (0 ppm) or to perdeutero Tris-d₁₁. In case of Tris-d₁₁, pressure and temperature dependent shifts were mapped for P4H (buffer in H₂O) and P4D (buffer in D₂O) as an independent experiment. ¹⁵N and ¹³C chemical shifts were indirectly referenced according to Wishart et al.¹⁰⁴ Atom names were used following IUPAC recommendations (Annex A).¹⁰⁵ Chemical shifts, intensities and volumes were manually extracted with

AUREMOL.¹⁰³ Chemical shifts were extracted mostly with three decimal places; ¹H chemical shifts in ¹H-¹⁵N-HSQC and ¹H in ¹H-¹³C-HSQC were extracted with four decimal places (average standard deviation estimated in 0.0005 ppm).

For quantitative experiments, a repetition time (D1 delay) of 10 s was used. This relatively high time is expected to be larger than 5-times the T_1 -value of the molecule with the slowest relaxation time in the sample. The T_1 of DSS, Tris and free A β were determined before by inversion recovery experiments at 277 K and are 1.4 s, 1.1 s, and < 0.8 s, respectively.⁵⁹ Since it is expected that DSS interacts with A β -aggregates,¹⁰⁶ it cannot be used as an internal standard for the concentration determination of A β . Therefore, the quantification of NMR-visible resonances was performed using the residual perdeuterated signal of Tris-d₁₁ inside the sample with a known concentration. The perdeuteration degree of Tris-d₁₁ was determined from the integrals of the corresponding methyl resonances as $99.34 \pm 0.03\%$ and $99.44 \pm 0.03\%$ for P4H and P4D buffers, respectively.

1.3.2.1 High pressure NMR instrumentation

High pressure data were recorded with a homebuilt online-pressure system using the method first developed by Yamada.⁹³ Pressure was either applied by a manually operated piston compressor or by an air-to-liquid-pressure intensifier (Barocyler HUB440, Pressure BioSciences Inc., South Easton, Massachusetts, USA) controlled by the spectrometer. The pressure was transmitted via a high pressure line (High Pressure Equipment Company, Linden, Pennsylvania, USA) by deionized water. The high pressure ceramic cell used has an outer diameter of 5 mm and an inner diameter of 3 mm (Daedalus Innovations LLC, Aston, Pennsylvania, USA). A polyethylene membrane was used as a separator between the pressure fluid and the aqueous sample. To reduce the sample volume in the ceramic cell, a cylindrical PEEK (polyether-ether-ketone) displacement body was employed (Figure 1.16).

The high-pressure cell was joined to the high-pressure line by a safety titan autoclave that closes rapidly in case of cell breaking. The Barocyler was coupled via a microprocessor unit with the NMR spectrometer that controlled and monitored the output pressures. In a Bruker Topspin auxiliary program, a user-defined series of high pressure NMR experiments were started including an equilibration time of 10 minutes and an automated shimming of the

sample after changing pressure before the actual experiments were started. Since the experimental setup is delicate and manually mounted, minor fluid leakages may occur at high pressures, preventing the achievement of desirable pressure values. After the acquisition of the whole high pressure series at a determined temperature, the pressure was decreased to the initial pressure (usually 0.1 MPa or 3 MPa) for reversibility checking.

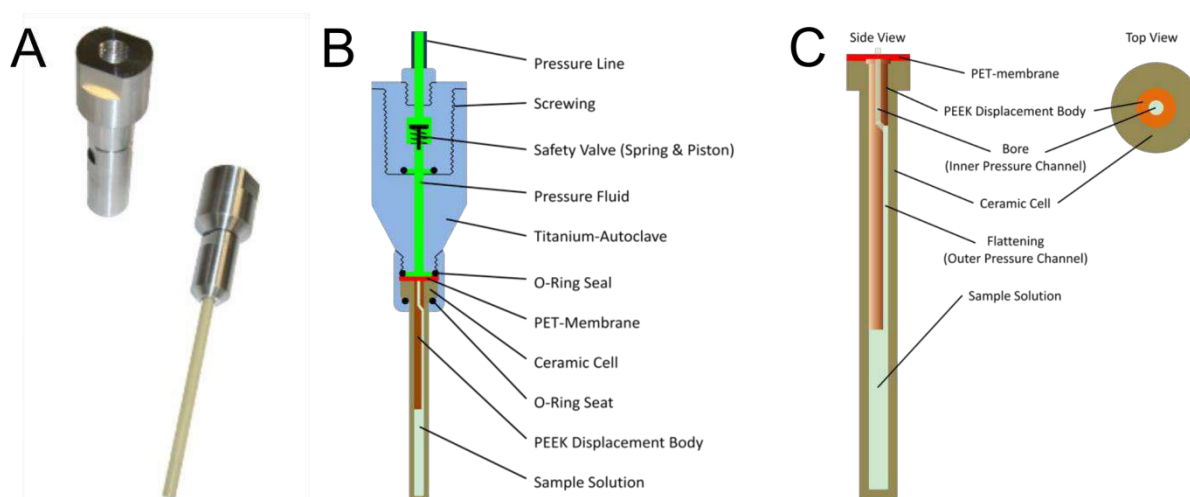


Figure 1.16 – High pressure NMR sample cell apparatus. A) Non-magnetic connection base and its attachment to the ceramic sample cell provided and marketed by Daedalus Innovations™. B) Scheme illustrating the assembly of the sample cell (bottom) and the connector to the pressure line (top). Each part or liquid is colored differently. C) Ceramic high pressure cell assembly in detail.

Source: DAEDALUS;¹⁰⁷ KOEHLER¹⁰⁸

To impede the formation of aggregates in samples with higher concentrations of A β (used to improve the quality of ^1H - ^1H -NOESY), we added depolymerization steps in between acquisition periods. As high hydrostatic pressures are able to depolymerize A β within a few hours and the repolymerization is a slow process (about a day to occur completely), the acquisition of the NOESY spectrum was divided into periods of eight hours each. Each period consisted of an initial pressurization for depolymerization at 200 MPa (two hours) followed by spectra acquisition (six hours). Posteriorly, the free induction decays (FIDs) from each period were added during processing and, with four periods, a NOESY spectra equivalent to 24 hours of acquisition was obtained.

1.3.3 NMR parameters and pulse programs

The center of the ^1H spectrum (transmitter frequency offset, O1) was determined using the center of the water residual peak. The 90-degree hard pulse output power (PL1) was initially set to values from -3 to 3 dB and the 90-degree hard pulse length was determined using a 360-degree pulse experiment, $P1(90^\circ) = P1(360^\circ)/4$.

1.3.3.1 One-dimensional ^1H spectra

One-dimensional ^1H spectrum is the simplest experiment in NMR spectroscopy. It shows all proton signals. *zggpw5* (water suppression using watergate W5 pulse sequence with gradients; using double echo)¹⁰⁹ and *noesygppr1d* (with presaturation during relaxation delay and mixing time and spoil gradient) pulse programs were used. *noesygppr1d* sequence was used for quantitative experiments since it does not create peak integrals artifacts.

Acquisition parameters used: number of scans (NS) = 8-256, spectral width (SW) = 9.6 kHz (or 12 ppm), fid size (TD) = 32-128 k, relaxation time (D1) = 2 s (*zggpw5*) or 10 s (*noesygppr1d*); Spectra were processed with an exponential function (EM) and line broadening (LB) of 0.3 or 2 Hz.

1.3.3.2 Translational diffusion ^1H spectra

Diffusion-ordered spectroscopy (DOSY) can be used to indirectly measure molecular hydrodynamic radius through the translational diffusion.¹¹⁰ Experiments were acquired with a One-Shot pulsed field gradient stimulated echo (PFGSTE) modified sequence (*diffu-oneshot* pulse sequence).¹¹¹ The NMR signal intensity is attenuated depending on the gradient parameters (Δ , δ and g) and the diffusion constant (D). Δ and δ delays were held constant ($\Delta = d20 = 0.3$ s and $\delta = p30/2 = 3000$ μs) and g was swept from 2-95% or 5-95% using typically 16 equally separated (linear) points. The stability of the gradient field was checked using a 20% polyacrylamide sample.

Acquisition parameters used: number of scans (NS) = 64-256, spectral width (SW) = 12.8 kHz (or 16 ppm), fid size (TD) = 8-32 k, relaxation time (D1) = 1.5 s. Spectra were processed with an exponential function (EM) and line broadening (LB) of 5 Hz.

1.3.3.3 ^1H - ^1H -TOCSY

mlevgpph19 pulse sequence (homonuclear Hartman-Hahn transfer using MLEV-17 sequence for mixing using two power levels for excitation and spinlock, phase sensitive, water suppression using 3-9-19 pulse sequence with gradients)¹¹²⁻¹¹⁴ was used (Figure 1.17). 2D- ^1H - ^1H -TOCSY experiments were used for the NMR assignment procedure (see section 1.3.4 NMR assignment) and for the extraction of $^3J_{\text{H}\alpha\text{-HN}}$ couplings (see section 1.4.3.4.2 NOEs and NMR coupling constant).

Acquisition parameters used: number of scans (NS) = 16-24, spectral width (SW) = 8.3 kHz (or 10.4 ppm) for both dimensions, size of fid (TD) = 4 or 8k for direct (F2) and 256 or 512 for indirect dimension (F1), relaxation delay (D1) = 1.3 s; mixing time (D8) = 55-80 ms. Before the Fourier transform, the FIDs were multiplied by a Lorentz-to-Gauss (GM) function with line broadening (LB) of -6 Hz in F2 and -8 Hz in F1 dimension and Gauss broadening (GB) of 0.12 and 0.1 in F2 and F1, respectively.

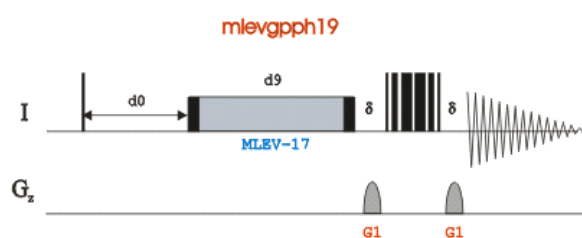


Figure 1.17 – ^1H - ^1H -TOCSY *mlevgpph19* pulse sequence.
Source: NMRGuide3.5¹¹⁵

1.3.3.4 ^1H - ^1H -NOESY

noesyphpr (2D homonuclear correlation via dipolar coupling, dipolar coupling may be due to NOE or chemical exchange, phase sensitive, with presaturation during relaxation delay

and mixing time)¹¹⁶ and *noesygppl9* (2D homonuclear correlation via dipolar coupling, dipolar coupling may be due to NOE or chemical exchange, phase sensitive, water suppression using 3-9-19 pulse sequence with gradients)^{112, 113} pulses sequence were used (Figure 1.18). 2D-¹H-¹H-NOESY experiments were used for the NMR assignment procedure (see section NMR assignment) and for the extraction of ³J_{H α -HN} couplings (see section NOEs and NMR couplings constant).

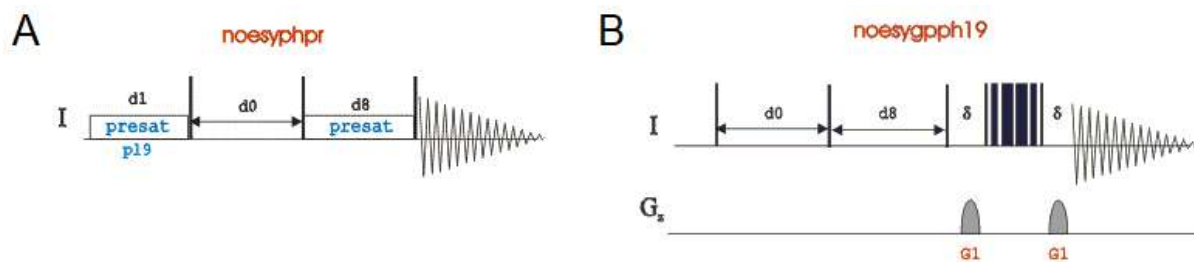


Figure 1.18 – ¹H-¹H-NOESY *noesyphpr* (A) and *noesygppl9* (B) pulse sequences.
Source: NMRGuide3.5^{115, 117}

Acquisition parameters used: number of scans (NS) = 48-96, spectral width (SW) = 8.3 kHz (or 10.4 ppm) for both dimensions, size of fid (TD) = 4 or 8k for direct (F2) and 256 or 512 for indirect dimension (F1), relaxation delay (D1) = 1.3 s; mixing time (D8) = 150-300 ms. Before the Fourier transform, the FIDs were multiplied by a Lorentz-to-Gauss (GM) function with line broadening (LB) of -6 Hz in F2 and -8 Hz in F1 dimension and Gauss broadening (GB) of 0.12 and 0.1 in F2 and F1, respectively.

1.3.3.5 ¹H-¹³C-, ¹⁵N-HSQC

2D-¹H-X-HSQC (HSQC, Heteronuclear Single Quantum Correlation), X being ¹³C or ¹⁵N, pulse sequences *hsqcetgpsi* (2D H-1/X correlation via double INEPT transfer; using sensitivity improvement; phase sensitive using Echo/Antiecho-TPPI gradient selection; with decoupling during acquisition; using trim pulses in INEPT transfer)¹¹⁸⁻¹²⁰ and *hsqcf3gppl9* (2D H-1/X correlation via double INEPT transfer; phase sensitive; with decoupling during acquisition; water suppression using 3-9-19 pulse sequence with gradients)^{112, 113} were used (Figure 1.19 shows a pulse sequence for a ¹H-¹³C-HSQC experiment).

Acquisition parameters used: number of scans (NS) = 16, spectral width (SW) = 8.0 kHz (or 10.0 ppm) for ^1H ; 1.9 kHz (or 24.0 ppm) for ^{15}N ; 7.4 kHz (or 37.0 ppm) for ^{13}C , size of fid (TD) = 2k for direct (F2) and 512 for indirect dimension (F1), relaxation delay (D1) = 1.2 s. Before the Fourier transform, the FIDs were multiplied by a Lorentz-to-Gauss (GM) function with line broadening (LB) of -4 Hz in F2 and F1 for ^{15}N and -20 Hz in F2 and -120 Hz in F1. Gauss broadening (GB) was 0.12 and 0.1 in F2 and F1, respectively.

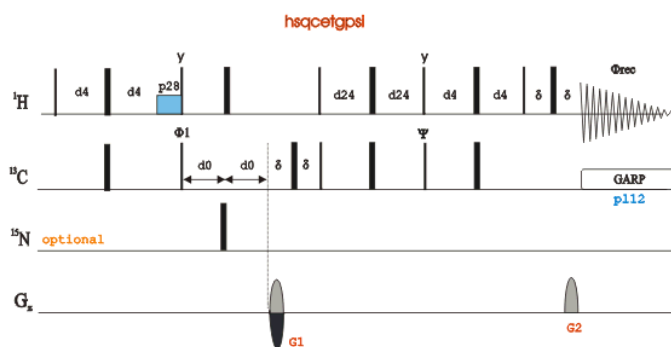


Figure 1.19 – Example of a ^1H - ^{13}C -HSQC *hsqcetgpsl* NMR pulse sequence.
Source: NMRGuide3.5¹²¹

1.3.3.6 Three-dimensional spectra

HNCA *hncagpwg3d* and HNC0 *hncogpwg3d* (Figure 1.20) pulse sequences were used. Both are 3D sequences with inverse correlation for triple resonance using multiple INEPT transfer steps, on/off resonance $\text{C}\alpha$ and C' pulses using shaped pulse, phase sensitive (t1), phase sensitive (t2), using constant time in t2, water suppression using watergate sequence.¹²²⁻¹²⁶

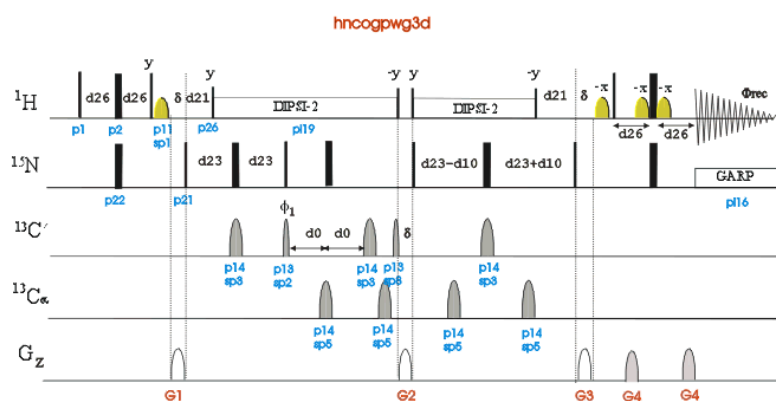


Figure 1.20 – Triple resonance *hncogpwg3d* pulse sequence for HNC0 experiment.
Source: NMRGuide3.5¹²⁷

CBCA(CO)NH *cbcaconhgpwg3d* pulse sequence was used. It is 3D sequence with inverse correlation for triple resonance using INEPT transfer steps, on/off resonance C α and C' pulses using shaped pulse, phase sensitive (t1), phase sensitive (t2), using constant time in t1, using constant time in t2, water suppression using watergate sequence.¹²⁸⁻¹³⁰

H(C)CH-TOCSY *hcchdigp3d* pulse sequence was used. It is a 3D sequence with inverse correlation using multiple INEPT transfer and carbon-carbon DIPSI3 spinlock, off resonance C' pulse using shaped pulse, phase sensitive (t1), phase sensitive (t2), spinlock during z-filter.¹³¹⁻¹³³

3D data was measured at 600 MHz Bruker spectrometer. Acquisition parameters used: number of scans (NS) = 24, spectral width (SW) = 6.0 kHz (or 10.0 ppm) for ^1H ; 1.4 kHz (or 24.0 ppm) for ^{15}N ; 3.6 kHz (or 24.0 ppm) for $^{13}\text{C}^\alpha$ in HNCA and CBCA(CO)NH; 8.3 kHz (or 55.0 ppm) for $^{13}\text{C}^\beta$; 8.8 kHz (or 58.0 ppm) for ^{13}C in H(C)CH-TOCSY; 1.1 kHz (or 7.2 ppm) for $^{13}\text{C}'$, size of fid (TD) = 2k for F3, 32 for F2 and 64 for F1, relaxation delay (D1) = 1.1 s. Before the Fourier transform, the FIDs were multiplied by a Lorentz-to-Gauss (GM) function with line broadening (LB) of -6 Hz in F3 and -8 Hz in F2 and F1 dimensions and Gauss broadening (GB) of 0.12 in F3 and 0.1 in F2 and F1, respectively.

1.3.4 NMR assignment

^1H , ^{13}C and ^{15}N chemical shift resonance assignments of A β (1-40) were first obtained using triple resonance spectra (assignment table in Appendix A, B): 2D- ^1H - ^1H -TOCSY (55 ms mixing time), 2D- ^1H - ^1H -NOESY (200 ms mixing time), 2D- ^1H - ^{15}N -HSQC, 2D- ^1H - ^{13}C -HSQC, 3D-HNCA, 3D-CBCA(CO)NH, 3D-HNCO and 3D-H(C)CH-TOCSY (60 ms mixing time). Experiments were recorded at 278 K, pH 7.1. Later, A β hydrogens at high pressure were (re)assigned by ^1H homonuclear experiments.

1.3.5 NMR data pretreatment

Data pretreatment was performed on chemical shifts in order to normalize or combine values from different nuclei (^1H , ^{13}C and ^{15}N). Additionally, in high pressure experiments, chemical shifts and peak intensities were corrected for intrinsic effects of pressure.

1.3.5.1 Normalization and combination of chemical shifts

^1H , ^{13}C and ^{15}N nuclei have chemical shifts of different magnitude. Even the same nucleus can present distinct δ values depending on its chemical group (e.g., ^{13}C can have chemical shifts as low as 0 ppm in methyl groups or as high as 220 ppm in carbonyl carbons). Therefore, weighting factors are needed to normalize chemical shifts values. The weighting factors w_{ik} are calculated not only for specific atom types i but also for specific amino acid types k and are based on inverse standard deviation (Equation 1) taken from the Biological Magnetic Resonance Data Bank (BMRB) in which more than six million chemical shifts are currently available.¹³⁴

$$w_{ik} = \frac{1}{\sigma_{ik}} \quad (1)$$

It is also more convenient to generate a unique, combined chemical shift (δ_{comb}) for each residue, which generally offers more stable values for data evaluation. Because of the required additivity of the chemical shifts the Hamming distance has been used to calculate δ_{comb} (Equation 2)¹³⁵

$$\delta_{\text{comb},j} = \frac{1}{N_a} \sum_{i=1}^{N_a} |w_i \delta_{ji}| \quad (2)$$

where N_a is the number of different atom types used and δ_{ji} the chemical shift of each atom type i in a residue j .

1.3.5.2 Pressure corrections

In most cases, the interpretation of high pressure NMR data is based on the analysis of chemical shift and intensity/volume changes,^{59, 97, 136} while only a few high pressure structures have been solved by NMR so far.¹³⁷ For a correct interpretation of the chemical shift and volume/intensity changes induced by pressure in proteins, non-structural effects present in the data should be removed.

Chemical shifts (δ) were corrected based on random coil peptides data. Complete ^1H , ^{13}C and ^{15}N data is now available.^{108, 138, 139} Corrected values (δ^*) were calculated applying first and second-order corrections according to Equation 3 (below)

$$\delta^*(p, T_0) = \delta(p_0, T_0) - [B_1(p - p_0) + B_2(p - p_0)^2] \quad (3)$$

Those B_1 and B_2 corrections are residue- and atom-specific and were studied in protected tetrapeptides Ac-Gly-Gly-Xxx-Ala-NH₂ (Xxx being one of the 20 standard amino acids).^{108, 138, 139}

Peak volumes and intensities were corrected for solvent compression based on Tris residual signal in the ^1H experiment or pure liquid water data reported by Chen et al.¹⁴⁰ The latter was extracted from sound speed measurements available up to 100 MPa and at a large range of temperature (273-373 K). The specific water volume reduces around 4% per 100 MPa and varies slightly with temperature.¹⁴⁰

1.3.6 NMR data analysis

In this section, we describe how the NMR data analysis was carried out. First, the methods used in the study of monomeric states of A β are presented. After that, there is a description on how diffusion NMR measurements were evaluated. Finally, we present the model used to explain the depolymerization of aggregated A β samples.

1.3.6.1 Monomeric thermodynamic characterization

Spectra of monomeric A β peptide were acquired to collect information about essentially all ^1H , ^{13}C , ^{15}N NMR-sensitive atoms. Chemical shifts and peak intensities properly corrected for pressure inherent response were fitted with a second-order polynomial function and with a thermodynamic state model.

1.3.6.1.1 Models and equations

In the absence of a suitable model, the fit of the chemical shifts pressure dependence can be done by a second order Taylor expansion, providing the first and second-order corrected pressure coefficient B_1^* and B_2^* according to Equation 4 (below)

$$\delta^*(p, T_0) = \delta_0^*(p_0, T_0) + B_1^*(p - p_0) + B_2^*(p - p_0)^2 \quad (4)$$

It was shown that in a two-state model, the ratio B_2^*/B_1^* is related to thermodynamic parameters, more specifically the ratio of the compressibility factors difference $\Delta\beta'$, and partial molar volumes ΔV between the states.¹⁴¹ To calculate B_2^*/B_1^* we used an inverse-variance ($1/\sigma^2$) weighting to give higher weights to curves with better quality (Equation 5)

$$\bar{R}_j = \frac{\sum_i \frac{R_{ji}}{\sigma_{ji}^2}}{\sum_i \frac{1}{\sigma_{ji}^2}} \quad (5)$$

where $R_j = B_2^*/B_1^*$ for residue j and the sums are calculated for each atom i in that residue. The standard deviation was calculated extrapolating the errors of B_1^* and B_2^* (Equation 6, some indexes were dropped out for clarity)

$$\sigma = \frac{|B_1^*| \sigma_{B_2^*} + |B_2^*| \sigma_{B_1^*}}{(B_1^*)^2} \quad (6)$$

When the quality of the pressure shifts is high enough, the data can be fitted using a detailed thermodynamic model. For fast exchange systems, an N -state model (generally two

or three-state) equation can be used to fit chemical shifts (Equations 7 – see Appendix L for formula demonstration – and 8)

$$\delta = \frac{\sum_{i=1}^N \delta_i \exp\left(-\frac{\Delta G_{1i}}{RT}\right)}{\sum_{i=1}^N \exp\left(-\frac{\Delta G_{1i}}{RT}\right)} \quad (7)$$

$$\Delta G_{1i}(p, T_0) = \Delta G_{1i}^0(p_0, T_0) + \Delta V_{1i}^0(p - p_0) - \frac{\Delta\beta_{1i}^{0'}}{2}(p - p_0)^2 \quad (8)$$

where ΔG_{1i}^0 , ΔV_{1i}^0 and $\Delta\beta_{1i}^{0'}$ are, respectively, the differences between the Gibbs free energy, the partial molar volumes and the partial molar compressibility factors between states 1 and i at temperature T_0 and pressure p_0 (the subscript '0' usually symbolizes $p = p_0$). The compressibility term is also called as $\Delta\kappa^{0'}$ by some authors. In this way, the chemical shifts are fitted according to Equation 7, writing ΔG_{1i} as described by Equation 8, allowing the determination of the thermodynamic parameters involved in the conformer(s) transition(s). For a two-state model, the equation is simplified and becomes a sigmoid fit, where the two horizontal plateaus are represented by δ_1 and δ_2 , the pure chemical shifts for state 1 and 2, in this order.

For systems in a mixed exchange, with N states, being M states in fast exchange and $N-M$ states in slow exchange, peak intensities (or volumes) are fitted with the following equation (Equation 9, this equation was fully demonstrated in Appendix M)⁹⁸

$$\frac{I_1(p)}{I_i} = a_i \frac{\sum_{i=1}^N \exp\left(\frac{-\Delta G_{1i}^0}{RT}\right) \sum_{i=1}^M \exp\left(\frac{-\Delta G_{1i}}{RT}\right)}{\sum_{i=1}^N \exp\left(\frac{-\Delta G_{1i}}{RT}\right) \sum_{i=1}^M \exp\left(\frac{-\Delta G_{1i}^0}{RT}\right)} \quad (9)$$

ΔG_{1i} is again expanded as Equation 8 and I_0 is the NMR peak intensity at $p = p_i$ (the lowest measured pressure point).

The probability of a molecule being in a certain state i (p_i) is a function of that state's energy (ΔG_{1i}) and the temperature of the system (T) and it is normalized by the canonical partition function (Equation 10)⁹⁸

$$p_i = \frac{\exp\left(\frac{-\Delta G_{1i}}{RT}\right)}{\sum_{j=1}^N \exp\left(\frac{-\Delta G_{1j}}{RT}\right)} \quad (10)$$

1.3.6.1.2 Fitting methodology

Chemical shifts and peak intensities were fitted in two separated fitting steps. Once intensities fitting need information from the fit of chemical shifts (Equation 9), the latter was accomplished first. All ^1H , ^{13}C , ^{15}N corrected chemical shifts from backbone and side chain nuclei were plotted against pressure and qualitatively classified in three groups, based on the curve appearance: (i) biphasic curves, which presents a parabolic behavior with an extremum; (ii) non-biphasic curves; (iii) linear and/or noisy curves. Curves from the last group were removed for providing few or no information. $^1\text{H}^{\text{N}}$ chemical shifts were obtained through ^1H - ^{15}N -HSQC and 2D-HNCO; values from the ^1H - ^{15}N -HSQC spectrum were used since it provided more accurate curves.

Corrected chemical shifts curves were subjected to a fitting routine using a three-state fast exchange model (Equation 7 with $N=3$, transitions 1-2 and 1-3) and a first-order approximation for ΔG_{ij} (Equation 8 with $\Delta\beta^0 = 0$). The fit was done with programming protocols written in R language¹⁴² using the Levenberg-Marquardt algorithm for non-linear fit. The thermodynamic parameters ΔG_{ij}^0 and ΔV_{ij}^0 were globally fitted (unique parameters for all plots) and δ_i were fitted individually (each curve with independent values). By this approach, the model presented $3n + 4$ parameters (n is the number of curves). Chemical shifts were normalized based on inverse standard deviation data of BMRB (see section 1.3.5.1 Normalization and combination of chemical shifts), where statistics are constantly updated.¹³⁴ Fitting parameters were initialized and limited to certain ranges according to Table 1.1.

Table 1.1 – Starting values and restriction of parameters used in chemical shifts fitting (transitions 1-2 and 1-3). ΔG^0 and ΔV^0 starting values was set according to the transition. δ_i (i being each considered state) was range-limited based on their initial values, depending on each nuclei.

| | Starting value | | Inferior limit | | Superior limit | Range limit |
|-------------------------------|---|--------------------|----------------|--------------------|----------------|-----------------------------|
| ΔG_{ij}^0 (J/mol) | 3000 1000 | for 1-2 for 1-3 | 0 -5000 | for 1-2 for 1-3 | 12000 | |
| ΔV_{ij}^0 (ml/mol) | -50 -30 | for 1-2 for 1-3 | -100 | | 0 | |
| δ_i (ppm) | $\delta_1, \delta(p)$ in the lowest p | | | | 2 | for ^1H |
| | $\delta_2, \delta(p)$ in the turning point | | | | 6 | for $^1\text{H}^{\text{N}}$ |
| | $\delta_3, \delta_1 + \text{average of } \delta(p)$ | | | | 10 | for ^{13}C |
| | | | | | 20 | for ^{15}N |
| | | | | | 30 | for $^{13}\text{C}'$ |

Source: By the author.

Intensity plots were also fitted with an R-language script according to Equation 9 and ignoring the use of the $\Delta\beta^0$ term in Equation 8. Noisy and/or linear plots were also removed from the analysis. ΔG^0_{slow} and ΔV^0_{slow} , the parameters involved in a probable slow transition, were obtained through global curves fitting (resulting in those two final parameters for all curves). I_0 in Equation 9 were adjusted individually for each plot. Parameters representing fast exchanges (ΔG^0_{12} , ΔG^0_{13} , ΔV^0_{12} , ΔV^0_{13}) were maintained fixed during intensities fit conforming to values found by chemical shift data fit previously performed. The fit presented $n + 2$ parameters (n is the number of curves) which were initialized and limited to certain ranges according to Table 1.2.

Table 1.2 – Starting values and restriction of parameters used in peak intensity fitting (transition 1-4).

| | Starting value | Inferior limit | Superior limit | Range limit |
|-------------------------------|--------------------------|----------------|----------------|-------------|
| ΔG_{ij}^0 (J/mol) | 6000 | 0 | 30000 | |
| ΔV_{ij}^0 (ml/mol) | -70 | -150 | 0 | |
| I_0 (a.u.) | $I(p)$ at the lowest p | | | 50% |

Source: By the author.

In order to obtain the statistics and errors of the fitting, we performed data sampling. In the chemical shifts fit, one of the plots in the pool was removed and the rest of the data was fitted as described before. At each step of this routine, only the $n-1$ remaining plots were selected and considered by the program. This step was repeated n times until all plots were removed exactly once. A distribution of the ΔG^0_{ij} and ΔV^0_{ij} parameters was treated as a

normal distribution. Errors were calculated for a confidence interval of 95% (3σ , where σ is half the Gaussian width at half height).

1.3.6.2 Monomeric structural characterization

Homo- and heteronuclear data were used in the structural characterization of A β monomers. Here we present the methods involved in the prediction of secondary structure and in the qualitative analysis of NOEs.

1.3.6.2.1 Prediction of secondary structures

Predictions of secondary structural elements (extended strands, helices and loops) were performed with $^{15}\text{N}^{\text{H}}$, $^{13}\text{C}^{\alpha}$, $^{13}\text{C}^{\beta}$, $^{13}\text{C}'$, $^1\text{H}^{\text{N}}$ and $^1\text{H}^{\alpha}$ chemical shift data using the program TALOS+ (torsion angle likelihood obtained from shift and sequence similarity).¹⁴³ TALOS+ uses two levels of classification: first, the sequence is divided in tri-peptides and δ parameter sets are generated; the second level is sequence-based and uses information of around 200 structures from the Protein Data Bank (PDB). It is an enhanced version of the earlier TALOS which improves upon the original database mining approach by including a neural network classifier. An online server was used to do the predictions.¹⁴⁴ Proteins which have an amino acid sequence identical to A β were excluded from the program database. The offset δ correction available in the program was turned off.

1.3.6.2.2 NOEs and $^3J_{\text{HN-H}\alpha}$ couplings

We analysed nuclear Overhauser effects (NOEs) extracted from ^1H - ^1H -NOESY spectra using a qualitative approach. In the analysis, short and medium-range NOEs were combined to the $^3J_{\text{HN-H}\alpha}$ NMR coupling constants to give a better picture of the secondary structures in the protein (although the boundaries of these segments are always difficult to

define precisely). Qualitative, or semi-quantitative as some authors prefer, NOEs are usually analyzed in the form of graphs as in Figure 1.21, where lines connect residues that have correlation on the spectrum with width denoting the intensity of the correlation (and representing indirectly the distance among the hydrogens involved, d_{ij}). The presence of certain contacts indicates different types of secondary structure and turns.^{145, 146}



Figure 1.21 – NOE patterns and $^3J_{HN-H\alpha}$ scalar couplings expected for different types of secondary structures in proteins. The width of the lines represents the NOE intensity (wide line, strong correlation; intermediate width, medium correlation; thin line, weak correlation).

Source: CLORE; GRONENBORN¹⁴⁶

NOESY cross-peak volumes were referred to the 2.5 Å distance of H^{δ} - H^{ϵ} protons in the aromatic ring of phenylalanine (Phe-4, Phe-19 and Phe-20) and tyrosine (Tyr-10) residues using an r^{-6} proportionality. Distances were divided into ‘weak’, ‘medium’ and ‘strong’ classes based on Table 1.3.

Table 1.3 – NOE classification based on distance ranges.

| Restrain class | Distance range (Å) |
|----------------|------------------------|
| Weak | 3.5 – 5.0 |
| Medium | 2.8 – 3.5 |
| Strong | 1.8 ^a – 2.8 |

^a twice the proton Van der Waals radius

Source: By the author.

$^3J_{HN-H\alpha}$ couplings were extracted from the direct dimension of 1H - 1H -TOCSY spectra recorded with 8k points. First, the digitally filtered data was converted into analog type data using the ‘convdta’ command. This conversion is necessary since the beginning of the FID in digital data is flat and this affects the backward linear prediction (typically leading to spectral

baseline distortions). We applied a backward prediction and processed the F2 dimension with 64k points. These couplings are related to ϕ (phi) backbone torsion angle accordingly to the following relation derived from the Karplus equation (Equation 11)¹⁴⁷

$${}^3J_{\text{HN-H}\alpha} = 6.4 \cos^2(\phi - 60) - 1.4 \cos(\phi - 60) + 1.9 \quad (11)$$

Using the ϕ angle reported for common secondary structures in proteins, it is possible to calculate the expected couplings constants: for α -helices the value is about 3.9 Hz, for 3_{10} helices it is 5.6 Hz and on β -strands it is higher, between 8.9 and 9.7 Hz. In general, ${}^3J_{\text{HN-H}\alpha}$ couplings sense the backbone degree of extension.

1.3.6.3 Diffusion NMR experiments

The intensity change in NMR diffusion experiments can be described as (Equation 12)

$$\frac{I(g)}{I_0} = \exp(-Dg^2\alpha) \quad (12)$$

where α depends on the pulse sequence used, the length and absolute maximum strength of gradients and length of different delays (as Δ and δ). But since the gradient strength $g = 0$ is perturbed by artifacts, we used the intensity in the lowest gradient as comparison (i.e., I_{rel} or typically, $I_{2\%}$) (Equation 13)

$$\frac{I(g)}{I_{rel}} = A \exp(-Cg^2) \quad (13)$$

with C being a constant proportional to the diffusion constant.

As smaller the molecule is, bigger is the diffusion constant (D) and, consequently, the signal intensity decay will have higher slope. We can obtain the values of parameters A and C by fitting the plot using Equation 13. By definition, C is proportional to D , the diffusion constant. The Stokes-Einstein diffusion law tells us that the diffusion constant is indirectly proportional to the hydrodynamic radius (R_h) or Stokes radius (Equation 14)

$$C \propto D = \frac{k_B T}{6\pi\eta R_h} \quad (14)$$

where k_B is the Boltzmann constant ($1.38 \cdot 10^{-23}$ J/K), T is temperature and η is the medium viscosity.

The radius R_h for a compound can be calculated knowing the same quantity for a reference compound, R_h^{ref} , using a simple relation (Equation 15)

$$R_h = \frac{D^{ref}}{D} R_h^{ref} \quad (15)$$

In the calculations we used R_h of 0.307 nm for Tris and/or 0.346 nm for DSS,¹⁴⁸ both contained in the sample as internal standard.

1.3.6.4 A β depolymerization model

The polymerization of A β into oligomers and amyloid fibers is an intricate mechanism, which involves several types of macromolecular intermediates of different structures and sizes. Despite of the fact that those conformers are interexchanging relatively rapid, the formation of mature fibers is a slow process.³⁵

Different methods have been proposed to analyze the amyloid aggregation process.¹⁴⁹ The simplest model^{150, 151} considers that polymerization can be described by a single binding constant of the monomer to the fiber, regardless of its size. This model also indirectly assumes that the aggregation nuclei have a defined structure and is composed by the same number of monomers.

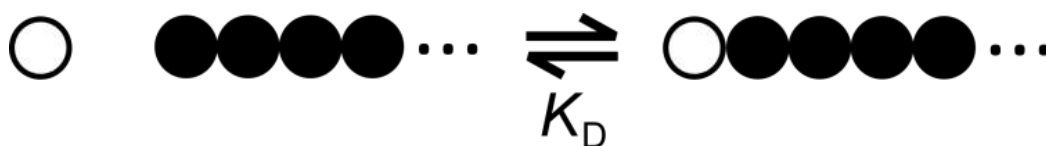


Figure 1.22 – Simple model to describe the polymerization of globular proteins.^{150, 151} A monomer (open circle) elongates a polymer constituted of n monomeric parts (closed circles) resulting in a polymer of $n+1$ monomeric parts.

Source: By the author.

The monomeric concentration (c_1) can be written in terms of the total concentration (c_T , measured in monomeric units) and the dissociation constant (K_D) (Equation 16, a full demonstration of the equation is presented in Appendix N)

$$c_1 = K_D \left(1 + \frac{K_D}{2c_T} - \sqrt{\left(1 + \frac{K_D}{2c_T}\right)^2 - 1} \right) \quad (16)$$

For systems where the total protein concentration is much higher than the dissociation constant K_D ($c_T \gg K_D$, mathematically), c_1 can be simply written as (Equation 17)

$$c_1 = K_D = \exp\left(\frac{-\Delta G}{RT}\right) \quad (17)$$

where ΔG is the Gibbs free energy difference involved in the addition of monomers to the fibers, R is the ideal gas constant and T is the absolute temperature (in Kelvin).

In case of pressure-related processes, K_D is calculated by expanding ΔG as a second order Taylor expansion (Equation 18)

$$K_D = \exp \left[- \left(\frac{\Delta G^0 + \Delta V^0(p - p_0) - \frac{\Delta\beta'^0}{2}(p - p_0)^2}{RT} \right) \right] \quad (18)$$

where ΔG^0 , ΔV^0 and $\Delta\beta'^0$ are the variation of Gibbs free energy at ambient pressure (0.1 MPa), partial molar volume and molar compressibility, respectively.

1.4 RESULTS

1.4.1 Attempts to obtain recombinant β -amyloid peptides

A protocol attempt was devised in order to obtain A β peptide samples that would present adequate purity and quantity to perform the desired NMR experiments. Many *in vitro* studies of A β reported in the literature have been conducted with synthetic A β . However, it was found that synthetic A β do not present the same aggregation behavior than recombinant

A β .¹⁵² Experiments suggest that synthetic A β aggregation is slower than A β recombinantly produced (Figure 1.23). It is believed that the presence of racemized peptides in synthetic A β slow A β incorporation into the regular quaternary structure of growing β -amyloid fibrils. Thus chemical synthesis seems not to be a suitable method to obtain β -amyloid peptide.

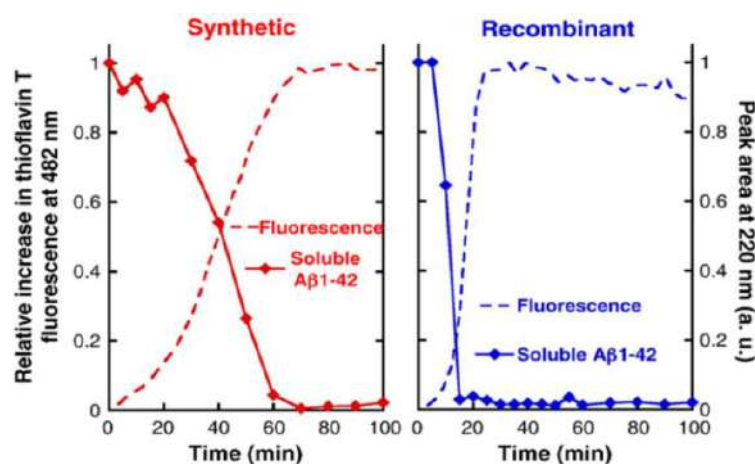


Figure 1.23 – Different aggregation behavior shown by fluorescence assays for chemically synthetic (left, red) and recombinant (right, blue) A β peptide.

Source: FINDER¹⁵²

A published protocol describes the recombinant production and purification of A β (1-40) and A β (1-42) peptides in a construct with no additional residues.¹⁵² The peptide is expressed in fusion with a His-tag and its solubility is increased by a segment comprising 19 repeats of the tetrapeptide sequence NANP (Asn-Ala-Asn-Pro). TEV protease recognition sequence (ENLYFQ↓) is placed right before the peptide sequence. The natural TEV recognition sequence contains an additional glycine in position P1' (residue C-terminal to the cleavage site), which becomes the first residue of the C-terminal cleavage product. As 90% cleavage efficiency of TEV protease is retained when the position P1' is occupied by aspartate,¹⁵³ which is the first residue of A β peptide, this allows the release of the authentic A β sequence.

The A β (1-40) and A β (1-42) plasmids cloned into pRSET_A vector were kindly provided by Prof. Dr. Rudi Glockshuber (ETH Zurich). However, the expression level was demonstrated to be rather low (Figure 1.24A). To improve the expression system, A β (1-40) and A β (1-42) sequences were transferred to pET28a vectors by using *Nde*I and *Hind*III restriction enzymes (Fast Digest[®], Thermo Scientific) and performing a ligation reaction using T4 DNA ligase (Invitrogen). Competent *E. coli* BL21(DE3) cells were transformed with

a pET28a vector containing the peptide constructions. The expression was conducted in LB medium containing 50 $\mu\text{g/ml}$ of kanamycin at 37 °C. After reaching $\text{OD}_{600\text{nm}}$ of 0.6, the culture was induced with 0.5 mM IPTG for 3 hours, also at 37°C. Cells were harvested by centrifugation (4500 rpm, 30 min, 4 °C), resuspended with 10 ml/g pellet of lysis buffer (20 mM Tris-HCl, 150 mM NaCl, pH 8), sonicated and centrifugated (11000 rpm, 30 min, 4 °C).

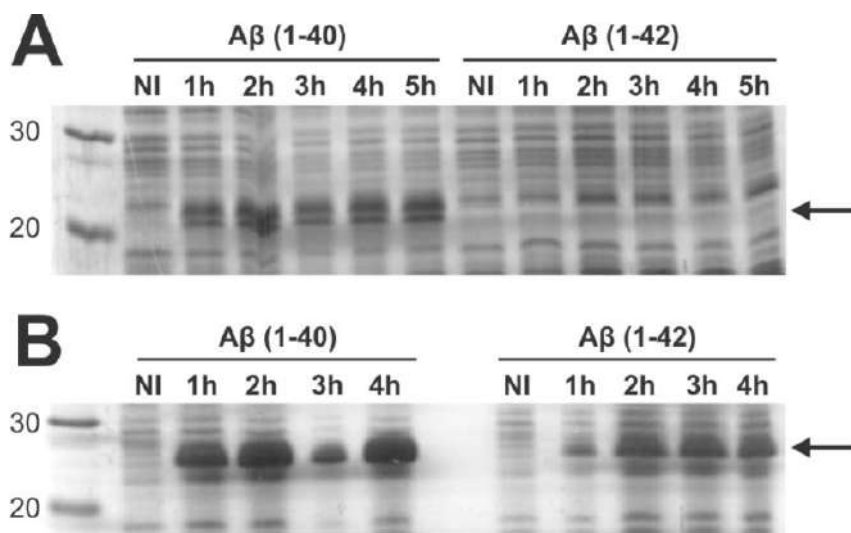


Figure 1.24 – Expression test of A β attached to fusion protein in LB medium using (A) pRSET_A construct and (B) pET28a construct. Cell extract was collected before (NI, non-induced) and after IPTG induction (1, 2, 3, 4 and 5 hours). Cultures were induced with 1 mM IPTG and kept after that at 37 °C, 150 rpm. Expressed protein position is indicated by arrows. First lane contains molecular mass markers with their approximate mass in kDa.

Source: By the author.

Solubilization buffer (20 mM Tris-HCl, 150 mM NaCl, 8 M urea, 20 mM imidazole, pH 8) was used to resuspend the insoluble fraction, fraction which around 90% of the expressed protein was found, at ambient temperature for 1-2 hours. The solution was centrifuged (11000 rpm, 20 min, 4 °C) and its soluble part was applied on Qiagen Ni-NTA resin, previously equilibrated with solubilization buffer. The resin was washed with 10-15 CV (column volume) with solubilization buffer. To remove the denaturant agent (urea), lysis buffer + 20 mM imidazole was used (~10 CV) followed by lysis buffer + 60 mM imidazole (~10 CV). Since TEV efficiency is reduced in sodium chloride, the protein was eluted with 10 CV directly into the cleavage buffer (20 mM Tris-HCl, 0.5 mM EDTA and 1 mM DTT, pH 8).

To cleave the expressed protein and to release the A β peptide, recombinant His₆-TEV(S219V)-Arg₅ was used (from 1:10 to 1:15 m/m TEV/expressed protein ratio). TEV clones were provided by Prof. Dr. Mauricio Báez Larach, Universidad de Chile. The cleavage reaction was performed overnight at 4 °C followed by 5 hours at 25 °C. After that, the pH was

shifted to 5.3 (isoelectric point of A β peptide) to induce peptide aggregation using diluted HCl. The pellet was separated by centrifugation (16000 rpm, 10 °C) and stored at -80 °C. After this point, the samples proceed to HPLC chromatography in order to obtain pure A β . A polyacrilamide gel showing all purification steps is presented in Figure 1.25.

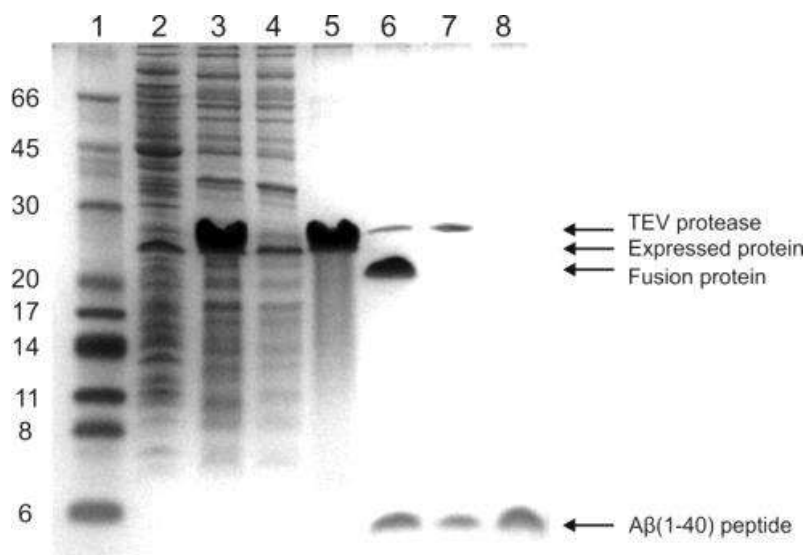


Figure 1.25 – Tricine/polyacrilamide (16%) SDS-PAGE of A β 40 peptide purification. 1) Molecular mass marker (MWs are presented in kDa), 2) soluble fraction, 3) insoluble fraction, 4) flowthrough, 5) elution by imidazol, 6) after TEV protease cleavage, 7) elution after second purification, 8) sample after HPLC purification.

Source: By the author.

Two separation approaches were tested (Figure 1.26), one using a SEC column (YMC-Pack Diol 60, 8.0 x 300 mm) and another with a reverse phase C8 column (YMC C8 Pack, 4.6 x 250 mm). The former used 50 mM sodium phosphate buffer pH 7.3 containing 8 M Gnd-HCl to solubilize the insoluble fraction of the cleavage and 50 mM sodium phosphate buffer pH 7.3 containing 30% (v/v) acetonitrile, 300 mM NaCl as mobile phase. The latter used 70% formic acid as solubilizing agent and 0.05% trifluoroacetic acid with acetonitrile/water as mobile phase, with gradient elution.

However, none of the HPLC columns used presented the performance needed to adequately purify A β (1-40) peptide. The SEC column showed a good resolution but failed in separate A β from guanidinium-chloride, which was used for solubilizing the sample. This guanidinium-chloride was later removed by high pH dialysis (typically 20 mM NaOH). Moreover, A β presented a high rate of adsorption (around 50%) into the stationary phase even using high amounts of NaCl and ACN in the running buffer. On the other hand, the C8 column showed an extremely broad A β elution.

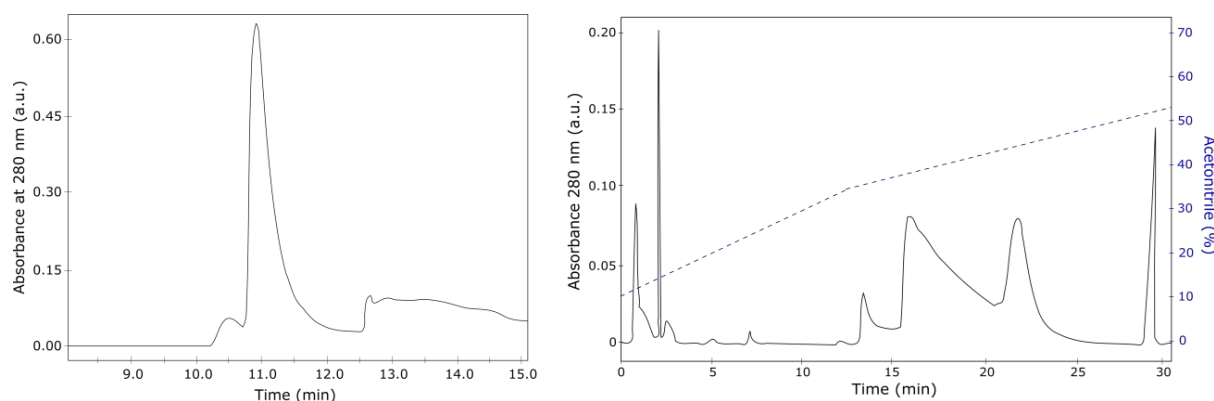


Figure 1.26 – HPLC purifications of A β 40 after tag removal. Flow rate: 1 ml/min. Left panel: size exclusion chromatography (column YMC-Pack Diol 60, 8.0 x 300 mm) using 50 mM sodium phosphate buffer pH 7.3, containing 30% (v/v) acetonitrile and 300 mM NaCl. The insoluble fraction of the cleavage was dissolved in 50 mM sodium phosphate buffer pH 7.3 containing 8 M guanidinium chloride. The major peak around 11 minutes corresponds to A β . Right panel: Reverse phase chromatography (column YMC C8 Pack, 4.6 x 250 mm). Mobile phase was composed by 0.05% trifluoroacetic acid with acetonitrile (ACN) in distilled Milli-Q water. The insoluble fraction of the cleavage was dissolved in 70% formic acid. To improve resolution, fractions were eluted by gradient of 2% ACN/min until 12 minutes and by 1% ACN/min after that. A β elutes in a broad peak between 15-20 minutes.

Source: By the author.

Another obstacle in A β purification could not be solved: the coelution of A β and the uncleaved protein. It is possible that after A β is released by the tag cleavage, it coaggregates with the expressed protein. These could not be separated either by HPLC or immobilized nickel columns. The reluctance of A β to be purified and the possibility to purchase such recombinant peptides commercially made us interrupt the optimization of the protocol to devote time to the NMR experiments.

1.4.2 Depolymerization of A β by high pressure

A β depolymerization study was conducted in order to obtain thermodynamic parameters of the polymerization process. Even if it is the depolymerization that is being monitored, important polymerization parameters as ΔG^0 (difference in Gibbs free energy) and ΔH^0 (difference in enthalpy of binding) remains the same in reversible processes (which is the case). The A β peptide in high concentrations aggregates into species of high molecular mass, which are not visible by the NMR technique due to the highly broadened peaks. Assuming that NMR visible signals in solution essentially correspond to monomeric A β ,¹⁵⁴ it is possible to quantify its free monomeric concentration, c_1 , using 1D NMR proton spectra (Figure 1.27).

The application of pressure leads to an increase of the NMR signal of the peptide indicating a depolymerization of polymers.

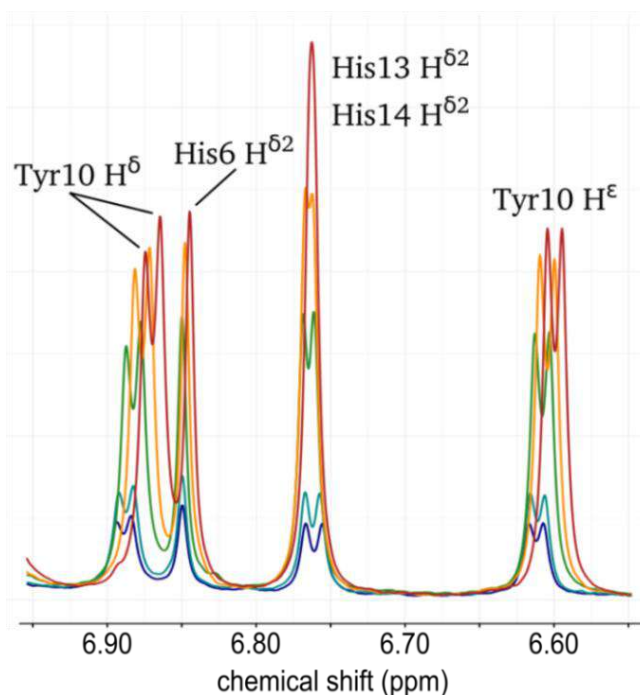


Figure 1.27 – Depolymerization of a 750 μM $\text{A}\beta$ sample followed by 1D- ^1H NMR spectra at 283 K. Five pressure points are depicted, 0.1 MPa (dark blue), 20 (cyan), 60 (green), 100 (yellow) and 150 MPa (red). Some of the peaks shown and labeled were used to quantify the monomeric concentration of $\text{A}\beta$.

Source: By the author.

Here it is useful to evaluate the role of each thermodynamic parameter (ΔG^0 , ΔV^0 and $\Delta\beta'^0$) in the depolymerization process. Figure 1.28 shows simulated curves changing one of the thermodynamic parameters (ΔG^0 , ΔV^0 or $\Delta\beta'^0$) individually, to access their impact on curve behavior. ΔG^0 , the molar difference in Gibbs free energy, roughly only shifts the curve vertically, being the only parameter responsible for the monomeric concentration at ambient pressure (Figure 1.28, panel A). ΔV^0 , the partial molar volume difference, modifies the derivative of the function at 0.1 MPa and changes the curve (up or down) in the same direction as ΔG^0 does (Figure 1.28, panel B). $\Delta\beta'^0$, the molar compressibility factor, has a great impact in function concavity (Figure 1.28, panel C). Differently from ΔV^0 , $\Delta\beta'^0$ presents a critical behavior around zero (Figure 1.28, panel C, light blue curve). Higher than zero, the curve saturates and never goes down in higher pressures. Below zero, the curve is concave down and it decays from an intermediate pressure on, which would be interpreted in a simple model as a repolymerization at high pressures. Note that, as expected, c_1 can never be higher than c_T in the same pressure.

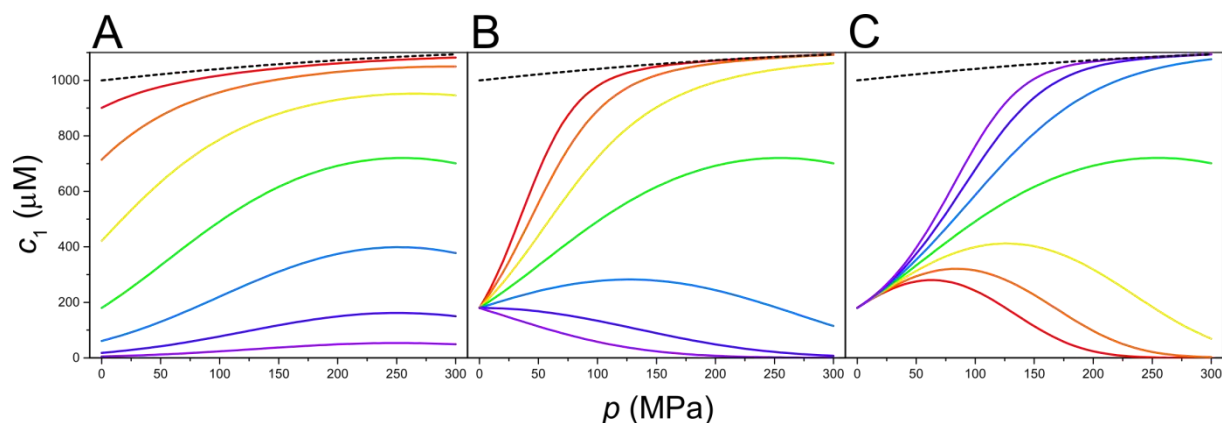


Figure 1.28 – Simulation of protein depolymerization curves by high hydrostatic pressures up to 300 MPa. Curves were plotted according to Equation 16. In all panels only one thermodynamic parameter was changed (ΔG^0 , ΔV^0 or $\Delta\beta^0$) in equal intervals. A) ΔG^0 from 10 (red) to 30 kJ/mol (purple). B) ΔV^0 from -125 (red) to +25 ml/mol (purple). C) $\Delta\beta^0$ from -0.8 (red) to +0.4 ml MPa⁻¹ mol⁻¹ (purple). c_T is 1 mM at ambient pressure and its value increases with pressure due to solvent compression (dashed black line). Temperature is 298 K. The intermediate curve (green) in all panels has the same parameters ($\Delta G^0 = 20$ kJ/mol, $\Delta V^0 = -50$ ml/mol and $\Delta\beta^0 = -0.2$ ml MPa⁻¹ mol⁻¹).

Source: By the author.

A sample of A β (1-40) at 750 μ M concentration was subjected to increasing pressures in three different temperatures (283, 288 and 293 K) and some NMR signals (Figure 1.29) were quantified and compared to the intensity of residual Tris peak present in the sample. Tris concentration was derived from an independent experiment using a known concentration of DSS added to the NMR buffer in D₂O (P4D buffer). Data fitting is shown in Figure 1.29. Those experiments were collected and initially treated by Dr. Markus Beck Erlach¹⁴⁸ and Prof. Dr. Claudia Elisabeth Munte and the following results were recently published.⁷²

High pressure was able to depolymerize the sample, increasing the signal of monomeric A β (closed circles, Figure 1.29). At around 180 MPa, curves reach a plateau and no depolymerization is further obtained. The maximum value achieved for c_1 is temperature dependent (closed circles, Figure 1.29), being higher at lower temperatures. However, even at the lowest temperature (283 K), the sample was not completely depolymerized. At this temperature, only 70% of the sample was monomeric at the highest pressure. No significant increase in peak intensity was observed for a low concentrated sample measured at 277 K (open circles, Figure 1.29). Table 1.4 presents values for important thermodynamic parameters obtained from the fit of the curves. In the temperature range used, from 283 to 303 K, all thermodynamic parameters behave linearly, which allows the extrapolation to near temperatures (Figure 1.30).

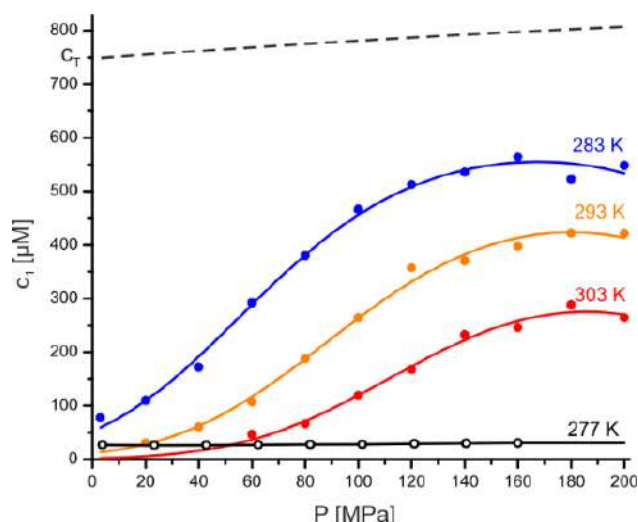


Figure 1.29 – Pressure induced depolymerization of A β . The monomeric concentration c_1 of A β is plotted as function of pressure and fitted with Equation 16 (see Methods and Materials). (Closed circles) Monomeric concentration from 1D NMR spectra of 750 μM A β at different temperatures and pressures in P4D buffer. The total A β concentration c_T is represented as broken line. Values for this figure are not corrected for solvent compressibility effects. The parameters obtained from the data fit are given in Table 1.4. (Open circles) Compressibility corrected c_1 for a sample containing 30 μM A β at 277 K, in P4H buffer. The quantification of the NMR visible peptide was performed by comparing the integrals of non-exchangeable protons of the H $^\epsilon$ -resonance line of Tyr-10 and the H $^\epsilon$ -resonances of His-6, His-13, and His-14.

Source: CAVINI⁷²

Table 1.4 – Thermodynamic data of A β polymerization. c_1 , free monomer concentration; c_T , total A β concentration; K_D , monomer-polymer dissociation constant; ΔG^0 , difference of Gibbs free energy at ambient pressure; ΔV^0 , difference of partial molar volume; $\Delta\beta^{*0}$, difference of molar compressibility. Errors were calculated for a confidence interval of 95%. Experimental conditions as in Figure 1.29.

| $T(\text{K})$ | c_1/c_T ($p = 200 \text{ MPa}$) | K_D ($p = 0.1 \text{ MPa}$) (μM) | K_D ($p = 200 \text{ MPa}$) (mM) |
|---------------|---------------------------------------|---|--|
| 283 | 0.70 | 88.3 | 2.7 |
| 293 | 0.55 | 14.6 | 1.5 |
| 303 | 0.38 | 2.8 | 0.7 |
| $T(\text{K})$ | ΔG^0 (kJ mol^{-1}) | ΔV^0 (mL mol^{-1}) | $\Delta\beta^{*0}$ ($\text{mL MPa}^{-1} \text{ mol}^{-1}$) |
| 283 | 22.0 ± 0.3 | -98 ± 6 | -0.59 ± 0.05 |
| 293 | 27.1 ± 0.4 | -125 ± 6 | -0.69 ± 0.04 |
| 303 | 32.2 ± 1.0 | -148 ± 15 | -0.78 ± 0.10 |

Source: CAVINI⁷²

The K_D of polymerization from the present experiment is an important quantity to estimate the presence of oligomers/polymers in A β samples, given that K_D is considered equal to the critical concentration for polymerization (often called as c_{CMC} , in allusion to detergents solubility). Figure 1.31 shows the maximum monomeric concentration for different total

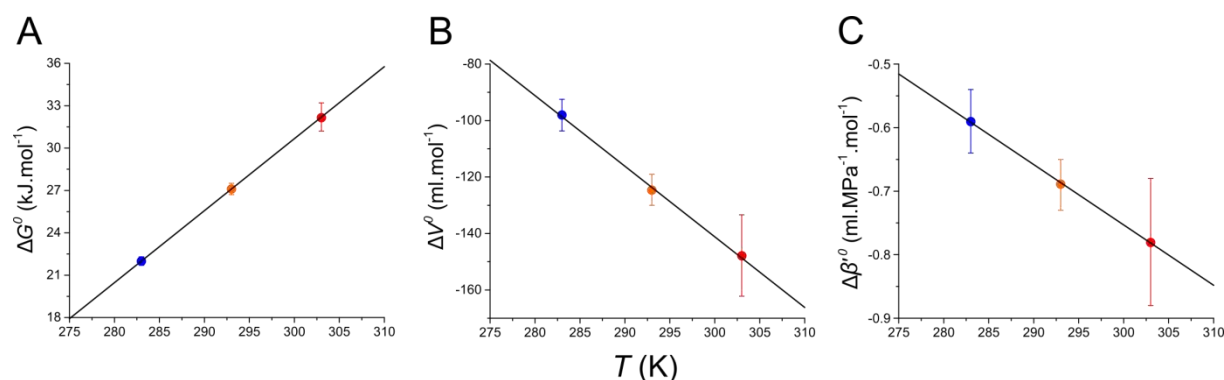


Figure 1.30 – Temperature dependence of ΔG^0 , ΔV^0 and $\Delta\beta^{*0}$ for A β polymerization. ΔG^0 , ΔV^0 and $\Delta\beta^{*0}$ (same data as in Table 1.4) are shown in panels A, B and C, respectively. In the temperature range shown, all three parameters behave linearly (linear fit is shown) which allows the extrapolation to other temperatures.

Source: By the author.

concentrations and K_D for each different temperature, using the parameters in Table 1.4. K_D is 280 μM at 277 K (extrapolated data) and increases strongly with decreasing temperatures, in line with the observed polymerization induced by high temperatures. The proportion of monomers when c_T is equal to K_D at 0.1 MPa goes from 89% at 277 K to 99% at 303 K (Figure 1.31).

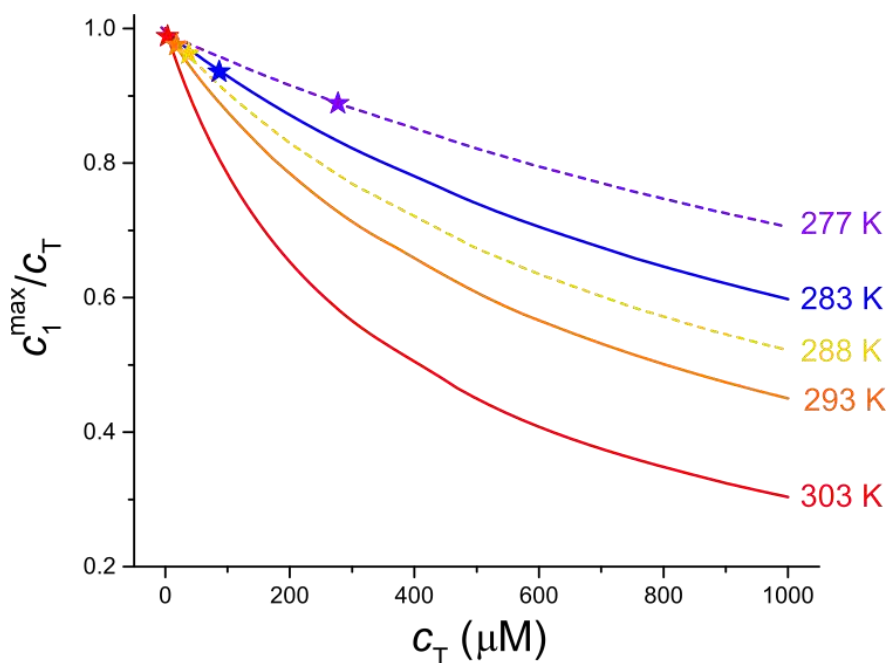


Figure 1.31 – A β maximum depolymerization obtained for different total sample concentrations at different temperatures. Data was calculated using parameters presented on Table 1.4. The vertical axis shows the maximum ratio of monomeric A β compared to its total concentration, represented in the horizontal axis. Temperatures of 277 and 288 K (dashed lines) were calculated extrapolating parameters obtained for the other temperatures. Stars represent the maximum relative depolymerization at K_D calculated at 0.1 MPa.

Source: By the author.

The negative values found for $\Delta\beta^0$ (values in Table 1.4) indicate that repolymerization at high pressures (when the compressibility term becomes comparable with the other terms in Equation 18) may occur. It is possible to see a slight decrease of the monomeric concentration over 180 MPa. Unfortunately, in this experiment, pressures higher than 200 MPa could not be measured in our NMR setup due to pressure limitation of the ceramic cell. In order to directly see the possible repolymerization at high pressures, another data set was recorded at 277 K using a high pressure ceramic cell that tolerates up to 300 MPa. Here, the buffer in H₂O (P4H buffer) was used. The concentration employed was 360 μ M and only points from 200 to 300 MPa were measured. Figure 1.32 shows the fitting of the data curve (panel A) and selected portions of 1D spectra, evidencing the decrease of A β signal with pressure (panel B). Tyr10 H ϵ peak reduction is even more pronounced if we consider the solvent compressibility (1.8% in the 200-300 MPa pressure range). The peak from residual undeuterated Tris (Figure 1.32, panel C) increases with pressure, similarly as c_T , and it is shown as an experimental control.

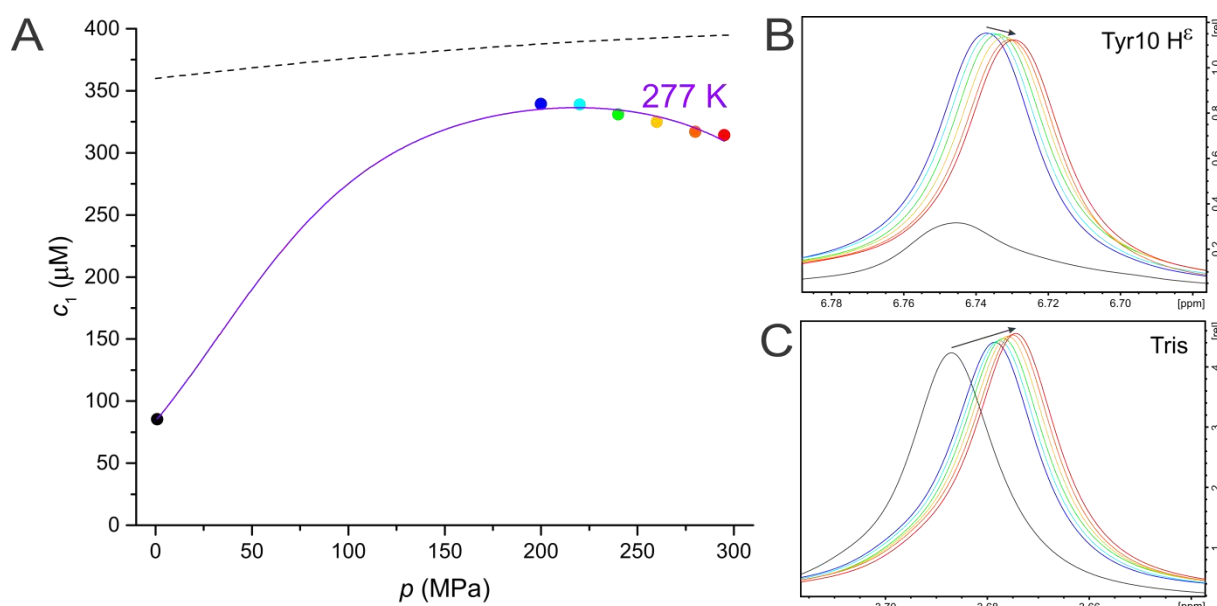


Figure 1.32 – A β shows repolymerization at high pressures. (A) Monomeric concentration from 1D NMR spectra of 360 μ M A β sample in P4H buffer at 277 K plotted against the pressure and fitted with Equation 16 (see Materials and methods). c_T is represented as a broken line. Concentration values were not corrected for solvent compressibility effects. The quantification of the NMR visible peptide was performed by averaging the integrals of non-exchangeable protons of the Tyr-10 H ϵ resonance line (in panel B) and all aliphatic H γ and H δ protons from 0.7 to 1.0 ppm. (B and C) Selected regions of 1D spectra processed with a high line broadening (15 Hz) to remove coupling splitting. Each pressure is shown in a different line color, keeping the same color scheme used for dots in panel A: black, 0.1 MPa; rainbow color, from 200 MPa (blue) to 295 MPa (red). (B) Tyr-10 H ϵ peak shows intensity decrease with pressure after 200 MPa. (C) Tris peak is affected by sample volume decrease with pressure, originated from solvent compression.

Source: By the author.

1.4.3 Characterization of A β monomer

The β -amyloid peptide 1-40 was characterized both thermodynamically and structurally using high pressure NMR experiments. Information from chemical shifts, peak intensities, NOEs and J couplings was used, which is presented next.

1.4.3.1 High pressure NMR data set

In order to obtain a reliable pressure dependence of the different conformational states of the A β (1-40) peptide, a complete set of high pressure (HP) NMR spectra was recorded. The pressure range was restricted by the limit of the sample ceramic cell (maximum pressure limit of 200 or 300 MPa). ^1H - ^{15}N -HSQC, ^1H - ^{13}C -HSQC, 2D-HNCO, ^1H - ^1H -TOCSY and ^1H - ^1H -NOESY HP-NMR spectra were acquired (important experimental variables and parameters are presented in Table 1.5). Heteronuclear spectra (^1H - ^{15}N -HSQC, ^1H - ^{13}C -HSQC and 2D-HNCO) allowed the thermodynamic characterization of A β monomers (section 1.4.3.3 Thermodynamic analysis) and the prediction of secondary structure content (section 1.4.3.4.1 Secondary structure propensities). Homonuclear NOESY and TOCSY spectra were used to provide proton contacts and $^3J_{\text{HN-H}\alpha}$ couplings, respectively (section 1.4.3.4.2 NOEs and NMR coupling constant).

Considering we used a low peptide concentration (below 90 μM , to prevent oligomer formation), a reduced sample volume in the high pressure cell (around 300 μl) and that irreversible processes can occur in aged samples, acquisition parameters were initially chosen to balance sensibility and time. Figures below show the high quality of the acquired spectra. All ^{15}N and $^1\text{H}^{\text{N}}$ resonances shift downfield with increasing pressures, most probably because of the expected shortening of the hydrogen bonds with pressure.¹⁵⁵ Such an effect has also been described earlier by Kalbitzer et al.¹⁵⁶ Those changes in chemical shifts induced by pressure were totally reversible.

Table 1.5 – Features of the recorded data set of high pressure NMR spectra. The NMR pulse sequences used are described in Materials and Methods section.

| | | NMR spectrum | | | | |
|---------------|--|---|--|---|--|--|
| | | Heteronuclear | | | Homonuclear | |
| | | ^1H - ^{15}N -HSQC | ^1H - ^{13}C -HSQC | 2D-HNCO | 2D-TOCSY | 2D-NOESY |
| <i>p, T</i> | Temperature (K) | 277, 288 | 277, 288 | 277, 288 | 277 | 277 |
| | Pressure points | 11 | 10 | 9 | 20 | 2 |
| | Pressure step (MPa) | 20 | 20 | 20 | 15 | 275 |
| | Pressure interval (MPa) | 3 to 200 ^a | 3 to 180 ^a | 3 to 160 ^a | 2.3 to 285 ^a | 0.1 to 275 ^a |
| <i>NMR</i> | Number of scans | 16 | 16 | 24 | 16 | 48 |
| | FID size | 2k (^1H) \times 512 (^{15}N) | 2k (^1H) \times 512 (^{13}C) | 2k (^1H) \times 256 (^{13}C) | 8k (^1H) \times 512 (^1H) | 8k (^1H) \times 512 (^1H) |
| | Spectral window (ppm) | 5-10 (^1H) \times 107-130 (^{15}N) | 0-10 (^1H) \times 11-48 ^b (^{13}C) | 5-10 (^1H) \times 173-178 (^{13}C) | 0-10 (^1H) | 0-10 (^1H) |
| | Probed nuclei | $^1\text{H}^{\text{N}}(i)$, $^{15}\text{N}^{\text{H}}(i)$ | $^1\text{H}^{\text{C}}(i)$, $^{13}\text{C}^{\text{H}}(i)^{\text{c}}$ | $^1\text{H}^{\text{N}}(i)$, $^{13}\text{C}^{\text{H}}(i-1)$ | $^1\text{H}(i)$, $^1\text{H}(i)$ | $^1\text{H}(i)$, $^1\text{H}(i+n)$ |
| <i>Sample</i> | Labelling | ^{15}N | $^{13}\text{C}/^{15}\text{N}$ | $^{13}\text{C}/^{15}\text{N}$ | none | none |
| | A β monomeric concentration ^d (μM) | 85 | 80 | 30 | 90 | 500 ^e |
| | D ₂ O concentration (%) | 8 | 99.5 | 8 | 8 | 8 |

^a Higher pressures could not be obtained due to pressure leakage and/or sample tube pressure limit

^b Folding of $^{13}\text{C}^{\alpha}$, $^{13}\text{C}^{\beta}$ resonances above 48 ppm

^c Except aromatic carbons

^d Estimated concentration by ^1H NMR signals of Tyr-10 H ^{ϵ 1,2} and/or Val-12, Val-18 H ^{γ 2}

^e Depolymerization steps were employed to assure a monomeric sample

Source: By the author.

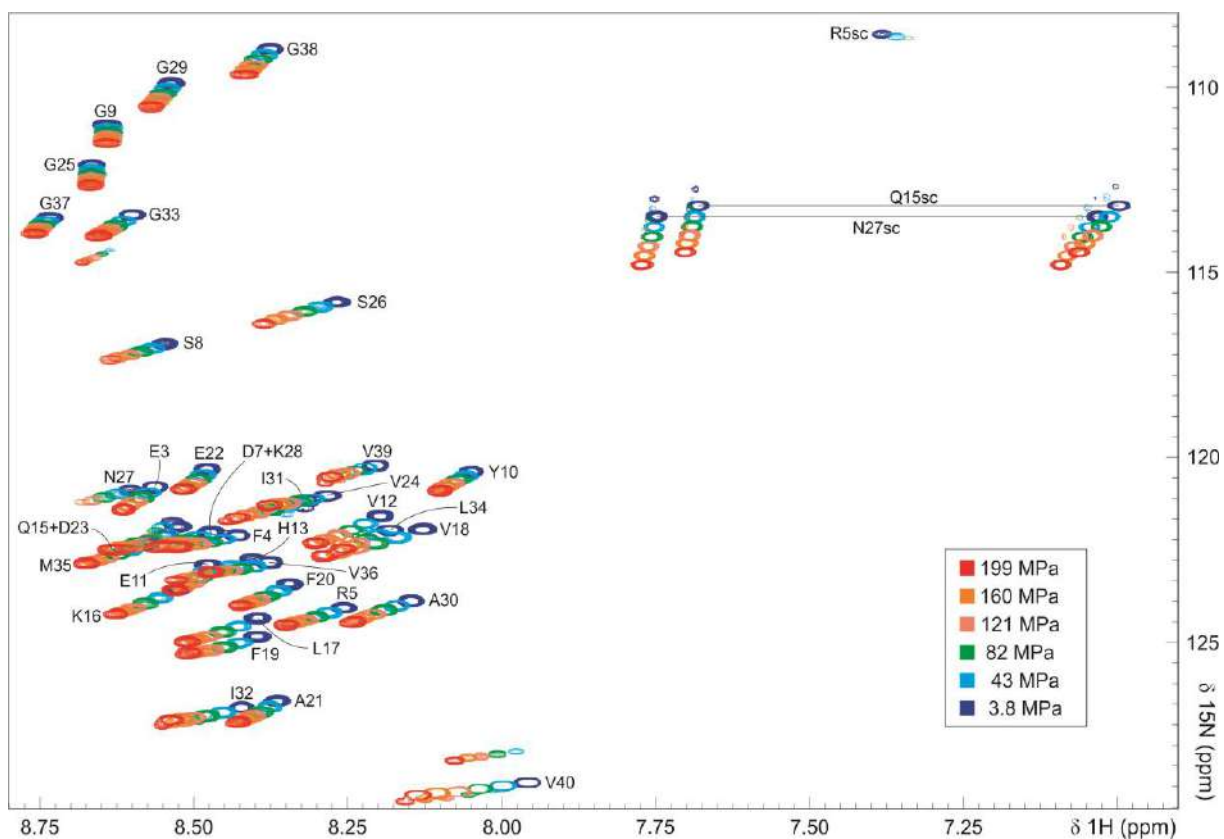


Figure 1.33 – High pressure NMR ^1H - ^{15}N -HSQC spectra at 277 K. Pressures values are shown in the figure insert. Every residue peak moves towards high frequencies, some of them presenting clearly nonlinear behavior as Phe-19, Ala-21 and Ile-32. Sample and NMR parameters are presented in Table 1.5.

Source: By the author.

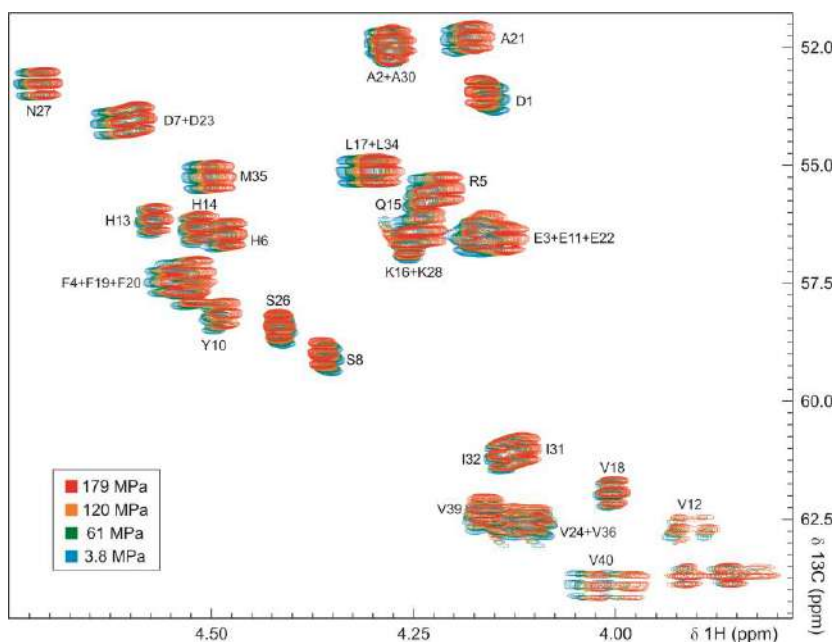


Figure 1.34 – $^1\text{H}^\alpha\text{-}^{13}\text{C}^\alpha$ section of high pressure $^1\text{H}\text{-}^{13}\text{C}$ -HSQC spectra at 277 K. Four pressures are shown and their values are in the figure insert. The triplets seen are due to carbon-carbon scalar couplings $^1J_{\text{C}^\alpha\text{-C}^\alpha}$ e $^1J_{\text{C}^\alpha\text{-C}^\beta}$. Sample and NMR parameters are presented in Table 1.5.

Source: By the author.

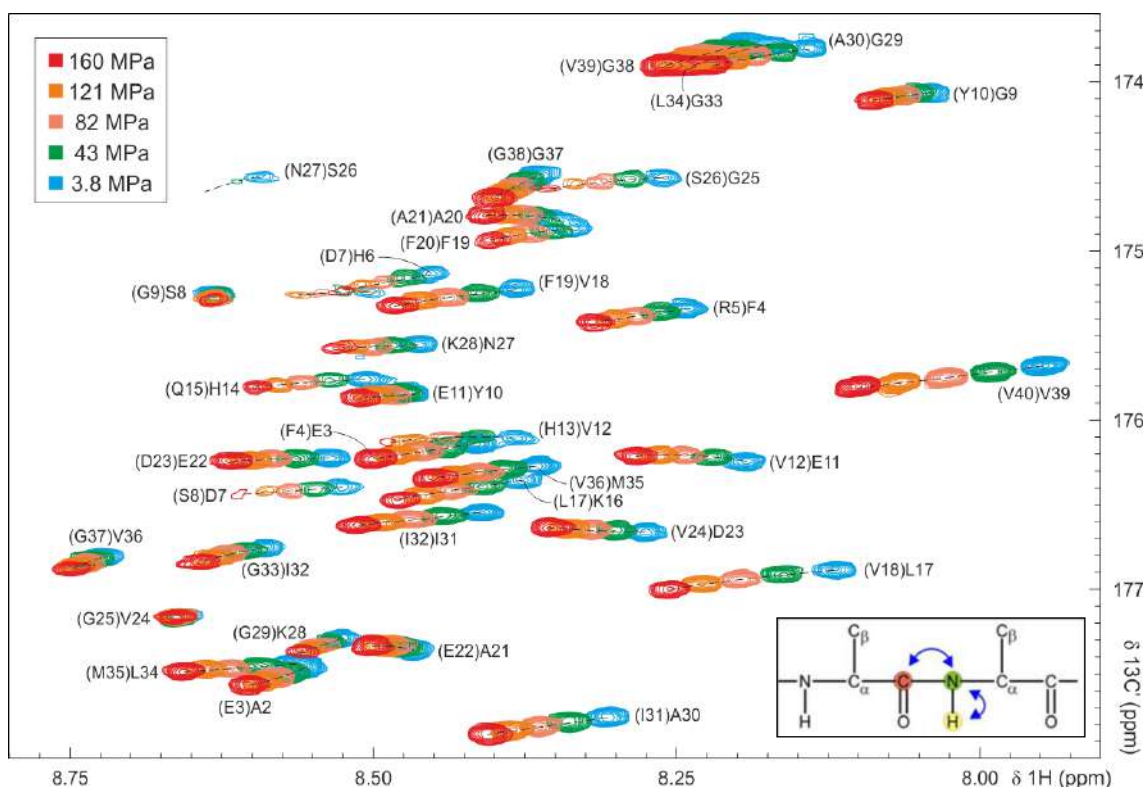


Figure 1.35 – Superposition of high pressure 2D-HNCO spectra at 277 K. Pressures values are shown in the figure superior insert. As presented by the insert at the bottom left, the spectrum correlates carbonyl carbons and the amide group of the next residue. Because of that, peak labels refer as '(residue $i+1$)residue i '. Chemical shifts of the residue $i+1$ and i can be seen in horizontally (δ_{HN}) and vertically (δ_{C}), respectively. Dashed lines indicate peak trajectories during pressure increase.

Source: By the author.

After spectra processing, we extracted chemical shifts values (δ) from two-dimensional spectra. Generally, chemical shifts are simply obtained after the ‘peak-picking’ routine. The algorithm recognizes the peak maximum and reports the chemical shifts using the nearest values determined by the digital resolution. However, peak distortion and low spectral resolution have a direct impact on curves quality, as seen in Figure 1.36. In order to obtain more accurate plots, chemical shifts were extracted manually. The method of manual extraction by itself yielded better curves since it does not rely directly on digital resolution. Additionally, adjustments in the chemical shifts were carried out since there is a range of acceptable values within the experimental error. Nowadays, a Bayesian method which extract peak positions with high accuracy is available.¹⁵⁷

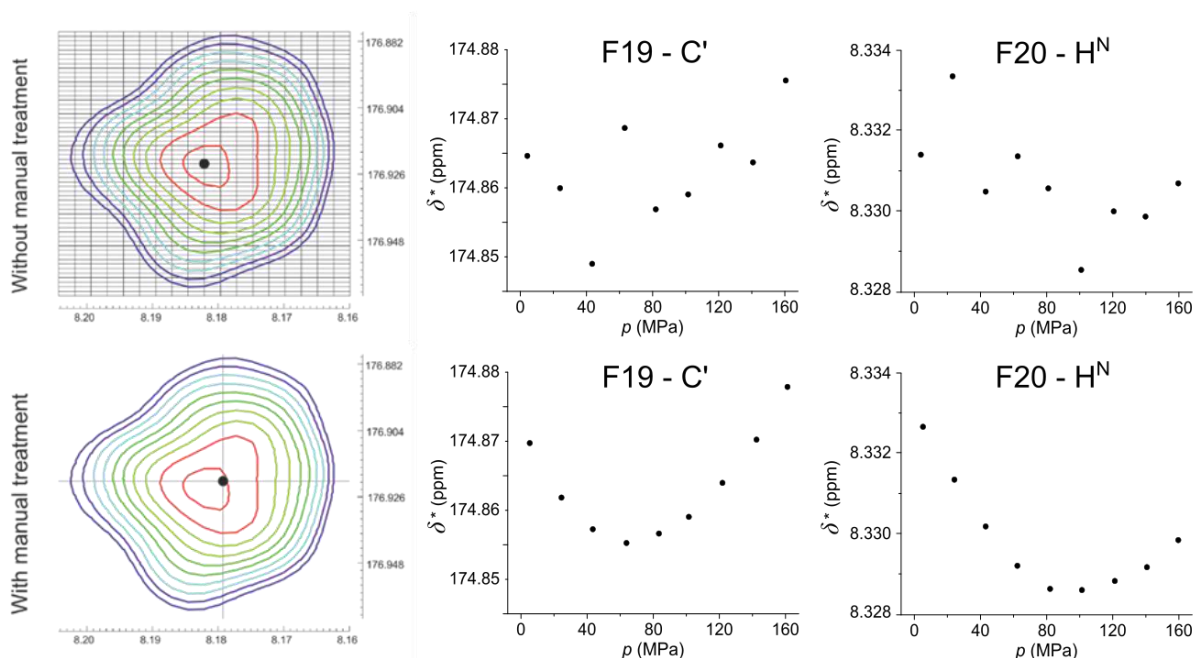


Figure 1.36 – Manual treatment effects on the data. (Left) Peak positions (black dot) with and without manual treatment. The grid shown represents the digital resolution of the 2D-HNCO spectra, used to define peak center in the peak-picking routine. The peak that is being depicted is (F20)F19 2D-HNCO signal at 277 K and 140 MPa. (Center) Plots from $^{13}\text{C}'$ corrected chemical shifts of Phe-19. (Right) Plots from $^1\text{H}^{\text{N}}$ corrected chemical shifts of Phe-20.

Source: By the author.

The chemical shifts observed are the sum of clearly trivial pressure effects (presumably compression) and significant conformational transitions that can be separated by using random coil shifts. Random coil peptide data was used to separate trivial pressure effects from effects caused by structural transitions.^{108, 138, 139} Figure 1.37 presents a plot of ^1H - ^{15}N -HSQC spectra before (gray dots) and after (colored dots) residue-specific correction. Due to the low degree of folding exhibited by the β -amyloid peptide, some residues like Glu-

3, Ser-8 and Gly-38 presents only the intrinsic random coil shift, with almost no information regarding structural changes (Figure 1.37).

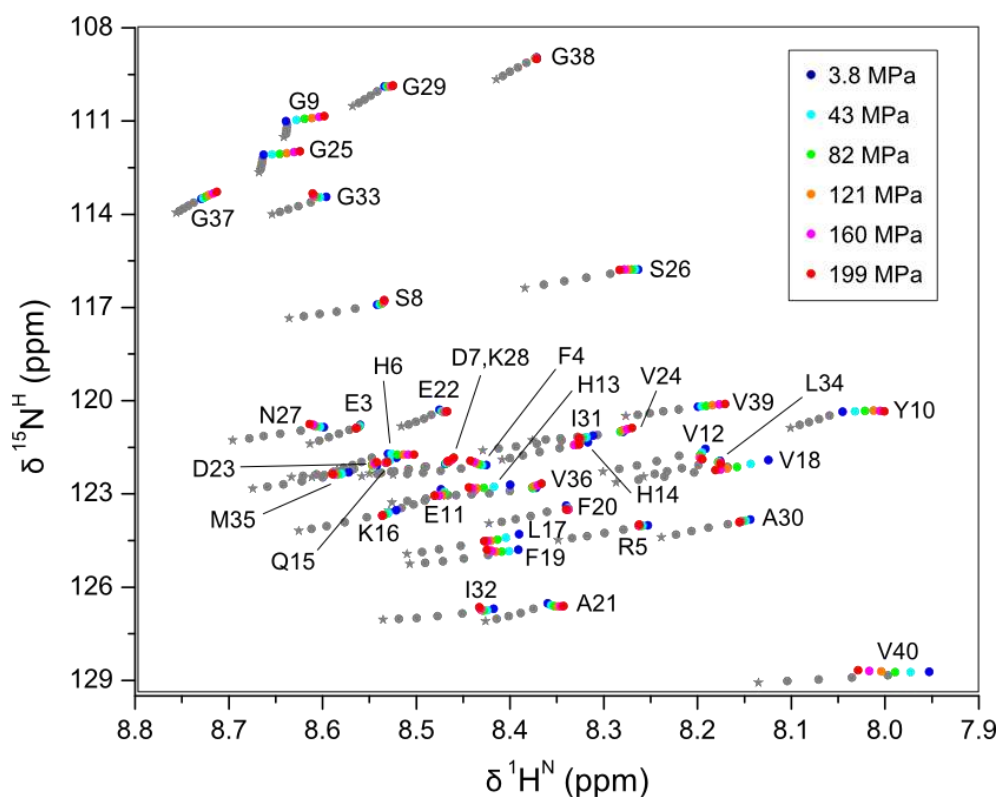


Figure 1.37 – Pressure dependence of $^1\text{H}^{\text{N}}$ and $^{15}\text{N}^{\text{H}}$ NMR chemical shifts before (gray) and after (color) pressure correction. Gray dots represent the peak center on ^1H - ^{15}N -HSQC spectra, recorded at different pressures. Gray stars represent the spectrum at the highest pressure, 199 MPa. Gray dots at 3.8 MPa were removed for clarity purpose.

Source: By the author.

An essentially complete mapping of all ^1H , ^{13}C and ^{15}N atoms in A β (1-40) was gathered (Figure 1.38 shows all chemical shift curves for residue Val-12). Some of the corrected curves are linear and/or noisy while others present a nonlinear behavior typical for residues involved in structural changes. Both temperatures (277 and 288 K) show curves of very similar shapes, which indicate similar thermodynamic transitions.

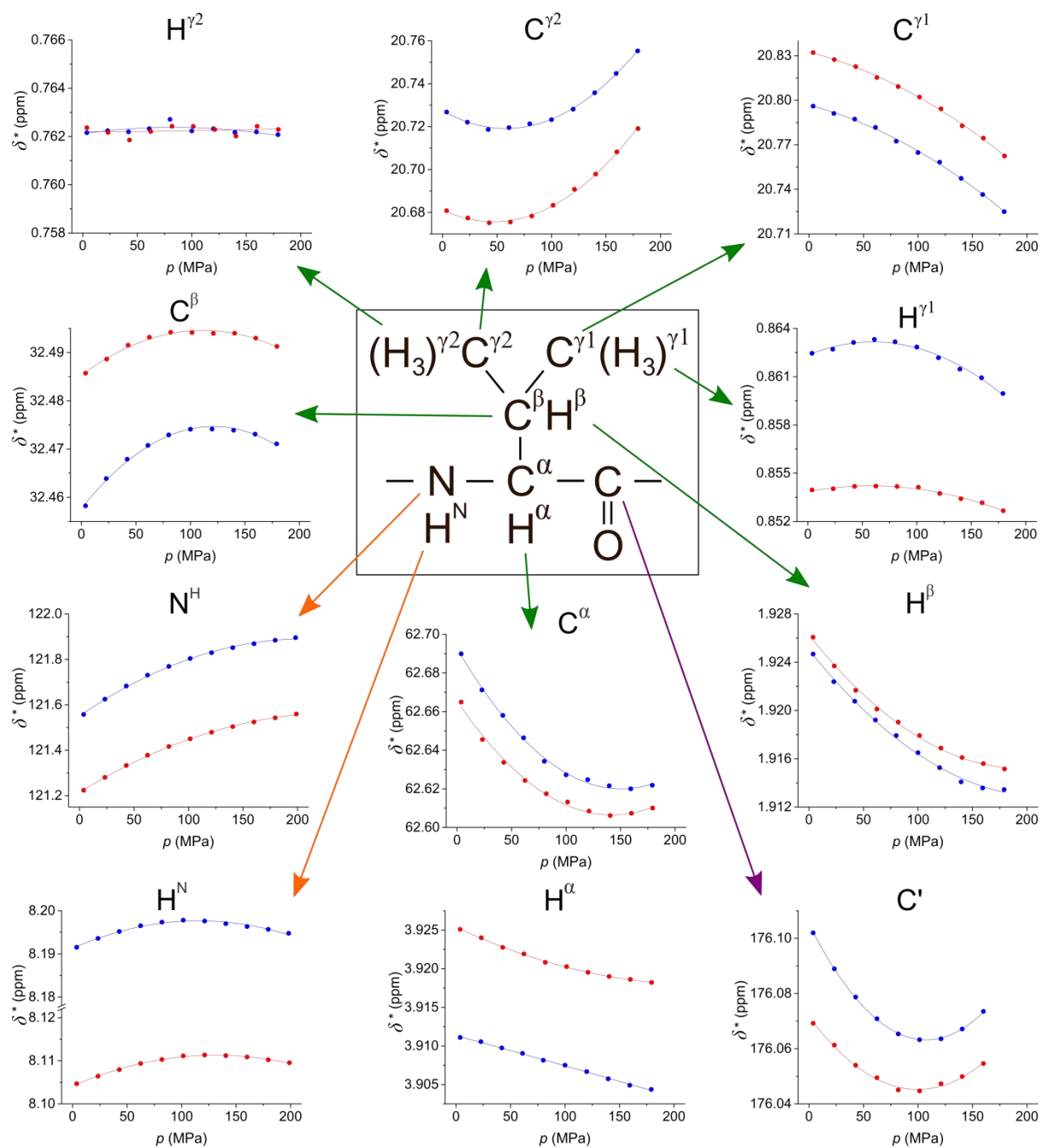


Figure 1.38 – Corrected chemical shift (δ^*) pressure curves for residue Val-12 of $A\beta(1-40)$. Arrow color indicates from which spectrum chemical shifts were taken: green, 1H - ^{13}C -HSQC; orange, 1H - ^{15}N -HSQC; purple, 2D-HNCO. Fit shown here were done using a second order polynomial, according to Equation 4. Data from two temperatures are presented, 277 (blue) and 288 K (red).

Source: By the author.

1.4.3.2 Pressure coefficients

After the complete assignment of peaks, the extraction of chemical shifts and the application of pressure corrections, the effects on chemical shift curves were initially analyzed by a second-order polynomial equation (Equation 4). Curve fitting generated B_1^* and B_2^* (B_1 and B_2 for pressure uncorrected data) pressure coefficients for all evaluated nuclei. The first order coefficient, B_1^* , describes the linear part of the curve, whereas the second order coefficient, B_2^* , denotes the nonlinearity of the chemical shift change with pressure. Values of B_1^* and B_2^* pressure coefficients are presented on Appendix C, D, E and F. A surprisingly high negative correlation between B_1^* and B_2^* values of the same nucleus can be seen on the data (Figure 1.39).

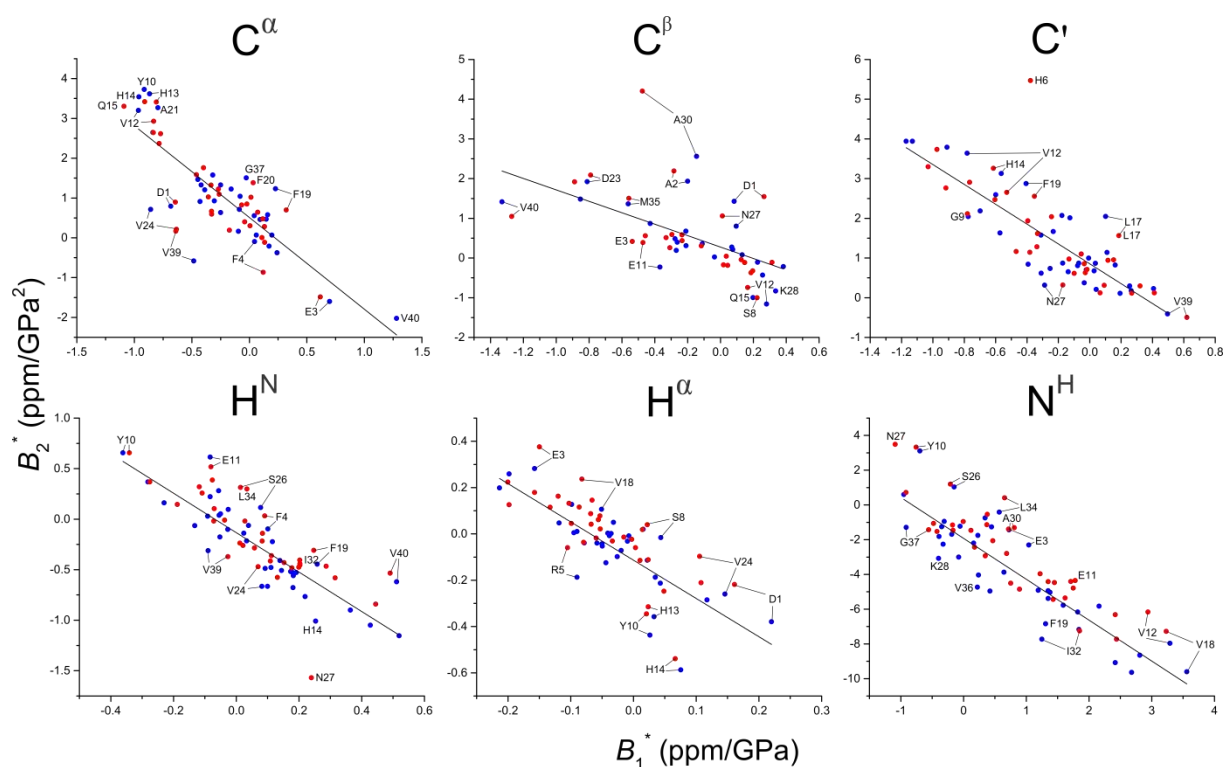


Figure 1.39 – Correlation between B_1^* (horizontal axis) and B_2^* (vertical axis) pressure coefficients. Blue and red dots represent data at 277 and 288 K, respectively. Outliers are labeled. The corresponding Pearson correlation coefficients are -0.83, -0.63, -0.85, -0.86, -0.78, -0.87 for $^{13}\text{C}^\alpha$, $^{13}\text{C}^\beta$, $^{13}\text{C}'$, $^1\text{H}^\text{N}$, $^1\text{H}^\alpha$ and ^{15}N , respectively.

Source: By the author.

In terms of B_1^* and B_2^* signs, atoms clearly divided into two groups: $^1\text{H}^\text{N}$, $^{15}\text{N}^\text{H}$ (positive B_1^* , negative B_2^*) and $^1\text{H}^\alpha$, $^{13}\text{C}^\alpha$, $^{13}\text{C}^\beta$, $^{13}\text{C}'$ (negative B_1^* , positive B_2^*). For this

reason, we combined the previously corrected chemical shifts from these nuclei in two different groups. For the amide group, the first order coefficient (B_1^*) is understood as compression of the hydrogen bonds whereas the second order coefficient (B_2^*) indicates the emergence of a new conformation, different from the native conformation.⁹⁹

B_1^* and B_2^* pressure coefficients agrees surprisingly well with the structural model proposed by Danielsson,⁴⁶ especially for the amide coefficients (Figure 1.40). The two extended regions predicted by this model (E1 and E2), which adopts β -strands conformation in the fibrils, have large pressure coefficients. The second region seems to be weaker mainly near residue Leu-34 but presents higher values at high temperature (288 K) compared to low temperature (277 K), contrarily to other regions. Residues in the second turn (T2, Gly-25 to

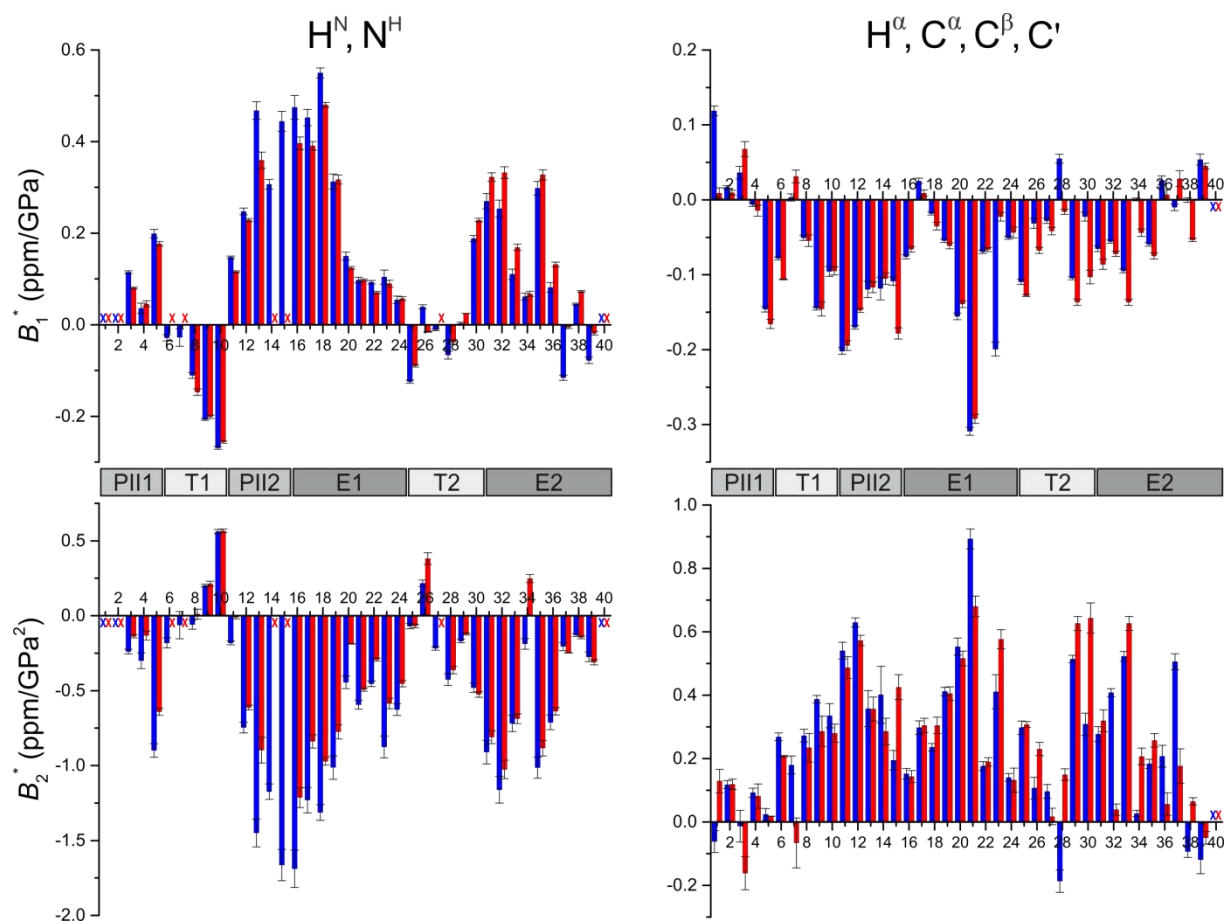


Figure 1.40 – First (B_1^*) and second order (B_2^*) pressure coefficients of A β (1-40) from combined chemical shifts. $^1\text{H}^{\text{N}}$, $^{15}\text{N}^{\text{H}}$ (left) and $^1\text{H}^{\alpha}$, $^{13}\text{C}^{\alpha}$, $^{13}\text{C}^{\beta}$, $^{13}\text{C}'$ (right) chemical shifts were combined separately using the combined chemical shift tool¹³⁵ in AUREMOL software and fitted by Equation 4. Two temperatures are shown, 277 (blue bars) and 288 K (red bars). The same set of nuclei was used for both temperatures. Residues labeled with 'X' could not be followed. A β (1-40) structural model reported by DANIELSSON⁴⁶ (PII, polyproline type-II helix; T, turn; E, extended region) is also depicted in gray color boxes.

Source: By the author.

Gly-29) and in the C-terminus (Gly-37 to Val-39) present low coefficients which indicates a more random coil-like conformation. The region around Lys-16 (beginning of region E1) have high B_1^* and B_2^* for the amide group but low values for $^1\text{H}^\alpha$, $^{13}\text{C}^\alpha$, $^{13}\text{C}^\beta$ and $^{13}\text{C}'$ combined curves. This effect might be due to hydrogen bonding in the backbone which affects amide atoms but not hydrogen-carbon groups.

It has been seen in two-state models that the B_2^*/B_1^* ratio is related to thermodynamic parameters of the transition between conformations, more specifically the quantity $-\Delta\beta^0/2\Delta V^0$, where $\Delta\beta^0$ represents the difference of molar compressibility and ΔV^0 is the difference between partial molar volumes.¹⁴¹ Even if these conditions may not apply to $\text{A}\beta$ (e.g. more than two states in exchange), B_2^*/B_1^* values are related to the apparent compressibility and can give information on the local pressure sensitivity.

We first inspect the statistics of B_2^*/B_1^* values in our $\text{A}\beta$ data (Figure 1.41). B_2^*/B_1^* ratios present a broad, normal distribution at both temperatures (277 and 288 K) with rather similar parameters. The average of B_2^*/B_1^* is -2.18 and -2.04 GPa^{-1} at 277 and 288 K, respectively. Sigma is in the same magnitude of B_2^*/B_1^* averages in both data sets and it is slightly higher at 277 K (2.75 GPa^{-1}) compared to 288 K (1.94 GPa^{-1}). A collection of B_2^*/B_1^* values in random coil Ac-GGXA-NH₂ peptides^{108, 138, 139} was gathered using exactly the same atoms used to calculate $\text{A}\beta$ data (Figure 1.41C). Random coil peptide presents a different B_2^*/B_1^* average (-0.71 GPa^{-1}) and a sharper distribution ($\sigma = 0.69 \text{ GPa}^{-1}$).

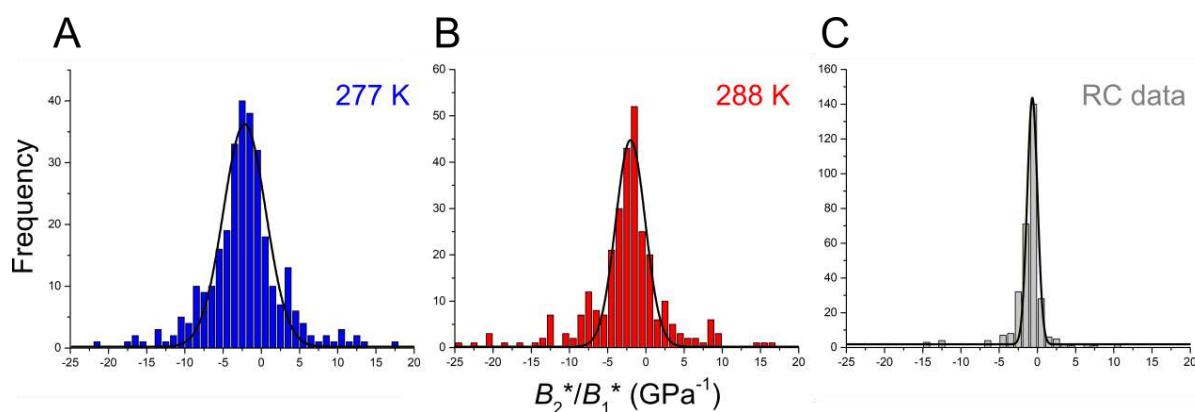


Figure 1.41 – Distribution of B_2^*/B_1^* values for all atoms in $\text{A}\beta$ peptide compared to random coil peptide data. A) $\text{A}\beta$ data at 277 K. B) $\text{A}\beta$ data at 288 K. C) Data from random coil peptides acquired at 283 K by KOEHLER and BECK ERLACH.^{108, 138, 139} The identical atom collection was used in all plots. Prior to the fit that generated B_1^* and B_2^* , chemical shifts were corrected for intrinsic pressure effects. Outliers are not shown.

Source: By the author.

Given that low B_1^* values generate extremely high B_2^*/B_1^* ratios (because B_1^* is the divisor in B_2^*/B_1^*), we used inverse-variance weighting (see Equation 5, Materials and Methods) to calculate a more stable average of all ^1H , ^{13}C , ^{15}N backbone and side chain nuclei. This weighting method handles the outliers present in the data, yielding more reliable values. The weighted averages are displayed in Table 1.6.

Table 1.6 – Average values for inverse-variance weighted B_2^*/B_1^* ratios at two different temperatures (277 and 288 K). Errors are estimated as one standard deviation (σ).

| | B_2^*/B_1^* (GPa ⁻¹) | |
|------------------------------------|------------------------------------|------------|
| | 277 K | 288 K |
| Backbone nuclei^a | -2.2 ± 0.3 | -2.0 ± 0.2 |
| Side chain nuclei | -2.7 ± 0.6 | -2.4 ± 0.4 |
| All nuclei^b | -2.1 ± 0.2 | -2.0 ± 0.2 |

^a ^{13}C , $^{13}\text{C}^\alpha$, $^{15}\text{N}^{\text{H}}$, $^1\text{H}^{\text{N}}$ and $^1\text{H}^\alpha$

^b Backbone and side chain

Source: By the author.

The B_2^*/B_1^* σ^2 -weighted average was also calculated for each residue in A β sequence using pressure coefficients calculated from each atom pressure response (Figure 1.42). Except for residue Gly-37, all other residues have a negative B_2^*/B_1^* ratio. The most negative values are present in the second polyproline helix region (PII2, residues Glu-11 to Gln15) and also along the second extended region (E2, residues Lys-16 to Val-24). If conditions are satisfied, negative values of B_2^*/B_1^* indicate that $\Delta\beta^0$ and ΔV^0 have same sign and, consequently, the conformational state of lower molar volume also has the lowest compressibility. Positive ratios, on the other hand, indicate that $\Delta\beta^0$ and ΔV^0 have opposite signs, a condition found less frequently in proteins.

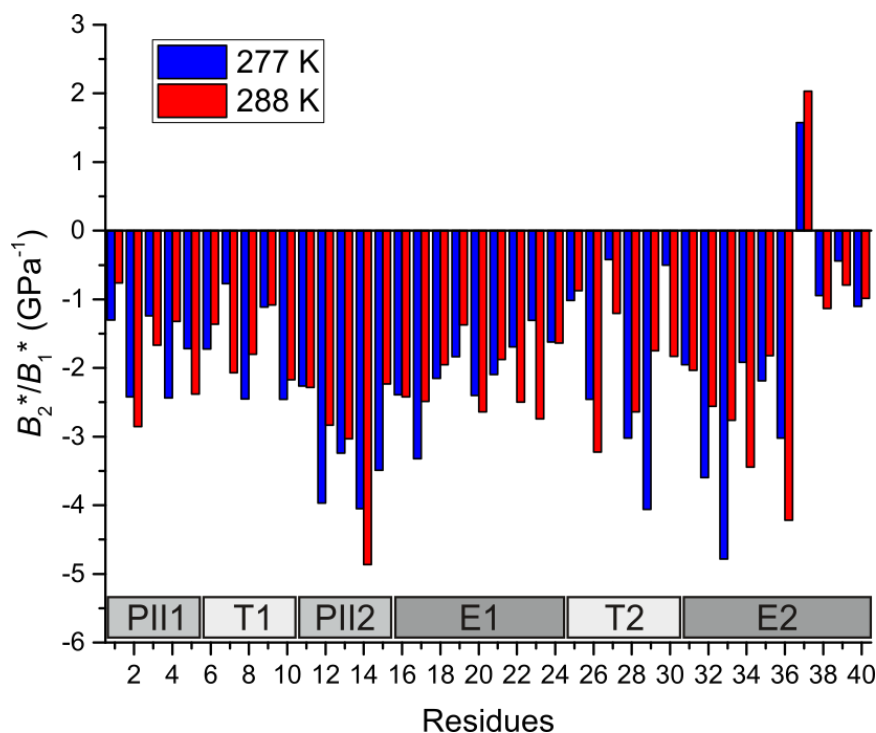


Figure 1.42 – Sequence dependence of the mean B_2^*/B_1^* ratio for A β (1-40) at different temperatures. The weighted mean B_2^*/B_1^* ratio of all assigned atoms (¹H, ¹³C and ¹⁵N) of A β (1-40) is depicted at 277 K (blue bars) and 288 K (red bars). The secondary structural model proposed by DANIELSSON⁴⁶ is indicated. The high pressure data were corrected for unspecific compression effects by using the pressure coefficients from model peptides and the weighting of individual B_2^*/B_1^* values was done on the basis of inverse-variance weighting as described in Materials and Methods.

Source: By the author.

1.4.3.3 Thermodynamic analysis

This thermodynamic study expands the characterization of monomeric species of A β (1-40) initially done by Munte and coworkers using ¹H^N and ¹⁵N^H data.⁵⁹ In the present work, side chains and carbon atoms were also included in the analysis, which is expected to yield a more comprehensive picture of the monomeric conformations of A β .

1.4.3.3.1 Fast exchange: Chemical shifts

In fast exchange regimes, the k_{ex} (exchange constant between states) is considered to be much larger than the resonance frequency difference of these states. This results in only

one peak in the spectrum for such conformations, where the chemical shift is equal to the weighted average of the individual chemical shifts of each state. As the pressure shifts the chemical equilibrium between these species, the populations also change, modifying the NMR δ parameter accordingly (see Figure 1.14, Introduction section).

In principle, a model with only two states in fast exchange using the second-order compressibility term of ΔG would be enough to explain the parabolic behavior of some chemical shift curves (Figure 1.38). Although, the magnitude of $\Delta\beta'^0$ fitting individual biphasic curves using this mode was above 1 mL MPa⁻¹ mol⁻¹ (data not shown), which is much higher than values previously reported^{158, 159, 160} and seems to be unlikely. Non-biphasic curves have really low $\Delta\beta'^0$ values when fitted independently and fit routines that use global thermodynamic parameters (i.e., same ΔG_{ij}^0 , ΔV_{ij}^0 , $\Delta\beta_{ij}'^0$ for all plots) did not achieve convergence using only two states in fast exchange. The parabolic form of the pressure plots could also implicate in the existence of (at least) three A β conformations in fast chemical exchange, according to the adopted model (Equation 7). However, a model with three states including $\Delta\beta'^0$ was computationally unfeasible since it requires a lot of time to run completely. The compressibility difference is certainly not zero and should not be totally neglected, but the approximation $\Delta\beta'^0 = 0$ seems to be reasonable in a relatively low pressure range.

After removing linear or noisy plots, data set was composed of 114, 113 and 34 plots from ¹H, ¹³C and ¹⁵N nuclei, respectively. Our first attempts were to globally fit the selected plots with reasonable starting parameters, using a three-state model without a compressibility term. Starting values and limits for the fitting parameters were adjusted and several attempts were necessary to achieved fit convergence. Once the initial fit was stable, an incremental addition of plots was performed to see the evolution of the fit and the impact of the each piece of data used. We started with one curve and added more curves, fitting globally all of curves in the pool after each step of addition. Biphasic plots (108 plots, added one by one) were added first since they contain more information, followed by the non-biphasic ones (153 plots, added in groups of five). Figure 1.43 shows the parameter evolution over the process. At the beginning, values are rather unstable and even restricted by the limits but finally converged as more curves are used (Figure 1.43). As expected, the final ΔG_{ij}^0 and ΔV_{ij}^0 values match the initial fit, depending only on which plots were used and the limits imposed (but not on the order they were included).

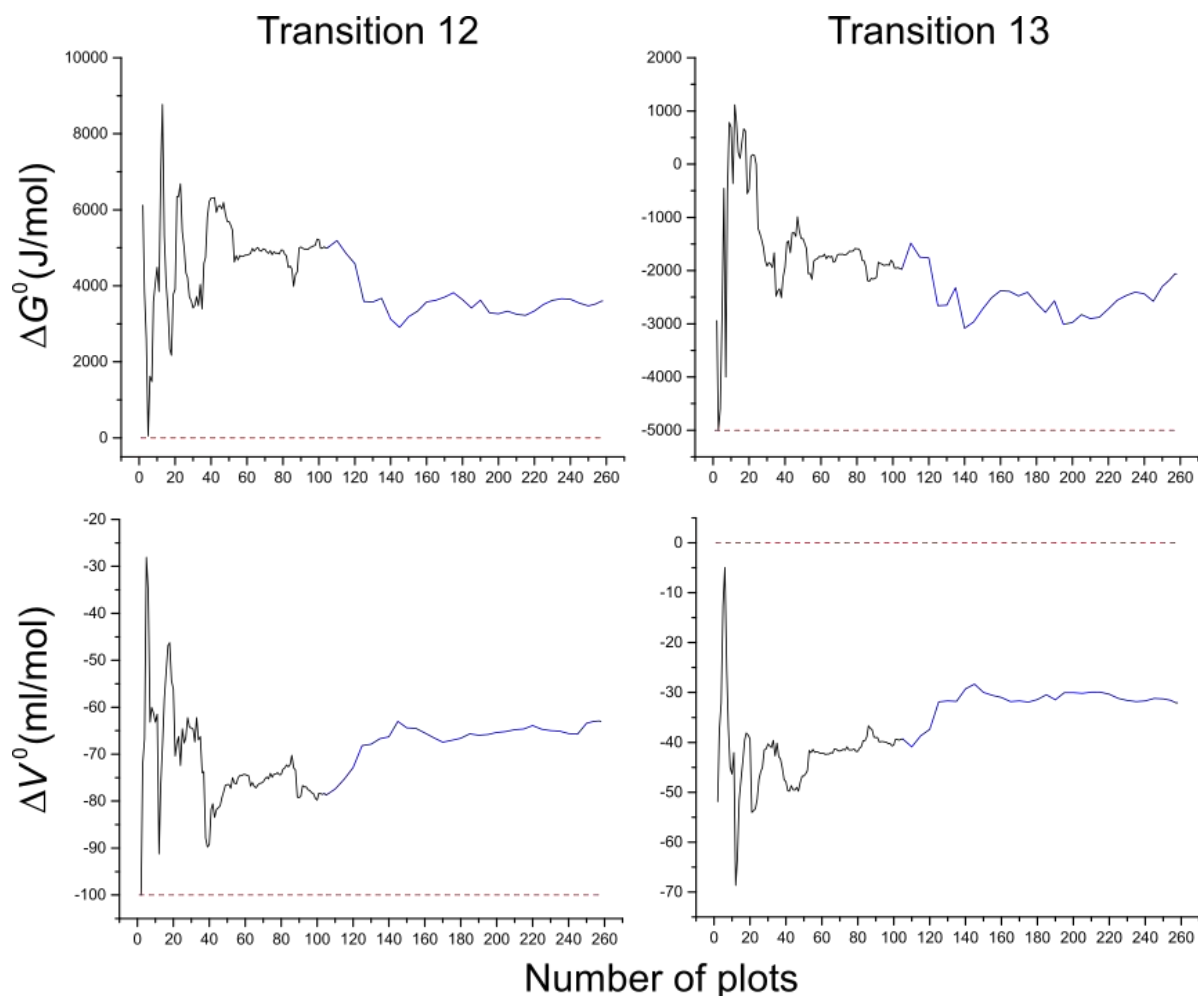


Figure 1.43 – Parameters evolution of chemical shifts fitting. Black, biphasic curves; blue, non-biphasic curves; red, limits imposed to ΔG^0 and ΔV^0 values. In the black portion, a data point is shown at every plot added to the fit. In the blue part, the addition was done at every five plots (since the workload due to the fit becomes computationally too demanding).

Source: By the author.

The chemical shift plateau for each one of the three states (δ_1 , δ_2 and δ_3) was restricted during the fit according to the atom type (see Table 1.2, Materials and Methods). This restriction enables fit convergence and avoids unlikely δ_i values. In the end of the fit, the maximum difference among δ_i ($\Delta\delta_i^{\max}$) was much lower than the restrictions imposed (Figure 1.44). This low difference among state chemical shifts is expected since in fast exchange processes the latter is much lower than the exchange constant ($\Delta\omega \ll k_{\text{ex}}$). The distribution of $\Delta\delta_i^{\max}$ shows a dependence on the nucleus, being higher for ^{15}N atom. Surprisingly, ^{13}C shows lower $\Delta\delta_i^{\max}$ values even having higher chemical shifts (non-weighted chemical shifts were used in Figure 1.44 so this comparison is valid).

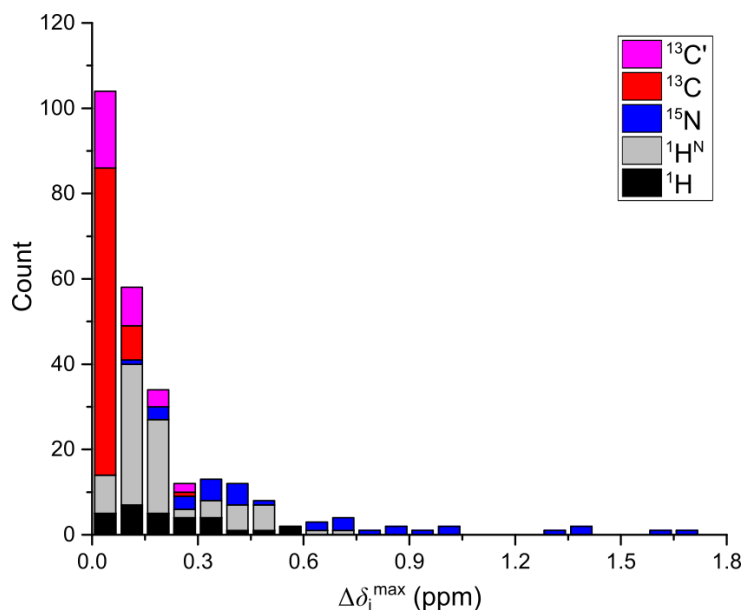


Figure 1.44 – Distribution of the largest absolute difference among final δ_1 , δ_2 and δ_3 plateau values ($\Delta\delta_i^{\max}$) in the chemical shifts fit routine. Non-normalized chemical shifts values were used. Differences were distributed among atom type (magenta, $^{13}\text{C}'$; red, others ^{13}C ; blue, ^{15}N ; gray, $^1\text{H}^{\text{N}}$; black, others ^1H).

Source: By the author.

In order to obtain the errors of the parameters, we did an iterative data sampling removing one curve at a time and calculating again ΔG_{ij}^0 and ΔV_{ij}^0 for the rest of the plots using the same starting parameters and restriction values. At each step of this routine, only the $n-1$ remaining plots were considered by the program. After n cycles, all plots were removed once and a list of $4n$ parameters was generated, with values of ΔG_{ij}^0 and ΔV_{ij}^0 for the two transitions (1-2 and 1-3). The distribution of ΔG_{12}^0 , ΔG_{13}^0 , ΔV_{12}^0 and ΔV_{13}^0 values is organized in the plots in Figure 1.45. They all have normal distribution which allowed average and error estimation (Table 1.7). Transitions 1-2 and 1-3 have similar absolute values of free Gibbs energy at ambient pressure (ΔG^0) but different signs (ΔG_{12}^0 is positive whereas ΔG_{13}^0 is negative). A negative ΔG_{ij}^0 value means that state j is more abundant at ambient pressure than state i .

Table 1.7 – Thermodynamic parameters of monomeric A β (1-40) conformational transitions at 277 K. Errors were calculated for a confidence interval of 95%.

| Transition | K_{ij} at 0.1 MPa ^a | ΔG^0 (kJ/mol) ± 0.1 | ΔV^0 (ml/mol) ± 0.4 |
|------------|----------------------------------|------------------------------------|------------------------------------|
| 1-2 | 0.30 | 2.8 | -58.3 |
| 1-3 | 3.17 | -2.6 | -29.1 |

^a K_{ij} = concentration of state j /concentration of state i

Source: By the author.

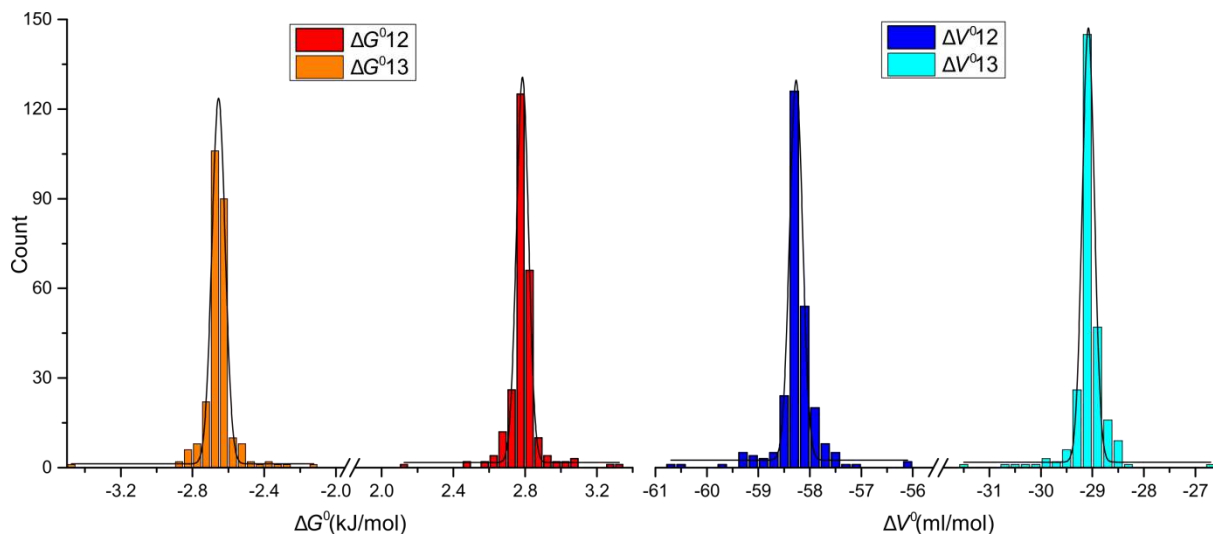


Figure 1.45 – Statistics of chemical shifts fitting using a three-state model. One curve was removed at each iteration, and repeated for all 261 plots. ΔG^0 (2.8 ± 0.1 and -2.6 ± 0.1 kJ/mol for transitions 1-2 and 1-3, respectively) and ΔV^0 (-58.3 ± 0.4 and -29.1 ± 0.4 ml/mol for transitions 1-2 and 1-3, respectively) values have normal distribution. Gaussian fits are shown as black lines.

Source: By the author.

1.4.3.3.2 Slow exchange: Peak intensities and volumes

Volumes and intensities from visible cross-peaks in the NMR spectra also provide relevant information on the conformational equilibrium. The peak volume or intensity was first corrected for compressibility. Here we used the volume of residual Tris peak in ^1H experiments to correct volume/intensities (see section 1.3.5.2 Pressure corrections for more information). After correction, peaks should present constant volume pressure curves if no slow or intermediate exchange processes exist among states (Figure 1.14). However, in our data set, most of $A\beta$ intensities and volumes from the main conformation decrease as pressure get higher.

Cross-peak volumes from the ^1H - ^{15}N -HSQC spectra were the most accurate and yielded well defined curves after being corrected by solvent compressibility. All volume plots from ^1H - ^{15}N -HSQC spectra were strictly decreasing and no plot from this experiment presented volume increase after pressure correction. At 200 MPa, some cross-peak volumes decrease dramatically (to less than $\sim 20\%$ of that in low pressure) but the one-dimensional ^1H signals remained at full volumes after solvent compressibility. This could suggest a heterogeneous disorder of the peptide that undergoes slow exchange, enough to broaden out

only the ^1H - ^{15}N -HSQC cross-peak but not peaks in the ^1H NMR experiment. A similar behavior was earlier reported for apomyoglobin.^{161, 162}

We calculated volume averages of cross-peaks in the ^1H - ^{15}N -HSQC spectra for different A β portions according to the structural model proposed by Danielsson (Figure 1.46).⁴⁶ At high temperature (288 K), peaks lose more volume as the sample is pressurized compared to the low temperature (277 K). Turn regions (T1, His-6 to Tyr-10 and T2, Gly-25 to Ala-30) have the most accentuated decay in volume curves. The first extended region (E1, Lys-16 to Val-24), which comprises the central hydrophobic cluster (CHC) of A β (Leu-17 to Ala-21), on the other side, have the highest volume average at high pressure among considered portions of A β . The extended region at the C-terminus (E2, Ile-31 to Val-40) have values near the average when all residues in A β are considered. In particular, the first five residues in the N-terminus (PII1, Asp-1 to Arg-5) show a similar decrease compared to the first extended region (E1, Lys-16 to Val-24).

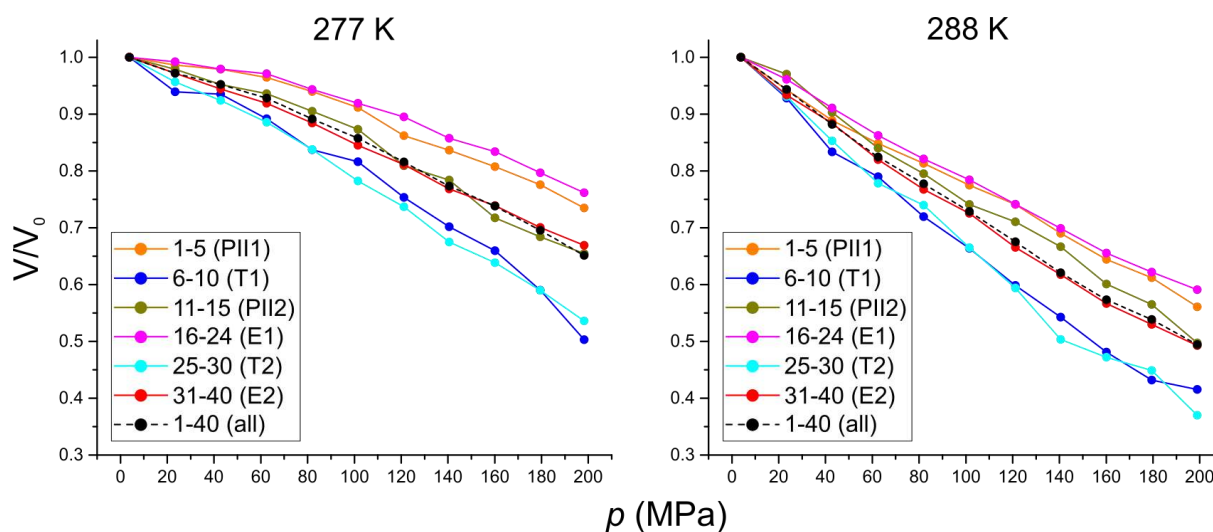


Figure 1.46 – Cross-peak volume changes are different in different structural portions of A β . Average values of ^1H - ^{15}N -HSQC relative volumes for different segments according to model proposed by DANIELSSON⁴⁶ was calculated at 277 (left) and 288 K (right). Volumes were corrected by solvent compressibility using residual Tris signal.

Source: By the author.

To use this information in our thermodynamic model, we first have to be sure that the volume/intensity changes is due to slow exchange only and does not come from other processes. Many processes can contribute to the volume change for A β peptide under pressure: (i) T_2 relaxation during the magnetization transfer in the INEPT sequence; (ii) saturation transfer from water molecules affecting exchangeable protons; (iii) possible

desagregation in high concentrated samples. The first process can be monitored by linewidths which are proportional to $1/T_2$. Similarly, a good indicator is the comparison between intensity and volume curves from the same peak, which can also monitor potential sample depolymerization by pressure. If the peaks gets broader (or alternatively, shaper), the intensity decreases (or increases) but the peak volume is not affected.

After removing noisy curves (most plots from 2D-HNCO), cross-peaks were classified into three groups: *a*) peaks where intensity changes follow the volume changes (Figure 1.47A), *b*) peaks where intensity changes and volume changes are significantly different at high pressure (Figure 1.47B), *c*) peaks where an increase in volume can be seen, possibly from sample depolymerization (Figure 1.47C). For the thermodynamic characterization, only cross-peaks from group *a*) can be safely used. Furthermore, the inclusion of a fourth state can only be reasonably explained if residues from group *a*) also display biphasic chemical shift curves. This would indicate three states in fast exchange (from chemical shifts) and one in slow exchange (from peak intensities). If it is not the case, the ‘fourth’ state could be one of the three states previously considered.

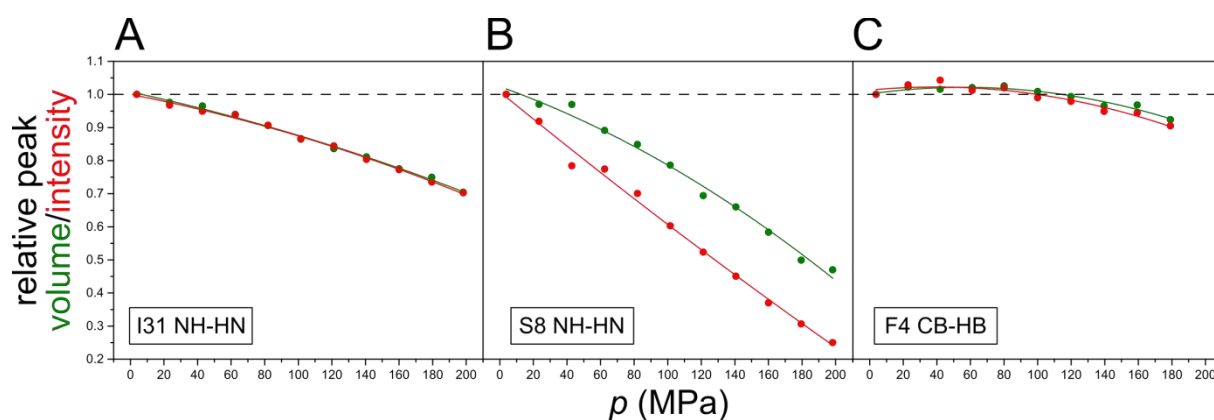


Figure 1.47 – Different behavior of cross-peak volumes (green) and intensities (red). Curves can be classified in three group: i) peaks where intensity follow volume, as presented by residue Ile-31 N^H-H^N (A); ii) peaks that intensity do not follow volume, as seen for Ser-8 N^H-H^N (B); iii) peaks in which other processes occur, as possibly sample depolymerization seen for Phe-4 $C^\beta-H^\beta$ (C).

Source: By the author.

In our data, there are only three plots which could potentially explain a four-state model (all from 1H - ^{15}N -HSQC spectra): Ile-31 N^H-H^N , Leu-34 N^H-H^N and Val-39 N^H-H^N . All of them have one biphasic chemical shifts curve (either $^1H^N$ or $^{15}N^H$) and significant volume changes that agrees with intensity changes. Only these relative peak intensities plots were fitted according to Equation 9 (slow exchange, two-state model) to derive a possible state

number 4. It was considered that state 4 was in slow exchange with state 3, which is the most abundant state from those three previously characterized. The global fit of the parameters shows that ΔG^0_{34} and ΔV^0_{34} from slow exchange are very similar to those from the 3-2 transition found by the chemical shift analysis (Table 1.8). This is probably suggesting that the possible state 4 and state 2 have the same identity and the transition 3-4 is, in fact, transition 3-2 for the residues in slow exchange. Unfortunately, the study of peak intensities did not yield any new thermodynamic information about A β states and the presence of a possible fourth state in slow exchange can not be easily proved in the present data.

Table 1.8 – Possible transition in slow exchange is ambiguous and is probably the same as transition 3-2 but for residues in slow exchange.

| Transition | Exchange rate | ΔG^0 (kJ/mol) | ΔV^0 (ml/mol) |
|------------------|---------------|------------------------------|-----------------------|
| 3-4 | Slow | 5.5 | -30.7 |
| 3-2 ^a | Fast | (5.4 \pm 0.2) ^a | (-29.2 \pm 0.8) |

^atransitions are additive, 3-2 can be considered as transition 3-1 plus 1-2

Source: By the author.

1.4.3.3 State populations

After the calculation of meaningful thermodynamic parameters, we can estimate relative populations for all three considered A β monomeric conformations in solution (states 1, 2 and 3) using Equation 10 (Materials and Methods). State number 3 is the most abundant at atmospheric pressure (~ 70%) followed by states 1 (~ 20%) and 2 (7%). By this reason, it is useful to rename the states according to their relative population at ambient pressure: states 3, 1 and 2 will be called from now on as states A, B and C, respectively. State A first increases its population and, after 50 MPa, have the population decreased at high pressure. State B is totally eliminated above 200 MPa whereas state C increases its concentration by more than 7-fold at 200 MPa compared to the concentration in ambient pressure (Figure 1.48).

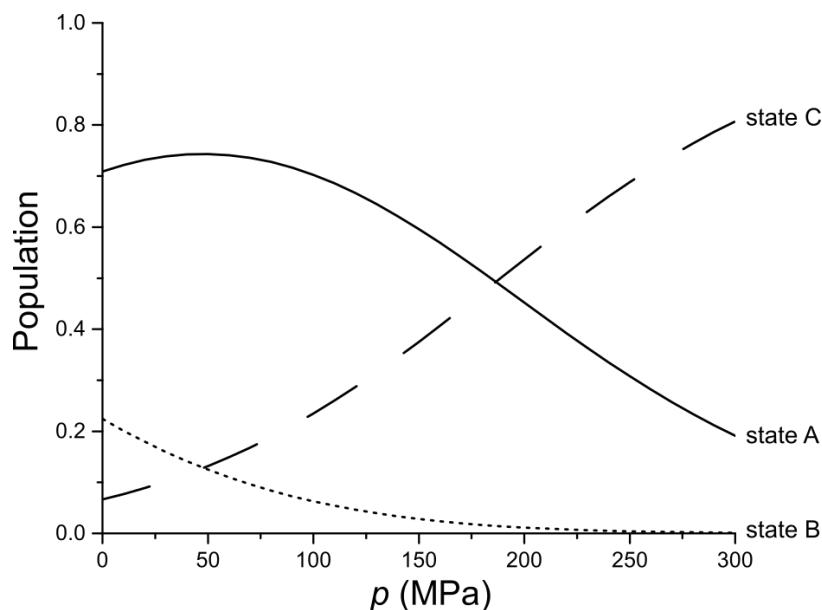


Figure 1.48 – Monomeric A β populations of different conformations at 277 K. State A (or 3) in solid line, state B (or 1) in dotted line, state C (or 2) in long-dashed line. States were obtained from the chemical shift curves only.

Source: By the author.

1.4.3.4 Structural analysis

In this section, we present information regarding the prediction of secondary structures by chemical shifts and the qualitative analysis of NOEs combined with 3J NMR coupling constants of $^1\text{H}^\alpha$ and $^1\text{H}^N$ atoms.

1.4.3.4.1 Secondary structure propensities

In protein NMR, there is a well-known observation that some chemical shifts correlate well with local structure.¹⁶³ The atoms that present a high correlation with secondary structures are usually $^{13}\text{C}^\alpha$, $^{13}\text{C}^\beta$, $^{13}\text{C}'$ and $^1\text{H}^\alpha$, which are near the backbone and sense differences in dihedral angles ϕ and ψ . Usually, the difference between chemical shifts and their corresponding random coil values ($\Delta\delta$), also known as secondary chemical shifts, is used for the secondary structure analysis. The secondary chemical shifts for $^{13}\text{C}^\alpha$ and $^{13}\text{C}'$ (carbonyl carbon) are usually positive for α -helix segments and negative for β -sheets. $\Delta\delta$ of

$^{13}\text{C}^\beta$ and $^1\text{H}^\alpha$ exhibit the opposite profile, being negative in α -helices and positive in β -sheets. Many programs, as CSI (chemical shift index)^{164, 165} and TALOS (torsion angle likelihood obtained from shift and sequence similarity),^{143, 166, 167} are able to predict secondary structure with a high level of confidence using chemical shift data.

We calculated $\Delta\delta^*$, the difference between the pressure-corrected chemical shifts and the random coil chemical shifts, at different pressures (Figure 1.49). Since higher pressures could not be obtained for the 2D-HNCO spectra, the higher pressure used in Figure 1.49 is 160 MPa. Besides $^1\text{H}^\alpha$ protons, which seems not to have a correlation with structural features, it is possible to see that $\Delta\delta^*$ values present a high propensity for a β -strand around the segment between residues Leu17 and Phe21, especially for $^{13}\text{C}'$ and $^{13}\text{C}^\beta$ atoms. Those residues are in the central hydrophobic cluster (CHC) of A β and are part of the first extended region (E1), region that is known to adopt a β -strand in fibril models.⁴¹ The second β -strand expected to exist in fibrils, found in the other extended region comprising residues from Ile-31 to Val-40 (E2), cannot be predicted with a high confidence. Even at 160 MPa, A β seems to maintain its partial folding, considering that only small changes can be seen by secondary chemical shifts with pressure (Figure 1.49). Those changes are mostly going towards zero (69% of backbone ^{13}C , 76% of $^1\text{H}^\alpha$ and 95% of $^1\text{H}^\text{N}$) as the pressure increases, trend which indicates that pressure shifts the equilibrium towards less folded A β states.

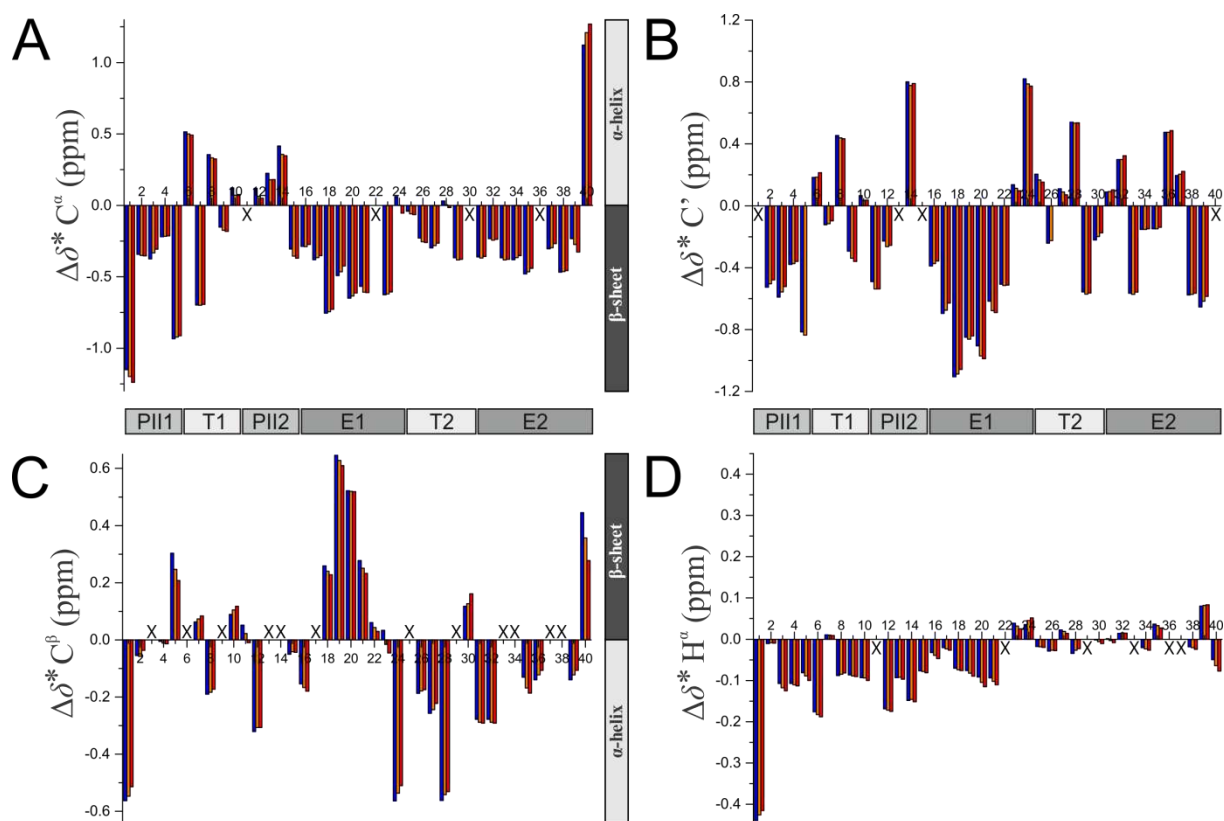


Figure 1.49 – A β (1-40) secondary chemical shifts at 277 K and at 3, 80 and 160 MPa. Plots show the difference between the corrected A β chemical shift and random coil chemical shifts ($\Delta\delta^*$) reported by KJAERGAARD et al. (peptide model Ac-QQXQQ-NH₂, pH 6.5, 278 K).¹⁶⁸ (A) ¹³C α , (B) ¹³C', (C) ¹³C β and (D) ¹H α nuclei. Blue bars, 3 MPa; orange bars, 80 MPa; red bars, 160 MPa. Residues with missing bars could not be analyzed. Horizontal boxes represent the structural model reported by DANIELSSON (PII, propensity to left-handed polyproline type-II helix; T, turns; E, extended regions).⁴⁶ Vertical boxes represent the trend expected for α -helices and β -strands segments.

Source: By the author.

Since the prediction of secondary structure by chemical shifts is usually more robust using different nuclei and taking into account neighboring effects, we used TALOS+.¹⁴³ The software output gives a relative high propensity for the existence of two β -strands in the sequence, the first for residues Leu-17 to Phe-20, in the same region as found by $\Delta\delta^*$ analysis previously presented, and the second for residues Ile-32 to Val-36 (Figure 1.50). The prediction of the first β -strand has a higher confidence than the second strand (average propensities at 277 K for those two regions are 0.78 and 0.50, respectively), also in agreement with the secondary chemical shifts analysis. Helical structures are predicted only with a low probability (Figure 1.50, yellow line); however it matches well with the regions of polyproline type-II helices (PII).

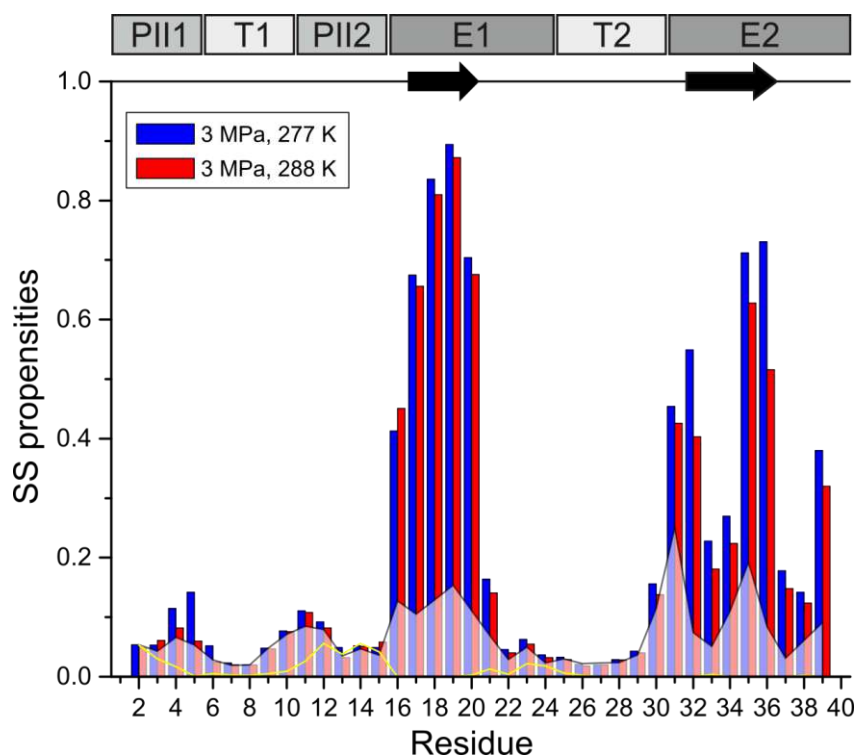


Figure 1.50 – A β secondary structure propensities calculated by TALOS+.¹⁴³ Pressure-corrected chemical shift data from $^{15}\text{N}^{\text{H}}$, $^{13}\text{C}^{\alpha}$, $^{13}\text{C}^{\beta}$, $^{13}\text{C}^{\gamma}$, $^1\text{H}^{\text{N}}$ and $^1\text{H}^{\alpha}$ nuclei was used. Bars: β -strand propensities at 277 K (blue bars) and 288 K (red bars). Yellow line: predicted α -helical propensities for A β data at 277 K. Gray background: β -strand propensities for random coil Ac-GGXGG-NH₂ peptide data at 277 K by KJAERGAARD (pH 6.5, 1M urea, extrapolated using temperature corrections reported by the same work).¹⁶⁹ At the top, it is presented the A β structural model reported by DANIELSSON⁴⁶ (PII, propensity to polyproline type-II helix; T, turns; E, extended regions) and an arrow diagram representing regions with propensity to adopt β -strand conformations, Leu-17 to Phe-20 and Ile-32 to Val-36.

Source: By the author.

To avoid bias towards the sequence component used for TALOS+ prediction, we also calculated the propensities using random coil NMR data instead of A β experimental data (Figure 1.50, gray area). β -strand propensities using data from random coil Ac-GGXGG-NH₂ peptides at 277 K¹⁶⁹ are relatively low (average propensities at 277 K of 0.12 and 0.10 for β -strand 1 and 2, respectively). However, using random coil data acquired at 278 for a different model peptide (Ac-QQXQQ-NH₂ peptides),¹⁶⁸ the average β -strand propensities for the two predicted regions are surprisingly high (0.62 and 0.53, respectively; data not shown), similar to those found using experimental A β chemical shifts. In all predictions, we excluded identical protein sequences in the TALOS+ database. Additionally, a search through its database showed no amyloid- β or derived sequences.

1.4.3.4.2 NOEs and NMR coupling constant

Distances between protons are one of the most important information for structural characterization in solution NMR spectroscopy. They are obtained through ^1H - ^1H -NOESY spectra which reports proton distances up to 5 Å. For a peptide that is only partially structured, it is not expected many long-range NOEs (nuclear Overhauser effects). However, a more compact structure of A β was published by Vivekanandan and coworkers (Figure 1.5B, PDB 2LFM) where N- and C-termini residues interact with residues at the center of the sequence (residues His13 to Asp23), folded into a 3_{10} helix.³⁹ Using a sample with a low concentration of A β (77 μM), they reported 26 long-range ($i, i > 4$) NOEs involving side chain protons of aromatic residues and aliphatic residues, like Phe-19,20 H $\epsilon^{1,2}$ /Val-36 H $\gamma^{1,2}$ and Phe-4 H δ /Val-24 H $\gamma^{1,2}$.³⁹ Many of them involved the proton- δ of aromatic residue Phe-4 in contact with aliphatic side chains protons (part of the spectra is reproduced in Figure 1.51B).

We first tried to record ^1H - ^1H -NOESY spectra using concentrations below the critical concentration for aggregation (~ 90 μM at 283 K) to avoid the presence of polymers which could potentially influence the monomeric equilibrium. The use of samples with low concentration of A β makes the detection of low intensity NOEs even harder. In the first attempts, no aromatic-aliphatic contact between protons could be seen in the spectra (data not shown). Given that we could not see relevant contacts, we repeated the acquisition of NOESY spectra under similar conditions from those employed by Vivekanandan but using a higher A β concentration (500 μM). The concentration is one of the factors that hinder the detection of NOEs by improving the spectral signal-to-noise (SNR) ratio. To avoid the formation of aggregates in low pressure, we intercalated steps of depolymerization at 200 MPa that, optimistically, can keep the sample monomeric (this process is better described in section 1.3.2.1 High pressure NMR instrumentation). The ^1H - ^1H -NOESY recorded was assigned and the chemical shifts were checked with the triple-resonance assignment earlier performed (Appendix A). After the NOESY assignment, we were not able to detect any of the long-range NOEs described by Vivekanandan.³⁹

A spectra comparison focusing on important NOEs between the one obtained by the present study and by Vivekanandan³⁹ can be seen in Figure 1.51. In the present study (Figure 1.51A), the resonance line of Phe-4 H $\delta^{1,2}$ is superposed with Phe-19 H $\delta^{1,2}$ and NOEs can not be unambiguously attributed to Phe-4 H $\delta^{1,2}$. Particularly, the chemical shifts of these protons

The SNR improvement due to the high A β concentration allowed the detection of medium-range NOEs which were analyzed qualitatively. Volumes from cross-peaks contacts present in the NOESY spectra at high concentration were extracted and classified in ‘weak’, ‘medium’ and ‘strong’ according to their converted distances referred to distance in aromatic side chain residues. Data at 275 MPa was also collected and volumes in this condition were corrected by the effect of the sample compressibility caused by pressure. Figure 1.52 organizes the obtained NOEs in a typical manner used for qualitative NOE analyses.

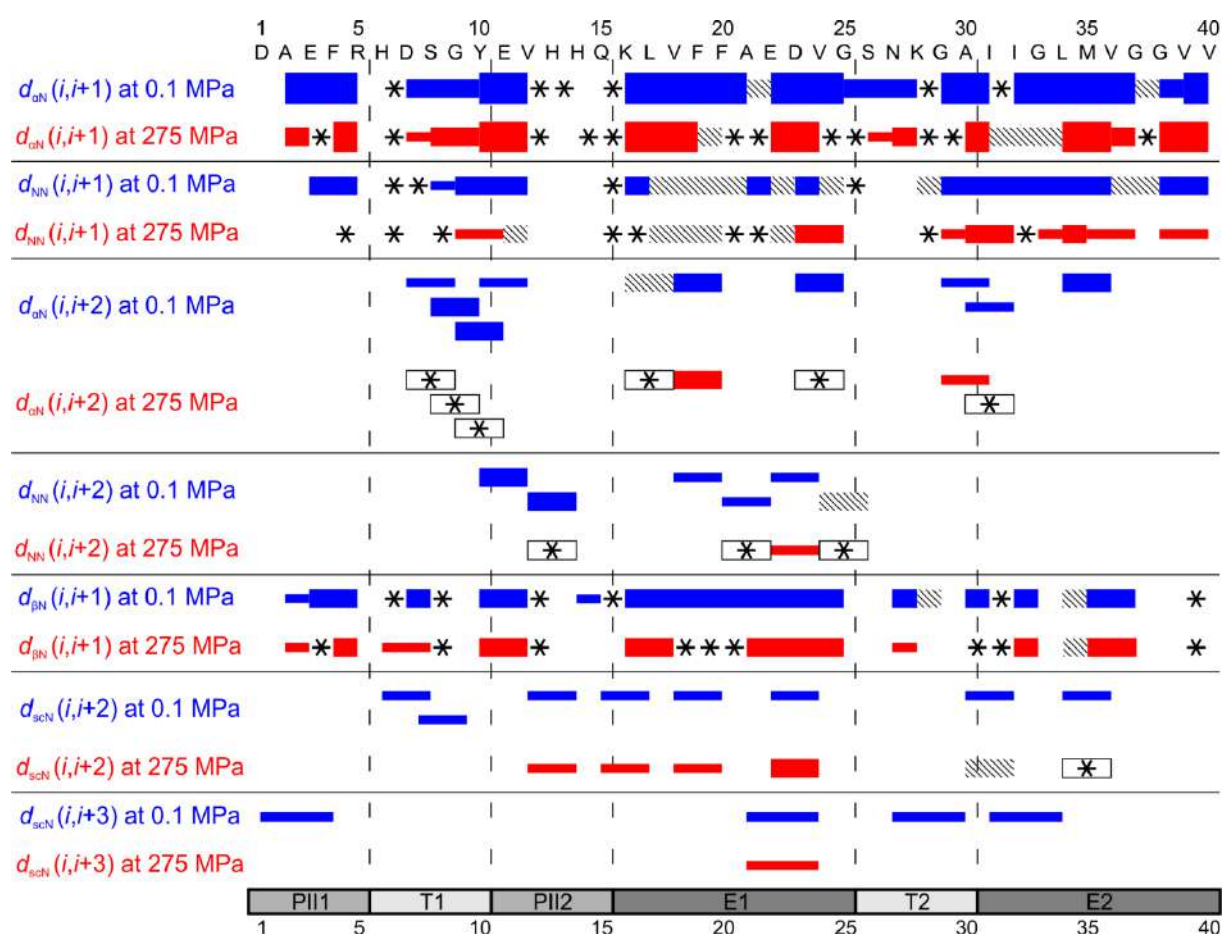


Figure 1.52 – NOE patterns for the A β peptide at 0.1 MPa (blue bars) and 275 MPa (red bars). Samples were in P4H buffer and were measured at 277 K, 500 μ M peptide concentration. The width of the bars represents the strength of the contact (‘weak’, ‘medium’, ‘strong’). Asterisks (*) indicate that the presence of NOE could not be determined due to peaks overlap. Hatching lines mean that the peak can be seen, but its volume could not be determined (partial overlap). ‘sc’ represents hydrogens from side chains (H^β , H^γ , H^δ and H^ϵ). Below, in gray, there is the representation of the structural model of A β proposed by DANIELSSON.⁴⁶

Source: By the author.

Strong $d_{\alpha N}(i,i+1)$ correlations can be seen in extended regions (Lys-16 to Ala-21 and Ile-32 to Gly-37), which indicates a propensity of these region to form a β -strand-like conformation. The pattern shows high similarity with the structural model proposed by

Danielsson et al.⁴⁶ However, it is possible to notice slight differences between certain limits of structural regions; especially the extension of the T1 region to Val-12 residue and the interruption of the E2 region around residue Val-36 (Figure 1.52). At low pressure, the presence of some $d_{\alpha\text{N}}(i,i+2)$ and $d_{\text{NN}}(i,i+2)$ contacts involving residues Lys-16 to Ser-26, although not as robust as reported by Vivekanandan et al.³⁹ (Annex B), do not completely rule out the existence of a helicoidal structure (such as a 3_{10} helix) in the center of the sequence. Since the β -amyloid peptide is known to exhibit several conformations that interconvert in solution, as previously shown, the NOEs are a concentration-weighted average for the entire ensemble of conformers and can potentially present mixed characteristics of diverse secondary segments.

Somehow, the spectrum at 275 MPa has a lower quality and displays fewer correlations than the one collected at ambient pressure. This fact is aggravated for peaks in the $\text{H}^{\alpha}\text{-H}^{\text{N}}$ region, which is affected by a spectral artifact near the water line (spectrum not shown). However, the scaffold of the interactions is maintained. In addition, several NOEs are weakened or disappear with increasing pressure, which indicates the appearance of a more unfolded conformation at high pressures.

To assist the qualitative analysis of NOEs, we measured ${}^3J_{\text{HN-H}\alpha}$ couplings at different pressures (2.3 to 285 MPa). Obtained values at 2.3 MPa are depicted in Figure 1.53 (black squares). At low pressure, high constant values are found for residues Val-18, Ile-31, Ile-32,

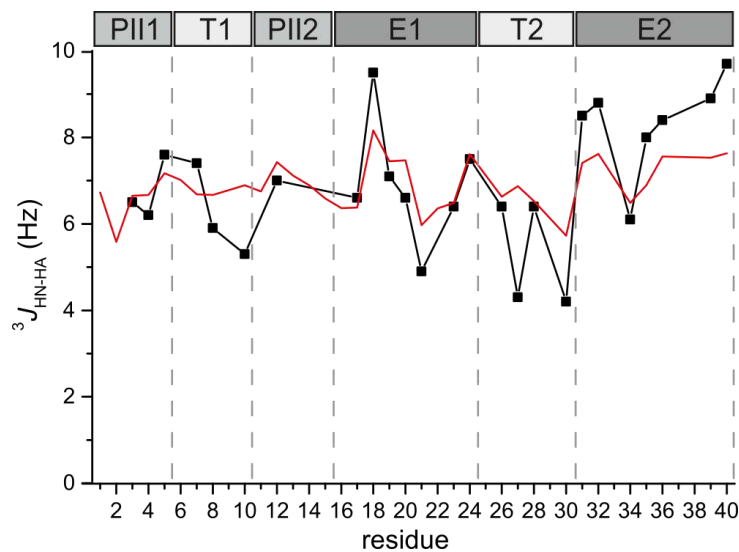


Figure 1.53 – ${}^3J_{\text{HN-H}\alpha}$ coupling constants for $\text{A}\beta(1\text{-}40)$ at 277 K. Experimental values at 2.3 MPa are presented (black squares) together with predicted values based on sequence information using RC_3JHNHa server.¹⁷⁰ Values for glycines are not presented. Above, boxes represent the $\text{A}\beta$ structural model reported by DANIELSSON.⁴⁶ Errors were estimated as 0.15 Hz (error bars are not depicted).

Source: By the author.

Met-35, Val-36, Val-39 and Val-40, all belonging to one of the extended regions (E1, E2 according to Danielsson). Low values can be seen for residues Ser-8, Tyr-10 (both at T1), Ala-21 (at E1), Asn-27 and Ala-30 (both T2). A prediction tool which estimates $^3J_{\text{HN-H}\alpha}$ couplings in disordered proteins using nearest neighbor effects^{170, 171} was used to help the analysis (Figure 1.53, red line). Surprisingly, values at the two supposed polyproline-like helix regions (PII1, PII2) are similar to predicted values in random coil sequences, indicating that these regions are barely structured.

The pressure dependence of $^3J_{\text{HN-H}\alpha}$ coupling constants was also studied (Figure 1.54). All plots reduce with pressure, most of them in a linear manner. Figure 1.54A shows plots of $^3J_{\text{HN-H}\alpha}$ by pressure for selected residues in A β . Some residues reaches values below 5 Hz at pressures higher than 225 MPa (similar to Lys-28 in Figure 1.54A) which usually prevents the calculation of the coupling magnitude. The average of the difference between $^3J_{\text{HN-H}\alpha}$ at 2.3 and 225 MPa is -0.6 Hz (Figure 1.54B). Apparently, no dependence on amino acid type is observed and the negative changes are spread all over the sequence. The most differences are observed at the PII1 region (residues Asp-1 and Glu-3) and in the second turn region (T2, residues Ser-26 and Lys-28).

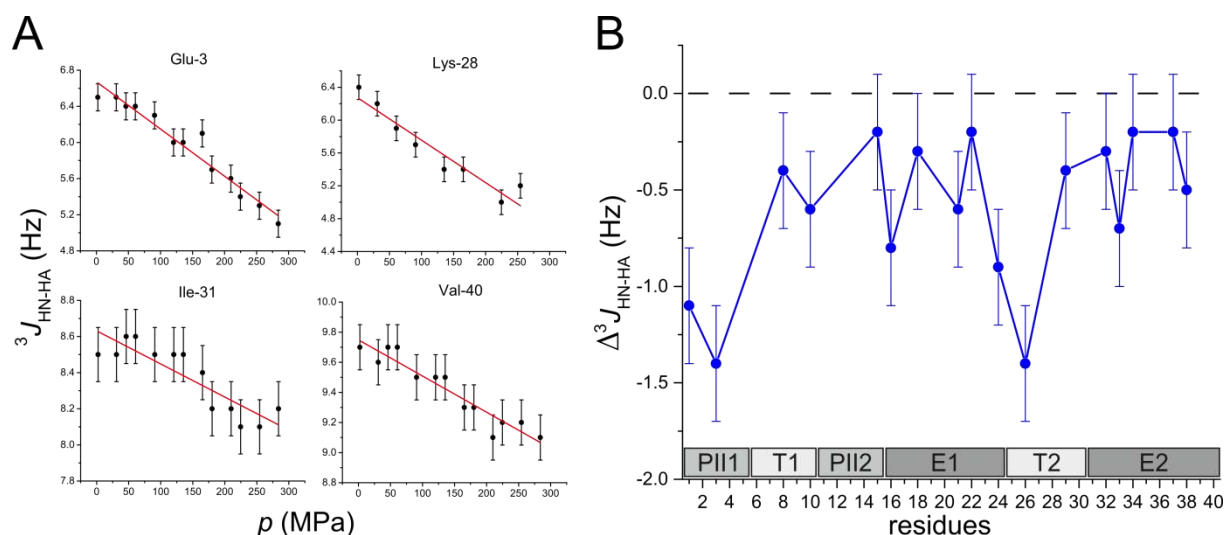


Figure 1.54 – Pressure dependence of $^3J_{\text{HN-H}\alpha}$ NMR couplings. A) Selected $^3J_{\text{HN-H}\alpha}$ curves from residues Glu-3, Lys-28, Ile-31 and Val-40 against pressure. Linear fits are shown in red. B) Difference of $^3J_{\text{HN-H}\alpha}$ between values at 2.3 and 225 MPa. Errors were estimated as 0.15 Hz (0.3 Hz for Δ^3J). boxes represent the A β structural model reported by DANIELSSON.⁴⁶

Source: By the author.

1.4.4 A β interaction with D3 peptide analogs

Two D-enantiomeric peptides, RD2 and RD2D3, were tested in their ability to interact with A β (1-40) peptide. The published experimental data focused mainly on conditions where a mixture of A β -oligomers and fibrils coexists.^{70, 71} Here, we studied the interaction of the D-peptides with monomeric A β , using concentrations below the K_D for A β oligomerization (see section 1.4.2 Depolymerization of A β by high pressure). Next, we present results relative to titration experiments with A β , the characterization of interaction sites and the proposed mode of action of the D-peptides. These results were recently published.⁷²

1.4.4.1 Titration experiments

In order to maintain A β concentration constant throughout the titration series and to avoid artifacts in the peak volume/intensity analysis, two samples were prepared (from the same original sample): a sample containing only A β (sample 1:0) and a sample containing A β at the same concentration and the peptide at the maximum concentration desired for titration (1:4). Then, the 1:4 sample was mixed with the 1:0 sample in order to obtain increasing intermediate concentrations (1:0.2, 1:0.4, 1:0.6, 1:0.8, 1:1 and 1:2). Effects were monitored by one-dimensional ¹H spectra for both D-peptides at 283 K.

At low relative concentrations of the D-peptides, the peak intensities of non-exchangeable protons in the 1D spectra decrease only moderately allowing the direct observation of the signals by solution NMR spectroscopy (Figure 1.55). In principle, this effect may indicate either (i) the decrease of monomeric species (visible by NMR) due to the formation of high mass aggregates/complexes, or (ii) the decrease in A β rotational correlation time (T_2) due to its binding to RD2 or RD2D3. Assuming a 1:1 complex, the decrease in correlation time can be estimated (by dividing the complex mass by the mass of A β , considering the molar ratio) in 15% and 29% at molar ratio of 1:0.4 for A β :RD2 and A β :RD2D3, respectively. These percentages are in agreement with signal reductions shown in Figure 1.55 and this is likely to be the mechanism behind the intensity loss.

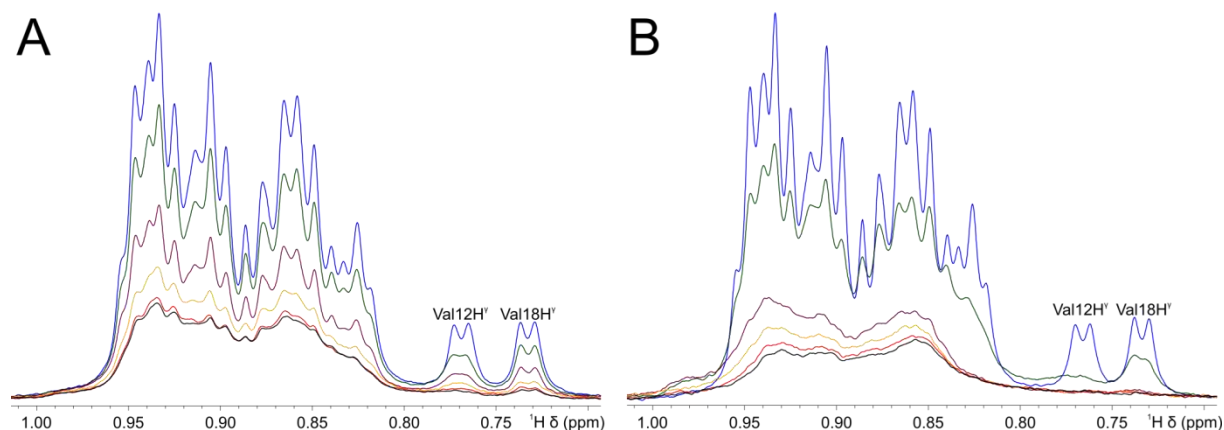


Figure 1.55 – ¹H NMR spectra of titration experiments with Aβ(1-40) in the presence of RD2 (A) and RD2D3 (B). Aβ peptide concentration was 60 μM in the titration shown in panel A and 65 μM in panel B. Experimental temperature is 283 K. Blue, Aβ only (1:0 Aβ:RD2 or RD2D3, molar); green, 1:0.4; purple, 1:0.6; yellow, 1:0.8; orange, 1:1; black, 1:2. Upfield shifted resonances of Val-12 and Val-18 H^γ are indicated.

Source: CAVINI⁷²

However, at higher concentrations of D-peptide, the monomeric Aβ signal is extremely reduced (note the signals of H^γ hydrogens of valines in Figure 1.55) and a broad component begins to be visible in the spectrum. The line broadening is more pronounced in RD2D3 titration possibly because of the enhanced properties of the *in tandem* RD2D3 peptide. In principle, it is reasonable to assume that such component is originated from the complex between Aβ and D-peptide. We could quantify concentrations of different species by integrating the respective NMR signals (Figure 1.56). With the concentrations at molar ratio 1:1, we estimated the dissociation constant (K_D) of the Aβ₄₀-RD2 and Aβ₄₀-RD2D3 complexes as 8 μM and < 1 μM.

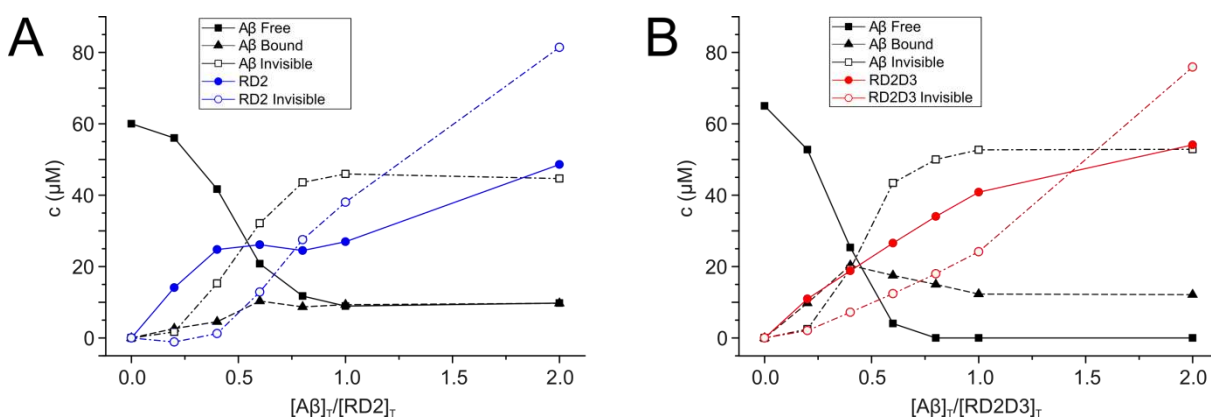


Figure 1.56 – Calculated concentrations of relevant species in Aβ titration with (A) RD2 and (B) RD2D3. Concentrations from NMR invisible species are represented in open symbols and were calculated considering the total concentration of Aβ, RD2 and RD2D3. Concentration shown are measured in monomeric units.

Source: CAVINI⁷²

In order to characterize the A β -RD2 and A β -RD2D3 heterocomplexes, experiments of diffusion-ordered spectroscopy (DOSY-NMR) were performed. The DOSY technique uses field gradients to selectively attenuate signals of molecules in the sample (the more intense the attenuation is, smaller the molecule). In the analysis, only the probable signal of the complex was analyzed. For this, the residual signal of monomeric A β was subtracted from the broad component using the signals of valine at 0.73 and 0.76 ppm. The remaining ‘broad’ component signal, thought to be the A β -peptide complex, is surprisingly smaller in size than monomeric A β .

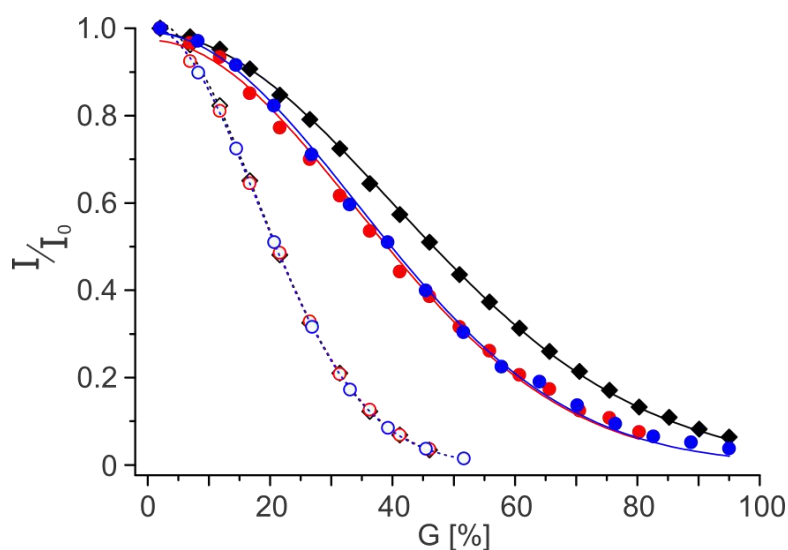


Figure 1.57 – A β -RD2 and A β -RD2D3 heterocomplexes have a reduced hydrodynamic radius. Black, A β ; blue, A β in RD2 presence; red, A β in RD2D3 presence. Calculated R_h (in nm): 1.58 ± 0.06 , 1.14 ± 0.04 and 1.12 ± 0.04 for A β , A β -RD2 and A β -RD2D3 heterocomplexes. Open symbols represent Tris decay which is near identical in all recorded experiments.

Source: CAVINI⁷²

¹H-¹⁵N-HSQC experiments acquired for titrated sample with the D-peptide RD2D3 revealed new cross-peaks in high concentration of RD2D3 (Figure 1.58). These additional peaks presumably come from the ‘broad’ component also seen in one-dimensional spectra at high concentrations of D-peptide (Figure 1.55). They might originate from the A β -RD2D3 heterocomplex, in slow exchange with other monomeric A β conformers.

The time dependence of 1:4 A β :RD2 and 1:4 A β :RD2D3 samples, used as ‘stock’ solutions on the titration, was also monitored (Figure 1.57). At first, the spectra are simply the sum of the A β and the D-peptide spectra. Although, with a relative long time, both signals from A β and the D-peptides decrease. This decrease is more intense for RD2 and RD2D3 than for A β , in a way that almost no RD2D3 is present in solution after about four days since the

sample preparation (see pink line on panel B, Figure 1.57). This different removal rate of D-peptide cannot be easily explained by a simple 1:1 binding model between the A β monomer and RD2D3 or RD2. A plausible hypothesis would be that RD2D3 is also able to bind aggregates previously formed in the solution, but the same does not hold true for A β .

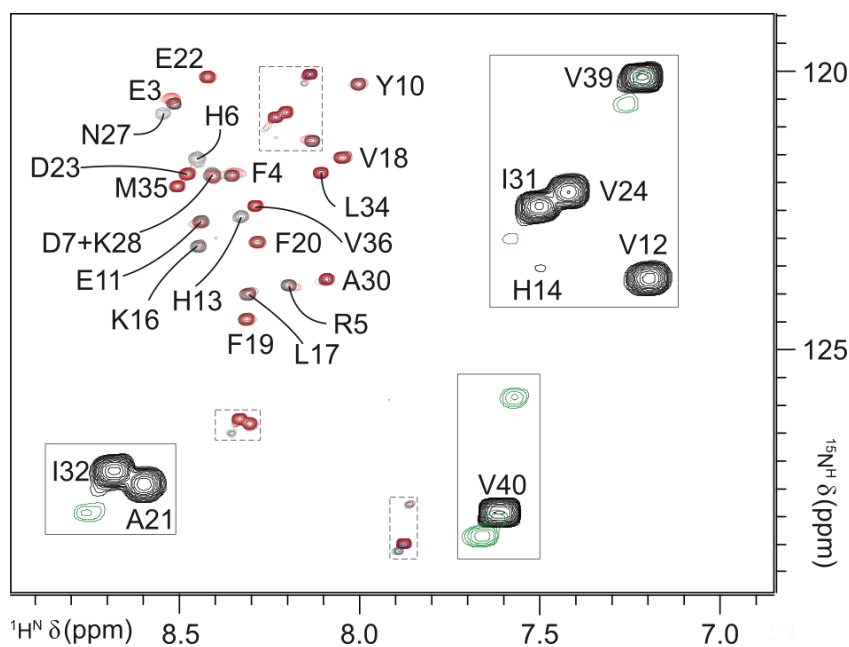


Figure 1.58 – Selected region of ^1H - ^{15}N -HSQC spectra showing the possible formation of A β -RD2D3 complexes. Several spectra are superimposed: black, 1:0 (A β :RD2D3); red, 1:0.4; blue, 1:0.8; green, 1:2. Boxes show enlarged regions containing new set of peaks (in green).

Source: CAVINI⁷²

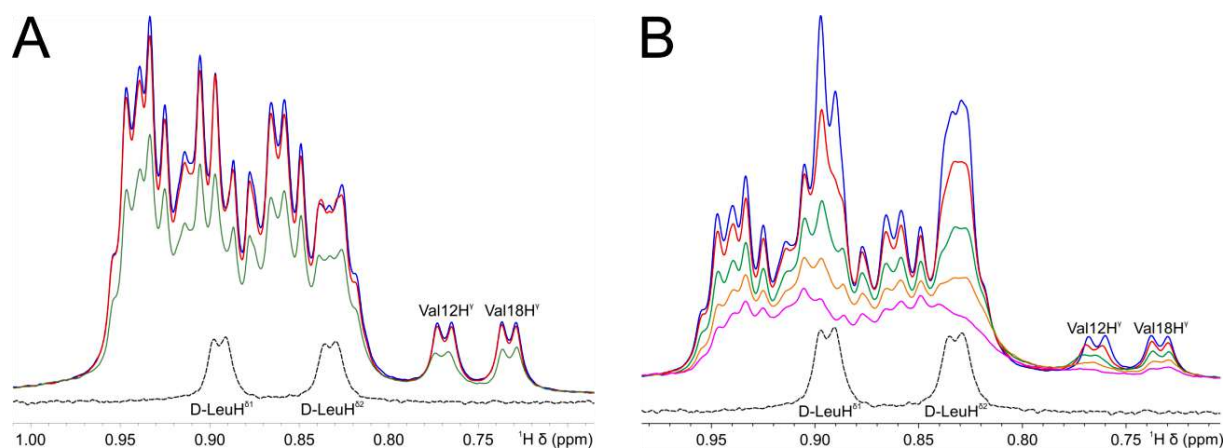


Figure 1.59 – Time dependence of 1:4 A β :RD2 (A) and 1:4 A β :RD2D3 (B) samples. Only aliphatic (CH_3 groups) NMR spectral region (0.7 to 1.0 ppm) is shown. Blue, initial spectrum ($t = 0$); red, $t = 20$ h; green, $t = 44$ h; orange, $t = 65$ h (only for A β :RD2D3); magenta, $t = 91$ h (only for A β :RD2D3). Dashed lines show the RD2 and RD2D3 respective spectra in A β absence. Leu residues in RD2D3 have $\text{H}^{\delta 1,2}$ proton resonance degenerate.

Source: By the author.

1.4.4.2 Investigation of interaction sites

To describe which residues in A β directly interacts with RD2D3, we used a ^{15}N -A β (1-40) labeled sample and recorded ^1H - ^{15}N -HSQC spectra, a NMR experiment commonly used to map protein interactions. A low concentration of RD2D3 (1:0.2 A β :RD2D3) was used in order to allow most peaks to be visible on the spectrum. ^1H and ^{15}N combined chemical shifts and the cross-peak volumes were extracted and their changes after RD2D3 addition are plotted in Figure 1.60.

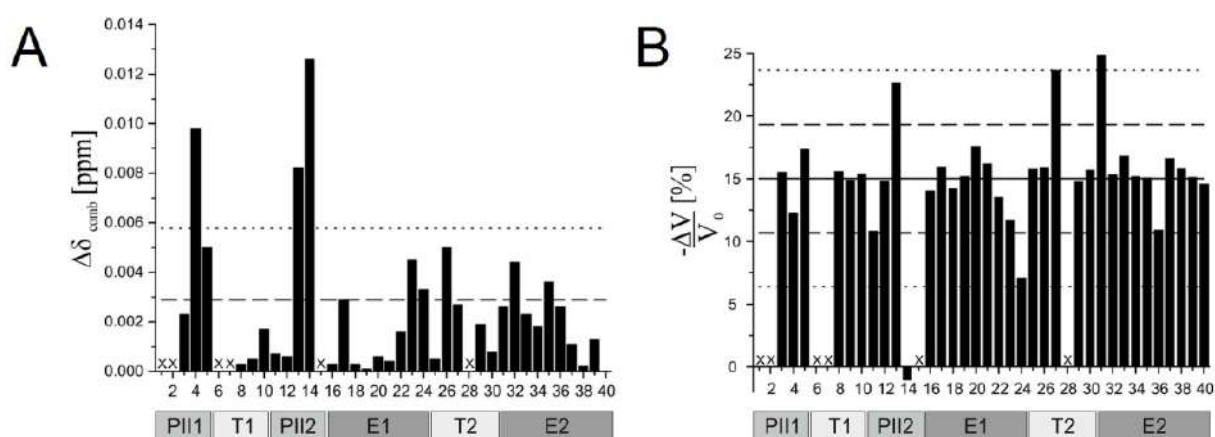


Figure 1.60 – Chemical shifts and peak volumes changes caused by A β interaction with RD2D3 peptide at 1:0.2 molar (concentrations of A β and RD2D3 are 60 μM and 12 μM , respectively). A) Changes in the $^1\text{H}/^{15}\text{N}$ combined chemical shifts of A β . Absolute values are shown. B) Relative reduction in volumes of cross-peaks on ^1H - ^{15}N -HSQC spectrum. Residues that could not be followed are marked with 'X'. Solid line (—), dashed lines (- - -) and dotted lines (····) represent the average, one standard deviation (σ_0) and two standard deviations ($2\sigma_0$), respectively. The structural model of A β are represented as boxes at the bottom of the plots.⁴⁶

Source: CAVINI⁷²

Regarding the chemical shifts changes, the largest ones were detected in the regions of polyproline II-like helices, more specifically at residues Phe-4, Arg-5, His-13 and His-14. Some residues around the turn region (Asp-23, Val-24, Ser-26, Ile-32 and Met-35) also present significant $\Delta\delta$ of interaction. For the volume changes, amino acid residues present a decrease of about 15%, in average. Volume changes are located at the same regions as the chemical shift changes, where residues Asn-27 and Ile-31 near the turn stand out.

We represented the detected changes in relevant three-dimensional structures of A β .^{39, 41, 43, 172} It seems that the least extended structures (i.e., the compact structure solved by NMR,³⁹ Figure 1.61B, and the fibrillar structure of A β ₄₂, Figure 1.61D⁴³) have a more contiguous regions of interaction, suggesting that RD2D3 binds to a more compact

conformation of A β . Unfortunately, the resolution of the heterocomplex structure by NMR was not possible since the critical concentration for aggregation is rather low ($\sim 15 \mu\text{M}$, see Figure 1.56). At this concentration, a NMR three-dimensional structure determination is not yet possible.

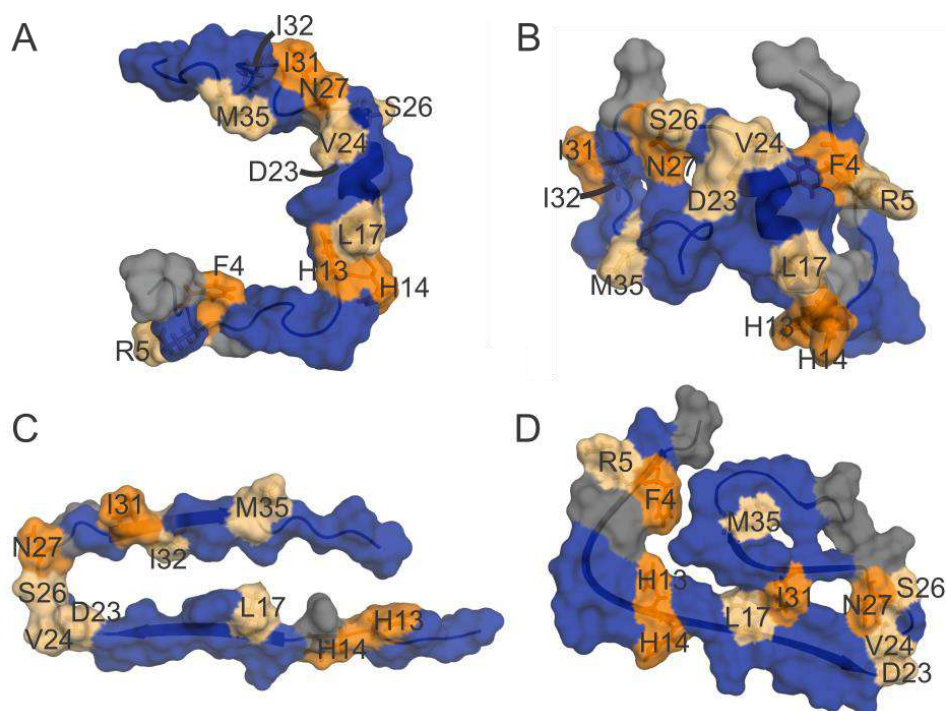


Figure 1.61 – Interaction sites of RD2D3 plotted on different A β three dimensional structures. Residues which present significant changes on cross-peak volume and combined chemical shift ($-\Delta V/V_0$ and $\Delta\delta_{\text{comb}}$) induced by the interaction with RD2R3 are colored in light and dark orange. (light orange) residues with chemical shift changes $>\sigma_0$ but $\leq 2\sigma_0$ and/or cross-peak volume changes $> \langle -\Delta V/V_0 \rangle + \sigma_0$ but $\leq \langle -\Delta V/V_0 \rangle + 2\sigma_0$; (dark orange), residues with chemical shift changes $> 2\sigma_0$ and/or cross-peak volume changes $> \langle -\Delta V/V_0 \rangle + 2\sigma_0$; (gray) residues that could not be followed in the titration series; (blue) residues not showing significant interactions. (A) the NMR solution structure reported by Watson et al.,¹⁷² (B) by Vivekanandan et al.,³⁹ (C) on the cross- β structure of a monomeric unit of a fibril from solid state NMR⁴¹ and (D) on the recent A β (1-42) cryoelectron microscopy fibril structure.⁴³

Source: CAVINI⁷²

1.5 DISCUSSION

1.5.1 Depolymerization of A β by high pressure

First, we studied the behavior of samples with a high concentration of A β (total concentration of 750 μ M) and we calculated the thermodynamic parameters involved in the polymerization (Table 1.4). A β is depolymerized by pressure since the partial molar volume (V^0) of the free monomer is smaller than the volume of the monomer bound to polymers/fibrils. The ΔG^0 calculated at 303 K (32.2 ± 1.0 kJ/mol) agrees with the value that was earlier determined by gel electrophoresis experiments as 34.7 kJ/mol at 300 K.¹⁷³ The positive ΔG^0 is in line with the fact that more compact states (i.e., free instead of aggregated monomers) are favored at high pressures. According to the model employed, K_D can be used as a guidance to estimate the A β monomeric content and it is useful in the preparation of almost purely monomeric samples.

The differences between partial molar volumes and compressibility factors (-98 ml/mol and -0.59 ml MPa⁻¹ mol⁻¹ at 283 K, respectively) are relatively high compared to other amyloid proteins, such as wild-type ($\Delta V^0 = -32.9$ ml/mol, $\Delta\beta'^0 = -0.0075$ ml MPa⁻¹ mol⁻¹)¹⁶⁰ and disulfide-deficient lysozyme ($\Delta V^0 = -52.7$ ml/mol, $\Delta\beta'^0 = -0.013$ ml MPa⁻¹ mol⁻¹),¹⁵⁹ both measured at 298 K. This indicates that large parts of the A β polymers might be protected and shielded from the solvent. It is assumed that water bound to the peptide have a smaller partial volume than the bulk water. In addition, the solid state NMR structures show larger cavities which would also explain the high (negative) compressibility found. Both factors should contribute to a larger partial molar volume of A β in fibrillary structures.

We repeated the experiments above 200 MPa to confirm the repolymerization at high pressures predicted by the thermodynamic analysis. Except for the $\Delta\beta'^0$ term, the fitting parameters extracted from the new data set (Figure 1.32) reasonably agrees with values from the initial experiment (Figure 1.29). The parameters obtained at 277 K from above 200 MPa (new data set) were $\Delta G^0 = (20.0 \pm 0.2)$ kJ/mol, $\Delta V^0 = (-74 \pm 3)$ ml/mol and $\Delta\beta'^0 = (-0.36 \pm 0.02)$ ml MPa⁻¹ mol⁻¹; in the first data set recorded in D₂O these values can be extrapolated to 277 K as $\Delta G^0 = (18.9 \pm 0.4)$ kJ/mol, $\Delta V^0 = (-84 \pm 6)$ ml/mol and $\Delta\beta'^0 = (-0.53 \pm 0.05)$ ml MPa⁻¹ mol⁻¹. Values are summarized in Table 1.9. This difference in compressibility factors

could be explained by the different solvents (H₂O or D₂O) used in the experiments, since distinct aggregation kinetics of A β (1-40) and A β (1-42) were observed in these two solvents.⁶⁰

In addition, the polymerization is a slow process; completion of the polymerization of A β at low temperature requires more than one day and the depolymerisation by high pressure takes about two hours. Yet, A β clearly repolymerizes above 200 MPa. To date, it is the first report of high pressure repolymerization of an amyloid protein. This repolymerization could be explained by structural changes in the oligomers and fibrils, which would shift again the equilibrium towards NMR invisible species at high pressures.

Table 1.9 – Comparison between two data sets of A β depolymerization at 277 K.

| | Data set 1^a (0-200 MPa) | Data set 2 (200-300 MPa) |
|--|---|---|
| ΔG^0 (kJ/mol) | 18.9 \pm 0.3 ^b | 20.0 \pm 0.2 |
| ΔV^0 (ml/mol) | -84 \pm 6 ^b | -74 \pm 3 |
| $\Delta\beta'^0$ (ml MPa ⁻¹ mol ⁻¹) | -0.53 \pm 0.05 ^b | -0.36 \pm 0.02 |

^a Extrapolated to 277 K using linear dependence of the parameters with the temperature

^b Errors considering the temperature of 283 K

Source: By the author.

1.5.2 Characterization of monomeric A β states

A paper recently published by Roche and colleagues⁶⁰ studied different NMR parameters in A β peptides: chemical shifts, nuclear Overhauser effects (NOEs) and *J* couplings. Since the same parameters were used in the present work to characterize the A β (1-40) peptide, we discussed the data comparing both data sets. They show backbone torsion angle distributions that closely resemble random coil for both A β 40 and A β 42 peptides, suggesting that intermolecular interactions between the hydrophobic regions of both peptides dominate the aggregation process. In their work, they reported ¹³C ^{α} and ¹³C' chemical shift data.

Except for the most histidines residues, our ¹³C ^{α} and ¹³C' corrected chemical shift data at 3 MPa is very similar to those reported by Roche for A β (1-40) (Figure 1.62).⁶⁰ We performed an analysis on the $\Delta\delta^*$ (pressure-corrected secondary chemical shifts) in our high

pressure data set. Even at ambient pressure $^{13}\text{C}^\alpha$, $^{13}\text{C}^\beta$ and $^{13}\text{C}'$ carbons present a significant propensity to adopt β -strand-like structure in the region comprising Leu17-Phe21 (also reported by Roche and others). In addition, this analysis shows that most of these nuclei shift somewhat towards their random coil values, which would suggest a higher population of a random coil-like state at high pressure.

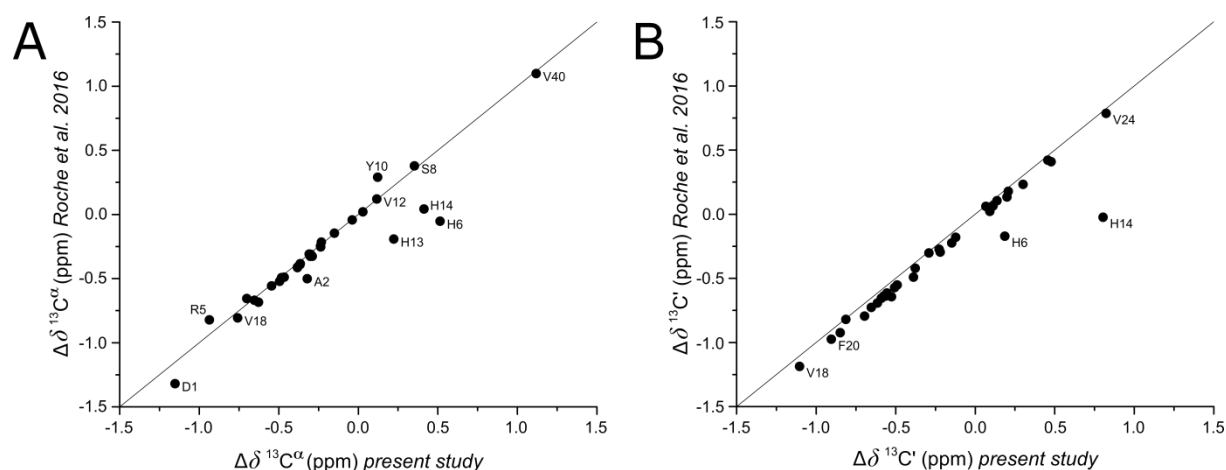


Figure 1.62 – A β secondary chemical shift comparison ($\Delta\delta$) between the present study and ROCHE.⁶⁰ A) $^{13}\text{C}^\alpha$ shifts and B) $^{13}\text{C}'$ shifts. Both data sets were acquired at 277 K with recombinant A β 40 peptide. Samples contained 150 μM peptide in 20 mM sodium phosphate buffer at pH 7.0 (ROCHE) or 90 μM in 50 mM Tris- d_{11} at pH 7.0, 100 mM NaCl (present study). Our data was corrected for pressure effects (acquisition at 3 MPa). $\Delta\delta$ was calculated using random coil data recorded at 278 K by Kjaergaard and colleagues (Ac-QXQQ-NH₂ model peptide).¹⁶⁸ Some residues are labeled and the major differences are presented by histidine residues, showing small changes in pH between samples.

Source: By the author.

Propensities predicted by TALOS+ indicate the existence of two extended regions in our data (Leu-17 to Phe-20 and Ile-32 to Val-36). The second region (Ile-32 to Val-36) could not be identified in $\Delta\delta$ analysis which is indeed understandable given the lower calculated propensities. At 288 K, the β -propensities are generally smaller compared to data at 277 K which is expected given the lower stability of the monomeric peptide at high temperatures. Other prediction softwares based on chemical shifts like $\delta 2\text{D}$ ¹⁷⁴ (developed by Prof. Michele Vendruscolo group, University of Cambridge - UK) and CSI 3.0¹⁷⁵ (from group of Prof. David Wishart, University of Alberta - Canada) failed to find any structured elements in our A β chemical shifts (data not shown). This may be due to how the data basis for the prediction in the two programs is evaluated: in the CSI and in $\delta 2\text{D}$ programs the random coil structures were defined in folded proteins as regions where a typical hydrogen bonding pattern for helices and β -pleated sheets could not be found. Since TALOS+ is primarily a program for the prediction of ϕ, ψ -angles from chemical shifts, it derives the propensities from the average

dihedral angle distribution predicted. Here, the hydrogen bonding pattern *per se* is not used. In a putative cross- β structure, no hydrogen bonding between strands are to be expected but only side chain-side chain contacts.

A surprisingly high β -propensity was found by TALOS+ for the prediction using random coil chemical shift data from the Ac-QQXQQ-NH₂ peptide. This result was surprising and might indicate that the information about secondary structure propensity is already contained in the primary sequence (a classic assumption in the field of protein folding) which is the information used in secondary structure prediction programs like PSIPRED.¹⁷⁶ The paper of Roche, however, indicates that both peptides lack highly populated structural features even reporting significant extended, β -like propensities for residues Val-18 to Phe-20 and Ile-31 to Val-36 (very similar from those reported here; Leu-17 to Phe-20 and Ile-32 to Val-36). The claiming they present is that β -branched and aromatic amino acid residues are known to have an intrinsically more extended backbone propensity as shown by Griffiths-Jones.¹⁷⁷ Although, our secondary chemical shifts ($\Delta\delta^*$) and our B_1^* and B_2^* pressure coefficients clearly refute the idea of A β being mostly random coil. A completely random coil *stricto sensu* certainly does not exist since in reality you always have some structural propensities to assume. Partly structured conformations are in a dynamic exchange with random coil-like structures.

From the corrected chemical shift curves, we obtained the pressure coefficients (B_1^* and B_2^*) for each nuclei. Some other studies also reported B_1^* and B_2^* amide pressure coefficients for A β (1-40).^{59, 61} The present work is the only one that reports amide pressure coefficients for all amino acids at 277 K (except Asp-1 and Ala-2 which undergo solvent exchange in all experiments). Values are rather similar for all studies and it is hard to detect any significant differences (Figure 1.63). Some of them can be seen near histidines residues (His-6, His-13 and His-14) probably due to sample pH differences among the studies.

The coefficients B_1^* and B_2^* display a high correlation in the present study. This effect might indicate that a unique physical process influences the pressure changes observed for the chemical shifts. A high correlation has been already reported by Beck Erlach et al. in random coil tetrapeptides (Table 1.10).^{138, 139} Except for the ¹³C ^{β} nucleus, the correlation between our pressure coefficients is higher (i.e. the Pearson correlation coefficient r is more negative) than the random coil peptide data.¹³⁹ On average, the absolute Pearson correlation coefficient ($|r|$) is 15% higher in the present data.

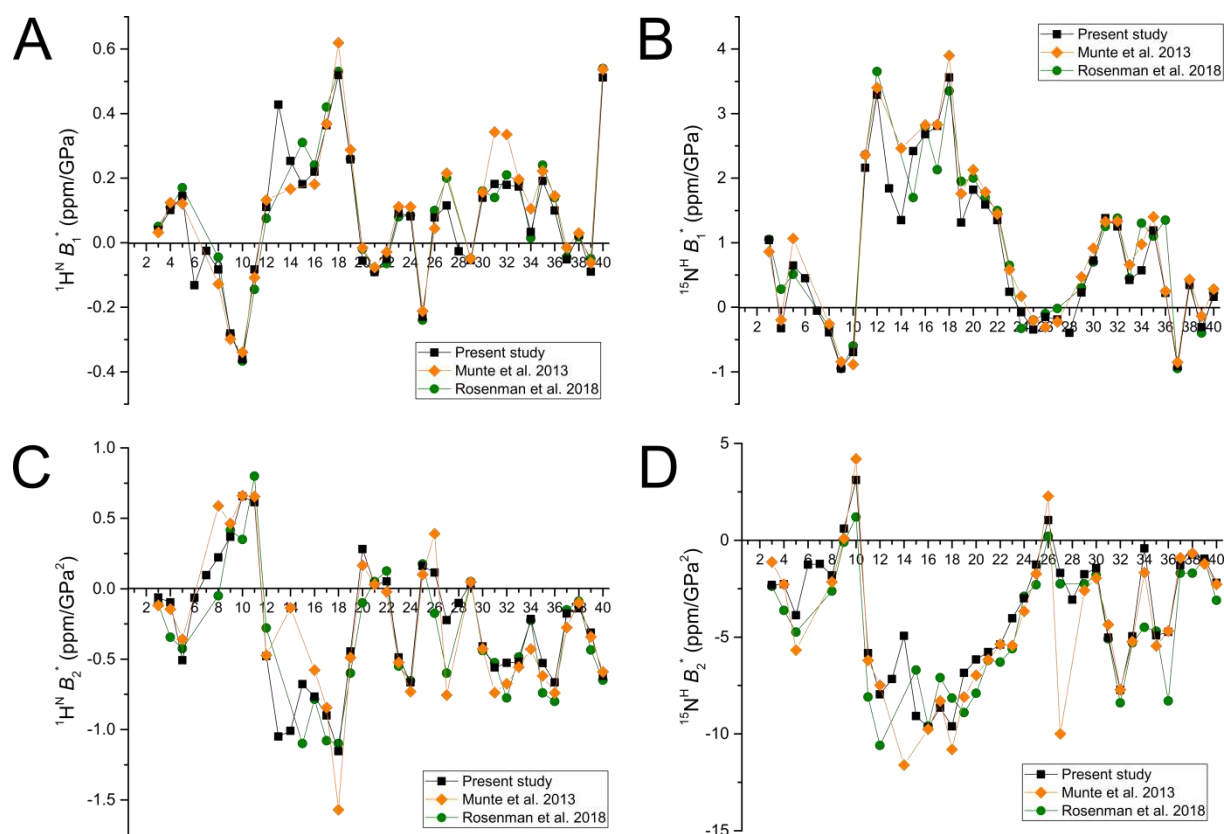


Figure 1.63 – A β (1-40) amide pressure coefficients comparison among the present and previous studies. A) $^1\text{H}^{\text{N}} B_1^*$, B) $^{15}\text{N}^{\text{H}} B_1^*$, C) $^1\text{H}^{\text{N}} B_2^*$ and D) $^{15}\text{N}^{\text{H}} B_2^*$ from the present study (black squares), MUNTE⁵⁹ (orange diamonds) and ROSENMAN⁶¹ (green circles). All data set were acquired at 277 K. B_2^* data from Rosenman et al.⁶¹ were divided by two to match the formula used by the present study. ^1H - ^{15}N -HSQC experiment was acquired using 85 μM A β , 50 mM deuterated Tris-HCl buffer, 100 mM NaCl, pH 7.0. MUNTE used 474 μM A β , 50 mM deuterated Tris-HCl buffer, 90 mM NaCl, pH 7.0. ROSENMAN used 100 μM A β , 10 mM deuterated Tris-HCl buffer, pH 7.3.

Source: By the author.

Table 1.10 – Pearson correlation coefficients (r) between B_1^* and B_2^* pressure coefficients. As a comparison, correlation coefficients from BECK ERLACH et al.¹³⁹ are also shown.

| | Present study | Beck Erlach <i>et al.</i> 2017 |
|--------------------------|---------------|--------------------------------|
| $^{13}\text{C}^{\alpha}$ | -0.83 | -0.75 |
| $^{13}\text{C}^{\beta}$ | -0.63 | -0.83 |
| $^{13}\text{C}'$ | -0.85 | -0.72 |
| $^1\text{H}^{\alpha}$ | -0.78 | -0.65 |
| $^1\text{H}^{\text{N}}$ | -0.86 | -0.80 |
| ^{15}N | -0.87 | -0.54 |

Source: By the author.

We also calculated the ratio B_2^*/B_1^* for the all the residues in A β . The value for A β is -2.0 GPa^{-1} and does not seem to depend much on the temperature (at least between 277 and 288 K). By comparison, non-structured Ac-GGXA-NH₂ peptides have an average B_2^*/B_1^*

value of -1.5 GPa^{-1} whereas for the HPr protein of *Staphylococcus carnosus* the value is way more negative, around -5.1 GPa^{-1} .¹⁴¹ Due to a limited database for analysis, no physical significance has been yet reported for B_2^*/B_1^* . However, it seems that high values of B_2^*/B_1^* indicate a relatively high compressibility difference between states, possibly indicating regions where states most differ structurally.

Strong short-range $d_{\alpha\text{N}}(i,i+1)$ NOEs indicate a propensity of the extended regions to adopt a β -strand-like conformation. Helical species can not be totally excluded because of the presence of some $i,i+2$ contacts; although they were more fragile than the ones described by Vivekanandan.³⁹ Vivekanandan and colleagues described some long-range NOEs in A β and solved a helical compact structure of the β -amyloid by solution NMR.³⁹ No long-range NOE was found in our ^1H - ^1H -NOESY spectra, even if samples conditions and NMR parameters used were rather similar from those employed by Vivekanandan. All contacts in the aromatic-aliphatic region, the spectral region where Vivekanandan reported most of the long-ranges NOEs, can be unambiguously attributed only to medium-range interactions in our spectra. Roche et al.⁶⁰ also studied A β NOEs and described the long-range as “much weaker” than the ones reported by Vivekanandan.

The study of Roche et al. also measured $^3J_{\text{HN-H}\alpha}$ couplings for the A β peptide.⁶⁰ The values range found by the group (range from 5.5 to 8.5 Hz) is smaller than the ones reported by the present study (range from 4.0 to 9.5 Hz) (Figure 1.64). The residue that deviates the most is Asn-27, even though neighboring residues (Ser-26 and Lys-28) presents very similar values in both studies. Nevertheless, residues that display above average $^3J_{\text{HN-H}\alpha}$ constants correlate quite well between themselves if approximately 1 Hz is added to the couplings constants calculated by Roche et al.. We determined the J -coupling constants from the TOCSY cross peaks in well resolved spectra with an error of about 0.15 Hz, whereas Roche et al. used a ^1H - ^{15}N -TROSY-HSQC spectrum with a long ^1H acquisition time (>250 ms). Although, the different approaches used to extract and calculate the couplings constants might have an influence in their values, the differences appear significant.

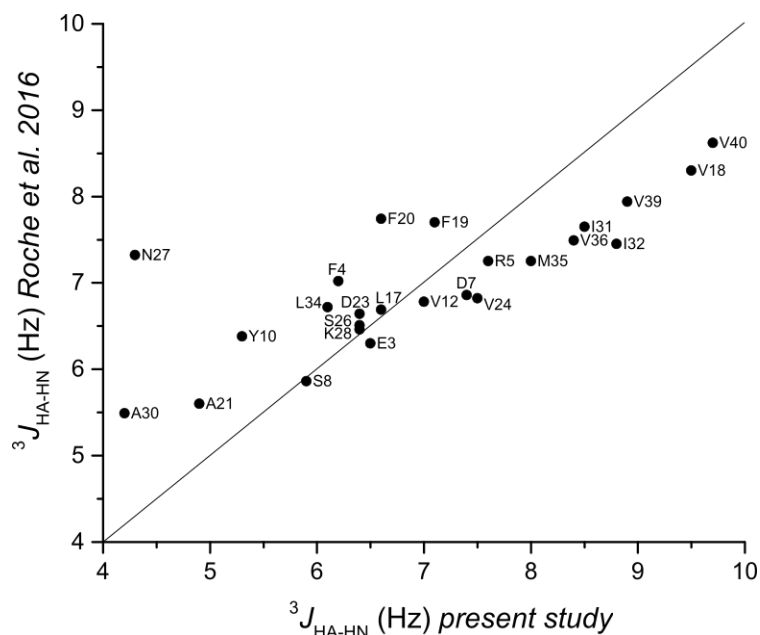


Figure 1.64 – Comparison of $^3J_{\text{HN-H}\alpha}$ A β couplings between the present work (horizontal axis) and data reported by ROCHE⁶⁰ (vertical axis). Both experiments were conducted at 277 K. The present study used 50 mM Tris buffer, pH 7.0 and a peptide concentration of 90 μM . The comparative study used 20 mM sodium phosphate buffer, pH 7.0 and a peptide concentration of 150 μM .

Source: By the author.

$^3J_{\text{HN-H}\alpha}$ NMR coupling constants systematically reduce with pressure. It is probable that the decrease in $^3J_{\text{HN-H}\alpha}$ coupling constants at high pressure is an intrinsic pressure effect. Unfortunately, pressure corrections are not yet available for these coupling constants (the only corrections available are for one-bond $^1J_{\text{N-H}}$ coupling and were based on random coil peptide data¹⁷⁸). A similar behavior was recently reported for the α -synuclein protein where an almost universally decrease in coupling constants can be seen on the high pressure data ($\Delta^3J_{\text{HN-H}\alpha}$ at 250 MPa = -0.20 ± 0.12 Hz).¹⁷⁹ However, in our case we observe J -coupling changes up to 1.5 Hz.

A three-state model was used to explain biphasic corrected chemical shift plots. Although the majority of the curves present a significant decrease with pressure, this decay can not be surely attributed to a new transition in slow exchange. Effects that are not related to monomeric structural changes, like intensity loss in the INEPT mixing time and/or volume increase because of sample depolymerization, can not be totally ignored. It was shown for a few plots that the transition seen in slow exchange is in fact one of the transitions already found for the chemical shift curves. The compressibility term ($\Delta\beta^{\text{H}}$) could not be included in our thermodynamic model because it increases the degree of freedom of the fit to a point that no convergence can be achieved. New relaxation measurements can help to better understand

the processes acting on cross peak intensities and/or volumes. A higher range of pressure can be applied nowadays (up to 300 MPa) which will certainly improve the description of A β monomers.

The thermodynamic characterization presented here present great improvements from the approach formerly used by Munte and coworkers.⁵⁹ There is a myriad of differences between the present work and the study performed by Munte⁵⁹ and published in 2013: (i) A β concentrations used by Munte are much higher than the critical concentration for oligomeric formation which could induce different monomeric states; (ii) nuclei information used by Munte is limited to amide groups; (iii) the individual fit of the curves, as used by Munte, results in decreased robustness and will likely increase model ambiguity. Nevertheless, it is compelling to trace similarities between both studies, mainly over the calculated populations of the states (Figure 1.65).

Munte interpreted the most abundant state at ambient pressure (her state 1) as a compactly folded conformation which is probably the state having a higher affinity to protofibrils. This state 1 seems to be ‘inhibited’ by the appearance of a partially folded state 2’ which is less populated at p_0 in her experiments. The shape of the curve for state 1, particularly its derivative at p_0 , is very similar to our state B (Figure 1.65), even having a very different population in our experiments. Her state 2’ would be our state A, given that both states decrease their population at high pressures to rather similar values. The difference in the populations for states A and B, compared respectively to states 2’ and 1, could be explained by the high A β concentration employed by Munte in her experiments (474 μ M). It is reasonable to suppose that high A β concentrations would increase the population of the aggregation-prone state (state B) over the less folded state (state A), which seems to be the case for Munte’s experiments. In more diluted solutions, a partially folded state (state A) dominates at low pressure and the A β monomer can be stable over several days at 277 K. State 2” in Munte’s data was interpreted as an unfolded state and possesses a very similar population compared to our state C over different pressures. Generally, high pressures induce unfolding of proteins and in the simplest case, random coil structures are expected. Since other results already presented in this thesis suggest that A β exhibits a more unfolded conformation in high pressure, it is straightforward to characterize states C as a random coil-like state.

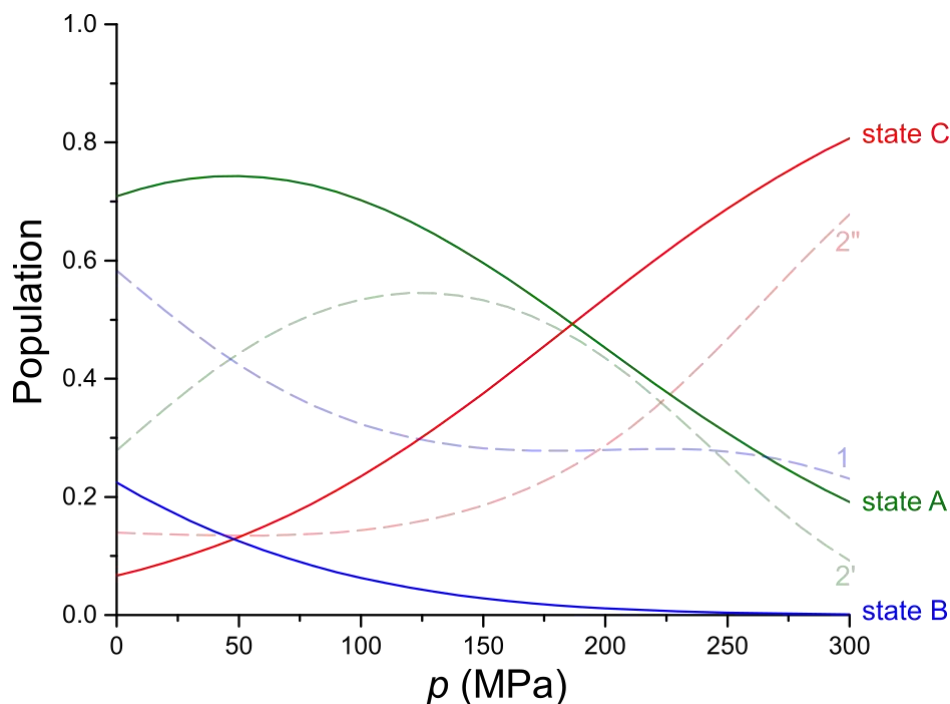


Figure 1.65 – Correlation between monomeric A β states calculated here and reported by MUNTE.⁵⁹ Conformational states described by MUNTE (1, 2, 2'') are shown with pale colors and dashed lines.

Source: By the author.

Table 1.11 directly compares the thermodynamic parameters reported by Munte and the ones presented in this thesis according to the state correspondence previously described. All parameters presented here possess lower errors which is most probably the result of a big amount (261 plots) of chemical shift data used in the calculation. As mentioned earlier, the concentration of the folded state (state B) at p_0 is much reduced in the present study which explains the considerably different values between ΔG^0_{B-A} and $\Delta G^0_{1-2'}$. ΔG^0_{B-C} and $\Delta G^0_{1-2''}$, on the other side, are rather similar between experiments. ΔV^0 are largely different and could be partially explained by the use of a second-order compressibility term by Munte. Side chain and carbon information would also improve the calculation of the thermodynamic parameters as demonstrated earlier in this thesis.

Table 1.11 – Comparison between thermodynamic parameters calculated by the present study and by MUNTE.⁵⁹ Parameters calculated by the present study are compared with reported transitions considering the following correspondence: state A, B and C corresponds to states 2', 1 and 2'' in the study of MUNTE (see more information in the text).

| | Present study | | Munte <i>et al.</i> 2013 | |
|---|---------------|---------------|--------------------------|----------------|
| ΔG^0 (kJ mol ⁻¹) | B-A | (-2.7 ± 0.1) | 1-2' | (1.7 ± 0.9) |
| | B-C | (2.8 ± 0.1) | 1-2'' | (3.3 ± 0.1) |
| ΔV^0 (ml mol ⁻¹) | B-A | (-29.1 ± 0.4) | 1-2' | (-44 ± 2) |
| | B-C | (-58.3 ± 0.4) | 1-2'' | (-12 ± 5) |
| $\Delta \beta'^0$ (ml MPa ⁻¹ mol ⁻¹) | | | 1-2' | (-0.30 ± 0.04) |
| | | | 1-2'' | (0.05 ± 0.03) |

Source: By the author.

1.5.3 A β interaction with D3 peptide analogs

Also by NMR spectroscopy, we were able to characterize the interaction of RD2 and RD2D3 D-peptides with A β (1-40). Students of Prof. Willbold measured the K_D of A β 42-RD2 and A β 42-RD2D3 complexes by surface plasmon resonance experiments (SPR) finding values of $\sim 2 \mu\text{M}$ ⁷⁵ and $0.49 \pm 0.07 \mu\text{M}$ ⁷² at 298 K, which agrees with the value found by NMR quantification (as 8 μM and below 1 μM , respectively, at 283 K), despite having used the A β 1-42 alloform. The hydrodynamic radii (R_h) calculated here for monomeric A β , A β -RD2 and A β -RD2D3 heterocomplexes are 1.58 ± 0.06 , 1.14 ± 0.04 and 1.12 ± 0.04 nm, respectively (Figure 1.57). The hydrodynamic radii of the complexes are surprisingly low. To give an idea, the theoretical R_h of a folded protein with the same mass as the A β -RD2D3 complex is 1.4 nm (R_h estimate for globular proteins using MW, Zetasizer software, Malvern). However, it is plausible that the shape of the complex is sufficiently compact to explain its high diffusion. The results indicating that the D-peptides selectively bind to a more compact conformation of A β (1-40) are in agreement with analytical ultracentrifugation experiments performed by the group of Prof. Willbold, which show a progressive decrease in the sedimentation coefficient (s) of A β as RD2D3 was added to the sample.⁷² In addition, the R_h of A β is a weighted average by the concentration of different conformations in chemical exchange. As seen by the thermodynamic analysis, at ambient pressure and 277 K, around 70% of the A β molecules (state A) are only partially folded, which presents greater R_h 's if compared to a folded peptide.

Based on our results, RD2 and RD2D3 are likely to recognize a more compact A β conformation, which is poorly populated at ambient pressure. The formation of an A β -D-peptide heterocomplex takes place because its dissociation constant is smaller (between 0.5 and 8 μ M) than the K_D found for the polymerization of A β (88 μ M). This heterodimer then forms large aggregates sequestering fibrillation competent A β and preventing the formation of toxic oligomers and fibrils. (Figure 1.66). It is tempting to assign the state B (named as state 1 by Munte et al.⁵⁹) as the structure interacting with the D-peptides. State B has a relative population of around 20% at 277 K as demonstrated by the characterization presented earlier, which is similar to the population seen for the 1:1 heterocomplex in our spectra (Figure 1.48). In fact, Munte et al.⁵⁹ speculate that the inhibition of state B (her state 1) by small molecules could be a useful mechanism to weaken the monomer-oligomer A β interaction.

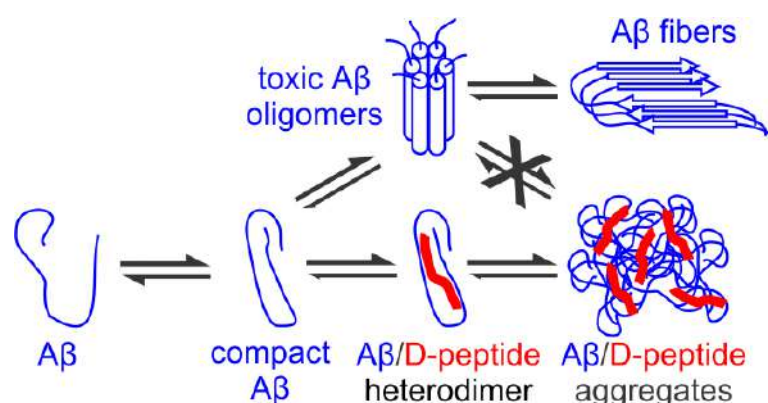


Figure 1.66 – Proposed mode of action of D-peptides. RD2 and RD2D3 recognize a compact A β conformation, leading to amorphous aggregates that are not able to form toxic oligomers, represented here as an annular assembly.

Source: CAVINI⁷²

1.6 CONCLUSIONS

A peptide called β -amyloid is mainly responsible for the mechanism that leads to Alzheimer's disease. In the last couple of decades, much has been learned about different aggregated products of A β . Soluble oligomers are the probable toxic species, triggering neuron death and destruction of synapses that mediate memory and cognition. Insoluble fibrils are rather innocuous and configure the ultimate step of the amyloidogenic pathway.

However, the aggregation initiates with the incorporation of A β monomers to existing seeds. One of these monomeric conformers might present a high-affinity to fibrils, being an attractive target for drug-design studies in preventing of the amyloid formation. Here, we characterized thermodynamically and structurally the monomeric states of the A β peptide of the Alzheimer's disease using high pressure NMR techniques. Also, the mode of action that they interact with specific D-enantiomeric inhibitor peptides was hypothesized, sustained by experimental evidence. The role of these conformations in the polymerization pathway was explored.

Initially, we presented a description on the thermodynamics of the depolymerization of A β oligomers formed in aqueous solution. A model with a single binding constant of the monomer to the oligomers was used to explain the effects of pressure. Originally polymeric, samples were partially depolymerized, and the degree of monomerization is highly temperature dependent. In line with values obtained by other techniques and present in the literature, the critical concentration, equal to the dissociation constant of the monomer to the oligomers/fibrils, was calculated as 88 μ M at ambient pressure and 283 K. This concentration value was used as a guide in further experiments in order to prepare essentially monomeric A β samples. Surprisingly, we showed that A β repolymerizes at pressures higher than 200 MPa, previously cogitated by the negative $\Delta\beta^{\circ}$ parameter. This repolymerization might occur due to pressure-induced structural changes in the NMR-invisible aggregated species.

After recording an extensive variety of NMR data (^1H - ^{15}N -HSQC, ^1H - ^{13}C -HSQC and 2D-HNCO) at monomeric conditions, we monitored most nuclei in A β sequence through chemical shifts and peak volumes. A three-state model was used to explain the biphasic chemical shift pressure curves. As demonstrated by the secondary chemical shifts ($\Delta\delta$) and NOEs pattern, A β occurs in solution under our experimental conditions dominantly in a structure containing a β -strand propensity. This propensity is found in the region where a cross- β structure is formed in fibrils. State A, the most abundant at ambient pressure, is only partially folded and state B is possibly responsible to promote amyloid fibrillar formation. The use of pressure shifts the equilibrium towards state C, which would represent an unfolded-like conformation of the β -amyloid peptide.

The interaction of the β -amyloid with designed D-enantiomeric peptides, RD2 and RD2D3, was assessed. It has already been shown that these D-peptides improve cognition in mutant rats with Alzheimer's disease. A β monomers bind to the D-enantiomeric peptides with

a substantially higher affinity than to the fibrils themselves. Calculated K_D values agree with the ones measured by other groups using SPR method. The interaction sites of the RD2D3 D-peptide on A β could be mapped by chemical shift perturbation which indicated that the peptide recognize a compact conformation of monomeric A β . This A β conformer is characterized by a more compact structure with a smaller hydrodynamic radius. Notably, the hydrodynamic radius of the heterodimer itself is smaller than the averaged R_h for the A β monomeric conformations. We speculate that the compact structure that binds to D-peptides could be the folded state B previously described. A reduction of the effective free A β concentration below the critical concentration leads to depolymerization of the polymers and toxic oligomers. After a slow process of heterodimerization, large heterocomplexes are formed thereby reducing the fibrillation competent A β conformation. It is expected that these D-peptides or the improved analogs recently designed can be soon tested in humans as an effective therapy against Alzheimer's disease.

**CHAPTER 2 ORIENTATION OF DIMERIC COILED-
COIL HUMAN SEPTINS**

2.1 INTRODUCTION

In parallel with the amyloid project, I started working with septins, a protein still poorly understood but essential in the cell division cycle in many organisms. These studies initiated in August 2016 as a consequence of an advisor change (former advisor Prof. Dr. Claudia Elisabeth Munte went on leave for personal reasons). The current advisor, Prof. Dr. Richard Charles Garratt, is the lead researcher of a project focused on structural and functional aspects of septins. This chapter presents the results obtained using nuclear magnetic resonance spectroscopy on C-terminal coiled-coils of human septins SEPT1, SEPT2, SEPT4 and SEPT5. Although the thesis title does not contemplate the septins study (it would become too long and intimidating), it certainly deserves attention with this separated chapter.

2.1.1 Septins

Septins constitute a family of guanine-nucleotide binding protein which is highly conserved in animals and fungi, but it is not found in plants. They are part of eukaryotic cytoskeleton protein class and are involved in a wide range of cellular processes. Septins have the ability to self-assemble into heterofilaments and high-organized polymers. It is known that septins play a key role in cytokinesis,¹⁸⁰ microtubule dynamics¹⁸¹ and the formation of diffusion barriers.¹⁸² Furthermore, it has been found that septins recognize regions of positive membrane curvature, being more localized in these regions.¹⁸³ Some septins are related to pathologies in humans, such as cancer, neurodegenerative diseases and male infertility.^{184, 185}

Septins were initially reported in *Saccharomyces cerevisiae* (baker's yeast) that were unable to complete the cell cycle due to mutations in four genes, *cdc3*, *cdc10*, *cdc11* and *cdc12*.¹⁸⁶ It is now known that those genes code for septins which form a ring structure at the bud neck during cell division.¹⁸⁷ In fact, the coinage of the term 'septin' is attributed to John Pringle and collaborators in reference to the importance of the protein for septal ring formation.

The human septins are encoded by 13 different genes (numbered from *SEPT1* to *SEPT12* and *SEPT14*) and are divided into four groups (I, II, III and IV) based on their

similarity (Figure 2.1). More than 13 encoded proteins are expected to exist due to alternative splicing, which results in different isoforms, in addition to post-translational modifications. Septins architecture is composed by an N-terminal portion, a GTP binding (G) domain and a C-terminal domain which includes α -helical coiled-coil sequences (Figure 2.1A).

The N-terminal domain has a variable size and sequence composition among different septins. Between the N-terminal and the G-domain, there is a polybasic region which binds phospholipids and is probably responsible (at least in part) for the septin-membrane interaction.¹⁸⁸ The G-domain is the most conserved domain throughout septins, displaying more than 75% sequence similarity between them. Like other GTPases, septins contain the canonical motifs known as G1 (GXXXXGK[ST]), G3 (DXXG), and G4 (XKXD) that interact with the phosphate groups. G4 also interacts with the guanine base.¹⁸⁹ At the end of the G-domain, a sequence element that is unique to septins (SUE, septin unique element) can be found (Figure 2.1).

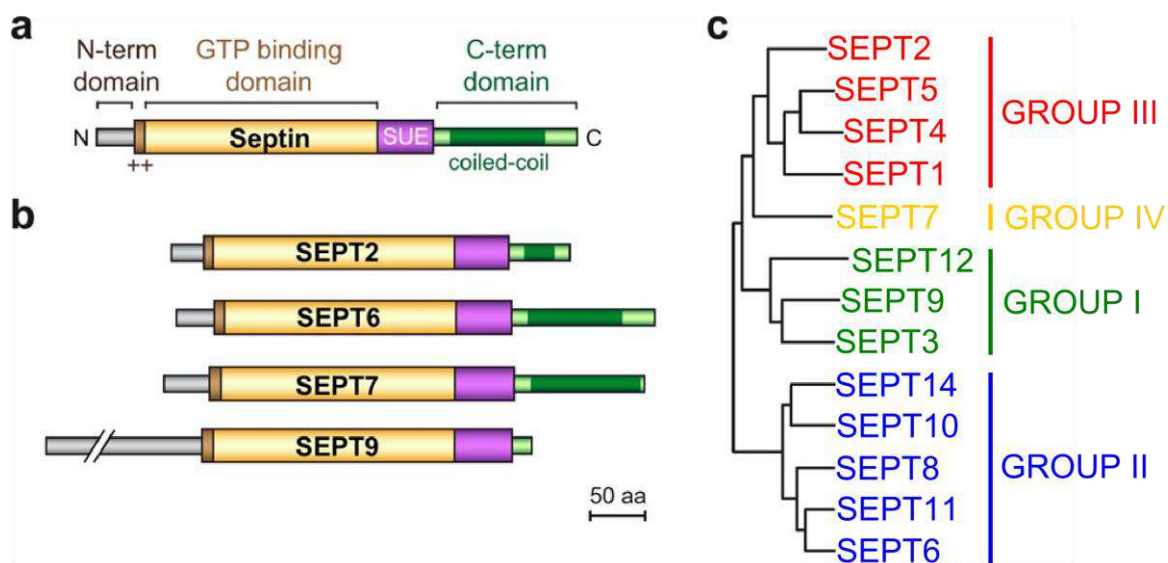


Figure 2.1 – Human septins architecture and homology clustering. a) Septins contain an N-terminal portion (gray box), a polybasic region (++), the GTP binding domain (yellow box), the septin unique element (SUE, purple box) and a C-terminal domain (light green) which has a region expected to form coiled-coils (dark green). b) Differences among relevant members of septins. SEPT6 and 7 have a long C-terminal domain whereas SEPT2 presents a short one. SEPT9 has a long N-terminal region with a proline-rich sequence and lacks the coiled-coil at the C-terminus. Domain sizes are intended to be about their sequence length. c) Human septins group into four clusters based on their sequence homology.

Source: Adapted from RIBET¹⁹⁰

The C-terminal domain of septins contains in its central part characteristic repeats of α -helical coiled-coils. These seems to be important in filament stabilization, bundle formation, and also in the interaction with other proteins, including other septins.¹⁹¹⁻¹⁹³ Except

for members of group I (SEPT9 group) that do not present a coiled-coil region, the C-terminal domain of human septins has a considerable degree of similarity (about 60% sequence identity).¹⁹⁴ Nevertheless, it has very different sizes among different groups of septins; groups II (from SEPT6) and IV (from SEPT7) have the most extensive C-terminal domain with about 130 amino acid residues, whereas members of group III (SEPT2 group) exhibit a C-terminus about half this size (around 60 residues) (Figure 2.1B).

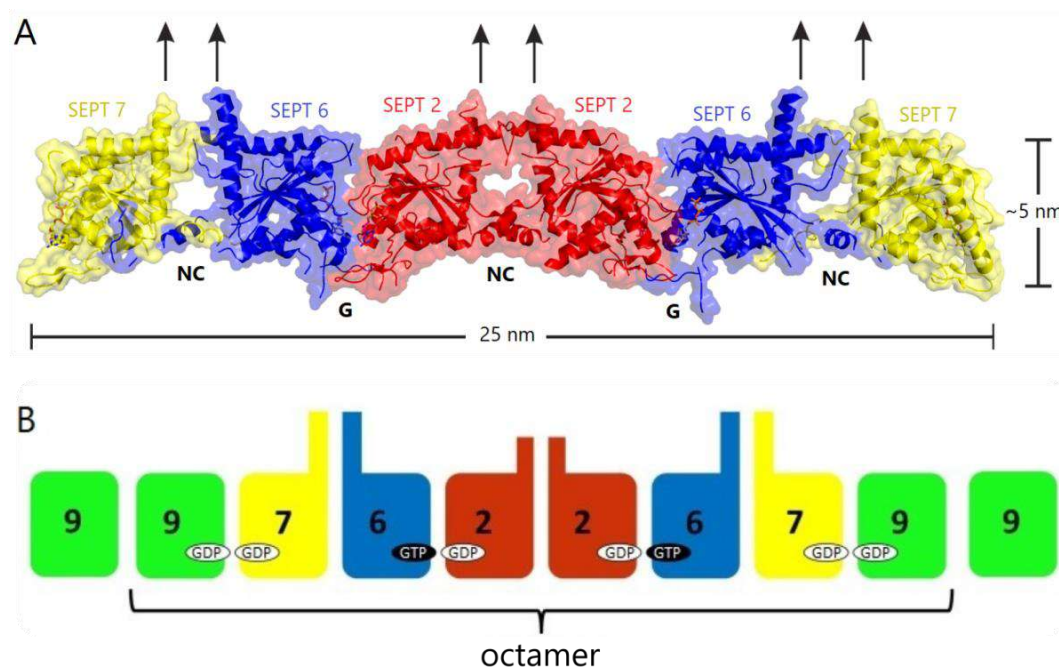


Figure 2.2 – Septins can form heterofilaments. A) Crystallographic structure of SEPT2-6-7 hexamer (PDB code 2QAG).¹⁹⁵ Black arrows indicate the position of the C-terminal domains, which seem to protrude perpendicularly to the filament axis. Interfaces are classified as G (interaction between GTPase domains) and NC (interaction between N- and C-termini). B) Studies suggest that an octamer might be the core unit, with SEPT9 occupying the extremities.¹⁹⁶ Expressed proteins normally come with bacterial endogenous GDP or GTP nucleotides, which are also presented. SEPT6 is probably catalytically inactive.¹⁹⁷ Septins are colored according to their group: I, green; II, blue; III, red; IV, yellow.

Source: Adapted from VALADARES¹⁹⁸

Both *in vivo* and *in vitro*, septins can self-assemble to form hetero-oligomers, which are the building blocks of filament formation. The first and only crystallographic structure of a septin heterofilament was published in 2007 by Sirajuddin et al. (PDB code 2QAG, resolution 4.0 Å).¹⁹⁵ The structure is a complex of septins SEPT2-6-7 whose primary unit (the core particle) is formed by a hexamer, forming the repeat 7-6-2-2-6-7, shown in Figure 2.2A. It is expected, for homology reasons, that one septin may substitute another of the same group within the filament.¹⁹⁹ It was later shown that filaments of mammalian septins can be composed of an octameric basic unit (Figure 2.2B),¹⁹⁶ rather than the hexamer found by

Sirajuddin and coworkers. In this octamer, a member of group I (in this case SEPT9) would occupy the terminal positions of the core particle, resulting in the repetition 9-7-6-2-2-6-7-9, similar to the octamer found in *S. cerevisiae*, Cdc11-12-3-10-10-3-12-11.¹⁸⁷

2.1.2 Coiled-coils

Coiled-coils are supercoiled structures consisting of α -helices coiled together usually with a left-handed twist.²⁰⁰ Two helices are the most common number of chains in coiled-coils, but others have been reported including one with seven helices.²⁰¹ They present a characteristic seven-residue repeat, *a-b-c-d-e-f-g*, which typically displays hydrophobic amino acid residues such as Leu, Ile, Val, and Ala at positions *a* and *d* and frequently polar or charged amino acid residues at positions *e* and *g*. Coiled-coils are often outlined as a wheel diagram, which shows its top view with the seven heptad positions (see for dimeric coiled-coils in Figure 2.3).

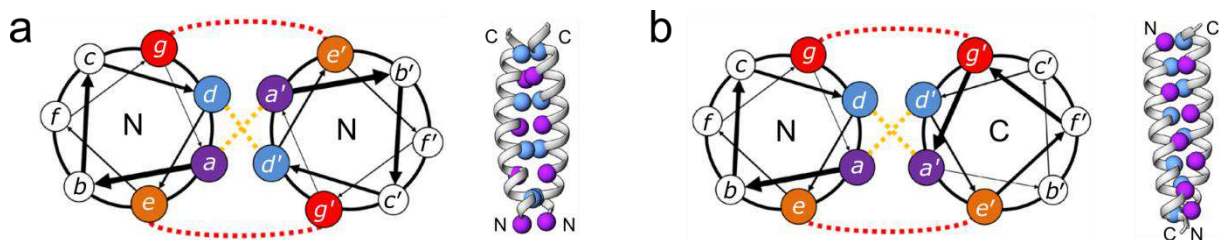


Figure 2.3 – Helical wheel diagram and side view of a parallel (panel a) and an antiparallel (panel b) dimeric coiled-coils. Coiled-coils have heptad repeats (positions *a*, *b*, *c*, *d*, *e*, *f* and *g*) which usually interact through hydrophobic (yellow dashed lines) and electrostatic (red dashed lines) intermolecular contacts. Positions *a*, *d*, *e* and *g* are highlighted in purple, blue, orange and red, respectively. Side views (right side) present the positions of *a* and *d* residues maintaining color code.

Source: Adapted from LJUBETIĆ²⁰²

In a two-stranded, parallel coiled-coil (Figure 2.3A), residues in *a* positions are at the same height as *a* positions on the opposing helix (same is valid for position *d*). The $C\alpha$ - $C\beta$ bond of a residue occupying position *a* is parallel to the peptide bond facing it on the other helix; and it is perpendicular for position *d*. In antiparallel coiled-coils (Figure 2.3B), *a* pairs with *d* positions, creating mixed core layers in the coiled-coil.²⁰³ The hydrophobic residues in *a* and *d* positions are generally buried between the cavities formed by the other helix or helices, a structural arrangement common in coiled-coils and typically known as the ‘knobs-

into-holes' motif.^{204, 205} This motif was hypothetical and theoretically predicted by Francis Crick in 1952 based on X-ray diffraction patterns of α -keratins.²⁰⁶ α -helical coiled-coils are one of the main subunit motif used for oligomerization in proteins and are commonly found in the parallel orientation. Antiparallel coiled-coils are generally composed of different portions of the same polypeptide chain.

2.1.3 Structures of septin coiled-coils

Several X-ray structures of the coiled-coil (CC) region of group III human septins have been recently solved in our research group. For this septin group, the CC portion comprises the 30 central amino acid residues of the C-terminal domain (Figure 2.4). The recombinant protein corresponding to the full C-terminal domain presents degradation (we tried to optimize the protocol with no success; data is not shown in this thesis) and no crystals have so far been obtained, probably because of the high flexibility of the tails (non coiled-coil regions). For group II, which presents a longer coiled-coil region, no experimental structure is yet available.

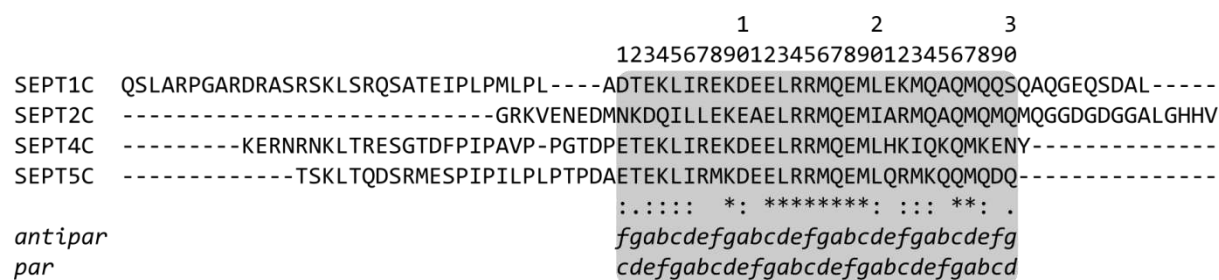


Figure 2.4 – Multiple sequence alignment of C-terminal domain of group-III septins. Alignment was made with Clustal Ω .²⁰⁷ The box highlights the coiled-coil (CC) region, composed of 30 amino acid residues. This sequence region shows high similarity among members: '*' identical; ':' similar; '.' partially similar. Below, there are assignments of parallel and antiparallel coiled-coil registers.

Source: By the author.

Except for SEPT2CC, our group has refined high resolution models for all other group-III members (SEPT1CC, SEPT4CC and SEPT5CC; structures not yet deposited). All CC peptides form dimeric coiled-coils within the crystals. SEPT1CC contains two antiparallel coiled-coils in the asymmetric unit (part of the crystallographic unit cell which can be used to generate the complete unit cell by applying symmetry operations), one is a 'blunt' coiled-coil

while the other has one helix shifted in relation to the other (Figure 2.5A). SEPT4CC presents one antiparallel coiled-coil in the asymmetric unit which is very similar to the ‘blunt’ dimer of SEPT1CC (Figure 2.5B). On the other hand, SEPT5CC is a parallel coiled-coil with no register shift (Figure 2.5C).

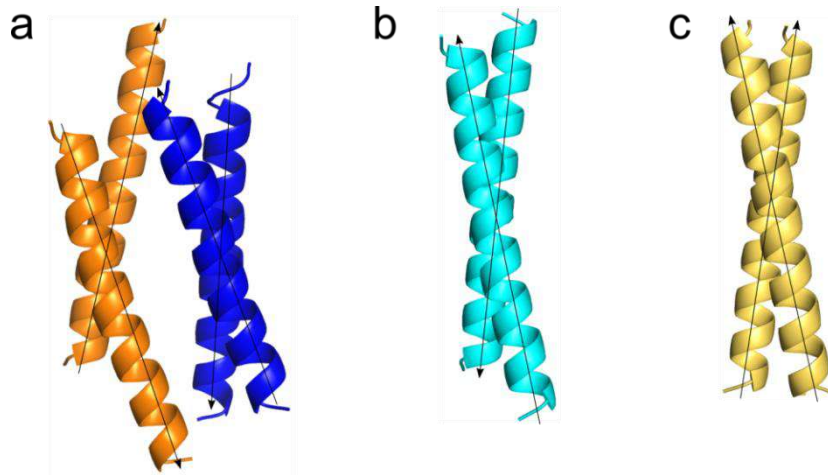


Figure 2.5 – Coiled-coil crystallography structures of human septins. Arrows indicate the helix orientation, towards the C-terminus. a) SEPT1CC, with two antiparallel dimers (blue and orange) inside the asymmetric unit; b) antiparallel SEPT4CC; c) parallel SEPT5CC.

Source: CABREJOS (not yet published).

At this point, it is useful to present different helix pairings that could be possible for homodimeric SEPTCC peptides and their nomenclature. Coiled-coils can be blunt (or nearly blunt in the case of the antiparallel orientation) or have a shift to one of the helices, maintaining register assignment. Helix shifts might exist to optimize side-chain packing in the core of the coiled-coil. Shifts larger than one heptad repeat (two helix turns of 3.5 residues each) should be rare given that it reduces the potential surface area of dimerization. In parallel coiled-coils, a shift leaves part of each extremity unpaired; the pairing is identical no matter which direction one of the helices moved. In antiparallel coiled-coils, N- or C-shifted helices might exist (N- or C- meaning which portion loses contact with the other helix) (Figure 2.6). The shifted dimer of SEPT1CC in Figure 2.5 (orange) is C-shifted according to this nomenclature.

Surprisingly, SEPT4CC shows unexpected residues at the *a* positions with polar and charged side-chains (aspartic and glutamic acids, glutamines). The structure, refined at 1.35 Å, displays two distinct sides of the interface: one is hydrophobic and formed by the *d*

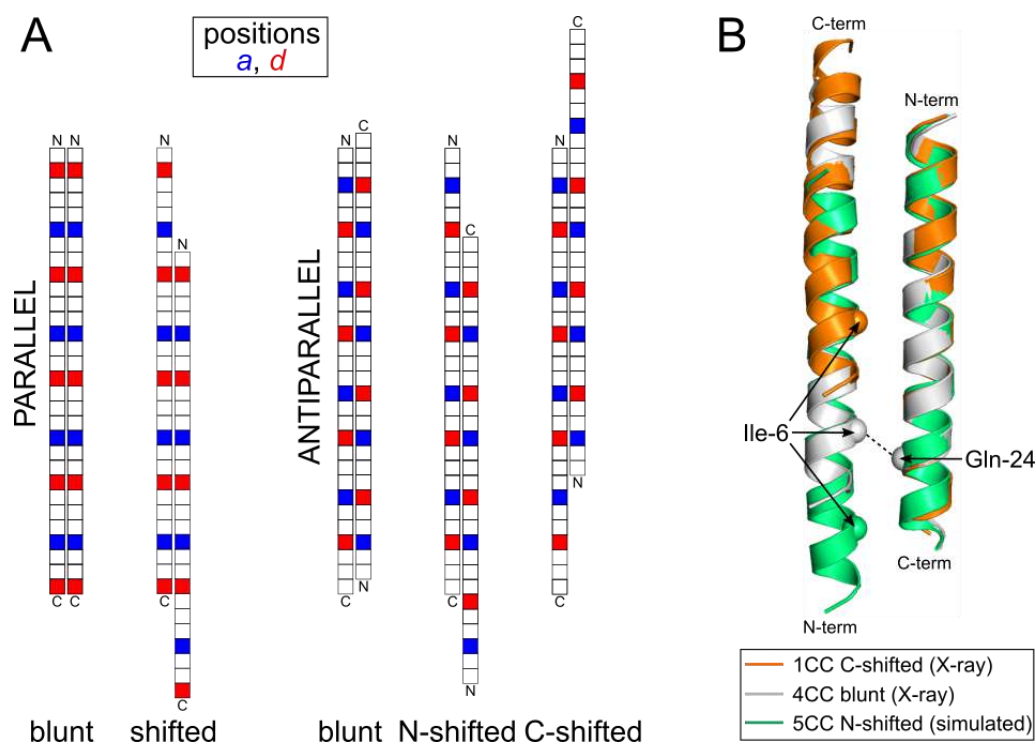


Figure 2.6 – Different helical pairings for septin coiled-coil peptides. A) Each square represents an amino acid residue of the 30 residues-long septin sequence. Positions *a* and *d* are labeled in blue and red, respectively. Only pairings with shift of one heptad repeat are shown. B) Structural alignment of antiparallel SEPTCC structures showing different pairings. Spatial alignment was done using the helix on the right only. Simulated and X-ray structures are shown (captions on insert). Spheres represent the α -carbon of residues number 6 and 24 for each coiled-coil in the respective color.

Source: By the author.

positions (Figure 2.7A, gray); another is hydrophilic and formed by the *a* positions (Figure 2.7A, cyan). Hydrophilic amino acid residues form well established hydrogen bonds (Figure 2.7B), which probably contribute to the stability of the dimer.

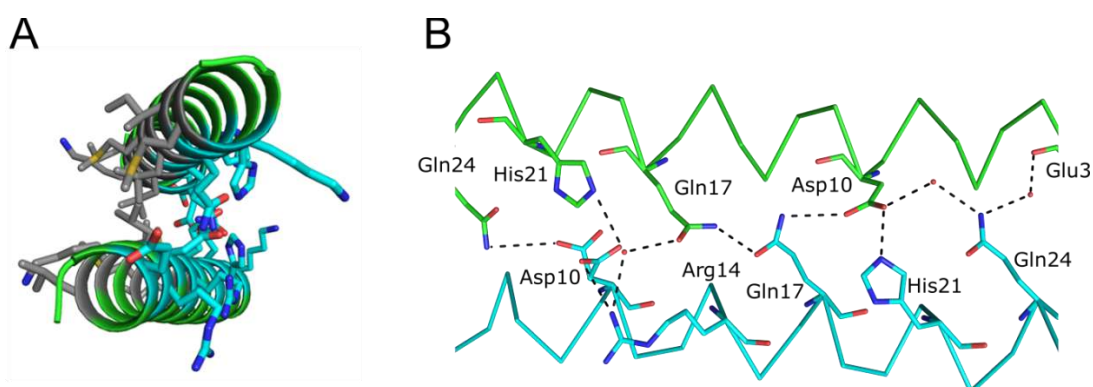


Figure 2.7 – Structure of antiparallel SEPT4CC in detail. A) SEPT4CC coiled-coil interface is amphipatic (hydrophobic side in gray; hydrophilic side in cyan). B) Hydrogen bond network composed of residues in *a* positions (Glu-3, Asp-10, Gln-17, Gln-24) which are expected to be hydrophobic in classic coiled-coils. Chains are depicted in different colors and red dots represent water oxygens that form hydrogen bonds.

Source: CABREJOS (not yet published).

A collaborator (Prof. Dr. Ingemar André, Lund University – Sweden) performed *in silico* simulations on group-III septin CC peptides. The energy of 50,000 coiled-coil structures was computed for each sequence and, surprisingly, lower energy SEPTCC structures can be clearly separated in two distinct ensembles: parallel and antiparallel. This indicates that both orientations are somewhat equally stable and both could possibly be present in solution. However, the detection of both orientations by the same experimental technique has not yet been reported.

Remarkably, the respective simulated structures superposes very well with experimental models. RMSD for all alpha-carbon atoms are below 1.3 Å for antiparallel SEPT4CC and parallel SEPT5CC structural alignments between crystallographic and the respective simulated model (see alignments in Figure 2.8). Nevertheless, the coiled-coil register pairing is different among antiparallel structures. The simulated structures of SEPT1CC, 2CC and 5CC are N-shifted (simulated SEPT4CC coiled-coil is blunt, Figure 2.8A).

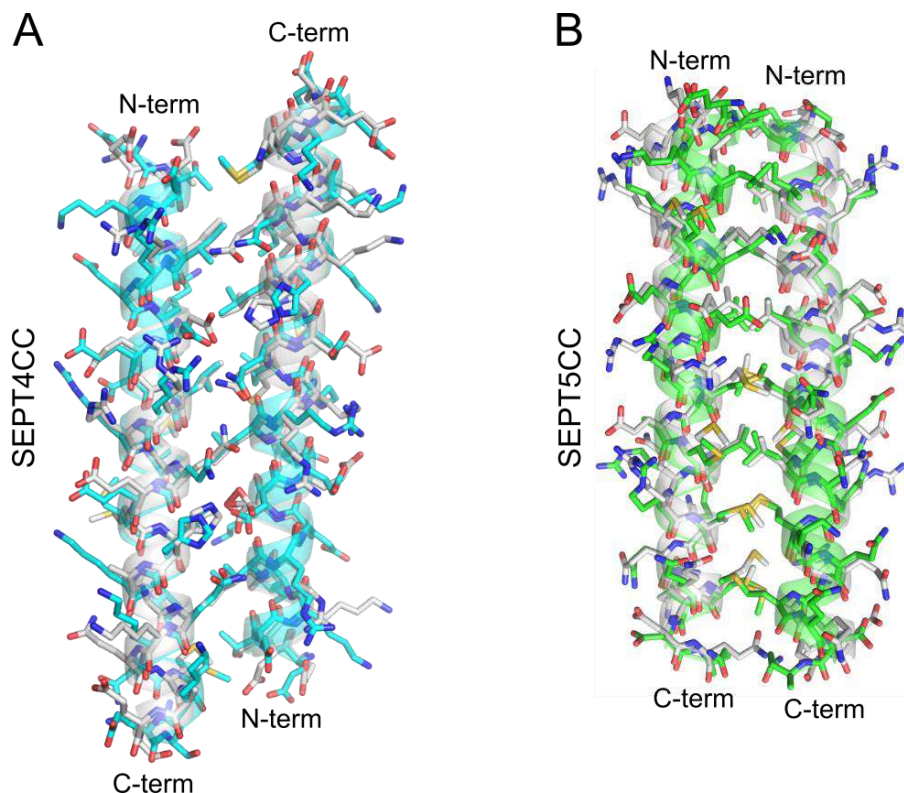


Figure 2.8 – Structural alignment of simulated SEPTCC structures with their respective crystallographic models. A) Antiparallel SEPT4CC, B) parallel SEPT5CC. X-ray structures are shown in light gray and simulated structures are shown in color (cyan or green).

Source: CABREJOS (not yet published).

2.2 RESEARCH OBJECTIVES

The formation and maintenance of septin complexes is still not fully understood. Given the lack of reliable structural information on the C-terminal domain of human septins in solution and the apparent dimorphism of these domains with respect to their adopted orientation, the present study aims to characterize their structure by using nuclear magnetic resonance (NMR). Solution NMR spectroscopy allows the use of conditions closer to those found physiologically.

2.3 MATERIALS AND METHODS

2.3.1 Sample preparation

Synthetic peptides containing the coiled-coil portions of C-terminal group-III human septins SEPT1CC (Ac-DTEKLIREKD EELRRMQEML EKMQAQMQQS-NH₂, MW = 3794.34 Da), SEPT2CC (Ac-NKDQILLEKE AELRRMQEMI ARMQAQMQM-Q-NH₂, MW = 3733.41 Da), SEPT4CC (Ac-ETEKLIREKD EELRRMQEML HKIQKQMKEN-NH₂, MW = 3883.50 Da) and SEPT5CC (ETEKLIRMKD EELRRMQEML QRMKQQMQDQ-NH₂, MW = 3880.54 Da) were purchased from GenScript (Piscataway, NJ, USA) or Biomatik (Cambridge, Ontario, Canada) with a purity of 95% or higher.

For NMR experiments, lyophilized samples were solubilized to low millimolar range concentration (0.5 mM for SEPT1CC, 1.0 mM for SEPT2CC and 5CC, and 3.8 mM for SEPT4CC) directly into sample buffer and sonicated to assure complete solubility. The buffer used was typically 50 mM potassium phosphate pH 5.0 containing 300 mM NaCl, 50 μ M DSS, 5% D₂O, 1 mM NaN₃. For SEPT4CC, 100 mM NaCl was used instead and 10% glycerol-d₈ was added. For SEPT5CC, 150 mM NaCl was used. If necessary, the pH was corrected using sodium hydroxide or hydrochloric acid solutions and samples were centrifuged for 10 minutes, 4 °C, 16,000 rpm to remove possible aggregates.

2.3.2 NMR spectroscopy

NMR spectra were recorded at Universität Regensburg, Germany with a Bruker Avance 800 MHz spectrometer operating at a ^1H frequency of 800.20 MHz and equipped with a 5 mm TCI cryo probe. Data was processed using Bruker TopSpin 3.5 (Bruker, Billerica, Massachusetts, USA) and analyzed with AUREMOL.¹⁰³ Two-dimensional, ^1H - ^1H -NOESY and ^1H - ^1H -TOCSY were acquired at 298 K. NOESY spectra were recorded using 2048 points for the direct dimension and 1024 points for the indirect dimension, 32 scans and a mixing time of 300 ms. TOCSY spectra were recorded using 8192 points for the direct dimension and 512 points for the indirect dimension, 12 scans and a mixing time of 80 ms. Water signal suppression was achieved using pulse-field gradients. For more information on these experiments, consult sections 1.3.3.3 and 1.3.3.4 on Chapter 1. Backbone and side-chain proton resonance assignment were obtained through the standard homonuclear TOCSY/NOESY approach (for a description on how the assignment was performed, see section 1.1.5.1 NMR assignment).⁸⁸ ^1H -NMR shifts were referenced relative to DSS (4,4-dimethyl-4-silapentane-1-sulfonic acid) used as internal standard at 0 ppm.¹⁰⁴

2.3.2.1 Back-calculation of NOESY NMR spectra

The relative orientations of C-terminal coiled-coil domains of group-III human septins (SEPT1, 2, 4 and 5) were determined in comparison with the structure obtained by X-ray crystallography. Two-dimensional NOESY spectra were simulated using the X-ray models with different orientations (parallel and antiparallel) and subsequently compared with experimentally acquired data. We used back-calculated NOESY spectra based on X-ray crystallographic 3D models of parallel SEPT5CC and antiparallel SEPT1CC and SEPT4CC (unpublished data). Model structures were prepared by mutating residues *in silico* when necessary in order to produce the correct sequence using Pymol. Hydrogens were added by using AUREMOL. The PDB file was converted to IUPAC format with AUREMOL for compatibility reasons. Terminal groups were added with Pymol and their names were manually changed (N-terminal acetyl group, residue name ACE, protons HH31, HH32, HH33; C-terminal amide group, residue name NH2, protons H1, H2). The simulated NOESY

spectra were back-calculated using RELAX²⁰⁸ with a cut-off distance of 0.5 nm and a noise of 0.95%. Processing was done with identical parameters from the experimental NOESY spectrum with no additional broadening.

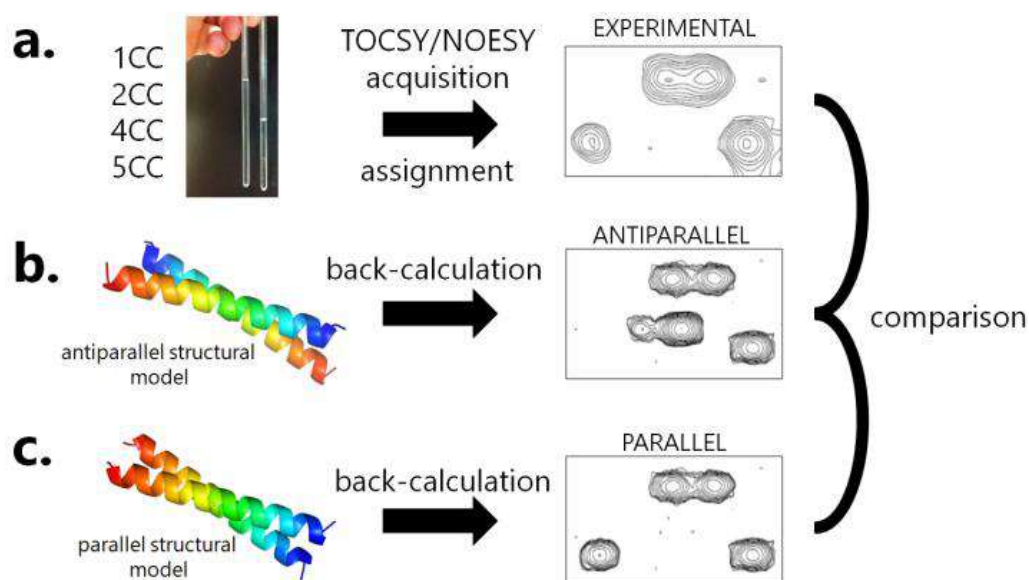


Figure 2.9 – Approach used to investigate the relative orientation of septins coiled-coils by NOESY NMR spectra. First, TOCSY and NOESY spectra were recorded for all peptides individually (a). Back-calculated spectra were generated by RELAX from antiparallel (b) and parallel (c) structures. The comparison between experimental and simulated data enables the identification of typical parallel/antiparallel contacts, leading to the coiled-coil orientation and register found in solution.

Source: By the author.

2.3.2.2 NMR paramagnetic relaxation enhancement

Peptides containing an additional cysteine residue at the C-terminus (Cys-31) were synthetically produced by solid-state peptide synthesis (kindly provided by Dr. Edson Crusca Júnior, UNESP campus Araraquara). MTSL (2,2,5,5-tetramethyl-1-oxyl-3-methyl methanethiosulfonate spin label) was covalently bound to the thiol group of cysteine (Figure 2.10). Before measurement, samples were freeze-dried and kept away from light sources to avoid MTSL detachment and reduction of the NO[•] group to diamagnetic hydroxylamine (NOH). Sample powder was resuspended directly into buffer. Only SEPT1CCys-MTSL and SEPT5CCys-MTSL peptide samples were analyzed. However, spectra underwent severe line broadening and only a few spin systems were detected. In order to identify more peaks, non-labeled peptide was added. A sample 3:1 (molar) non-labeled:MTSL-labeled was prepared. The sample oligomeric state was monitored by diffusion NMR experiments.

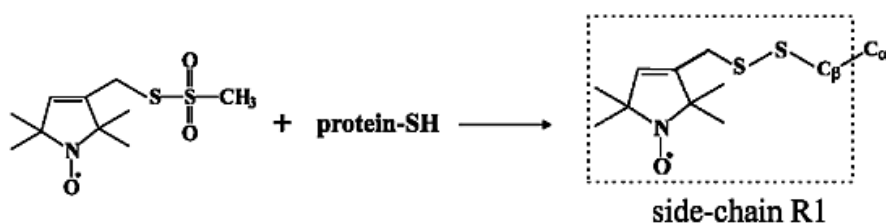


Figure 2.10 – Methanethiosulfonate spin labeling (MTSL) in proteins. A cysteine residue is used to covalently bind a paramagnetic label.

Source: HUBBELL²⁰⁹

2.3.3 Oligomeric state investigation

2.3.3.1 SEC-MALS experiments

Size exclusion chromatography coupled to multi angle light scattering (SEC-MALS) is a useful methodology to characterize protein size and oligomeric state.²¹⁰ Different running buffers were used for SEC-MALS experiments: 50 mM potassium phosphate, pH 5.0 (buffer A); 50 mM potassium phosphate, 300 mM NaCl, pH 5.0 (buffer B); 50 mM potassium phosphate, 100 mM NaCl, pH 7.0 (buffer C) and 20 mM Tris, 300 mM NaCl, pH 8.0 (buffer D). A Waters HPLC (Milford, MA, USA) was connected in-line to a GE Healthcare Superdex 75 5/150 GL size-exclusion (SEC) column (Piscataway, NJ, USA), a multiangle light scattering (MALS) Wyatt miniDAWN-TREOS (Santa Barbara, CA, USA), and a Wyatt Optilab T-rEX refractive index detector. The flow rate was 0.3 ml/min. Data was analyzed with ASTRA 7 integrated software.

2.3.3.2 Diffusion NMR experiments

In 1D-¹H translational diffusion NMR experiments, the gradient strength was swept from 2 to 95% using 16 equally separated points. Experiments were acquired with a One-Shot pulsed field gradient stimulated echo (PFGSTE) modified sequence.¹¹¹ We used in the calculations a hydrodynamic radius (R_h) of 0.346 nm for DSS¹⁴⁸ which was used as internal standard.

2.3.4 SEPTCC heptameric position analysis

In order to study the stability of our α -helical coiled coils, we gave a score S_{pos} for each sequence based on the occurrence of each residue in its heptameric repeat position. We used the CC+ database²¹¹ to extract the swissprot-normalized data for each of the 20 common amino acids in each of the seven heptameric positions ($o_{aa,pos}$, $aa = 20$ different amino acids, $pos =$ seven different heptameric positions). CC+ database contains assigned sequences for coiled-coil structures present in the Protein Data Bank (PDB). Data were searched for interchain, homodimeric coiled-coil sequences longer than 21 residues, with canonical heptameric repeats. Sequences were separated by orientation (133 sequences were parallel and 66 were antiparallel coiled coils) and redundancy was kept at a low level (lower or equal 50%). Data used is presented in Appendix K. The scores for position a , d , a,d -combined and for all positions (S_a , S_d , $S_{a,d}$ and S_{all} , respectively) was computed as the average of $o_{aa,pos}$ for all residues in the selected positions.

2.4 RESULTS

2.4.1 Relative coiled-coil orientation by NMR

2.4.1.1 NOEs analysis

To investigate the relative coiled-coil orientation by solution NMR, we used back-calculated NOESY spectra based on X-ray crystallographic 3D models of antiparallel SEPT1CC (Figure 2.5A), SEPT4CC (Figure 2.5B) and parallel SEPT5CC (Figure 2.5C) previously presented in the Introduction. Analysis was done by comparing the (i) fully assigned ^1H - ^1H -NOESY spectrum (assignment tables attached in Appendix) recorded at 298 K with the (ii) back-calculated NOESY from the parallel model and with the (iii) back-calculated NOESY from the antiparallel model (Figure 2.9).

Contacts in the 2D-NOESY spectra can be divided in intra-, intermolecular and mixed (intra- and intermolecular contacts superposed). The analysis of the intermolecular NOEs, mainly side-chain contacts, will result in the indication of the relative orientation of the coiled-coil. Intermolecular NOEs from antiparallel contacts are easily identified since most of them do not appear in the structure of the monomer as intramolecular correlations. Although, pure intermolecular contacts from a parallel coiled-coil cannot be identified without the use of labeling^{212, 213} or simulation techniques²¹⁴. This usually happens in proteins with a high degree of symmetry, which have a high number of mixed NOEs.

We first manually searched for typical antiparallel contacts in uncrowded regions of the experimental spectrum. If some, unambiguous NOE antiparallel contacts can be seen on the spectrum, this clearly indicates an antiparallel conformation. However, if none can be found, it seems likely that the coiled-coil is parallel (since we ruled out the existence of high-order oligomers, section 2.4.3 Oligomeric studies). If experimental peaks were not present in neither calculated spectra, they were identified and a different structural model was tested in order to explain their existence. In the following sections, we present the results of the analysis separately for each of the coiled-coil sequences. Later we present some possible intermolecular contacts for the parallel structures found.

2.4.1.1.1 SEPT1CC

The experimental spectrum of the peptide SEPT1CC showed no intermolecular contacts derived from its blunt, antiparallel coiled-coil obtained by X-ray (Figure 2.11). It also lacks important antiparallel NOEs when compared with back-calculated spectra using the X-ray structure of SEPT4CC or with the N-shifted simulated structure of SEPT1CC (Table 2.1).

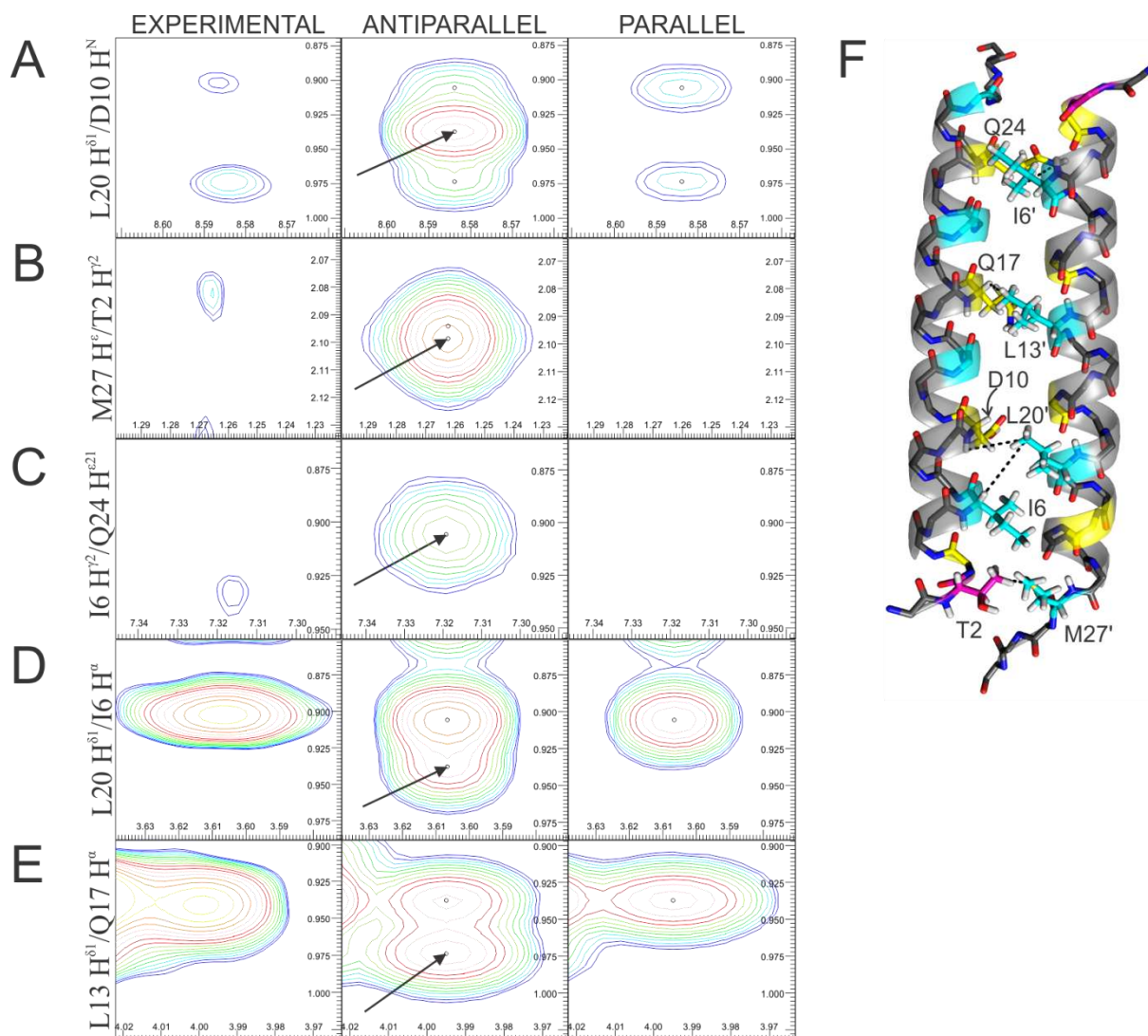


Figure 2.11 – SEPT1CC presents no antiparallel contacts. A-E) Selected regions of NOESY spectrum of SEPT1CC (left panel), simulated spectra from antiparallel (central panel) and parallel (right panel) models. Scales shown represent ^1H chemical shifts in ppm. Arrows indicate some intermolecular antiparallel contacts not found in the experimental spectrum: L20 $\text{H}^{\delta 1}/\text{D10 } \text{H}^{\text{N}}$ (A); M27 $\text{H}^{\epsilon}/\text{T2 } \text{H}^{\gamma 2}$ (B); I6 $\text{H}^{\gamma 2}/\text{Q24 } \text{H}^{\epsilon 21}$ (C); L20 $\text{H}^{\delta 1}/\text{I6 } \text{H}^{\alpha}$ (D); L13 $\text{H}^{\delta 1}/\text{Q17 } \text{H}^{\alpha}$ (E). F) SEPT1CC antiparallel X-ray structure (blunt coiled-coil) used for spectra back-calculation showing each contact in A-E. *a*, *d* and *g* positions are colored in yellow, cyan and magenta, respectively. Residues involved in the contacts are labeled and their side chains are shown. Residues from the right helix are labeled with ‘prime’.

Source: By the author.

Table 2.1 – Comparison between expected NOEs and backcalculated NOEs in antiparallel SEPT1CC. (Left column), critical NOEs that should be observable experimentally since the corresponding groups were unequivocally assigned. ‘X’, NOE did not exist in the experimental data. Contacts from three structures of SEPT1CC are presented: two blunt structures (the SEPT1CC X-ray structure and another one based on the SEPT4CC X-ray model) and the N-shifted simulated structure.

| Contact | Contact type | X-ray 1CC (blunt) | X-ray 4CC-based (blunt) | Simulated 1CC (N-shifted) |
|--|--------------|-------------------|-------------------------|---------------------------|
| I6 H ^{γ2} / Q24 H ^{ε21} | <i>d-a</i> | X | X | |
| I6 H ^{δ1} / Q24 H ^{ε21} | <i>d-a</i> | | X | |
| L13 H ^{δ1} / Q17 H ^α | <i>d-a</i> | X | X | X* |
| L20 H ^{δ1} / I6 H ^α | <i>d-d</i> | X | X | |
| L20 H ^{β3} , H ^{δ1} / D10 H ^N | <i>d-a</i> | X | X | |
| M23 H ^N / I6 H ^{γ2} | <i>g-d</i> | X | | |
| M27 H ^ε / T2 H ^{γ2} | <i>d-g</i> | X | X | |
| I6 H ^{δ1} / M27 H ^{β2} | <i>d-d</i> | | X* | X |
| I6 H ^{γ2} / Q28 H ^{ε21,22} | <i>d-e</i> | | | X |
| I6 H ^{δ1} / S30 H ^N | <i>d-g</i> | | | X |
| D10 H ^{β2} / Q24 H ^{ε21} | <i>a-a</i> | | X* | X |
| L13 H ^{δ1} / M23 H ^N | <i>d-g</i> | | | X |
| L13 H ^{δ1,2} / Q24 H ^{ε21} | <i>d-a</i> | | | X |
| L13 H ^{δ1} / A25 H ^N | <i>d-b</i> | | | X |
| Q28 H ^{ε22} / I6 H ^{γ2} | <i>e-d</i> | | | X |

*weak correlation

Source: By the author.

2.4.1.1.2 SEPT4CC

The peptide SEPT4CC was recorded in buffer containing 10% glycerol-*d*₃. Glycerol increases the buffer viscosity, decreasing the T_1 and T_2 relaxation times. Glycerol also allows the use of higher peptide concentrations without sample precipitation (3.8 mM was used in the experiments). The result was a spectrum with a better signal to noise ratio (Figure 2.12). SEPT4CC showed no intermolecular contacts derived from its antiparallel structure solved by X-ray diffraction (Figure 2.13). High pressure NMR experiments up to 250 MPa were acquired in order to see a probable orientation transition since higher pressures shift the conformational equilibrium favoring states with smaller partial molar volumes. The spectrum revealed no new contacts which indicate that the parallel structure is maintained at high pressure (data not shown). At 200 MPa, the sample is still dimeric as shown by diffusion NMR experiments (Table 2.5). Similar to SEPT1CC, the peptide SEPT4CC showed no

intermolecular contacts derived from its antiparallel structure (Figure 2.13). It also lacks antiparallel NOEs when a SEPT4CC N-shifted structure is used as model (Table 2.2).

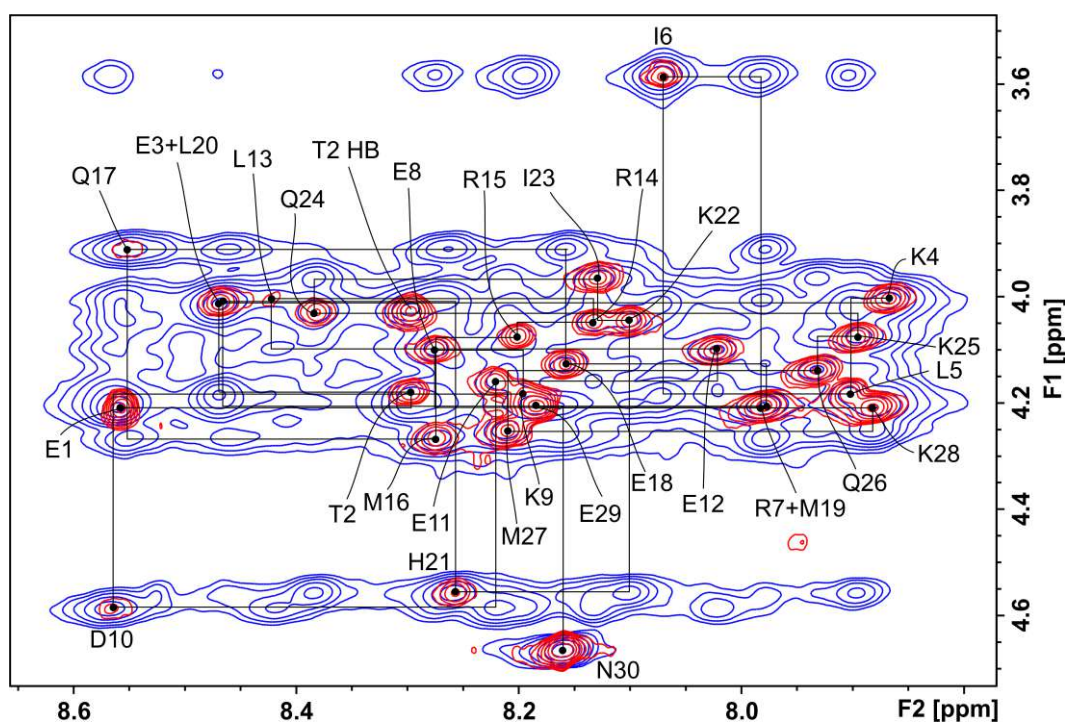


Figure 2.12 – Assigned fingerprint region of SEPT4CC spectra. NOESY and TOCSY are superposed and depicted in blue and red, respectively. Horizontal and vertical axes represent $^1\text{H}^{\text{N}}$ and $^1\text{H}^{\alpha}$ chemical shifts. Lines connecting $\text{H}^{\alpha}(i)\text{-H}^{\alpha}(i+1)$ resonances are shown.

Source: By the author.

Table 2.2 – Comparison between expected NOEs and backcalculated NOEs in antiparallel SEPT4CC. (Left column), critical NOEs that should be observable experimentally since the corresponding groups were unequivocally assigned. ‘X’, NOE did not exist in the experimental data. Contacts of two structures of SEPT4CC are presented: the blunt X-ray structure and the N-shifted simulated structure.

| Contact | Contact type | X-ray 4CC (blunt) | Simulated 4CC (N-shifted) |
|--|--------------|-------------------|---------------------------|
| T2 $\text{H}^{\gamma 2}$ / M27 $\text{H}^{\gamma 2}$ | <i>g-d</i> | X* | |
| I6 $\text{H}^{\delta 1}$ / Q24 H^{N} , $\text{H}^{\gamma 3}$ | <i>d-a</i> | X | |
| I6 $\text{H}^{\delta 1}$ / M27 $\text{H}^{\gamma 2,3}$ | <i>d-d</i> | X | |
| D10 H^{α} / Q17 H^{α} | <i>a-d</i> | X | |
| D10 $\text{H}^{\beta 2}$ / Q24 $\text{H}^{\epsilon 21,22}$ | <i>a-a</i> | X | X* |
| Q24 $\text{H}^{\epsilon 21}$ / R7 H^{α} | <i>a-e</i> | X | |
| T2 $\text{H}^{\gamma 2}$ / C-term amide $\text{H}^{1,2}$ | <i>g-a</i> | | X |
| I6 H^{α} / M27 H^{α} , $\text{H}^{\gamma 3}$ | <i>d-d</i> | | X |
| I6 $\text{H}^{\delta 1}$, $\text{H}^{\gamma 13}$ / N30 $\text{H}^{\beta 2,3}$ | <i>d-g</i> | | X |
| I6 $\text{H}^{\delta 1}$ / C-term amide H^2 | <i>d-a</i> | | X |
| D10 H^{α} / Q24 $\text{H}^{\gamma 2,3}$ | <i>a-a</i> | | X |
| M27 $\text{H}^{\gamma 2,3}$ / K9 $\text{H}^{\beta 3}$ | <i>d-g</i> | | X |

*weak correlation

Source: By the author.

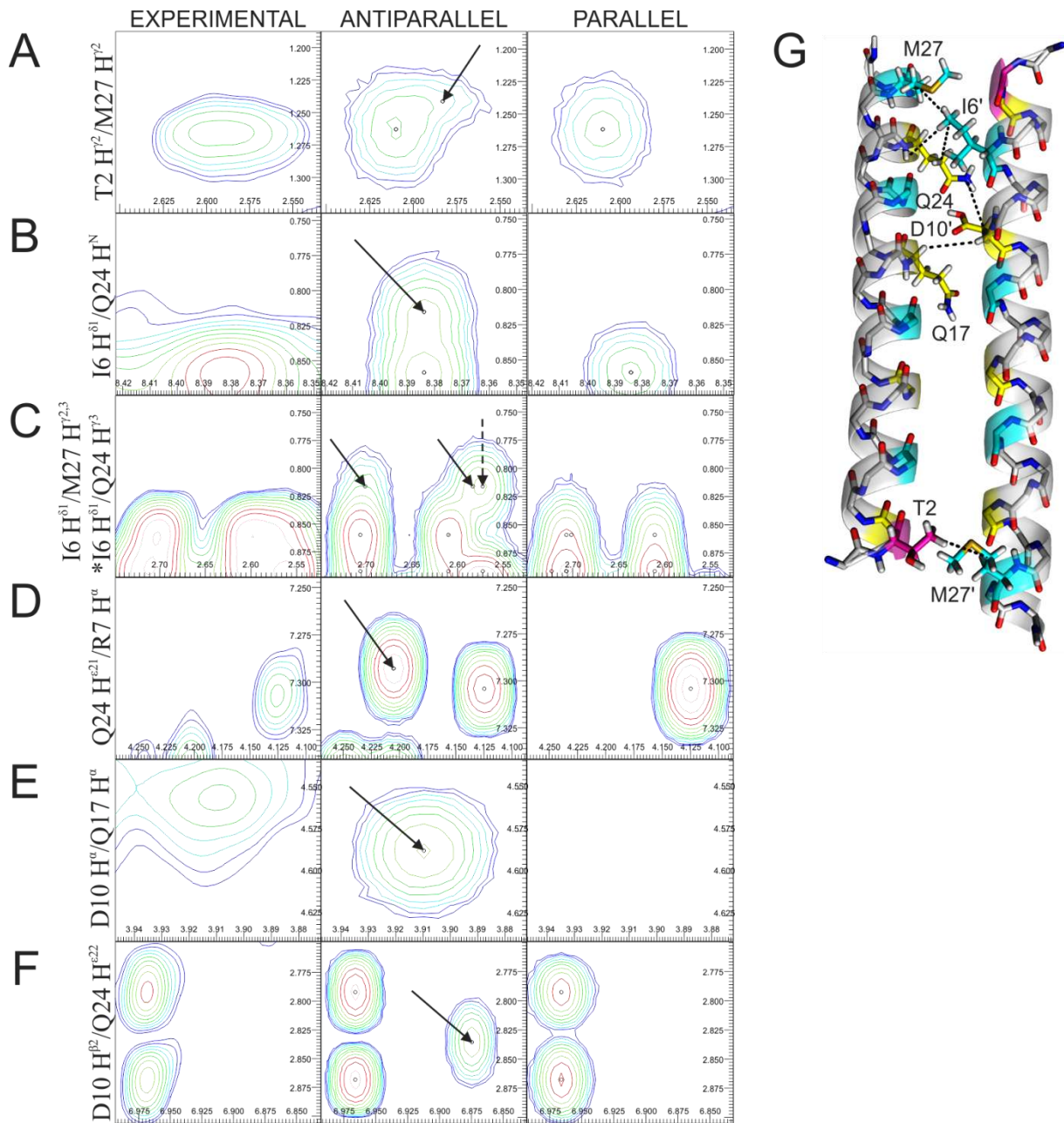


Figure 2.13 – SEPT4CC presents no antiparallel contacts. A-F) Selected regions of NOESY spectrum displaying $T2 H^{\beta 2} / M27 H^{\gamma 2}$ (A); $I6 H^{\delta 1} / Q24 H^N$ (B); $I6 H^{\delta 1} / Q24 H^{\gamma 3}$ (*, dashed arrow) and $I6 H^{\delta 1} / Q24 H^{\gamma 2,3}$ (C); $Q24 H^{\epsilon 21} / R7 H^{\alpha}$ (D); $D10 H^{\alpha} / Q17 H^{\alpha}$ (E); $D10 H^{\beta 2} / Q24 H^{\epsilon 22}$ (F) contacts. G) SEPT4CC antiparallel structure used for spectra back-calculation showing each contact in A-F. Figure was prepared as Figure 2.11 (for more information see caption).

Source: By the author.

2.4.1.1.3 SEPT5CC

Similar to SEPT1CC and SEPT4CC, the peptide SEPT5CC also showed no intermolecular contacts derived from the antiparallel structure of SEPT4CC (Figure 2.13). It also lacks antiparallel NOEs when a SEPT5CC N-shifted structure is used as model (Table 2.3).

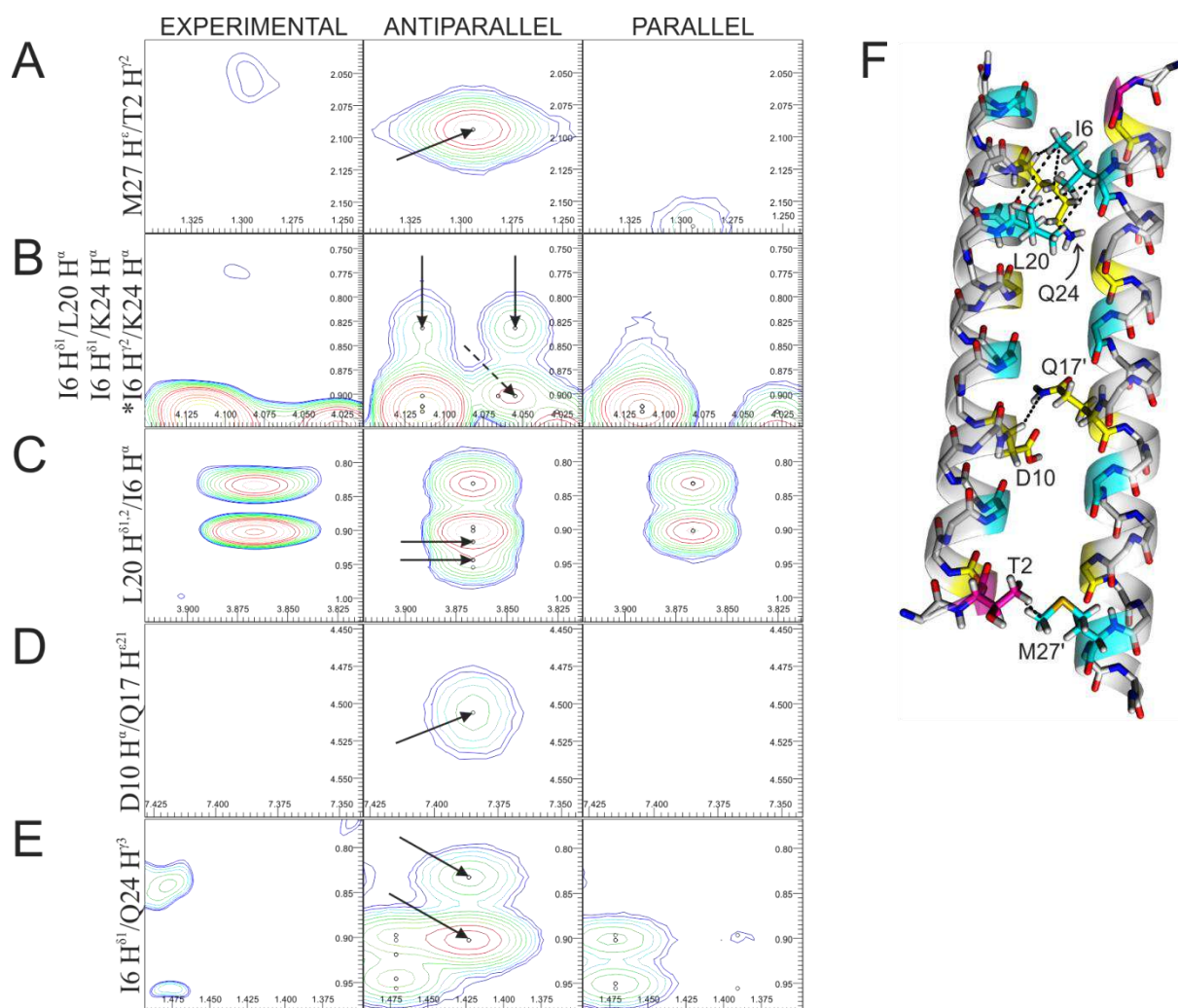


Figure 2.14 – SEPT5CC presents no antiparallel contacts. A-E) Selected regions of NOESY spectrum displaying M27 H^ε/T2 H^ε (A); I6 H^{δ1}/K24 H^α (*, dashed arrow) and I6 H^{δ1}/L20, K24 H^α (B); L20 H^{δ1,2}/I6 H^α (C); D10 H^α/Q17 H^{ε21} (D); I6 H^{δ1}/Q24 H^{γ3} (E) contacts. F) SEPT5CC antiparallel structure used for spectra back-calculation showing each contact in A-E. Figure was prepared as Figure 2.11 (for more information see caption).

Source: By the author.

Table 2.3 – Comparison between expected NOEs and backcalculated NOEs in antiparallel SEPT5CC. (Left column), critical NOEs that should be observable experimentally since the corresponding groups were unequivocally assigned. ‘X’, NOE did not exist in the experimental data. Contacts from two structures of SEPT5CC are presented: the blunt structure (based on SEPT4CC X-ray model) and the N-shifted simulated structure.

| Contact | Contact type | X-ray 4CC-based (blunt) | Simulated 5CC (N-shifted) |
|--|--------------|-------------------------|---------------------------|
| I6 H ^{δ1} / L20 H ^α | <i>d-d</i> | X | |
| I6 H ^{δ1} / K24 H ^α | <i>d-a</i> | X | |
| I6 H ^{δ1} , H ^{γ2} / K24 H ^{γ3} | <i>d-a</i> | X | |
| D10 H ^α / Q17 H ^{ε21} | <i>a-a</i> | X | |
| R14 H ^{γ2} / Q17 H ^{ε21} | <i>e-a</i> | X | |
| M27 H ^ε / T2 H ^{γ2} | <i>d-g</i> | X | |
| I6 H ^{δ1} , H ^{γ2} / Q30 H ^{β3} | <i>d-g</i> | | X |
| K9 H ^{β2} , H ^{δ2,3} / M27 H ^{γ2} | <i>g-d</i> | | X |
| D10 H ^α / K24 H ^{γ3} | <i>a-a</i> | | X |
| D10 H ^{β3} / K24 H ^{γ2,3} | <i>a-a</i> | | X |
| L13 H ^{δ1} / K24 H ^{γ3} | <i>d-a</i> | | X |
| L20 H ^N , H ^{β3} / Q17 H ^{ε21} | <i>d-a</i> | | X |
| M27 H ^{β3} / I6 H ^α | <i>d-d</i> | | X |

Source: By the author.

2.4.1.1.4 SEPT2CC

Contrary to SEPT1CC, 4CC and 5CC which show all the hallmarks of parallel coiled-coils in solution, SEPT2CC presented some antiparallel contacts. NOEs involving N-terminal residues (Gln-4 and Leu-6) with the C-terminal amide modification, which is highly upfield shifted and can be easily identified in the spectra (Figure 2.15A), undoubtedly indicates an antiparallel dimer. Initially, the antiparallel structure based on SEPT4CC did not explain well the detected intermolecular contacts. An N-shifted register structure is a better model to justify the existence of those NOEs, mainly because of the terminal amide contacts (Figure 2.16).

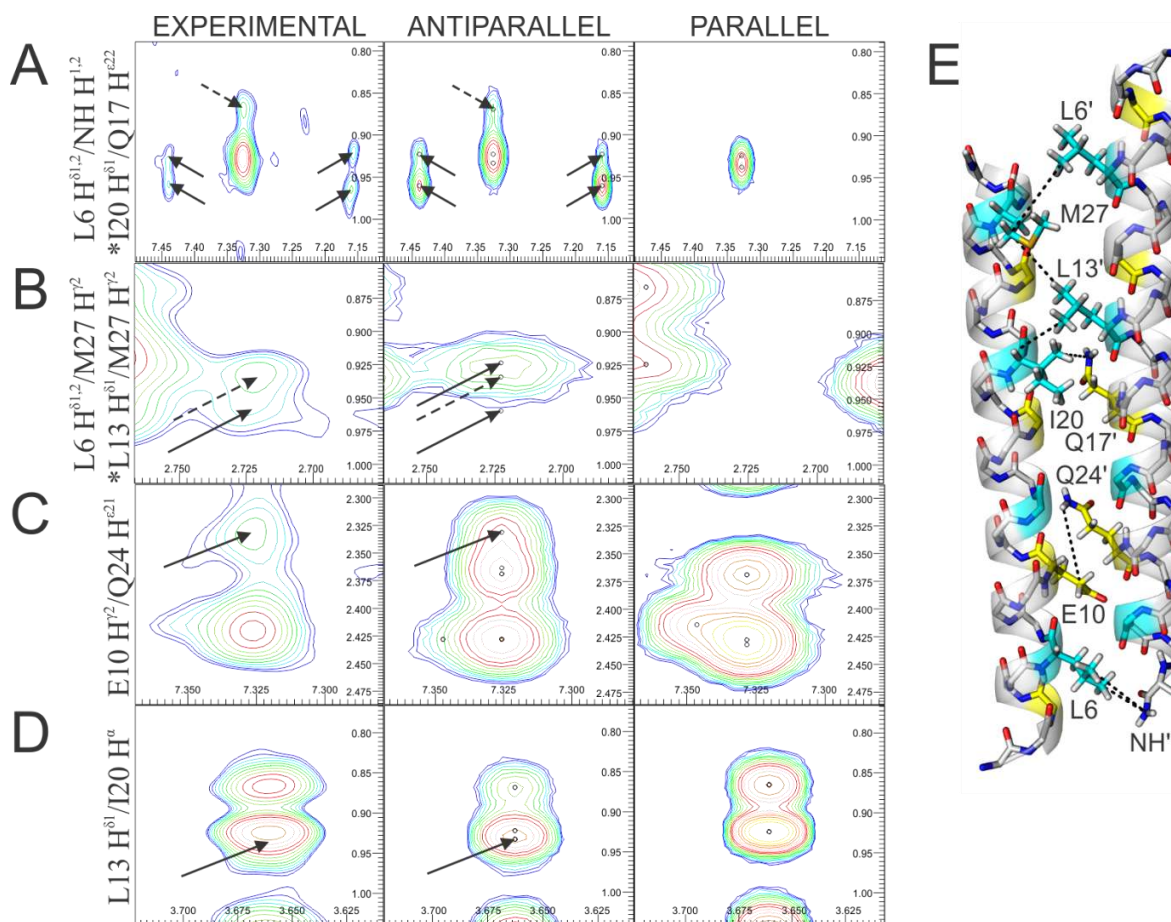


Figure 2.15 – SEPT2CC, differently from 1CC, 4CC and 5CC, presents characteristic antiparallel contacts. A-D) Selected regions of NOESY spectrum displaying I20 H^{δ1}/Q17 H^{ε22} (*, dashed arrow) and L6 H^{δ1.2}/C-terminal amide H^{1.2} (A); L13 H^{δ1}/ M27 H^{γ2} (*, dashed arrow) and L6 H^{δ1.2}/M27 H^{γ2} (B); E10 H^{γ2}/Q24 H^{ε21} (C); L13 H^{δ1}/I20 H^α (E) contacts. In B) the routine inversely predicts contacts involving H^{δ1} and H^{δ2} of L13. E) SEPT2CC antiparallel structure used for spectra back-calculation showing each contact in A-D. This structure is an N-shifted structure based on SEPT4CC antiparallel dimer (shift was done manually). Figure was prepared as Figure 2.11 (for more information see caption).

Source: By the author.

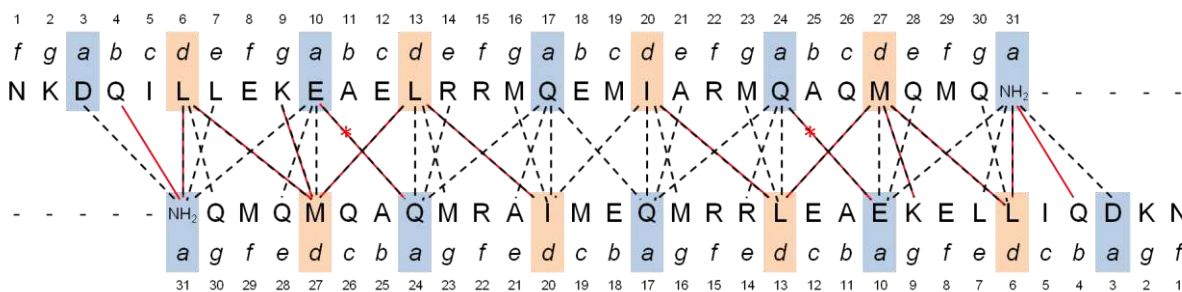


Figure 2.16 – Interaction contacts for SEPT2CC. An N-shifted structure was used. Red lines represent proton dipolar contacts seen on NOESY-NMR spectrum. Dashed, black lines represent each of the contacts among residues in the ‘knob-into-hole’ motifs. *a-g* letters represent the heptameric positions with *a* and *d* positions highlighted in blue and salmon, respectively. “*” represents assignment ambiguity between Q17 H^{ε21,22} and Q24 H^{ε21,22}. The C-terminal amide is represented as residue number 31.

Source: By the author.

2.4.1.1.5 Potential intermolecular NOE in parallel conformations

During the analysis, we identified several experimental NOEs that were present in the back-calculated spectrum generated with a parallel structure but absent when an antiparallel structure was used. Most of them were discarded because they were likely to be intramolecular NOEs according to the rules reported by O'Donoghue and colleagues, used to interpret and classify dipolar connectivities.²¹⁵ Particularly noteworthy were $N^H(i)/\text{side-chain}(i+1)$ cross-peaks. However, NOEs found in experimental data between residues number 6 (Leu or Ile) and 9 (Lys) can be probably regarded as intermolecular since the distances of the involved nuclei are always significantly above 5 Å in the monomer. Figure 2.17 presents the contact I6 $H^{\delta 1}/K9 H^{\epsilon 2,3}$ among different structures. The contact has the maximum intramonomer distance d_{intra} of 6.3, 8.1 and 9.4 Å for SEPT1CC, 4CC and 5CC, respectively. In SEPT2CC, its analog contact, L6 $H^{\delta 2}/K9 H^{\epsilon 2,3}$, is present in a parallel structure; but it should be absent experimentally since SEPT2CC was observed as antiparallel. However, the aforementioned NOE is superposed and its absence cannot be entirely certified (Figure 2.17). The existence of the parallel orientation for SEPT2CC in solution, coexisting with the antiparallel coiled-coil, cannot be ruled out.

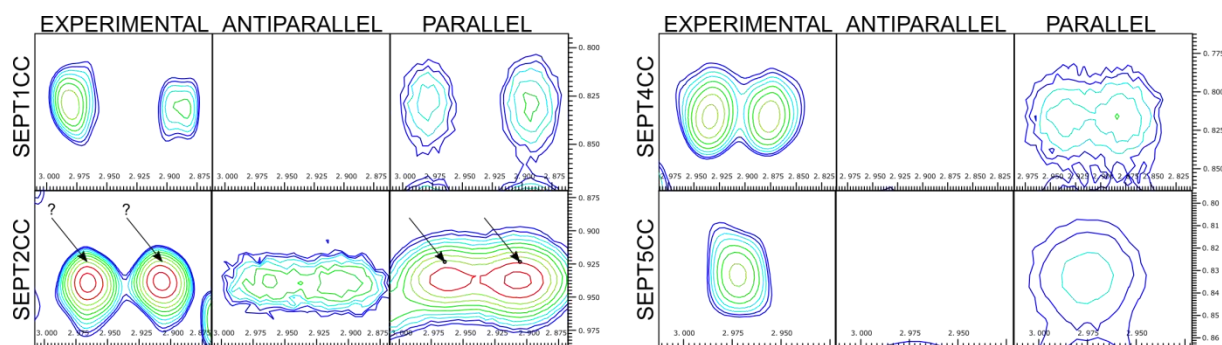


Figure 2.17 – I6 $H^{\delta 2}/K9 H^{\epsilon 2,3}$ contacts are potential intermolecular NOEs in parallel SEPT1CC, 4CC and 5CC structures. Scales represent 1H chemical shifts in ppm. SEPT5CC has $H^{\epsilon 2,3}$ of Lys-9 degenerated. Unfortunately, the absence of the analog contact in antiparallel SEPT2CC, L6 $H^{\delta 2}/K9 H^{\epsilon 2,3}$, cannot be entirely attested since it is superposed on the spectra (SEPT2CC panel).

Source: By the author.

Additionally, SEPT5CC NMR data shows several NOEs between Glu-1 and Ile-6 side-chains, namely E1 $H^{\beta 2, \beta 3, \gamma 2, \gamma 3}/I6 H^{\delta 1, \gamma 12, \gamma 13}$ (data not shown). These NOEs were not predicted by any parallel structure and were not present in other parallel peptides (SEPT1CC and SEPT4CC). This is a ‘*c-a*’ contact and hence not a ‘knob-into-hole’ interaction. A

plausible explanation for these NOEs is that SEPT5CC deviates from standard coiled-coil geometry in its N-terminus. Moreover, we used the SEPT5CC peptide without any N-terminal modifications (other peptides have acetylated N-terminus) giving Glu-1 an extra charge, which could have contributed to this effect.

2.4.1.2 Paramagnetic relaxation enhancement (PRE) NMR

The peptides SEPT1CC and SEPT5CC with MTSL (2,2,5,5-tetramethyl-1-oxyl-3-methyl methanethiosulfonate label) attached to an additional cysteine at the C-terminus (SEPTCCys-MTSL) were studied by NMR. Unpaired electrons (definition of paramagnetism) increase the transverse relaxation time (T_2) of the nearby nuclei, resulting in peak broadening and ultimately, disappearance. This effect in NMR is called paramagnetic relaxation enhancement (PRE).^{216, 217} ^1H - ^1H -TOCSY spectra was used to monitor the effect of the label on peak intensities. The idea of these experiments is to use information from missing peaks in the NMR spectra to infer the orientation of the coiled-coil.

A sample initially measured was composed only of SEPT1CCys-MTSL, which showed a strong disappearance of the signals in different region of the spectrum. The acquisition was done in buffer identical to that used for SEPT1CC NMR assignment, allowing the identification of the few peaks present. Side-chain correlations of residues Thr-2, Glu-3 and Lys-4 at the N-terminus were the only resonances present (data not shown). Such disappearance is not surprising since the paramagnetic spin label MTSL affects nuclei from 15 to 35 Å around it, approximately (the coiled-coil is about 40 Å long). Thus, in order to observe a more complete set of peaks and the location where the spin label mostly affects, a mixture between labeled and unlabeled SEPT5CC peptide was prepared and measured (SEPT5CC: SEPT5CCys-MTSL 3:1 molar solution).

A DOSY experiment showed that the labeled peptide remained dimeric (Table 2.5, section 2.4.3.2 Diffusion NMR experiments). The use of unlabeled peptide allowed most of the correlations to be detected. An intensity ratio between correlations in the spin labeled and in a control (unlabeled) sample was calculated (Figure 2.18) An interesting feature in the acquired data set is the progressive decrease of H^α - H^{N} correlation intensities in the first five residues (arrow in Figure 2.18). Moreover, there is a disappearance of sequential residues

(most residues in the region from Met-8 to Leu-13) near the N-terminus. These results indicate that the probe is close to N-terminal residues and, since it is attached to the C-terminus, suggests that the SEPT5CCys-MTSL coiled-coil may be antiparallel.

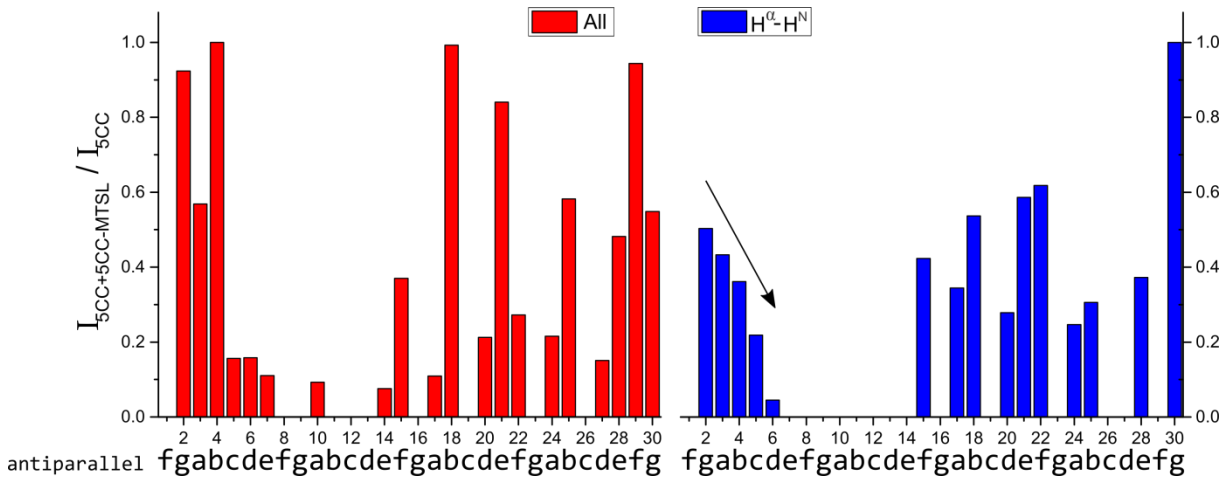


Figure 2.18 – Intensity changes caused by the presence of MTSL. The relative intensity was normalized by the most intense peak present on each set. Intensity values were extracted from 2D-TOCSY experiments. (Left, red) Average of all detected correlations for each residue. (Right, blue) $H\alpha$ - H^N correlations only. The arrow indicates a progressive reduction of cross-peak intensities at the N-terminus. Below each plot, there is the coiled-coil register for the antiparallel orientation.

Source: By the author.

Another result that stands out is the disappearance of all *c* and *g* positions in the C-terminus (residues Met-16, Met-19, Met-23 and Gln-26, in red in Figure 2.19). These residues are disposed on the same side in antiparallel coiled-coils (Figure 2.19C) which points out that

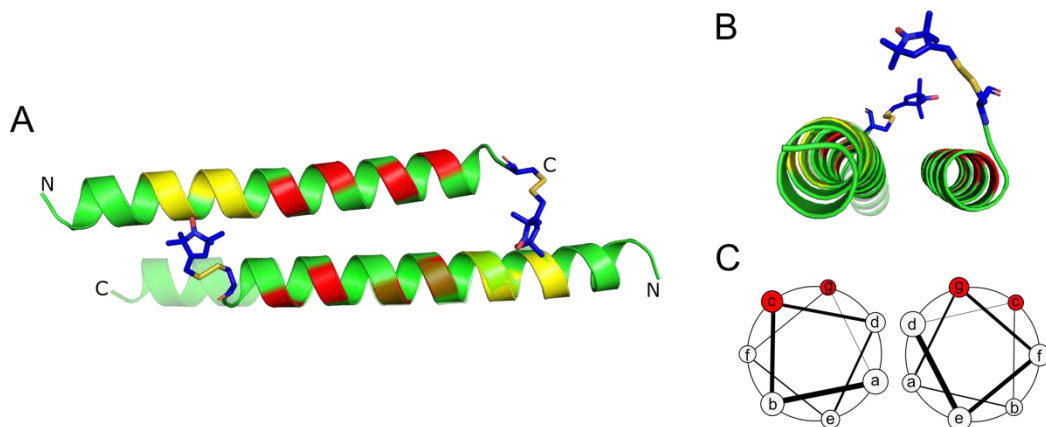


Figure 2.19 – MTS label selectively affects SEPT5CC residues. A) Possible structural model of antiparallel SEPT5CCys-MTSL with a double N-shifted pairing. Positions that are sequentially and specifically erased in the 2D-TOCSY spectrum are shown in yellow and red, respectively. The transparent helix is from a single-N-shifted coiled-coil shown as comparison. Figure prepared with MtsslWizard²¹⁸ plugin, using Pymol program. B) Side view showing both labels above the helices. C) Helical wheel scheme for an antiparallel coiled-coil. Positions *c* and *g* are highlighted in red.

Source: By the author.

the labels are both on the same side of the ‘plane’ formed by the helices (Figure 2.19B). Figure 2.19A shows a possible sketch of the conformation for the antiparallel SEPT5CCys with the spin label. Since the most affected residues are on the region Glu-8 to Leu-13 (in yellow in Figure 2.19), it is reasonable to use a double N-shifted antiparallel coiled-coil to explain our results. A single shifted structure could also be possible, but the C-terminus had to be highly flexible, allowing the label to turn towards a region which signals from sequential residues are totally quenched.

2.4.2 Analysis of SEPTCC heptameric positions

A score was given for each SEPTCC sequence in order to quantify the stability of their parallel and antiparallel orientations. The occurrence of each residue in the seven different positions of the coiled-coil was extracted from the CC+ database²¹¹ for parallel and antiparallel sequences whose structures are present in the PDB. The analysis was made comparing the score from SEPTCC sequences with scores from different coiled-coil structures also annotated in the database (Table 2.4).

The parallel orientation of SEPTCC has a relatively high score for *a* positions (2.32, for other sequences it varies between 1.57 and 2.52), which comes from leucines (residues number 13 and 20), isoleucines (residue number 6) and methionines (residue number 27). However, it presents an unusual low score for *d* positions (0.79, for other sequences it is between 1.94-5.28), composed by methionines (residues number 16 and 23) and other polar residues as lysines (residue number 9) and threonines (residue number 2).

On the other hand, for the antiparallel coiled-coil, the score for *a* and *d* positions are inverted, with *d*-score being the high score (3.00, other sequences show scores from 2.29 to 3.80) and *a*-score the low one (0.82; from 1.64 to 2.88 for other coiled-coils). *a* positions are occupied exclusively by polar amino acids, namely glutamic and aspartic acid (residues number 3 and 10, respectively) and glutamines (residues number 17 and 24), which explains the low score. This is expected since the *a* position in the parallel coiled-coil becomes the *d* position in an antiparallel conformation. However, those residues in *a* positions establish a hydrogen bond network all the way through one interface of the antiparallel dimer in the crystallographic structure (Figure 2.7B).

Table 2.4 – Scores based on residue occurrence profiles for coiled-coil positions *a*, *d*, *a,d*-combined and for all heptameric positions. Septins sequences are presented at the top, also with average values. Scores for other parallel and antiparallel coiled-coils from the PDB are provided.

| | Sequence | PDB entry | <i>PARALLEL coiled-coils</i> | | | | <i>ANTIPARALLEL coiled-coils</i> | | | |
|---------------------|---|-----------|------------------------------|-------------------|------------|------|----------------------------------|-------------|------------|------|
| | | | <i>a</i> | <i>d</i> | <i>a,d</i> | all* | <i>a</i> | <i>d</i> | <i>a,d</i> | all* |
| <i>SEPTINS</i> | SEPT1CC | | 2.32 | 0.80 | 1.47 | 1.98 | 0.82 | 3.00 | 1.91 | 1.73 |
| | SEPT2CC | | 2.32 | 0.85 | 1.50 | 1.81 | 0.82 | 3.00 | 1.91 | 1.56 |
| | SEPT4CC | | 2.32 | 0.65 | 1.39 | 1.96 | 0.82 | 3.00 | 1.91 | 1.66 |
| | SEPT5CC | | 2.32 | 0.85 | 1.50 | 1.87 | 0.83 | 3.00 | 1.91 | 1.65 |
| | All SEPTCCs | | 2.32 | 0.79 | 1.47 | 1.91 | 0.82 | 3.00 | 1.91 | 1.65 |
| <i>PARALLEL</i> | GCN4 | 1CE9 | 2.05 | 5.28 ^L | 3.66 | 2.54 | | | | |
| | C-Jun homodimer | 1JUN | 1.84 | 5.28 ^L | 3.40 | 2.33 | | | | |
| | Vitellogenin gene-binding protein, VBP | 4U5T | 1.77 | 4.44 | 3.25 | 2.32 | | | | |
| | Rab interacting lysosomal protein, RILP | 1YHN | 1.57 | 2.87 | 2.22 | 2.01 | | | | |
| | Thap1 l cell cycle regulator | 5AJS | 2.24 | 2.58 | 2.42 | 1.82 | | | | |
| | <i>Saccharomyces cerevisiae</i> Sir4p | 1PL5 | 2.52 | 1.94 | 2.25 | 1.80 | | | | |
| <i>ANTIPARALLEL</i> | <i>Thermus thermophilus</i> chorismate mutase | 2D8E | | | | | 2.59 | 3.80 | 3.19 | 2.26 |
| | <i>E. coli</i> ZntR | 1Q09 | | | | | 1.87 | 2.86 | 2.37 | 2.02 |
| | <i>Pyrococcus furiosus</i> hypothetical protein | 1YBZ | | | | | 2.88 | 2.91 | 2.89 | 1.98 |
| | Bovine ATPase inhibitor protein, IF1 | 1HF9 | | | | | 2.50 | 2.29 | 2.39 | 1.90 |
| | <i>Thermotoga maritima</i> hypothetical protein | 2ESH | | | | | 1.64 | 3.16 | 2.40 | 1.86 |

*Average of all *a*, *b*, *c*, *d*, *e*, *f*, *g* positions.

^LContain exclusively leucines in *d* positions.

Source: By the author.

Scores for *a,d* combined for both orientation are the lowest among all presented sequences. Scores are 1.47 and 1.91 for parallel and antiparallel, respectively, whereas these values vary between 2.22 and 3.66 for other parallel coiled-coils and between 2.37 and 3.19 for antiparallel coiled-coils. This analysis shows that what probably holds the coiled-coils together are residues sharing *a* and *d* positions in both orientations: Ile-6 (Leu-6 for SEPT2CC), Leu-13, Leu-20 (Ile-20 for SEPT2CC) and Met-27.

2.4.3 Oligomeric studies

In order to verify the monodispersity of the samples and exclude the existence of high-order oligomers (mainly trimers and tetramers), we performed size exclusion chromatography combined with multi angle light scattering (SEC-MALS) and diffusion NMR experiments (DOSY).

2.4.3.1 SEC-MALS experiments

Four buffers with different salt concentrations and pH were tested in SEC-MALS experiments and no significant differences were found regarding SEPTCC calculated masses (Figure 2.20 and Figure 2.21). All peptides were dimeric with average masses calculated by SEC-MALS of 6.6, 7.2, 6.7 and 5.8 (in kilodaltons, average standard deviation σ of 0.6 kDa) for SEPT1CC, 2CC, 4CC and 5CC, respectively. Molecular weights for dimers of these molecules are 7.5, 7.4, 7.7 and 7.8 kilodaltons, respectively.

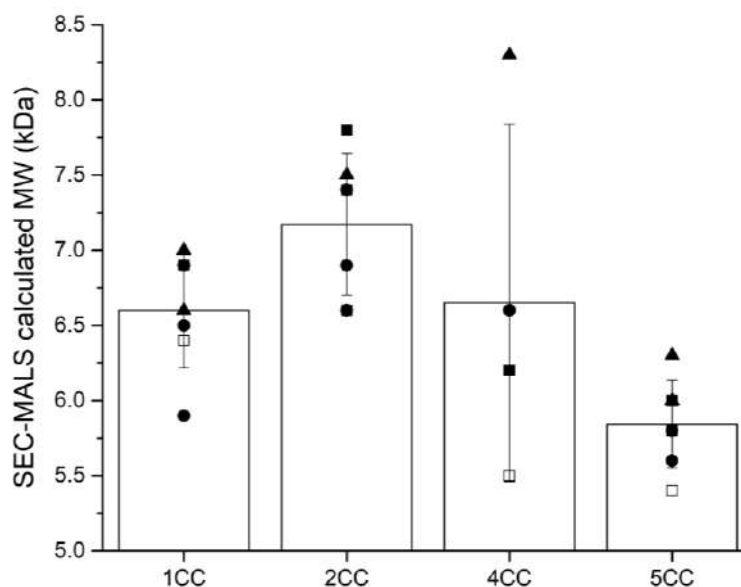


Figure 2.20 – SEPTCC peptides are dimers in different buffer systems according to SEC-MALS experiments. Open squares, 50 mM potassium phosphate, pH 5.0 (buffer A); closed squares, 50 mM potassium phosphate, 300 mM NaCl, pH 5.0 (buffer B); triangles, 50 mM potassium phosphate, 100 mM NaCl, pH 7.0 (buffer C) and circles, 20 mM Tris, 300 mM NaCl, pH 8.0 (buffer D). Error bars represent the standard deviation of different measurements shown in the figure.

Source: By the author.

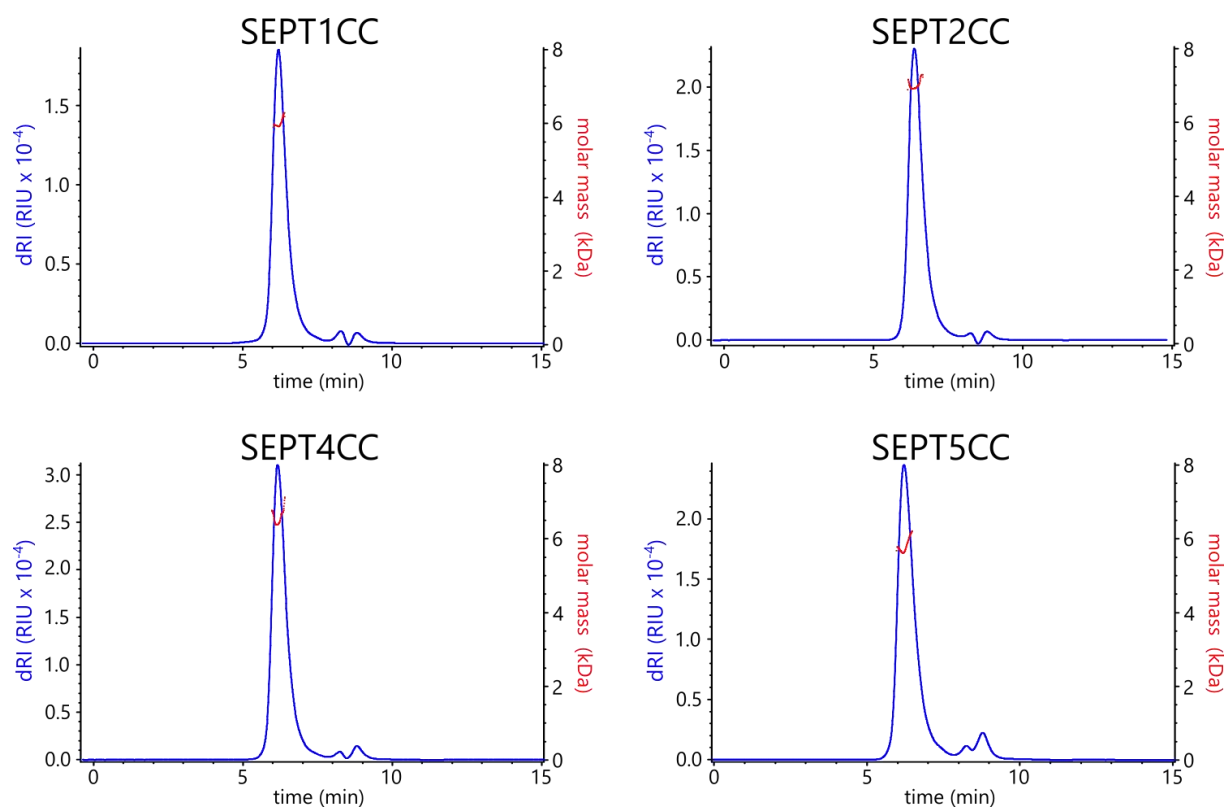


Figure 2.21 – SEC-MALS chromatograms and calculated masses for SEPTCC peptides. Blue lines represent the differential refractive index (dRI) and red dots represent the calculated molar mass. The condition shown is using 20 mM Tris buffer, 300 mM NaCl, pH 8.0.

Source: By the author.

2.4.3.2 Diffusion NMR experiments

Diffusion-ordered spectroscopy (DOSY) experiments were carried for different SEPTCC peptides in different conditions (salt and peptide concentrations, temperature) (Table 2.5). Considering the error of 0.2 nm, all measurements showed similar R_h values. Even the use of high pressure ($p = 200$ MPa) for SEPT4CC, which could break dimers and decrease its size, did not significantly change the hydrodynamic radius. The calculated R_h for SEPTCC monomers, dimers and tetramers are 1.05, 1.42 and 1.90 nm, respectively (R_h estimate for globular proteins using MW, Zetasizer software, Malvern) corroborating the existence of essentially dimeric samples.

Table 2.5 – Hydrodynamic radius (R_h) measured by diffusion NMR experiments for different coiled-coil septins in different conditions. All measurements employed 50 mM potassium phosphate buffer, pH 5.0. The expected R_h for dimers using a globular protein model is 1.42 nm.

Source: By the author.

| Peptide | Concentration (mM) | Conditions | Temperature (K) | $R_h \pm 0.2$ (nm) |
|----------|--------------------|------------------------------|-----------------|--------------------|
| SEPT1CC | 0.5 | 300 mM NaCl | 298 | 1.2 |
| SEPT2CC | 1.0 | 300 mM NaCl | 278 | 1.7 |
| | | | 298 | 1.7 |
| | 0.1 | 300 mM NaCl | 278 | 1.5 |
| | | | 298 | 1.6 |
| SEPT4CC | 0.5 | 300 mM NaCl | 278 | 1.4 |
| | 0.5 | 300 mM NaCl | | 1.3 |
| | 3.8 | 100 mM NaCl | 298 | 1.3 |
| | 2.5 | 100 mM NaCl ($p = 200$ MPa) | | 1.5 |
| SEPT5CC* | 0.5 | 150 mM NaCl | 298 | 1.3 |

*Peptide labeled with MTSL.

2.5 DISCUSSION

We used two-dimensional NOESY NMR spectra to assess the molecular orientation of group-III coiled-coils of SEPT1CC, 2CC, 4CC and 5CC. While the analysis shows that SEPT2CC is likely to be an antiparallel coiled-coil, the other members show only a parallel orientation in our experiments. The existence of both orientations for SEPT2CC cannot be ruled out given the difficulty to unequivocally determine intermolecular NOEs for symmetric, parallel coiled-coils. The fact that SEPT2CC has the most different sequence among the studied coiled-coils could explain why it was the only member to display an antiparallel orientation by solution NMR. However, it is hard to pinpoint exact amino acid residues responsible for the different behavior.

Since NOESY spectra reports only low distance contacts (up to 5 Å), residues participating in the core of the coiled-coil are potential targets for important intermolecular NOEs. In addition, up- and downfield shift resonances helps identifying unambiguous interactions between hydrogens at the atomic level. For example, resonances of Thr-2 H γ^2 , Ile-6 H δ^1 , Met-27 H γ^2 and the C-terminal amide modification proved valuable probes to study the

relative orientation of group-III septin coiled-coils. The NMR approach allows, with a sufficient number of NOEs, to obtain the relative orientation of the helical coiled-coils, and also to know which helix pairing they adopt in solution. The NOE pattern for SEPT2CC suggests an N-shifted antiparallel structure which has one helix shifted by one heptad repeat towards the N-terminus, differently from the SEPT1CC and SEPT4CC blunt coiled-coils seen by X-ray crystallography.

Together with other evidence, a simple analysis on the primary sequences of the coiled-coils reveals that both orientations have similar degrees of stability, both being equally likely to exist. X-ray structures show that the parallel orientation is a typical coiled-coil, having a hydrophobic interface formed by *a* and *d* residues. On the other side, the antiparallel coiled-coil displays two interfaces, one side is hydrophobic and the other is hydrophilic. The change of parallel into an antiparallel orientation (or *vice versa*) requires residues to exchange heptad positions in order to maintain favorable interactions. Figure 2.22 represents what occurs to register reassignment when the change in orientation takes place. Highly favorable residues in the *a* positions in the parallel coiled-coil start to occupy the *d* positions in the antiparallel coiled-coil. This group of hydrophobic residues is likely to be essential for the coiled-coil stability for both orientations. The change requires that acidic and polar residues in the *e* positions in the parallel coiled-coil occupy the *a* positions in the antiparallel structures. Although, hydrogen bonds found in the antiparallel structure involving these residues somehow compensate the presence of unusual amino acids in an interface that is generally hydrophobic.

It is expected that in solution, the parallel conformation might be partially favored over the antiparallel, given that it buries hydrophobic residues in the core of the coiled-coil. In the crystals, on the other hand, the peptides are in a different environment. The crystal packaging excludes many solvent molecules and creates non-physiological interaction interfaces, which can benefit the antiparallel orientation. Inside a cell, it is uncertain how hydrated the surrounding might be, and the interaction of septins with membranes and other filaments will certainly create a different chemical environment than the one found in solution. Moreover, it seems reasonable that the amphipathic antiparallel conformation could possibly be more favored in a less hydrophilic environment *in vivo*.

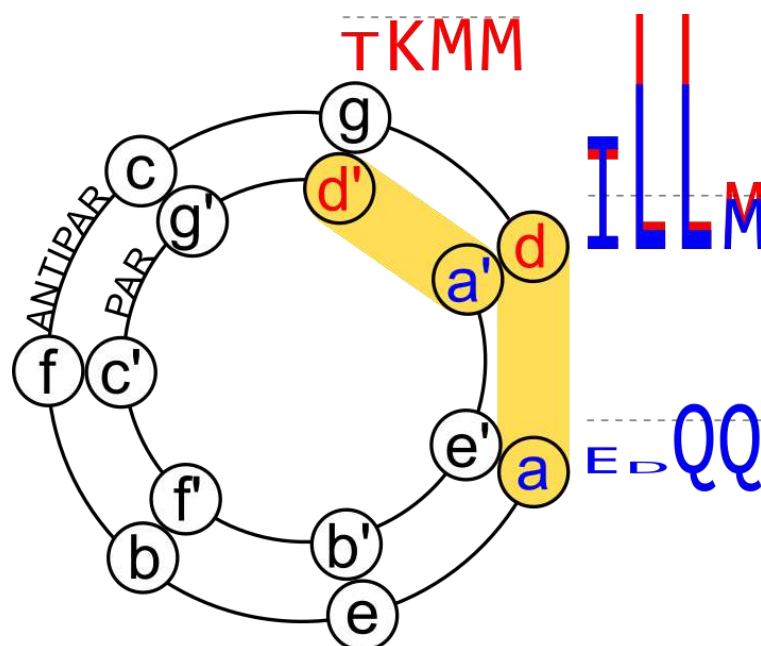


Figure 2.22 – Correspondence of amino acid residues between parallel and antiparallel coiled-coils of group-III septins. Heptad positions of the antiparallel and the parallel orientations are shown in the outer and in the inner wheels, respectively. Corresponding residues are represented by circles in contact with each other. *a-d* interfaces are highlighted in orange. The most common residues in each *a* and/or *d* positions are shown sequentially (in blue and red, respectively) and the height of the representative letter is proportional to the occurrence of the residue in the respective position and orientation, according to data presented in Appendix K. The dashed line indicates the height where the occurrence is one (meaning the residue has no preference for occupying that position).

Source: By the author.

The existence of two probable coiled-coil orientations with moderate stability could be relevant in the role played by the C-terminal domain in filament assembly of septins. As suggested by some structures, it is likely that the septin coiled-coils have a parallel orientation in a single heterofilament. In this scenario, the parallel orientation would be important to stabilize the NC-interface between SEPT2-SEPT2 (or other group-III member) whereas the antiparallel orientation would be possibly responsible for the crosslink interactions among filaments (Figure 2.23). Moreover, it is not hard to imagine that septins could use different coiled-coil helix pairings, as it was verified for some antiparallel structures by X-ray and NMR (blunt for SEPT1CC and SEPT4CC, C-shifted for SEPT1CC, N-shifted for SEPT2CC), to build a variety of supramolecular complexes. Although, this could also be a consequence of the usage of a truncated C-terminal sequence. The ability to adopt different conformations gives the septins flexibility to assemble/disassemble into several filamentous arrangements.

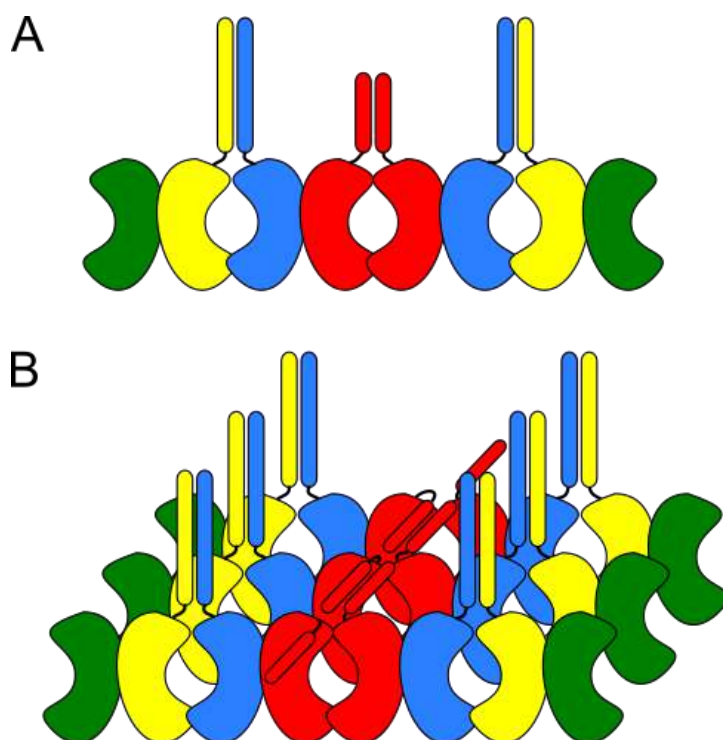


Figure 2.23 – Importance of ‘chameleon’-like behavior of group-III septin coiled-coils in the formation and cross-linking of filaments. Each septin is represented in a different color: green, SEPT9 (group I); yellow, SEPT7 (group IV); blue, SEPT6 (group II); red, SEPT2 (group III). A) The parallel orientation of the coiled-coil would stabilize the interface between red septins. B) The antiparallel orientation would interconnect mature filaments.

Source: By the author.

The oligomeric state of SEPTCC peptides studied by SEC-MALS and DOSY-NMR techniques showed that the dimer is the major conformation in solution. We excluded the presence of higher-order oligomers, which would complicate the NOE analysis. Interestingly, the antiparallel SEPT2CC peptide possesses the highest hydrodynamic radius measured by DOSY-NMR. Despite the R_h value of SEPT2CC (1.7 nm) does not deviate much from the theoretical value (1.4 nm) considering the estimated error (0.2 nm), it is tempting to say that the long, N-shifted antiparallel coiled-coil adopted for SEPT2CC is related to the apparent higher R_h . Unlike multi-angle light scattering, diffusion DOSY experiments are sensitive to molecular shape.

Samples containing MTS (methanethiosulfonate label), initially synthesized to be studied by electron paramagnetic resonance (EPR) technique, were also used by NMR to report the coiled-coils orientations of group-III septins. The label was attached at the C-terminus of SEPT5CC and affected NMR signals from residues at the N-terminus on the other helix (residues Glu-8 to Leu-13), suggesting an antiparallel, N-shifted structure similar to the structure found for SEPT2CC through NOEs analysis. Nevertheless, no antiparallel contact

was seen on NOESY spectra of unlabeled SEPT5CC. The attachment of MTSL, rather voluminous label, might create steric effects which could disfavor the parallel conformer.

2.6 CONCLUSIONS

Septins are involved in several cellular processes and are capable of self-assembling into heterofilaments and high-order complexes. Many studies in our research group have been done in order to better understand how septins form these structures. Here, we studied the coiled-coil sequences present in the C-terminal domain of group-III septins by NMR spectroscopy. Using ^1H - ^1H -NOESY spectra, we could undoubtedly detect an antiparallel conformation of SEPT2CC in solution. On the other hand, there is no indication in our data set that SEPT1CC, SEPT4CC and SEPT5CC form antiparallel coiled-coils. Sequence analysis, simulation and experimental data support that all septins from this group have a C-terminal domain capable of forming both parallel and antiparallel orientations, each one being possibly relevant in different stages of filament formation.

The reason why several septin isoforms of group-III are produced in many organisms remains something to be further investigated and might be related to other septin domains, not only the C-terminal domain. The heteromeric septin coiled-coil, formed by SEPT6 and SEPT7, might also be able to adopt both orientations, since similar probabilities were computed by prediction programs using each of them. Future studies with SEPT6-SEPT7 coiled-coil are planned in order to also understand their role on stabilizing the filament and other high-order structures. By dissecting interactions in septins, we have an opportunity to increase our comprehension of the structural basis for the spontaneous assembly of such heterofilaments.

REFERENCES

- 1 ALZHEIMER'S ASSOCIATION. Alzheimer's disease facts and figures. **Alzheimer's & Dementia**, v. 14, n. 3, p. 367–429, 2018.
- 2 PRINCE, M. et al. **World Alzheimer report 2015: the global impact of dementia**. Available from: <<http://www.alz.co.uk/research/world-report-2015>>. Accessible at: 26 Oct. 2018.
- 3 ALZHEIMER, A. Uber einen eigenartigen schweren Erkrankungsprozess der Hirnrinde. **Neurologisches Centralblatt**, v. 25, p. 1134, 1906.
- 4 KATZMAN, R. The prevalence and malignancy of Alzheimer disease: a major killer. **Archives of Neurology**, v. 3, n. 4, p. 217–218, 1976.
- 5 BLENNOW, K.; DE LEON, M. J.; ZETTERBERG, H. Alzheimer's disease. **Lancet**, v. 368, n. 9533, p. 387–403, 2006.
- 6 MASTERS, C. L. et al. Amyloid plaque core protein in Alzheimer disease and Down syndrome. **Proceedings of the National Academy of Sciences**, v. 82, n. 12, p. 4245–4249, 1985.
- 7 GLENNER, G. G. Reprint of "Alzheimer's disease: initial report of the purification and characterization of a novel cerebrovascular amyloid protein". **Biochemical and Biophysical Research Communications**, v. 425, n. 3, p. 534–539, 2012.
- 8 HANGER, D. P.; ANDERTON, B. H.; NOBLE, W. Tau phosphorylation: the therapeutic challenge for neurodegenerative disease. **Trends in Molecular Medicine**, v. 15, n. 3, p. 112–119, 2009.
- 9 FITZPATRICK, A. W. P. et al. Cryo-EM structures of tau filaments from Alzheimer's disease. **Nature**, v. 547, n. 7662, p. 185–190, 2017.
- 10 HARDY, J.; SELKOE, D. J. The amyloid hypothesis of Alzheimer's disease: progress and problems on the road to therapeutics. **Science**, v. 297, n. 5580, p. 353–356, 2002.
- 11 WIRTHS, O.; MULTHAUP, G.; BAYER, T. A. A modified β -amyloid hypothesis: intraneuronal accumulation of the β -amyloid peptide - the first step of a fatal cascade. **Journal of Neurochemistry**, v. 91, n. 3, p. 513–520, 2004.
- 12 HARDY, J. The amyloid hypothesis for Alzheimer's disease: a critical reappraisal. **Journal of Neurochemistry**, v. 110, n. 4, p. 1129–1134, 2009.
- 13 HERRUP, K. The case for rejecting the amyloid cascade hypothesis. **Nature Neuroscience**, v. 18, n. 6, p. 794–799, 2015.
- 14 SELKOE, D. J.; HARDY, J. The amyloid hypothesis of Alzheimer's disease at 25 years. **EMBO Molecular Medicine**, v. 8, n. 6, p. 595–608, 2016.
- 15 LING, Y.; MORGAN, K.; KALSHEKER, N. Amyloid precursor protein (APP) and the

biology of proteolytic processing: relevance to Alzheimer's disease. **International Journal of Biochemistry & Cell Biology**, v. 35, n. 11, p. 1505–1535, 2003.

16 DE STROOPER, B. Proteases and proteolysis in Alzheimer disease: a multifactorial view on the disease process. **Physiological Reviews**, v. 90, n. 2, p. 465–494, 2010.

17 NICOLAS, M.; HASSAN, B. A. Amyloid precursor protein and neural development. **Development**, v. 141, n. 13, p. 2543–2548, 2014.

18 ROHER, A. E. et al. Amyloid- β peptides in human plasma and tissues and their significance for Alzheimer's disease. **Alzheimer's & Dementia**, v. 5, n. 1, p. 18–29, 2009.

19 JANELIDZE, S. et al. CSF A β 42/A β 40 and A β 42/A β 38 ratios: better diagnostic markers of Alzheimer disease. **Annals of Clinical and Translational Neurology**, v. 3, n. 3, p. 154–165, 2016.

20 BALDEIRAS, I. et al. Addition of the A β 42/40 ratio to the cerebrospinal fluid biomarker profile increases the predictive value for underlying Alzheimer's disease dementia in mild cognitive impairment. **Alzheimer's Research and Therapy**, v. 10, n. 1, p. 1–15, 2018.

21 JANELIDZE, S. et al. Plasma β -amyloid in Alzheimer's disease and vascular disease. **Scientific Reports**, v. 6, p. 26801, 2016.

22 CITRON, M. et al. Mutant presenilins of Alzheimer's disease increase production of 42-residue amyloid beta-protein in both transfected cells and transgenic mice. **Nature Medicine**, v. 3, n. 1, p. 67–72, 1997.

23 BROUWERS, N.; SLEEGERS, K.; VAN BROECKHOVEN, C. Molecular genetics of Alzheimer's disease: an update. **Annals of Medicine**, v. 40, n. 8, p. 562–583, 2008.

24 CACACE, R.; SLEEGERS, K.; VAN BROECKHOVEN, C. Molecular genetics of early-onset Alzheimer's disease revisited. **Alzheimer's and Dementia**, v. 12, n. 6, p. 733–748, 2016.

25 ALZFORUM. **Mutations APP**. Available from: <<http://www.alzforum.org/mutations/app>>. Accessible at: 26 Oct. 2018.

26 JONSSON, T. et al. A mutation in APP protects against Alzheimer's disease and age-related cognitive decline. **Nature**, v. 488, n. 7409, p. 96, 2012.

27 CORDER, E. H. et al. Gene dose of apolipoprotein E type 4 allele and the risk of Alzheimer's disease in late onset families. **Science**, v. 261, n. 5123, p. 921–923, 1993.

28 FARRER, L. A. Effects of age, sex, and ethnicity on the association between apolipoprotein E genotype and Alzheimer disease. A meta-analysis. APOE and Alzheimer disease meta analysis consortium. **JAMA**, v. 278, n. 16, p. 1349–1356, 1997.

29 KANEKIYO, T.; XU, H.; BU, G. ApoE and A β in Alzheimer's disease: accidental encounters or partners? **Neuron**, v. 81, n. 4, p. 740–754, 2014.

30 LAFERLA, F. M.; GREEN, K. N.; ODDO, S. Intracellular amyloid- β in Alzheimer's disease. **Nature Reviews Neuroscience**, v. 8, n. 7, p. 499–509, 2007.

- 31 GOURAS, G. K. et al. Intraneuronal β -amyloid accumulation and synapse pathology in Alzheimer's disease. **Acta Neuropathologica**, v. 119, n. 5, p. 523–541, 2010.
- 32 TAKAHASHI, R. H.; NAGAO, T.; GOURAS, G. K. Plaque formation and the intraneuronal accumulation of β -amyloid in Alzheimer's disease. **Pathology International**, v. 67, n. 4, p. 185–193, 2017.
- 33 SERPELL, L. C. Alzheimer's amyloid fibrils: structure and assembly. **Biochimica et Biophysica Acta - molecular basis of disease**, v. 1502, n. 1, p. 16–30, 2000.
- 34 LU, J. X. et al. Molecular structure of β -amyloid fibrils in Alzheimer's disease brain tissue. **Cell**, v. 154, n. 6, p. 1257–1268, 2013.
- 35 GARAI, K.; FRIEDEN, C. Quantitative analysis of the time course of A β oligomerization and subsequent growth steps using tetramethylrhodamine-labeled A β . **Proceedings of the National Academy of Sciences**, v. 110, n. 9, p. 3321–3326, 2013.
- 36 JUCKER, M.; WALKER, L. C. Self-propagation of pathogenic protein aggregates in neurodegenerative diseases. **Nature**, v. 501, n. 7465, p. 45–51, 2013.
- 37 CRESCENZI, O. et al. Solution structure of the Alzheimer amyloid β -peptide (1-42) in an apolar microenvironment. **European Journal of Biochemistry**, v. 269, n. 22, p. 5642–5648, 2002.
- 38 YAMAGUCHI, T.; MATSUZAKI, K.; HOSHINO, M. Transient formation of intermediate conformational states of amyloid- β peptide revealed by heteronuclear magnetic resonance spectroscopy. **FEBS Letters**, v. 585, n. 7, p. 1097–1102, 2011.
- 39 VIVEKANANDAN, S. et al. A partially folded structure of amyloid-beta(1-40) in an aqueous environment. **Biochemical and Biophysical Research Communications**, v. 411, n. 2, p. 312–316, 2011.
- 40 YU, L. et al. Structural characterization of a soluble amyloid beta-peptide oligomer. **Biochemistry**, v. 48, n. 9, p. 1870–1877, 2009.
- 41 PETKOVA, A. T. et al. A structural model for Alzheimer's β -amyloid fibrils based on experimental constraints from solid state NMR. **Proceedings of the National Academy of Sciences**, v. 99, n. 26, p. 16742–16747, 2002.
- 42 LUHRS, T. et al. 3D structure of Alzheimer's amyloid- β (1-42) fibrils. **Proceedings of the National Academy of Sciences**, v. 102, n. 48, p. 17342–17347, 2005.
- 43 GREMER, L. et al. Fibril structure of amyloid- β (1–42) by cryo–electron microscopy. **Science**, v. 358, n. 6359, p. 116–119, 2017.
- 44 LU, J.-X. et al. Molecular structure of β -amyloid fibrils in Alzheimer's disease brain tissue. **Cell**, v. 154, n. 6, p. 1257–1268, 2013.
- 45 COLVIN, M. T. et al. Atomic resolution structure of monomeric A β 42 amyloid fibrils. **Journal of the American Chemical Society**, v. 138, n. 30, p. 9663–9674, 2016.
- 46 DANIELSSON, J. et al. 15N relaxation study of the amyloid β -peptide: structural

propensities and persistence length. **Magnetic Resonance in Chemistry**, v. 44, n. S1, p. S114–S121, 2006.

47 CHIMON, S. et al. Evidence of fibril-like β -sheet structures in a neurotoxic amyloid intermediate of Alzheimer's β -amyloid. **Nature Structural and Molecular Biology**, v. 14, n. 12, p. 1157–1164, 2007.

48 AHMED, M. et al. Structural conversion of neurotoxic amyloid- β (1-42) oligomers to fibrils. **Nature Structural and Molecular Biology**, v. 17, n. 5, p. 561–567, 2010.

49 BENILOVA, I.; KARRAN, E.; DE STROOPER, B. The toxic A β oligomer and Alzheimer's disease: an emperor in need of clothes. **Nature Neuroscience**, v. 15, n. 3, p. 349–357, 2012.

50 HAASS, C.; SELKOE, D. J. Soluble protein oligomers in neurodegeneration: lessons from the Alzheimer's amyloid β -peptide. **Nature Reviews Molecular Cell Biology**, v. 8, n. 2, p. 101–112, 2007.

51 JANG, H. et al. Truncated β -amyloid peptide channels provide an alternative mechanism for Alzheimer's Disease and Down syndrome. **Proceedings of the National Academy of Sciences**, v. 107, n. 14, p. 6538–6543, 2010.

52 GIUFFRIDA, M. L. et al. Amyloid monomers are neuroprotective. **Journal of Neuroscience**, v. 29, n. 34, p. 10582–10587, 2009.

53 KURUVA, C. S.; REDDY, P. H. Amyloid- β modulators and neuroprotection in Alzheimer's disease: a critical appraisal. **Drug Discovery Today**, v. 22, n. 2, p. 223–233, 2017.

54 OTTO, M. et al. Decreased β -amyloid1-42 in cerebrospinal fluid of patients with Creutzfeldt-Jakob disease. **Neurology**, v. 54, n. 5, p. 1099–1102, 2000.

55 NOGUCHI, M. et al. Decreased β -amyloid peptide42 in cerebrospinal fluid of patients with progressive supranuclear palsy and corticobasal degeneration. **Journal of the Neurological Sciences**, v. 237, n. 1–2, p. 61–65, 2005.

56 BIBL, M. et al. CSF amyloid- β -peptides in Alzheimer's disease, dementia with Lewy bodies and Parkinson's disease dementia. **Brain**, v. 129, n. 5, p. 1177–1187, 2006.

57 HOU, L. et al. Solution NMR studies of the A β (1-40) and A β (1-42) peptides establish that the Met35 oxidation state affects the mechanism of amyloid formation. **Journal of the American Chemical Society**, v. 126, n. 7, p. 1992–2005, 2004.

58 NAG, S. et al. Nature of the amyloid- β monomer and the monomer-oligomer equilibrium. **Journal of Biological Chemistry**, v. 286, n. 16, p. 13827–13833, 2011.

59 MUNTE, C. E. et al. Distinct conformational states of the alzheimer beta-amyloid peptide can be detected by high-pressure NMR spectroscopy. **Angewandte Chemie International Edition**, v. 52, n. 34, p. 8943–8947, 2013.

60 ROCHE, J. et al. Monomeric A β 1-40 and A β 1-42 peptides in solution adopt very similar Ramachandran map distributions that closely resemble random coil. **Biochemistry**, v. 55, n.

5, p. 762–775, 2016.

61 ROSENMAN, D. J. et al. High pressure NMR reveals conformational perturbations by disease-causing mutations in amyloid β -peptide. **Chemical Communications**, v. 54, n. 36, p. 4609–4612, 2018.

62 MEHTA, M.; ADEM, A.; SABBAGH, M. New acetylcholinesterase inhibitors for Alzheimer's disease. **International Journal of Alzheimer's Disease**, 2012.

63 MELZER, D. et al. Long-term donepezil treatment in 565 patients with Alzheimer's disease (AD2000): randomised double-blind trial. **Lancet**, v. 363, n. 9427, p. 2105–2115, 2004.

64 RÖSLER, M. et al. Efficacy and safety of rivastigmine in patients with Alzheimer's disease: international randomised controlled trial. **BMJ**, v. 318, n. 7184, p. 633–640, 1999.

65 RASKIND, M. A. et al. Galantamine in AD: a 6-month randomized, placebo-controlled trial with a 6-month extension. **Neurology**, v. 54, n. 12, p. 2261–2268, 2000.

66 TERRY, A. V., BUCCAFUSCO, J. J. The cholinergic hypothesis of age and Alzheimer's disease-related cognitive deficits: recent challenges and their implications for novel drug development. **Journal of Pharmacology and Experimental Therapeutics**, v. 306, n. 3, p. 821–827, 2003.

67 OLIVARES, D. et al. N-methyl D-aspartate (NMDA) receptor antagonists and memantine treatment for Alzheimer's disease, vascular dementia and Parkinson's disease. **Current Alzheimer Research**, v. 9, n. 6, p. 746–758, 2012.

68 MANGIALASCHE, F. et al. Alzheimer's disease: clinical trials and drug development. **Lancet**, v. 9, n. 7, p. 702–716, 2010.

69 RYAN, P. et al. Peptides, peptidomimetics, and carbohydrate-peptide conjugates as amyloidogenic aggregation inhibitors for Alzheimer's disease. **ACS Chemical Neuroscience**, v. 9, n. 7, p. 1530–1551, 2018.

70 VAN GROEN, T. et al. Reduction of Alzheimer's disease amyloid plaque load in transgenic mice by D3, a D-enantiomeric peptide identified by mirror image phage display. **ChemMedChem**, v. 3, n. 12, p. 1848–1852, 2008.

71 AILEEN FUNKE, S. et al. Oral treatment with the D-enantiomeric peptide D3 improves the pathology and behavior of Alzheimer's disease transgenic mice. **ACS Chemical Neuroscience**, v. 1, n. 9, p. 639–648, 2010.

72 CAVINI, I. A. et al. Inhibition of amyloid A β aggregation by high pressures or specific D-enantiomeric peptides. **Chemical Communications**, v. 54, n. 26, p. 3294–3297, 2018.

73 VAN GROEN, T. et al. Treatment with D3 removes amyloid deposits, reduces inflammation, and improves cognition in aged A β PP/PS1 double transgenic mice. **Journal of Alzheimer's Disease**, v. 34, n. 3, p. 609–620, 2013.

74 OLUBIYI, O. O.; STRODEL, B. Structures of the amyloid β -peptides A β 1-40 and A β 1-42 as influenced by pH and a D-peptide. **Journal of Physical Chemistry B**, v. 116, n. 10, p.

3280–3291, 2012.

75 OLUBIYI, O. O. et al. Amyloid aggregation inhibitory mechanism of arginine-rich D-peptides. **Current Medicinal Chemistry**, v. 21, n. 12, p. 1448–1457, 2014.

76 BRENER, O. et al. QIAD assay for quantitating a compounds efficacy in elimination of toxic A β oligomers. **Scientific Reports**, v. 5, n. 13222, p. 1–13, 2015.

77 KLEIN, A. N. et al. Optimization of the All-D peptide D3 for A β oligomer elimination. **PLoS ONE**, v. 11, n. 4, p. 1–16, 2016.

78 KLEIN, A. N. et al. Optimization of D-peptides for A β monomer binding specificity enhances their potential to eliminate toxic A β oligomers. **ACS Chemical Neuroscience**, v. 8, n. 9, p. 1889–1900, 2017.

79 KUTZSCHE, J. et al. Large-scale oral treatment study with the four most promising D3-derivatives for the treatment of Alzheimer's disease. **Molecules**, v. 22, n. 10, p. 1693, 2017.

80 RÖSENER, N. S. et al. A D-enantiomeric peptide interferes with hetero-association of amyloid- β oligomers and prion protein. **Journal of Biological Chemistry**, v. 293, n. 41, p. 15748–15764, 2018.

81 UM, J. W. et al. Alzheimer amyloid- β oligomer bound to post-synaptic prion protein activates Fyn to impair neurons. **Nature Neuroscience**, v. 15, n. 9, p. 1227–1235, 2012.

82 DEROME, A. E. **Modern NMR techniques for chemistry research**. Oxford: Pergamon Press, 1995.

83 FRIEBOLIN, H. **Basic one- and two-dimensional NMR spectroscopy**. 5th ed. Weinheim: Wiley-VCH, 2010.

84 BLOCH, F.; HANSEN, W. W.; PACKARD, M. Nuclear induction. **Physical Review**, v. 70, p. 474–485, 1946.

85 PURCELL, E.; BLOEMBERGEN, N.; POUND, R. Resonance absorption by nuclear magnetic moments in a single crystal of CaF₂. **Physical Review**, v. 70, n. 11–12, p. 988–988, 1946.

86 JEENER, J. **Ampere international summer school**. Basko Polje, Yugoslavia, 1971.

87 ERNST, R. R.; BODENHAUSEN, G.; WOKAUN, A. **Principles of nuclear magnetic resonance in one and two dimensions**. Oxford: Clarendon Press, 1987.

88 WÜTHRICH, K. **NMR of proteins and nucleic acids**. New York: Wiley, 1986.

89 SATTLER, M.; SCHLEUCHER, J.; GRIESINGER, C. Heteronuclear multidimensional NMR experiments for the structure determination of proteins in solution. **Progress in Nuclear Magnetic Resonance Spectroscopy**, v. 34, p. 93–158, 1999.

90 KIM, S. **NMR experiments and sequences**. Available from: <http://chemsites.chem.rutgers.edu/~skim/nmr_exp_TRE_backbone>. Accessible at: 2 June 2018.

- 91 MEERSMAN, F. et al. High-pressure biochemistry and biophysics. **Reviews in Mineralogy and Geochemistry**, v. 75, n. 1, p. 607–648, 2013.
- 92 JONAS, J. Nuclear magnetic resonance at high pressure. **Review of Scientific Instruments**, v. 43, n. 4, p. 643–649, 1972.
- 93 YAMADA, H. Pressure-resisting glass cell for high pressure, high resolution NMR measurement. **Review of Scientific Instruments**, v. 45, n. 5, p. 640–642, 1974.
- 94 JONAS, J. High-resolution nuclear magnetic resonance studies of proteins. **Biochimica et Biophysica Acta - protein structure and molecular enzymology**, v. 1595, n. 1–2, p. 145–159, 2002.
- 95 PETERSON, R. W.; WAND, A. J. Self-contained high-pressure cell, apparatus, and procedure for the preparation of encapsulated proteins dissolved in low viscosity fluids for nuclear magnetic resonance spectroscopy. **Review of Scientific Instruments**, v. 76, n. 9, p. 094101, 2005.
- 96 BECK ERLACH, M. et al. Ceramic cells for high pressure NMR spectroscopy of proteins. **Journal of Magnetic Resonance**, v. 204, n. 2, p. 196–199, 2010.
- 97 KREMER, W. et al. Species-specific differences in the intermediate states of human and Syrian hamster prion protein detected by high pressure NMR spectroscopy. **Journal of Biological Chemistry**, v. 282, n. 31, p. 22689–22698, 2007.
- 98 KALBITZER, H. R. et al. Intrinsic allosteric inhibition of signaling proteins by targeting rare interaction states detected by high-pressure NMR spectroscopy. **Angewandte Chemie - International Edition**, v. 52, n. 52, p. 14242–14246, 2013.
- 99 AKASAKA, K.; LI, H. Low-lying excited states of proteins revealed from nonlinear pressure shifts in ¹H and ¹⁵N NMR. **Biochemistry**, v. 40, n. 30, p. 8665–8671, 2001.
- 100 WAUDBY, C. **Chemical exchange**. Available from: <<http://www.ucl.ac.uk/biosciences/departments/smb/christodoulou/people/chris-waudby/exchange-part-I>>. Accessible at: 1 Nov. 2018.
- 101 KITAMURA, Y.; ITOH, T. Reaction volume of protonic ionization for buffering agents. Prediction of pressure dependence of pH and pOH. **Journal of Solution Chemistry**, v. 16, n. 9, p. 715–725, 1987.
- 102 RAIFORD, D. S.; FISK, C. L.; BECKER, E. D. Calibration of methanol and ethylene glycol nuclear magnetic resonance thermometers. **Analytical Chemistry**, v. 51, n. 12, p. 2050–2051, 1979.
- 103 GRONWALD, W.; KALBITZER, H. R. Automated structure determination of proteins by NMR spectroscopy. **Progress in Nuclear Magnetic Resonance Spectroscopy**, v. 44, n. 1–2, p. 33–96, 2004.
- 104 WISHART, D.; BIGAM, C.; YAO, J. ¹H, ¹³C and ¹⁵N chemical shift referencing in biomolecular NMR. **Journal of Biomolecular NMR**, v. 6, n. 2, p. 135–140, 1995.
- 105 MARKLEY, J. L. et al. Recommendations for the presentation of NMR structures of

proteins and nucleic acids--IUPAC-IUBMB-IUPAB Inter-Union Task Group on the standardization of data bases of protein and nucleic acid structures determined by NMR spectroscopy. **European Journal of Biochemistry**, v. 256, n. 1, p. 1–15, 1998.

106 LAURENTS, D. V. et al. Alzheimer's A β 40 studied by NMR at low pH reveals that sodium 4,4-dimethyl-4-silapentane-1-sulfonate (DSS) binds and promotes β -ball oligomerization. **Journal of Biological Chemistry**, v. 280, n. 5, p. 3675–3685, 2005.

107 DAEDALUS INNOVATIONS. **High pressure NMR**. Available from: <<http://www.daedalusinnovations.com/apparatus/high-pressure>>. Accessible at: 1 June 2018.

108 KOEHLER, J. et al. Pressure dependence of ¹⁵N chemical shifts in model peptides Ac-Gly-Gly-X-Ala-NH₂. **Materials**, v. 5, n. 10, p. 1774–1786, 2012.

109 LIU, M. et al. Improved watergate pulse sequences for solvent suppression in NMR spectroscopy. **Journal of Magnetic Resonance**, v. 132, n. 1, p. 125–129, 1998.

110 PRICE, W. S. **NMR studies of translational motion: principles and applications**. Cambridge: Cambridge University Press, 2009.

111 PELTA, M. D. et al. A one-shot sequence for high-resolution diffusion-ordered spectroscopy. **Magnetic Resonance in Chemistry**, v. 40, n. 13, p. S147–S152, 2002.

112 PIOTTO, M.; SAUDEK, V.; SKLENÁŘ, V. Gradient-tailored excitation for single-quantum NMR spectroscopy of aqueous solutions. **Journal of Biomolecular NMR**, v. 2, n. 6, p. 661–665, 1992.

113 SKLENAR, V.; PIOTTO, M.; LEPPIK, R.; SAUDEK, V. Gradient-tailored water suppression for ¹H-¹⁵N HSQC experiments optimized to retain full sensitivity. **Journal of Magnetic Resonance**, v. 102, n. 2, p. 241–245, 1993.

114 BAX, A.; DAVIS, D. G. MLEV-17-based two-dimensional homonuclear magnetization transfer spectroscopy. **Journal of Magnetic Resonance (1969)**, v. 65, n. 2, p. 355–360, 1985.

115 PARELLA, T. **AVANCE tutorials**. ge-2D TOCSY using 3-9-19 WATERGATE. Available from: <<http://triton.iqfr.csic.es/guide/tutorials/2Dhom/mlevgptp19>>. Accessible at: 29 Aug. 2018.

116 WIDER, G.; HOSUR, R. V.; WÜTHRICH, K. Suppression of the solvent resonance in 2D NMR spectra of proteins in H₂O solution. **Journal of Magnetic Resonance (1969)**, v. 52, n. 1, p. 130–135, 1983.

117 PARELLA, T. **AVANCE tutorials**. 2D NOESY using presaturation. Available from: <<http://triton.iqfr.csic.es/guide/tutorials/2Dhom/noesypr>>. Accessible at: 29 Aug. 2018.

118 PALMER, A. G. et al. Sensitivity improvement in proton-detected two-dimensional heteronuclear correlation NMR spectroscopy. **Journal of Magnetic Resonance (1969)**, v. 93, n. 1, p. 151–170, 1991.

119 KAY, L. E.; KEIFER, P.; SAARINEN, T. Pure absorption gradient enhanced heteronuclear single quantum correlation spectroscopy with improved sensitivity. **Journal of the American Chemical Society**, v. 114, n. 26, p. 10663–10665, 1992.

- 120 SCHLEUCHER, J. et al. A general enhancement scheme in heteronuclear multidimensional NMR employing pulsed field gradients. **Journal of Biomolecular NMR**, v. 4, n. 2, p. 301–306, 1994.
- 121 PARELLA, T. **AVANCE tutorials**. ge-2D 1H-13C HSQC with improved sensitivity. Available from: <<http://triton.iqfr.csic.es/guide/tutorials/2Dhet/invietgssi>>. Accessible at: 29 Aug. 2018.
- 122 GRZESIEK, S.; BAX, A. Improved 3d triple resonance NMR techniques applied to a 31 kDa protein. **Journal of Magnetic Resonance**, v. 96, n. 2, p. 432–440, 1992.
- 123 KAY, L. E.; XU, G. Y.; YAMAZAKI, T. Enhanced-sensitivity triple-resonance spectroscopy with minimal H₂O saturation. **Journal of Magnetic Resonance A**, v. 109, n. 1, p. 129–133, 1994.
- 124 KAY, L. E. et al. Three-dimensional triple-resonance NMR spectroscopy of isotopically enriched proteins. **Journal of Magnetic Resonance (1969)**, v. 89, n. 3, p. 496–514, 1990.
- 125 FARMER, B. T. et al. A refocused and optimized HNCA: increased sensitivity and resolution in large macromolecules. **Journal of Biomolecular NMR**, v. 2, n. 2, p. 195–202, 1992.
- 126 SCHLEUCHER, J.; SATTLER, M.; GRIESINGER, C. Coherence selection by gradients without signal attenuation: application to the three-dimensional HNCO experiment. **Angewandte Chemie International Edition**, v. 32, n. 10, p. 1489–1491, 1993.
- 127 PARELLA, T. **AVANCE tutorials**. 3D HNCO. Available from: <<http://triton.iqfr.csic.es/guide/eNMR/eNMR3Dprot/hnco>>. Accessible at: 29 Aug. 2018.
- 128 GRZESIEK, S.; BAX, A. Correlating backbone amide and side chain resonances in larger proteins by multiple relayed triple resonance NMR. **Journal of the American Chemical Society**, v. 114, n. 16, p. 6291–6293, 1992.
- 129 GRZESIEK, S.; BAX, A. Amino acid type determination in the sequential assignment procedure of uniformly ¹³C / ¹⁵N-enriched proteins. **Science**, v. 3, n. 2, p. 185–204, 1993.
- 130 MUHANDIRAM, D. R.; KAY, L. E. Gradient-enhanced triple-resonance three-dimensional NMR experiments with improved sensitivity. **Journal of Magnetic Resonance B**, v. 103, n. 3, p. 203–216, 1994.
- 131 BAX, A.; CLORE, G. M.; GRONENBORN, A. M. 1H-1H correlation via isotropic mixing of ¹³C magnetization, a new three-dimensional approach for assigning 1H and ¹³C spectra of ¹³C-enriched proteins. **Journal of Magnetic Resonance (1969)**, v. 88, n. 2, p. 425–431, 1990.
- 132 OLEJNICZAK, E. T.; XU, R. X.; FESIK, S. W. A 4D HCCH-TOCSY experiment for assigning the side chain 1H and ¹³C resonances of proteins. **Journal of Biomolecular NMR**, v. 2, n. 6, p. 655–659, 1992.
- 133 KAY, L. E. et al. A gradient-enhanced HCCH-TOCSY experiment for recording side-chain 1H and ¹³C correlations in H₂O samples of proteins. **Journal of Magnetic Resonance, Series B**, v. 101, n. 3, p. 333–337, 1993.

- 134 BMRB. **Statistics calculated for selected chemical shifts from atoms in the 20 common amino acids.** Available from: <http://www.bmrb.wisc.edu/ftp/pub/bmrb/statistics/chem_shifts/selected/statsel_prot.txt>. Accessible at: 10 Oct. 2018.
- 135 SCHUMANN, F. et al. Combined chemical shift changes and amino acid specific chemical shift mapping of protein–protein interactions. **Journal of Biomolecular NMR**, v. 39, n. 4, p. 275–289, 2007.
- 136 KITAHARA, R. et al. Pressure-induced chemical shifts as probes for conformational fluctuations in proteins. **Progress in Nuclear Magnetic Resonance Spectroscopy**, v. 71, p. 35–58, 2013.
- 137 KITAHARA, R.; YOKOYAMA, S.; AKASAKA, K. NMR snapshots of a fluctuating protein structure: ubiquitin at 30 bar–3 kbar. **Journal of Molecular Biology**, v. 347, n. 2, p. 277–285, 2005.
- 138 BECK ERLACH, M. et al. Pressure dependence of backbone chemical shifts in the model peptides Ac-Gly-Gly-Xxx-Ala-NH₂. **Journal of Biomolecular NMR**, v. 65, n. 2, p. 65–77, 2016.
- 139 BECK ERLACH, M. et al. Pressure dependence of side chain ¹³C chemical shifts in model peptides Ac-Gly-Gly-Xxx-Ala-NH₂. **Journal of Biomolecular NMR**, v. 69, n. 2, p. 53–67, 2017.
- 140 CHEN, C.; FINE, R. A.; MILLERO, F. J. The equation of state of pure water determined from sound speeds. **Journal of Chemical Physics**, v. 66, n. 5, p. 2142–2144, 1977.
- 141 BECK ERLACH, M. et al. Relationship between nonlinear pressure-induced chemical shift changes and thermodynamic parameters. **Journal of Physical Chemistry B**, v. 118, n. 21, p. 5681–5690, 2014.
- 142 THE R FOUNDATION. **The R project for statistical computing.** Available from: <<http://www.r-project.org/>>. Accessible at: 13 fev. 2014.
- 143 SHEN, Y. et al. TALOS+: a hybrid method for predicting protein backbone torsion angles from NMR chemical shifts. **Journal of Biomolecular NMR**, v. 44, n. 4, p. 213–223, 2009.
- 144 DELAGLIO, F. **TALOS+ server:** prediction of protein backbone torsion angles from chemical shifts. Available from: <<http://spin.niddk.nih.gov/bax/nmrserver/talos/>>. Accessible at: 3. Nov. 2018.
- 145 WAGNER, G. et al. Nuclear magnetic resonance identification of “half-turn” and ₃₁₀-helix secondary structure in rabbit liver metallothionein-2. **Journal of Molecular Biology**, v. 187, n. 1, p. 131–135, 1986.
- 146 CLORE, G. M.; GRONENBORN, A. M. Determination of three-dimensional structures of proteins and nucleic acids in solution by nuclear magnetic resonance spectroscopy. **Critical Reviews in Biochemistry and Molecular Biology**, v. 24, n. 5, p. 479–564, 1989.
- 147 PARDI, A.; BILLETER, M.; WÜTHRICH, K. Calibration of the angular dependence of

the amide proton- $C\alpha$ proton coupling constants, $3J_{HNH\alpha}$, in a globular protein: use of $3J_{HNH\alpha}$ for identification of helical secondary structure. **Journal of Molecular Biology**, v. 180, n. 3, p. 741–751, 1984.

148 WIERSCHEM, C. **Strukturelle und funktionelle Charakterisierung der Kalziumbindungsdomäne des Kalziumkanals TRPP1 mit Hilfe der hochauflösenden NMR Spektroskopie**. 2003. (Master thesis) - Universität Regensburg, Regensburg, 2003.

149 MORRIS, A. M.; WATZKY, M. A.; FINKE, R. G. Protein aggregation kinetics, mechanism, and curve-fitting: a review of the literature. **Biochimica et Biophysica Acta - Proteins and Proteomics**, v. 1794, n. 3, p. 375–397, 2009.

150 OOSAWA, F.; KASAI, M. A theory of linear and helical aggregations of macromolecules. **Journal of Molecular Biology**, v. 4, n. 1, p. 10–21, 1962.

151 OOSAWA, F. Size distribution of protein polymers. **Journal of Theoretical Biology**, v. 27, n. 1, p. 69–86, 1970.

152 FINDER, V. H. et al. The recombinant amyloid- β peptide A β 1-42 aggregates faster and is more neurotoxic than synthetic A β 1-42. **Journal of Molecular Biology**, v. 396, n. 1, p. 9–18, 2010.

153 KAPUST, R. B. et al. The P1' specificity of tobacco etch virus protease. **Biochemical and Biophysical Research Communications**, v. 294, n. 5, p. 949–955, 2002.

155 FAWZI, N. L. et al. Atomic-resolution dynamics on the surface of amyloid- β protofibrils probed by solution NMR. **Nature**, v. 480, n. 7376, p. 268–272, 2011.

155 ASAKAWA, N. et al. Structural studies of hydrogen-bonded peptides and polypeptides by solid-state NMR. **Annual Reports on NMR Spectroscopy**, v. 35, p. 55–137, 1998.

156 KALBITZER, H. R. et al. ^{15}N and 1H NMR study of histidine containing protein (HPr) from *Staphylococcus carnosus* at high pressure. **Protein Science**, v. 9, n. 4, p. 693–703, 2000.

157 CHENG, Y.; GAO, X.; LIANG, F. Bayesian peak picking for NMR spectra. **Genomics, Proteomics and Bioinformatics**, v. 12, n. 1, p. 39–47, 2014.

158 LASSALLE, M. W.; YAMADA, H.; AKASAKA, K. The pressure-temperature free energy-landscape of staphylococcal nuclease monitored by 1H NMR. **Journal of Molecular Biology**, v. 298, n. 2, p. 293–302, 2000.

159 ABDUL LATIF, A. R. et al. Kinetic analysis of amyloid protofibril dissociation and volumetric properties of the transition state. **Biophysical Journal**, v. 92, n. 1, p. 323–329, 2007.

160 SHAH, B. R. et al. Pressure-accelerated dissociation of amyloid fibrils in wild-type hen lysozyme. **Biophysical Journal**, v. 102, n. 1, p. 121–126, 2012.

161 AKASAKA, K. Highly fluctuating protein structures revealed by variable-pressure nuclear magnetic resonance. **Biochemistry**, v. 42, n. 37, p. 10875–10885, 2003.

162 KITAHARA, R. et al. High pressure NMR reveals that apomyoglobin is an equilibrium

mixture from the native to the unfolded. **Journal of Molecular Biology**, v. 320, n. 2, p. 311–319, 2002.

163 WISHART, D. S.; SYKES, B. D.; RICHARDS, F. M. Relationship between nuclear magnetic resonance chemical shift and protein secondary structure. **Journal of Molecular Biology**, v. 222, n. 2, p. 311–333, 1991.

164 WISHART, D. S.; SYKES, B. D.; RICHARDS, F. M. The chemical shift index: a fast and simple method for the assignment of protein secondary structure through NMR spectroscopy. **Biochemistry**, v. 31, n. 6, p. 1647–1651, 1992.

165 WISHART, D. S.; SYKES, B. The ¹³C chemical-shift index: a simple method for the identification of protein secondary structure using ¹³C chemical-shift data. **Journal of Biomolecular NMR**, v. 4, n. 2, p. 171–180, 1994.

166 CORNILESCU, G.; DELAGLIO, F.; BAX, A. Protein backbone angle restraints from searching a database for chemical shift and sequence homology. **Journal of Biomolecular NMR**, v. 13, n. 3, p. 289–302, 1999.

167 SHEN, Y.; BAX, A. Protein backbone and sidechain torsion angles predicted from NMR chemical shifts using artificial neural networks. **Journal of Biomolecular NMR**, v. 56, n. 3, p. 227–241, 2013.

168 KJAERGAARD, M.; POULSEN, F. M. Sequence correction of random coil chemical shifts: correlation between neighbor correction factors and changes in the Ramachandran distribution. **Journal of Biomolecular NMR**, v. 50, n. 2, p. 157–165, 2011.

169 KJAERGAARD, M.; BRANDER, S.; POULSEN, F. M. Random coil chemical shift for intrinsically disordered proteins: Effects of temperature and pH. **Journal of Biomolecular NMR**, v. 49, n. 2, p. 139–149, 2011.

170 SHEN, Y. et al. Prediction of nearest neighbor effects on backbone torsion angles and NMR scalar coupling constants in disordered proteins. **Protein Science**, v. 27, n. 1, p. 146–158, 2018.

171 YANG, S.; AD, B. **RC_3JHNHa server**: IDP random coil 3JHNHa coupling constants. Available from: <https://spin.niddk.nih.gov/bax/nmrserver/rc_3Jhnha/>. Accessible at: 18 Jun. 2018.

172 WATSON, A. A.; FAIRLIE, D. P.; CRAIK, D. J. Solution structure of methionine-oxidized amyloid β -peptide (1-40). Does oxidation affect conformational switching? **Biochemistry**, v. 37, n. 37, p. 12700–12706, 1998.

173 WULFF, M. et al. Enhanced fibril fragmentation of N-terminally truncated and pyroglutamyl-modified A β peptides. **Angewandte Chemie International Edition**, v. 55, n. 16, p. 5081–5084, 2016.

174 CAMILLONI, C. et al. Determination of secondary structure populations in disordered states of proteins using nuclear magnetic resonance chemical shifts. **Biochemistry**, v. 51, n. 11, p. 2224–2231, 2012.

175 HAFSA, N. E.; ARNDT, D.; WISHART, D. S. CSI 3.0: a web server for identifying

secondary and super-secondary structure in proteins using NMR chemical shifts. **Nucleic Acids Research**, v. 43, n. W1, p. W370–W377, 2015.

176 MCGUFFIN, L. J.; BRYSON, K.; JONES, D. T. The PSIPRED protein structure prediction server. **Bioinformatics**, v. 16, n. 4, p. 404–405, 2000.

177 GRIFFITHS-JONES, S. R. et al. Modulation of intrinsic ϕ , ψ propensities of amino acids by neighbouring residues in the coil regions of protein structures: NMR analysis and dissection of a β -hairpin peptide1. **Journal of Molecular Biology**, v. 284, n. 5, p. 1597–1609, 1998.

178 KOEHLER, J. et al. Pressure response of amide one-bond J-couplings in model peptides and proteins. **Journal of Biomolecular NMR**, v. 60, n. 1, p. 45–50, 2014.

179 ROCHE, J. et al. Impact of hydrostatic pressure on an intrinsically disordered protein: a high-pressure NMR study of α -synuclein. **ChemBioChem**, v. 14, n. 14, p. 1754–1761, 2013.

180 SURKA, M. C.; TSANG, C. W.; TRIMBLE, W. S. The mammalian septin MSF localizes with microtubules and is required for completion of cytokinesis. **Molecular Biology of the Cell**, v. 13, n. 10, p. 3532–3545, 2002.

181 BAI, X. et al. Novel septin 9 repeat motifs altered in neuralgic amyotrophy bind and bundle microtubules. **Journal of Cell Biology**, v. 203, n. 6, p. 895–905, 2013.

182 HU, Q. et al. A septin diffusion barrier at the base of the primary cilium maintains ciliary membrane protein distribution. **Science**, v. 329, n. 5990, p. 436–439, 2010.

183 BRIDGES, A. A. et al. Micron-scale plasma membrane curvature is recognized by the septin cytoskeleton. **Journal of Cell Biology**, v. 213, n. 1, p. 23–32, 2016.

184 PETERSON, E. A.; PETTY, E. M. Conquering the complex world of human septins: implications for health and disease. **Clinical Genetics**, v. 77, n. 6, p. 511–524, 2010.

185 LIN, Y.-H. et al. The role of the septin family in spermiogenesis. **Spermatogenesis**, v. 1, n. 4, p. 298–302, 2011.

186 HARTWELL, L. H. Genetic control of the cell division cycle in yeast. IV. Genes controlling bud emergence and cytokinesis. **Experimental Cell Research**, v. 69, n. 2, p. 265–276, 1971.

187 BERTIN, A. et al. *Saccharomyces cerevisiae* septins: supramolecular organization of heterooligomers and the mechanism of filament assembly. **Proceedings of the National Academy of Sciences**, v. 105, n. 24, p. 8274–8279, 2008.

188 ZHANG, J. et al. Phosphatidylinositol polyphosphate binding to the mammalian septin H5 is modulated by GTP. **Current Biology**, v. 9, n. 24, p. 1458–1467, 1999.

189 PAN, F.; MALMBERG, R. L.; MOMANY, M. Analysis of septins across kingdoms reveals orthology and new motifs. **BMC Evolutionary Biology**, v. 7, 2007.

190 RIBET, D. et al. SUMOylation of human septins is critical for septin filament bundling and cytokinesis. **Journal of Cell Biology**, v. 216, n. 12, p. 4041–4052, 2017.

- 191 NAKAHIRA, M. et al. A draft of the human septin interactome. **PLoS ONE**, v. 5, n. 11, p. 13799, 2010.
- 192 DE ALMEIDA MARQUES, I. et al. Septin C-terminal domain interactions: implications for filament stability and assembly. **Cell Biochemistry and Biophysics**, v. 62, n. 2, p. 317–328, 2012.
- 193 SALA, F. A. et al. Heterotypic coiled-coil formation is essential for the correct assembly of the septin heterofilament. **Biophysical Journal**, v. 111, n. 12, p. 2608–2619, 2016.
- 194 MARTINEZ, C.; WARE, J. Mammalian septin function in hemostasis and beyond. **Experimental Biology and Medicine**, v. 229, n. 11, p. 1111–1119, 2004.
- 195 SIRAJUDDIN, M. et al. Structural insight into filament formation by mammalian septins. **Nature**, v. 449, n. 7160, p. 311–315, 2007.
- 196 KIM, M. S. et al. SEPT9 occupies the terminal positions in septin octamers and mediates polymerization-dependent functions in abscission. **Journal of Cell Biology**, v. 195, n. 5, p. 815–826, 2011.
- 197 SIRAJUDDIN, M. et al. GTP-induced conformational changes in septins and implications for function. **Proceedings of the National Academy of Sciences**, v. 106, n. 39, p. 16592–16597, 2009.
- 198 VALADARES, N. F. et al. Septin structure and filament assembly. **Biophysical Reviews**, v. 9, n. 5, p. 481–500, 2017.
- 199 KINOSHITA, M. Assembly of mammalian septins. **Journal of Biochemistry**, v. 134, n. 4, p. 491–496, 2003.
- 200 TRUEBESTEIN, L.; LEONARD, T. A. Coiled-coils: the long and short of it. **BioEssays**, v. 38, n. 9, p. 903–916, 2016.
- 201 LIU, J. et al. A seven-helix coiled coil. **Proceedings of the National Academy of Sciences**, v. 103, n. 42, p. 15457–15462, 2006.
- 202 LJUBETIČ, A. et al. Design of coiled-coil protein-origami cages that self-assemble in vitro and in vivo. **Nature Biotechnology**, v. 35, n. 11, p. 1094–1101, 2017.
- 203 HARBURY, P. B. et al. A switch between two-, three-, and four-stranded coiled coils in GCN4 leucine zipper mutants. **Science**, v. 262, n. 5138, p. 1401–1407, 1993.
- 204 WALSHAW, J.; WOOLFSON, D. N. Extended knobs-into-holes packing in classical and complex coiled-coil assemblies. **Journal of Structural Biology**, v. 144, n. 3, p. 349–361, 2003.
- 205 LUPAS, A. N.; GRUBER, M. The structure of α -helical coiled coils. **Advances in Protein Chemistry**, v. 70, p. 37–78, 2005.
- 206 CRICK, F. H. C. Is alpha-keratin a coiled coil? **Nature**, v. 170, n. 4334, p. 882–883, 1952.

- 207 SIEVERS, F. et al. Fast, scalable generation of high-quality protein multiple sequence alignments using Clustal Omega. **Molecular Systems Biology**, v. 7, n. 1, p. 539–539, 2014.
- 208 GÖRLER, A.; KALBITZER, H. R. Relax, a flexible program for the back calculation of NOESY spectra based on complete-relaxation-matrix formalism. **Journal of Magnetic Resonance**, v. 124, n. 1, p. 177–188, 1997.
- 209 HUBBELL, W. L.; CAFISO, D. S.; ALTENBACH, C. Identifying conformational changes with site-directed spin labeling. **Nature Structural and Molecular Biology**, v. 7, n. 9, p. 735–739, 2000.
- 210 FOLTA-STOGNIEW, E.; WILLIAMS, K. Determination of molecular masses of proteins in solution: implementation of an HPLC size exclusion chromatography and laser light scattering service in a core laboratory. **Journal of Biomolecular Techniques**, v. 10, n. 2, p. 51, 1999.
- 211 TESTA, O. D.; MOUTEVELIS, E.; WOOLFSON, D. N. CC+: a relational database of coiled-coil structures. **Nucleic Acids Research**, v. 37, n. S1, p. D315–D322, 2009.
- 212 FOLKERS, P. J. M. et al. Overcoming the ambiguity problem encountered in the analysis of nuclear overhauser magnetic resonance spectra of symmetric dimer proteins. **Journal of the American Chemical Society**, v. 115, n. 9, p. 3798–3799, 1993.
- 213 WALTERS, K. J.; MATSUO, H.; WAGNER, G. A simple method to distinguish intermonomer nuclear overhauser effects in homodimeric proteins with C2 symmetry. **Journal of the American Chemical Society**, v. 119, n. 25, p. 5958–5959, 1997.
- 214 O'DONOGHUE, S. I.; KING, G. F.; NILGES, M. Calculation of symmetric multimer structures from NMR data using a priori knowledge of the monomer structure, co-monomer restraints, and interface mapping: the case of leucine zippers. **Journal of Biomolecular NMR**, v. 8, n. 2, p. 193–206, 1996.
- 215 O'DONOGHUE, S.; JUNIUS, F.; KING, G. Determination of the structure of symmetrical coiled-coil proteins from nmr data - application of the leucine-zipper proteins Jun and Gcn4. **Protein Engineering**, v. 6, n. 6, p. 557–564, 1993.
- 216 IWAHARA, J.; TANG, C.; CLORE, G. M. Practical aspects of (1)H transverse paramagnetic relaxation enhancement measurements on macromolecules. **Journal of Magnetic Resonance**, v. 184, n. 2, p. 185–195, 2007.
- 217 SJODT, M.; CLUBB, R. Nitroxide labeling of proteins and the determination of paramagnetic relaxation derived distance restraints for NMR studies. **Bio-Protocol**, v. 7, n. 7, 2017.
- 218 HAGELUEKEN, G. et al. MtsslWizard: In silico spin-labeling and generation of distance distributions in PyMOL. **Applied Magnetic Resonance**, v. 42, n. 3, p. 377–391, 2012.

APPENDIX

Appendix A – ^1H and ^{15}N chemical shifts (δ) of A β (1-40) at 0.1 MPa and 277 K.^a

| Residue | δ ($^{15}\text{N}^{\text{H}}$) [ppm] | δ ($^1\text{H}^{\text{N}}$) [ppm] | δ ($^1\text{H}^{\text{a}}$) [ppm] | δ ($^1\text{H}^{\text{b}}$) [ppm] | δ ($^1\text{H}^{\text{c}}$) [ppm] | δ (other) [ppm] |
|---------|--|---|---|---|---|--|
| Asp1 | – ^b | – ^b | 4.09 | 2.77/2.64 | | |
| Ala2 | – ^b | – ^b | 4.27 | 1.35 | | |
| Glu3 | 120.6 | 8.55 | 4.16 | 1.88/1.88 | 2.18/2.10 | |
| Phe4 | 122.0 | 8.38 | 4.53 | 2.98/2.98 | | H ^δ : 7.15 ^c , H ^ε : 7.24 ^c , H ^ζ : 7.24 ^c |
| Arg5 | 124.1 | 8.20 | 4.24 | 1.70/1.60 | 1.46/1.46 | H ^δ : 3.12 ^c , H ^ε : 7.39 |
| His6 | 121.9 | 8.45 | 4.48 | 3.07/3.07 | | H ^{δ2} : 7.06 ^c , H ^{ε1} : 8.04 ^c |
| Asp7 | 121.9 | 8.42 | 4.60 | 2.64/2.64 | | |
| Ser8 | 116.8 | 8.49 | 4.35 | 3.90/3.86 | | |
| Gly9 | 110.9 | 8.61 | 3.93/3.87 | | | |
| Tyr10 | 120.2 | 8.02 | 4.50 | 3.00/2.92 | | H ^δ : 7.04, H ^ε : 6.76 |
| Glu11 | 122.8 | 8.46 | 4.25 | 1.90/1.81 | 2.14/2.14 | |
| Val12 | 121.4 | 8.18 | 3.92 | 1.92 | 0.86/0.76 | |
| His13 | 122.8 | 8.34 | 4.56 | 3.10 ^c /3.04 ^c | | H ^{δ2} : 7.03, H ^{ε1} : 8.05 |
| His14 | 121.5 | 8.22 | 4.51 | 3.04/2.97 | | H ^{δ2} : 7.03, H ^{ε1} : 8.06 |
| Gln15 | 121.7 | 8.45 | 4.25 | 2.04/1.95 | 2.30/2.30 | N ^{δ2} : 113.1, H ^{ε2} : 7.66/6.98 |
| Lys16 | 123.1 | 8.47 | 4.25 | 1.79/1.74 | 1.43/1.36 | H ^δ : 1.65/1.65, H ^ε : 2.97 ^c |
| Leu17 | 124.1 | 8.34 | 4.32 | 1.58/1.58 | 1.57 | H ^δ : 0.90/0.83 |
| Val18 | 121.8 | 8.09 | 4.00 | 1.89 | 0.83/0.73 | |
| Phe19 | 124.7 | 8.36 | 4.55 | 2.96/2.90 | | H ^δ : 7.16 ^c , H ^ε : 7.30 ^c , H ^ζ : 7.28 ^c |
| Phe20 | 123.2 | 8.32 | 4.55 | 3.07/2.91 | | H ^δ : 7.24 ^c , H ^ε : 7.32 ^c , H ^ζ : 7.24 ^c |
| Ala21 | 126.4 | 8.33 | 4.20 | 1.35 | | |
| Glu22 | 120.2 | 8.45 | 4.18 | 2.02/1.90 | 2.27/2.24 | |
| Asp23 | 122.0 | 8.52 | 4.63 | 2.74/2.62 | | |
| Val24 | 120.9 | 8.25 | 4.11 | 2.16 | 0.94/0.94 | |
| Gly25 | 112.0 | 8.64 | 3.96/3.96 | | | |
| Ser26 | 115.8 | 8.24 | 4.41 | 3.90/3.86 | | |
| Asn27 | 121.1 | 8.58 | 4.73 | 2.86/2.79 | | N ^{δ2} : 113.4, H ^{ε2} : 7.73/7.02 |
| Lys28 | 121.8 | 8.45 | 4.25 | 1.87/1.75 | 1.45/1.39 | H ^δ : 1.66/1.66, H ^ε : 2.99 ^c |
| Gly29 | 109.8 | 8.51 | 3.91/3.91 | | | |
| Ala30 | 123.8 | 8.12 | 4.28 | 1.35 | | |
| Ile31 | 121.0 | 8.29 | 4.13 | 1.85 | 1.49/1.19 | H ^{γ2} : 0.86, H ^{δ1} : 0.84 |
| Ile32 | 126.6 | 8.39 | 4.13 | 1.85 | 1.49/1.19 | H ^{γ2} : 0.91, H ^{δ1} : 0.87 |
| Gly33 | 113.4 | 8.57 | 3.94/3.90 | | | |
| Leu34 | 121.9 | 8.15 | 4.32 | 1.58/1.58 | 1.58 | H ^δ : 0.90/0.86 |
| Met35 | 122.2 | 8.54 | 4.51 | 2.05/2.01 | 2.58/2.49 | H ^ε : 2.07 |
| Val36 | 122.8 | 8.34 | 4.11 | 2.07 | 0.93/0.93 | |
| Gly37 | 113.3 | 8.71 | 3.97/3.97 | | | |
| Gly38 | 108.9 | 8.35 | 3.99/3.93 | | | |
| Val39 | 120.1 | 8.18 | 4.16 | 2.07 | 0.92/0.92 | |
| Val40 | 128.7 | 7.93 | 4.03 | 2.04 | 0.90/0.88 | |

^a Sample buffer was 50 mM Tris- d_{11} , pH 7.0, 100 mM NaCl, 0.5 mM EDTA- d_{16} , 1 mM sodium azide in 8% D_2O .

^b Peaks were unassignable due to exchange with solvent.

^c Chemical shifts extracted from ^1H - ^1H -NOESY experiment.

Source: By the author.

Appendix B – ^{13}C chemical shifts (δ) of A β (1-40) at 0.1 MPa and 277 K.^a

| Residue | δ ($^{13}\text{C}^{\alpha}$) [ppm] | δ ($^{13}\text{C}^{\beta}$) [ppm] | δ ($^{13}\text{C}^{\gamma}$) [ppm] | δ ($^{13}\text{C}^{\delta}$) [ppm] | δ (other) [ppm] |
|---------|--|---|--|--|--|
| Asp1 | 53.8 | 41.0 | - ^b | | |
| Ala2 | 52.7 | 19.0 | 177.5 | | |
| Glu3 | 56.5 | 30.2 | 176.1 | 36.2 | |
| Phe4 | 57.7 | 39.5 | 175.3 | | C ^ε : 131.4; C ^ζ : 129.9 |
| Arg5 | 55.6 | 31.1 | 175.5 | 27.0 | 43.2 |
| His6 | 56.6 | 30.8 | 175.3 | 133.8 | 119.8 |
| Asp7 | 54.0 | 41.1 | 176.4 | | H ^{ε1} : 137.9 |
| Ser8 | 59.1 | 63.7 | 175.2 | | |
| Gly9 | 45.3 | | 174.0 | | |
| Tyr10 | 58.1 | 38.7 | 175.8 | 130.4 | 133.2 |
| Glu11 | 56.6 | 30.2 | 176.2 | 36.2 | C ^ε : 118.2; C ^ζ : 157.2 |
| Val12 | 62.7 | 32.6 | 176.1 | 20.7/20.9 | |
| His13 | 56.3 | 30.9 | 175.4 | 134.0 | 119.7 |
| His14 | 56.5 | 29.9 | 175.6 | 133.7 | 120.0 |
| Gln15 | 56.0 | 29.3 | 175.3 | 33.7 | H ^{ε1} : 137.9 |
| Lys16 | 56.4 | 32.9 | 176.4 | 24.7 | 29.0 |
| Leu17 | 55.1 | 42.5 | 176.9 | 27.0 | 24.9/23.6 |
| Val18 | 61.9 | 32.9 | 175.2 | 20.6/21.2 | |
| Phe19 | 57.4 | 40.2 | 174.9 | | 131.8 |
| Phe20 | 57.4 | 40.1 | 174.8 | | 131.9 |
| Ala21 | 52.3 | 19.4 | 177.3 | | C ^ε : 131.4; C ^ζ : 129.9 |
| Glu22 | 56.5 | 30.2 | 176.2 | 36.2 | C ^ε : 131.4; C ^ζ : 129.9 |
| Asp23 | 54.1 | 41.0 | 176.6 | | |
| Val24 | 62.7 | 32.2 | 177.1 | 21.1/20.2 | |
| Gly25 | 45.4 | | 174.6 | | |
| Ser26 | 58.5 | 63.8 | 174.6 | | |
| Asn27 | 53.2 | 38.5 | 175.4 | | |
| Lys28 | 56.7 | 32.5 | 177.3 | 24.7 | 29.0 |
| Gly29 | 45.1 | | 173.8 | | C ^ε : 42.1 |
| Ala30 | 52.3 | 19.2 | 177.7 | | |
| Ile31 | 61.1 | 38.4 | 176.5 | 27.3/17.5 | 12.6 |
| Ile32 | 61.1 | 38.4 | 176.7 | 27.3/17.3 | 12.6 |
| Gly33 | 45.1 | | 173.8 | | |
| Leu34 | 55.1 | 42.5 | 177.4 | 27.0 | 24.9/23.5 |
| Met35 | 55.3 | 32.6 | 176.3 | 31.9 | C ^ε : 16.9 |
| Val36 | 62.7 | 32.8 | 176.8 | 21.2/20.5 | |
| Gly37 | 45.3 | | 174.5 | | |
| Gly38 | 45.2 | | 173.8 | | |
| Val39 | 62.5 | 32.8 | 175.7 | 21.2/20.5 | |
| Val40 | 63.8 | 33.2 | - | 21.5/20.2 | |

^a Sample buffer was 50 mM Tris- d_{11} , pH 7.0, 100 mM NaCl, 0.5 mM EDTA- d_{16} , 1 mM sodium azide in 8% D_2O .

^b Peaks were unassignable due to exchange with solvent.

^c Chemical shifts extracted from ^1H - ^1H -NOESY experiment.

Source: By the author.

Appendix C – ^1H and ^{15}N random coil-corrected first order pressure coefficients (B_1^*) of A β (1-40).^a Values at 277 and 288 K (latter inside parentheses) are presented.

| | B_1^* ($^{15}\text{N}^{\text{H}}$) ± 0.05 [ppm GPa $^{-1}$] | B_1^* ($^1\text{H}^{\text{N}}$) ± 0.007 [ppm GPa $^{-1}$] | B_1^* ($^1\text{H}^{\alpha}$) ± 0.004 [ppm GPa $^{-1}$] | B_1^* ($^1\text{H}^{\beta}$) ± 0.007 [ppm GPa $^{-1}$] | B_1^* ($^1\text{H}^{\gamma}$) ± 0.004 [ppm GPa $^{-1}$] | B_1^* (other) ± 0.003 [ppm GPa $^{-1}$] |
|-------|--|--|--|---|--|--|
| Asp1 | _b | _b | 0.220 (0.161) | -0.029 (-0.041) 0.014 (0.019) | | |
| Ala2 | _b | _b | 0.043 (0.049) | 0.007 (0.002) | | |
| Glu3 | 1.04 (0.72) | 0.039 (0.028) | -0.158 (-0.150) | | -0.040 (-0.057) -0.201 (-0.163) | |
| Phe4 | -0.32 (-0.17) | 0.101 (0.091) | -0.036 (-0.068) | 0.019 (0.004) | | |
| Arg5 | 0.65 (0.69) | 0.145 (0.112) | -0.090 (-0.105) | -0.082 (-0.108) -0.026 (-0.062) | -0.044 (-0.056) | 0.022 (-0.004) |
| His6 | 0.45 | -0.132 | -0.098 (-0.099) | | | |
| Asp7 | -0.05 (0.12) | -0.026 (-0.109) | -0.007 (0.003) | -0.037 (-0.049) | | |
| Ser8 | -0.39 (-0.48) | -0.083 (-0.118) | 0.044 (0.022) | -0.059 (-0.067) -0.050 (-0.061) | | |
| Gly9 | -0.95 (-0.92) | -0.281 (-0.275) | -0.106 (-0.139) 0.043 (0.032) | | | |
| Tyr10 | -0.70 (-0.76) | -0.361 (-0.340) | 0.026 (0.021) | -0.118 (-0.076) 0.029 (-0.005) | | |
| Glu11 | 2.16 (1.78) | -0.083 (-0.080) | | -0.078 (-0.056) -0.190 (-0.279) | -0.136 (-0.075) -0.232 (-0.178) | |
| Val12 | 3.29 (2.94) | 0.111 (0.109) | -0.038 (-0.066) | -0.112 (-0.113) | 0.027 (0.012) 0.003 | |
| His13 | 1.84 (1.62) | 0.428 (0.287) | 0.033 (0.024) | | | |
| His14 | 1.35 | 0.253 | 0.075 (0.067) | | | |
| Gln15 | 2.42 | 0.181 (0.084) | -0.020 (-0.033) | -0.071 (-0.072) -0.078 (-0.083) | -0.019 (-0.025) | |
| Lys16 | 2.68 (2.44) | 0.220 (0.153) | -0.095 (-0.079) | -0.039 (-0.037) 0.023 (0.002) | 0.039 (0.023) 0.128 (0.090) | 0.030 (0.024) 0.084 (0.057) |
| Leu17 | 2.81 (2.42) | 0.364 (0.315) | -0.041 (-0.056) | 0.112 (0.119) 0.227 (0.206) | 0.075 (0.069) | 0.092 (0.075) 0.085 (0.068) |
| Val18 | 3.56 (3.23) | 0.519 (0.445) | -0.051 (-0.082) | 0.007 (-0.001) | 0.118 (0.098) 0.102 (0.093) | |
| Phe19 | 1.31 (1.43) | 0.258 (0.247) | -0.078 (-0.157) | 0.017 (-0.027) 0.200 (0.104) | | |
| Phe20 | 1.82 (1.71) | 0.056 (-0.076) | -0.198 (-0.200) | -0.213 (-0.205) -0.044 | | |
| Ala21 | 1.59 (1.45) | -0.091 (-0.072) | -0.119 (-0.133) | -0.067 (-0.050) | | |
| Glu22 | 1.35 (1.22) | -0.050 (-0.070) | | 0.040 (0.044) -0.062 (-0.041) | 0.036 (0.028) | |
| Asp23 | 0.24 (0.35) | 0.092 (0.058) | -0.090 (-0.120) | -0.065 (-0.088) -0.113 (-0.092) | | |
| Val24 | -0.08 (0.18) | 0.082 (0.070) | 0.146 (0.106) | -0.067 (-0.080) | -0.042 (-0.034) -0.008 (-0.012) | |
| Gly25 | -0.35 (-0.17) | -0.230 (-0.188) | -0.012 (-0.015) -0.007 (-0.015) | | | |
| Ser26 | -0.15 (-0.21) | 0.078 (0.014) | 0.035 (-0.003) | -0.050 (-0.067) (-0.061) | | |

(to be continued)

(continuation)

| | B_1^* ($^{15}\text{N}^{\text{H}}$) ± 0.05 [ppm GPa $^{-1}$] | B_1^* ($^1\text{H}^{\text{N}}$) ± 0.007 [ppm GPa $^{-1}$] | B_1^* ($^1\text{H}^{\text{a}}$) ± 0.004 [ppm GPa $^{-1}$] | B_1^* ($^1\text{H}^{\text{b}}$) ± 0.007 [ppm GPa $^{-1}$] | B_1^* ($^1\text{H}^{\text{v}}$) ± 0.004 [ppm GPa $^{-1}$] | B_1^* (other) ± 0.003 [ppm GPa $^{-1}$] |
|-------|--|--|--|--|--|--|
| Asn27 | -0.19 (-1.09) | 0.116 (0.240) | -0.050 (-0.067) | -0.080 (-0.068) -0.099 (-0.113) | | |
| Lys28 | -0.40 (-0.42) | -0.027 (0.012) | 0.117 (0.108) | -0.031 (-0.006) -0.031 (-0.067) | 0.028 (0.027) 0.091 (0.061) | 0.029 (0.024) 0.028 (0.005) |
| Gly29 | 0.23 (0.37) | -0.054 (-0.037) | | | | |
| Ala30 | 0.72 (0.81) | 0.139 (0.177) | -0.050 (-0.103) | | | |
| Ile31 | 1.38 (1.75) | 0.182 (0.203) | -0.058 (-0.086) | -0.041 (-0.040) | 0.001 (0.006) 0.076 (0.088) 0.027 (0.026) 0.001 (0.006) | |
| Ile32 | 1.25 (1.85) | 0.179 (0.203) | 0.022 (0.024) | -0.041 (-0.040) | 0.076 (0.088) 0.034 (0.037) | |
| Gly33 | 0.42 (0.89) | 0.173 (0.199) | | | | |
| Leu34 | 0.57 (0.65) | 0.033 (0.034) | -0.041 (-0.056) | 0.102 (0.065) | 0.024 (0.069) | 0.017 (0.010) 0.025 (0.009) |
| Met35 | 1.19 (1.35) | 0.191 (0.203) | -0.044 (-0.059) | -0.069 (-0.095) -0.022 (-0.065) | 0.022 (0.028) -0.005 (-0.008) | 0.003 (0.003) |
| Val36 | 0.22 (0.75) | 0.100 (0.132) | | | 0.000 (-0.001) | |
| Gly37 | -0.91 (-0.56) | -0.052 (0.022) | (0.011) | | | |
| Gly38 | 0.35 (0.38) | 0.024 (0.083) | 0.046 (-0.059) 0.057 (-0.047) | | | |
| Val39 | -0.31 (0.00) | -0.090 (-0.026) | 0.016 (0.014) | | 0.025 (0.019) | |
| Val40 | 0.16 (0.47) | 0.512 (0.491) | -0.213 (-0.198) | -0.077 (-0.085) | 0.051 (0.037) 0.099 (0.073) | |

^a Sample buffer was 50 mM Tris-d₁₁, pH 7.0, 100 mM NaCl, 0.5 mM EDTA-d₁₆, 1 mM sodium azide in 8% D₂O.

^b Peaks were unassignable due to exchange with solvent.

Source: By the author.

Appendix D – ^{13}C random coil-corrected first order pressure coefficients (B_1^*) in A β (1-40).^a Values at 277 and 288 K (latter inside parentheses) are presented.

| | B_1^* ($^{13}\text{C}^\alpha$) ± 0.03 [ppm GPa $^{-1}$] | B_1^* ($^{13}\text{C}^\beta$) ± 0.02 [ppm GPa $^{-1}$] | B_1^* ($^{13}\text{C}'$) ± 0.02 [ppm GPa $^{-1}$] | B_1^* ($^{13}\text{C}^\gamma$) ± 0.01 [ppm GPa $^{-1}$] | B_1^* ($^{13}\text{C}^\delta$) ± 0.01 [ppm GPa $^{-1}$] | B_1^* (other) ± 0.01 [ppm GPa $^{-1}$] |
|-------|--|---|--|--|--|---|
| Asp1 | -0.68 (-0.64) | 0.08 (0.26) | | | | |
| Ala2 | -0.09 (-0.17) | -0.20 (-0.28) | 0.25 (0.32) | | | |
| Glu3 | 0.70 (0.62) | (-0.54) | 0.41 (0.41) | -0.38 (-0.27) | | |
| Phe4 | 0.05 (0.12) | -0.11 (-0.12) | 0.03 (-0.05) | | | |
| Arg5 | 0.17 (0.13) | -0.85 (-0.89) | -0.31 | -0.10 (-0.13) | 0.10 (0.04) | |
| His6 | -0.25 (-0.26) | | -0.13 (-0.38) | | | |
| Asp7 | -0.09 (-0.04) | 0.13 (0.13) | -0.01 | | | |
| Ser8 | -0.42 (-0.36) | 0.07 (0.22) | -0.25 (-0.34) | | | |
| Gly9 | -0.39 (-0.33) | | -0.77 (-0.78) | | | |
| Tyr10 | -0.91 (-0.91) | 0.26 (0.19) | -0.60 (-0.60) | | | |
| Glu11 | | -0.37 (-0.47) | -0.91 (-0.77) | -0.44 (-0.35) | | |
| Val12 | -0.96 (-0.83) | 0.28 (0.17) | -0.78 (-0.53) | -0.29 (-0.24) | -0.19 (-0.19) | |
| His13 | -0.87 (-0.81) | | | | | |
| His14 | -0.96 (-0.83) | | -0.56 (-0.61) | | | |
| Gln15 | -0.84 (-1.09) | 0.20 (0.02) | | -0.43 (-0.39) | | |
| Lys16 | -0.08 (-0.02) | -0.21 (-0.23) | 0.19 (0.12) | -0.17 (-0.18) | 0.05 (0.04) | -0.02 (-0.05) |
| Leu17 | 0.24 (0.11) | | 0.10 (0.19) | 0.20 (0.21) | -0.58 (-0.50) | 0.12 (0.02) |
| Val18 | 0.09 (0.12) | -0.26 (-0.33) | 0.16 (0.15) | -0.04 -0.10 | | |
| Phe19 | 0.23 (0.32) | -0.27 (-0.31) | -0.41 (-0.35) | | | |
| Phe20 | 0.15 (0.03) | -0.04 (0.04) | -1.17 (-1.03) | | | |
| Ala21 | -0.79 (-0.77) | -0.43 (-0.46) | -1.13 (-0.92) | | | |
| Glu22 | | -0.28 (-0.30) | -0.17 (-0.10) | -0.39 (-0.36) | | |
| Asp23 | 0.04 (-0.07) | -0.81 (-0.79) | -0.39 (-0.38) | | | |
| Val24 | -0.86 (-0.63) | 0.38 (0.31) | -0.57 (-0.47) | -0.34 (-0.37) | -0.09 (-0.17) | |
| Gly25 | -0.30 (-0.33) | | -0.70 (-0.97) | | | |
| Ser26 | -0.45 (-0.46) | 0.07 (0.04) | 0.11 | | | |

(to be continued)

(continuation)

| | B_1^* ($^{13}\text{C}^\alpha$) ± 0.03 [ppm GPa $^{-1}$] | B_1^* ($^{13}\text{C}^\beta$) ± 0.02 [ppm GPa $^{-1}$] | B_1^* ($^{13}\text{C}^\gamma$) ± 0.02 [ppm GPa $^{-1}$] | B_1^* ($^{13}\text{C}^\delta$) ± 0.01 [ppm GPa $^{-1}$] | B_1^* ($^{13}\text{C}^\epsilon$) ± 0.01 [ppm GPa $^{-1}$] | B_1^* (other) ± 0.01 [ppm GPa $^{-1}$] |
|-------|--|---|--|--|--|---|
| Asn27 | 0.20 (0.13) | 0.10 (0.01) | -0.29 (-0.17) | | | |
| Lys28 | -0.43 (-0.78) | 0.34 (0.20) | -0.14 (-0.33) | -0.09 (-0.09) | 0.05 (0.04) | -0.01 (-0.04) |
| Gly29 | -0.32 (-0.40) | | -0.31 (-0.40) | | | |
| Ala30 | | -0.15 (-0.48) | 0.26 (0.27) | | | |
| Ile31 | -0.16 (-0.27) | -0.21 (-0.23) | -0.02 (-0.03) | 0.13 (0.15) -0.19 (-0.22) | -0.30 (-0.32) | |
| Ile32 | -0.25 (-0.33) | -0.21 (-0.23) | -0.18 (-0.24) | 0.13 (0.15) -0.09 (-0.14) | -0.30 (-0.32) | |
| Gly33 | -0.32 (-0.40) | | -0.23 (-0.40) | | | |
| Leu34 | 0.24 (0.11) | | -0.03 (-0.13) | 0.14 (0.09) | -0.58 (-0.45) -0.11 (-0.14) | |
| Met35 | 0.16 (0.01) | -0.56 (-0.56) | -0.08 (-0.02) | 0.13 (0.10) | | -0.05 (-0.14) |
| Val36 | | 0.23 (0.15) | -0.07 (-0.03) | -0.38 (-0.29) | | |
| Gly37 | -0.03 (0.07) | | 0.04 (0.09) | | | |
| Gly38 | 0.06 (0.01) | | 0.04 (0.07) | | | |
| Val39 | -0.48 (-0.64) | 0.23 (0.15) | 0.50 (0.62) | -0.18 (-0.15) | | |
| Val40 | 1.28 | -1.33 (-1.27) | | -0.24 (-0.26) 0.63 (0.50) | | |

^a Sample buffer was 50 mM Tris-d₁₁, pH 7.0, 100 mM NaCl, 0.5 mM EDTA-d₁₆, 1 mM sodium azide in 8% D₂O.

^b Peaks were unassignable due to exchange with solvent.

Source: By the author.

Appendix E – ^1H and ^{15}N random coil-corrected second order pressure coefficients (B_2^*) in A β (1-40).^a Values at 277 and 288 K (latter inside parentheses) are presented.

| | B_2^* ($^{15}\text{N}^{\text{H}}$) ± 0.2 [ppm GPa $^{-2}$] | B_2^* ($^1\text{H}^{\text{N}}$) ± 0.04 [ppm GPa $^{-2}$] | B_2^* ($^1\text{H}^{\alpha}$) ± 0.02 [ppm GPa $^{-2}$] | B_2^* ($^1\text{H}^{\beta}$) ± 0.04 [ppm GPa $^{-2}$] | B_2^* ($^1\text{H}^{\gamma}$) ± 0.02 [ppm GPa $^{-2}$] | B_2^* (other) ± 0.02 [ppm GPa $^{-2}$] |
|-------|---|---|---|--|---|---|
| Asp1 | - ^b | - ^b | -0.38 (-0.22) | 0.02 (0.07) 0.13 (0.05) | | |
| Ala2 | - ^b | - ^b | -0.21 (-0.25) | -0.02 (0.02) | | |
| Glu3 | -2.3 (-1.4) | -0.06 (-0.02) | 0.28 (0.38) | | 0.02 (0.06) -0.17 (-0.15) | |
| Phe4 | -2.3 (-1.5) | -0.10 (0.03) | 0.00 (0.09) | -0.19 (-0.10) | | |
| Arg5 | -3.9 (-2.8) | -0.51 (-0.36) | -0.19 (-0.06) | -0.05 (0.10) -0.08 (0.07) | 0.02 (0.06) | -0.22 (-0.12) |
| His6 | -1.3 | -0.06 | 0.13 (0.05) | | | |
| Asp7 | -1.2 (-1.5) | 0.10 (0.26) | -0.01 (-0.06) | 0.03 (0.07) | | |
| Ser8 | -1.8 (-1.1) | 0.22 (0.32) | -0.02 (0.04) | 0.15 (0.18) 0.06 (0.11) | | |
| Gly9 | 0.6 (0.7) | 0.37 (0.37) | 0.17 (0.23) -0.07 (-0.07) | | | |
| Tyr10 | 3.1 (3.3) | 0.66 (0.66) | -0.44 (-0.35) | 0.06 (-0.21) -0.06 (0.21) | | |
| Glu11 | -5.8 (-4.4) | 0.61 (0.52) | | 0.00 (0.14) 0.23 (0.52) | 0.08 (-0.01) 0.63 (0.47) | |
| Val12 | -8.0 (-6.2) | -0.48 (-0.41) | -0.01 (0.15) | 0.26 (0.29) | -0.23 (-0.10) -0.02 | |
| His13 | -7.2 (-5.4) | -1.05 (-0.47) | -0.36 (-0.32) | | | |
| His14 | -4.9 | -1.01 | -0.59 (-0.54) | | | |
| Gln15 | -9.1 | -0.68 (-0.14) | -0.07 (-0.03) | 0.18 (0.20) 0.18 (0.17) | -0.12 (-0.06) | |
| Lys16 | -9.6 (-7.7) | -0.77 (-0.43) | 0.01 (-0.04) | 0.07 (0.08) -0.04 (0.02) | -0.26 (-0.15) -0.35 (-0.13) | -0.20 (-0.15) -0.38 (-0.21) |
| Leu17 | -8.7 (-6.3) | -0.90 (-0.58) | 0.00 (0.06) | -0.48 (-0.54) -0.61 (-0.48) | -0.71 (-0.61) | -0.37 (-0.25) -0.29 (-0.18) |
| Val18 | -9.6 (-7.3) | -1.15 (-0.84) | 0.11 (0.24) | 0.10 (0.10) | -0.40 (-0.26) -0.27 (-0.21) | |
| Phe19 | -6.8 (-5.4) | -0.45 (-0.31) | -0.04 (0.18) | -0.61 (-0.19) -0.53 (0.00) | | |
| Phe20 | -6.2 (-4.4) | 0.28 (0.39) | 0.26 (0.22) | 0.32 (0.30) 0.04 | | |
| Ala21 | -5.8 (-4.5) | 0.03 (-0.02) | 0.05 (0.11) | 0.12 (0.06) | | |
| Glu22 | -5.4 (-4.0) | 0.05 (0.10) | | -0.02 (-0.03) 0.10 (-0.01) | 0.10 (0.14) | |
| Asp23 | -4.0 (-2.9) | -0.49 (-0.29) | 0.01 (0.16) | 0.00 (0.11) 0.11 (0.06) | | |
| Val24 | -3.0 (-2.4) | -0.67 (-0.47) | -0.26 (-0.10) | 0.03 (0.10) | -0.07 (-0.06) -0.10 (-0.06) | |
| Gly25 | -1.3 (-1.2) | 0.16 (0.15) | -0.02 (-0.01) -0.04 (-0.01) | | | |
| Ser26 | 1.0 (1.2) | 0.11 (0.31) | -0.19 (-0.02) | 0.15 (0.18) 0.06 (0.11) | | |

(to be continued)

(continuation)

| | B_2^* ($^{15}\text{N}^{\text{H}}$) ± 0.2 [ppm GPa $^{-2}$] | B_2^* ($^1\text{H}^{\text{N}}$) ± 0.04 [ppm GPa $^{-2}$] | B_2^* ($^1\text{H}^{\text{a}}$) ± 0.02 [ppm GPa $^{-2}$] | B_2^* ($^1\text{H}^{\text{b}}$) ± 0.04 [ppm GPa $^{-2}$] | B_2^* ($^1\text{H}^{\text{c}}$) ± 0.02 [ppm GPa $^{-2}$] | B_2^* (other) ± 0.02 [ppm GPa $^{-2}$] |
|-------|---|---|---|---|---|---|
| Asn27 | -1.7 (3.5) | -0.22 (-1.57) | -0.04 (0.04) | 0.14 (0.08) 0.13 (0.19) | | |
| Lys28 | -3.1 (-1.5) | -0.10 (-0.24) | -0.29 (-0.21) | -0.11 (-0.13) -0.13 (0.07) | -0.22 (-0.21) -0.43 (-0.27) | -0.16 (-0.15) -0.24 (-0.10) |
| Gly29 | -1.8 (-1.1) | 0.04 (-0.01) | | | | |
| Ala30 | -1.4 (-1.3) | -0.41 (-0.48) | -0.05 (0.13) | | | |
| Ile31 | -5.0 (-4.8) | -0.56 (-0.45) | -0.04 (0.12) | -0.02 (-0.01) | 0.10 (0.10) -0.23 (-0.30) 0.00 (-0.02) | |
| Ile32 | -7.7 (-7.3) | -0.53 (-0.41) | -0.11 (-0.11) | -0.02 (-0.01) | 0.10 (0.10) -0.23 (-0.30) -0.15 (-0.15) | |
| Gly33 | -5.0 (-4.8) | -0.52 (-0.48) | | | | |
| Leu34 | -0.4 (0.4) | -0.21 (0.30) | 0.00 (0.06) | -0.88 (-0.51) | -0.62 (-0.61) | -0.18 (-0.13) -0.22 (-0.11) |
| Met35 | -4.9 (-4.4) | -0.53 (-0.44) | -0.12 (-0.02) | 0.13 (0.26) -0.04 (0.15) | -0.13 (-0.12) -0.02 (0.01) | -0.16 (-0.13) |
| Val36 | -4.7 (-4.5) | -0.67 (-0.58) | | | -0.14 (-0.15) | |
| Gly37 | -1.3 (-1.4) | -0.18 (-0.26) | (-0.11) | | | |
| Gly38 | -0.8 (-0.5) | -0.14 (-0.22) | (0.00) -0.07 (0.04) | | | |
| Val39 | -1.0 (1.0) | -0.31 (-0.37) | 0.02 (0.02) | | -0.21 (-0.14) | |
| Val40 | -2.2 (-2.1) | -0.62 (-0.53) | 0.20 (0.13) | 0.17 (0.22) | -0.17 (-0.10) -0.20 (-0.09) | |

^a Sample buffer was 50 mM Tris-d₁₁, pH 7.0, 100 mM NaCl, 0.5 mM EDTA-d₁₆, 1 mM sodium azide in 8% D₂O.

^b Peaks were unassignable due to exchange with solvent.

Source: By the author.

Appendix F – ^{13}C random coil-corrected second order pressure coefficients (B_2^*) in A β (1-40).^a Values at 277 and 288 K (latter inside parentheses) are presented.

| | B_2^* ($^{13}\text{C}^\alpha$) ± 0.1 [ppm GPa $^{-2}$] | B_2^* ($^{13}\text{C}^\beta$) ± 0.1 [ppm GPa $^{-2}$] | B_2^* ($^{13}\text{C}^\gamma$) ± 0.1 [ppm GPa $^{-2}$] | B_2^* ($^{13}\text{C}^\delta$) ± 0.1 [ppm GPa $^{-2}$] | B_2^* ($^{13}\text{C}^\epsilon$) ± 0.1 [ppm GPa $^{-2}$] | B_2^* (other) ± 0.1 [ppm GPa $^{-2}$] |
|-------|---|--|---|---|---|--|
| Asp1 | 0.8 (0.9) | 1.4 (1.5) | | | | |
| Ala2 | 0.2 (0.2) | 1.9 (2.2) | 0.3 (0.3) | | | |
| Glu3 | -1.6 (-1.5) | (0.4) | 0.2 (0.1) | 0.0 (-0.1) | | |
| Phe4 | -0.1 (-0.9) | 0.4 (0.3) | 0.7 (1.1) | | | |
| Arg5 | -0.2 (-0.1) | 1.5 (1.9) | 0.6 | 0.4 (0.6) | 0.3 (0.6) | |
| His6 | 0.6 (1.1) | | 2.0 (5.5) | | | |
| Asp7 | 0.7 (0.4) | 0.1 (0.0) | 1.0 | | | |
| Ser8 | 1.3 (1.0) | 0.3 (-1.0) | 0.7 (1.3) | | | |
| Gly9 | 1.2 (0.6) | | 2.0 (2.1) | | | |
| Tyr10 | 3.7 (3.4) | -0.4 (-0.4) | 2.6 (2.5) | | | |
| Glu11 | | -0.2 (0.4) | 3.8 (2.9) | 0.9 (0.7) | | |
| Val12 | 3.2 (2.9) | -1.2 (-0.7) | 3.6 (2.7) | 2.5 (2.5) -1.2 (-1.1) | | |
| His13 | 3.6 (3.4) | | | | | |
| His14 | 3.5 (2.6) | | 3.1 (3.3) | | | |
| Gln15 | 2.6 (3.3) | -1.0 (-0.2) | | 1.7 (1.5) | | |
| Lys16 | 1.0 (0.8) | 0.3 (0.4) | 0.1 (0.9) | 0.7 (0.7) | 0.0 (0.0) | -0.3 (-0.1) |
| Leu17 | -0.4 (0.0) | | 2.0 (1.6) | -1.1 (-1.2) | 3.8 (3.5) 3.6 (3.8) | |
| Val18 | 0.5 (0.5) | 0.4 (0.5) | 0.8 (1.0) | 1.8 (2.0) -1.0 (-0.9) | | |
| Phe19 | 1.2 (0.7) | 0.2 (0.3) | 2.9 (2.6) | | | |
| Phe20 | 0.5 (1.4) | 0.0 (-0.2) | 3.9 (3.3) | | | |
| Ala21 | 3.3 (2.6) | 0.9 (0.6) | 3.9 (2.8) | | | |
| Glu22 | | 0.5 (0.6) | 0.9 (0.6) | 0.3 (0.4) | | |
| Asp23 | 0.6 (0.8) | 1.9 (2.1) | 0.8 (1.1) | | | |
| Val24 | 0.7 (0.2) | -0.2 (-0.1) | 1.6 (1.2) | 2.5 (2.9) -0.9 (-0.6) | | |
| Gly25 | 0.9 (0.7) | | 2.2 (3.7) | | | |
| Ser26 | 1.5 (1.6) | 0.2 (0.0) | 1.1 | | | |

(to be continued)

(continuation)

| | B_2^* ($^{13}\text{C}^\alpha$) ± 0.1 [ppm GPa $^{-2}$] | B_2^* ($^{13}\text{C}^\beta$) ± 0.1 [ppm GPa $^{-2}$] | B_2^* ($^{13}\text{C}^\gamma$) ± 0.1 [ppm GPa $^{-2}$] | B_2^* ($^{13}\text{C}^\delta$) ± 0.1 [ppm GPa $^{-2}$] | B_2^* ($^{13}\text{C}^\epsilon$) ± 0.1 [ppm GPa $^{-2}$] | B_2^* (other) ± 0.1 [ppm GPa $^{-2}$] |
|-------|---|--|---|---|---|--|
| Asn27 | 0.1 (0.3) | 0.8 (1.1) | 0.3 (0.3) | | | |
| Lys28 | 0.9 (2.4) | -0.8 (-0.3) | 0.7 (1.6) | 0.5 (0.4) | 0.0 (0.0) | -0.4 (-0.1) |
| Gly29 | 1.6 (1.8) | | 1.6 (1.9) | | | |
| Ala30 | | 2.6 (4.2) | 0.2 (0.1) | | | |
| Ile31 | 1.2 (1.2) | 0.7 (0.6) | 0.7 (0.9) | 0.7 (0.5) 1.6 (1.6) | 2.8 (2.4) | |
| Ile32 | 1.3 (1.3) | 0.7 (0.6) | 2.1 (2.0) | 0.7 (0.5) 1.1 (1.4) | 2.8 (2.4) | |
| Gly33 | 1.6 (1.8) | | 1.7 (1.9) | | | |
| Leu34 | -0.4 (0.0) | | 0.4 (1.0) | -1.1 (-0.8) | 3.7 (3.3) 4.0 (4.0) | |
| Met35 | 0.6 (1.0) | 1.4 (1.5) | 0.8 (0.7) | 0.1 (0.0) | | 1.4 (1.7) |
| Val36 | | -0.1 (-0.1) | 0.9 (0.6) | 2.1 (2.2) | | |
| Gly37 | 1.5 (0.6) | | 0.9 (0.3) | | | |
| Gly38 | 0.1 (0.3) | | 0.2 (0.1) | | | |
| Val39 | -0.6 (0.2) | -0.1 (-0.1) | -0.4 (-0.5) | 1.6 (1.8) | | |
| Val40 | -2.0 | 1.4 (1.0) | | -0.6 (-0.5) 1.4 (1.7) | | |

^a Sample buffer was 50 mM Tris-d₁₁, pH 7.0, 100 mM NaCl, 0.5 mM EDTA-d₁₆, 1 mM sodium azide in 8% D₂O.

^b Peaks were unassignable due to exchange with solvent.

Source: By the author.

Appendix G – ¹H chemical shifts of SEPT1CC at 298 K.^a

| Residue | δ (¹ H ^N) [ppm] | δ (¹ H ^{α}) [ppm] | δ (¹ H ^{β}) [ppm] | δ (side chain) [ppm] |
|---------------|---|---|--|---|
| N-term acetyl | | | | H _{Ac} 2.071 |
| Asp1 | 8.371 | 4.660 | 2.803/2.720 | |
| Thr2 | 8.253 | 4.247 | 4.065 | H ^{γ2} 1.262 |
| Glu3 | 8.404 | 4.094 | 2.103 | H ^{γ2,3} 2.417 |
| Lys4 | 7.921 | 4.007 | 1.874/1.696 | H ^{γ2,3} 1.503/1.375, H ^{δ2,3} 1.503, H ^{ϵ2,3} 3.003 |
| Leu5 | 7.858 | 4.180 | 1.826/1.669 | H ^{γ} 1.601, H ^{δ1,2} 0.942/0.905 |
| Ile6 | 8.071 | 3.608 | 1.943 | H ^{γ12,13} 1.684/1.081, H ^{γ2} 0.905, H ^{δ1} 0.831 |
| Arg7 | 8.008 | 4.182 | 1.952 | H ^{γ2,3} 1.824/1.676, H ^{δ2,3} 3.247, H ^{ϵ} 7.362 |
| Glu8 | 8.211 | 4.113 | 2.239/2.164 | H ^{γ2,3} 2.417 |
| Lys9 | 8.252 | 4.140 | 2.012/1.777 | H ^{γ2,3} 1.588/1.512, H ^{δ2,3} 1.682, H ^{ϵ2,3} 2.980/2.891 |
| Asp10 | 8.586 | 4.571 | 2.919/2.734 | |
| Glu11 | 8.227 | 4.149 | 2.245/2.148 | H ^{γ2,3} 2.482/2.322 |
| Glu12 | 8.115 | 4.244 | 2.246/2.152 | H ^{γ2,3} 2.590/2.318 |
| Leu13 | 8.446 | 4.040 | 1.960/1.643 | H ^{γ} 1.737, H ^{δ1,2} 0.974/0.938 |
| Arg14 | 8.031 | 4.095 | 1.770/1.638 | H ^{γ2,3} 1.962, H ^{δ2,3} 3.238, H ^{ϵ} 7.462 |
| Arg 15 | 8.128 | 4.101 | 1.845/1.650 | H ^{γ2,3} 1.997/1.943, H ^{δ2,3} 3.248, H ^{ϵ} 7.496 |
| Met16 | 8.282 | 4.267 | 2.331/2.096 | H ^{γ2,3} 2.769/2.571, H ^{ϵ} 2.102 |
| Gln17 | 8.518 | 3.997 | 2.289/2.172 | H ^{γ2,3} 2.465/2.404, H ^{ϵ21,22} 7.420/6.799 |
| Glu18 | 8.120 | 4.096 | 2.244 | H ^{γ2,3} 2.590/2.401 |
| Met19 | 7.992 | 4.191 | 2.335/2.204 | H ^{γ2,3} 2.755/2.631, H ^{ϵ} 2.124 |
| Leu20 | 8.448 | 4.047 | 1.821 | H ^{γ} 1.735, H ^{δ1,2} 0.937 |
| Glu21 | 8.227 | 4.085 | 2.233/2.145 | H ^{γ2,3} 2.623/2.460 |
| Lys22 | 8.004 | 4.132 | 1.977 | H ^{γ2,3} 1.636/1.465, H ^{δ2,3} 1.710, H ^{ϵ2,3} 2.991 |
| Met23 | 8.159 | 4.230 | 2.239/2.142 | H ^{γ2,3} 2.738/2.586, H ^{ϵ} 2.092 |
| Gln24 | 8.448 | 4.030 | 2.205/2.099 | H ^{γ2,3} 2.495/2.380, H ^{ϵ21,22} 7.317/6.799 |
| Ala25 | 7.892 | 4.223 | 1.522 | |
| Gln26 | 7.902 | 4.175 | 2.207 | H ^{γ2,3} 2.520/2.421, H ^{ϵ21,22} 7.420/6.828 |
| Met27 | 8.046 | 4.328 | 2.196/2.145 | H ^{γ2,3} 2.722/2.603, H ^{ϵ} 2.099 |
| Gln28 | 8.011 | 4.259 | 2.190/2.117 | H ^{γ2,3} 2.482/2.445, H ^{ϵ21,22} 7.489/6.852 |
| Gln29 | 8.100 | 4.335 | 2.198/2.076 | H ^{γ2,3} 2.465/2.404, H ^{ϵ21,22} 7.517/6.854 |
| Ser30 | 8.150 | 4.415 | 3.924 | |
| C-term amide | 7.491/7.194 | | | |

^a Acetylated N-terminal, amidated C-terminal peptide. Buffer used was 50 mM potassium phosphate buffer pH 5.0, 300 mM NaCl, 1 mM NaN₃, 50 μ M DSS, 5% D₂O. Peptide concentration, 0.5 mM.

Source: By the author.

Appendix H – ^1H chemical shifts of SEPT2CC at 298 K.^a

| Residue | δ ($^1\text{H}^{\text{N}}$) [ppm] | δ ($^1\text{H}^{\text{a}}$) [ppm] | δ ($^1\text{H}^{\text{b}}$) [ppm] | δ (side chain) [ppm] |
|---------------|---|---|---|---|
| N-term acetyl | | | | H _{Ac} 2.040 |
| Asn1 | 8.386 | 4.689 | 2.860 | H $^{\delta 21,22}$ 7.653/6.998 |
| Lys2 | 8.553 | 4.160 | 1.848/1.692 | H $^{\gamma 2,3}$ 1.439, H $^{\delta 2,3}$ 1.534, H $^{\epsilon 2,3}$ 3.017 |
| Asp3 | 8.308 | 4.525 | 2.775 | |
| Gln4 | 8.167 | 4.072 | 2.142 | H $^{\gamma 2,3}$ 2.452/2.419, H $^{\epsilon 21,22}$ 7.555/6.855 |
| Ile5 | 8.081 | 3.881 | 1.826/1.669 | H $^{\gamma 12,13}$ 1.606/1.243, H $^{\gamma 2}$ 0.939, H $^{\delta 1}$ 0.850 |
| Leu6 | 7.887 | 4.071 | 1.867/1.776 | H $^{\gamma}$ 1.631, H $^{\delta 1,2}$ 0.962/0.926 |
| Leu7 | 8.097 | 4.186 | 1.945 | H $^{\gamma}$ 1.575, H $^{\delta 1,2}$ 0.933/0.903 |
| Glu8 | 8.099 | 4.188 | 2.261/2.210 | H $^{\gamma 2,3}$ 2.574/2.261 |
| Lys9 | 8.358 | 4.139 | 1.812/1.710 | H $^{\gamma 2,3}$ 1.586, H $^{\delta 2,3}$ 1.617, H $^{\epsilon 2,3}$ 2.966/2.907 |
| Glu10 | 7.987 | 4.140 | 2.164/2.096 | H $^{\gamma 2,3}$ 2.365/2.330 |
| Ala11 | 8.095 | 4.071 | 1.577 | |
| Glu12 | 8.552 | 4.040 | 2.245/2.090 | H $^{\gamma 2,3}$ 2.656/2.422 |
| Leu13 | 8.255 | 4.078 | 1.849/1.743 | H $^{\gamma}$ 1.649, H $^{\delta 1,2}$ 0.935 |
| Arg14 | 7.988 | 4.146 | 2.020/1.965 | H $^{\gamma 2,3}$ 1.840/1.651, H $^{\delta 2,3}$ 3.272, H $^{\epsilon}$ 7.421 |
| Arg15 | 7.986 | 4.140 | 1.982/1.945 | H $^{\gamma 2,3}$ 1.819/1.621, H $^{\delta 2,3}$ 3.260, H $^{\epsilon}$ 7.316 |
| Met16 | 8.255 | 4.241 | 2.361 | H $^{\gamma 2,3}$ 2.786/2.556, H $^{\epsilon}$ 2.109 |
| Gln17 | 8.536 | 4.037 | 2.131/2.092 | H $^{\gamma 2,3}$ 2.579/2.428, H $^{\epsilon 21,22}$ 7.326/6.792 |
| Glu18 | 8.142 | 4.131 | 2.271/2.122 | H $^{\gamma 2,3}$ 2.587/2.413 |
| Met19 | 8.090 | 4.150 | 2.338/2.226 | H $^{\gamma 2,3}$ 2.763/2.601, H $^{\epsilon}$ 2.119 |
| Ile20 | 8.430 | 3.660 | 1.939 | H $^{\gamma 12,13}$ 1.788/1.055, H $^{\gamma 2}$ 0.925, H $^{\delta 1}$ 0.867 |
| Ala21 | 8.040 | 4.262 | 1.528 | |
| Arg22 | 8.040 | 4.151 | 2.014/1.981 | H $^{\gamma 2,3}$ 1.848/1.660, H $^{\delta 2,3}$ 3.245, H $^{\epsilon}$ 7.348 |
| Met23 | 8.178 | 4.168 | 2.284/2.143 | H $^{\gamma 2,3}$ 2.805/2.551, H $^{\epsilon}$ 2.087 |
| Gln24 | 8.720 | 4.017 | 2.255/2.080 | H $^{\gamma 2,3}$ 2.544/2.368, H $^{\epsilon 21,22}$ 7.328/6.803 |
| Ala25 | 7.850 | 4.202 | 1.539 | |
| Gln26 | 7.934 | 4.203 | 2.223/2.173 | H $^{\gamma 2,3}$ 2.548/2.429, H $^{\epsilon 21,22}$ 7.465/6.830 |
| Met27 | 8.033 | 4.270 | 2.176 | H $^{\gamma 2,3}$ 2.722/2.601, H $^{\epsilon}$ 2.083 |
| Gln28 | 8.034 | 4.153 | 2.172/2.071 | H $^{\gamma 2,3}$ 2.551/2.431, H $^{\epsilon 21,22}$ 7.439/6.824 |
| Met29 | 7.911 | 4.406 | 2.178/2.118 | H $^{\gamma 2,3}$ 2.691/2.614, H $^{\epsilon}$ 2.118 |
| Gln30 | 8.088 | 4.268 | 2.171/2.058 | H $^{\gamma 2,3}$ 2.434, H $^{\epsilon 21,22}$ 7.504/6.840 |
| C-term amide | 7.439/7.159 | | | |

^a Acetylated N-terminal, amidated C-terminal peptide. Buffer used was 50 mM potassium phosphate buffer pH 5.0, 300 mM NaCl, 1 mM NaN₃, 50 μM DSS, 5% D₂O. Peptide concentration, 1.0 mM.

Source: By the author.

Appendix I – ¹H chemical shifts of SEPT4CC at 298 K.^a

| Residue | δ (¹ H ^N) [ppm] | δ (¹ H ^{α}) [ppm] | δ (¹ H ^{β}) [ppm] | δ (side chain) [ppm] |
|---------------|---|---|--|---|
| N-term acetyl | | | | H _{Ac} 2.111 |
| Glu1 | 8.559 | 4.207 | 2.106/2.017 | H ^{γ2,3} 2.320 |
| Thr2 | 8.298 | 4.025 | 4.183 | H ^{γ2} 1.239 |
| Gln3 | 8.467 | 4.012 | 2.043 | H ^{γ2,3} 2.317 |
| Lys4 | 7.866 | 4.001 | 1.883 | H ^{γ2,3} 1.493/1.356, H ^{δ2,3} 1.683, H ^{ϵ2,3} 2.971 |
| Leu5 | 7.901 | 4.183 | 1.835/1.681 | H ^{γ} 1.612, H ^{δ1,2} 0.949/0.907 |
| Ile6 | 8.071 | 3.583 | 1.930 | H ^{γ12,13} 1.682/1.068, H ^{γ2} 0.900, H ^{δ1} 0.817 |
| Arg7 | 7.984 | 4.203 | 1.949/1.806 | H ^{γ2,3} 1.671, H ^{δ2,3} 3.239, H ^{ϵ} 7.454 |
| Glu8 | 8.276 | 4.095 | 2.124/2.100 | H ^{γ2,3} 2.529/2.322 |
| Lys9 | 8.196 | 4.194 | 2.008/1.779 | H ^{γ2,3} 1.597, H ^{δ2,3} 1.681, H ^{ϵ2,3} 2.936/2.876 |
| Asp10 | 8.567 | 4.585 | 2.833/2.654 | |
| Glu11 | 8.215 | 4.157 | 2.195 | H ^{γ2,3} 2.400/2.380 |
| Glu12 | 8.021 | 4.099 | 2.251/2.156 | H ^{γ2,3} 2.445/2.314 |
| Leu13 | 8.418 | 4.001 | 2.007/1.929 | H ^{γ} 1.693, H ^{δ1,2} 0.970/0.929 |
| Arg14 | 8.132 | 4.042 | 1.960/1.784 | H ^{γ2,3} 1.606, H ^{δ2,3} 3.210, H ^{ϵ} 7.613 |
| Arg15 | 8.201 | 4.086 | 2.008/1.931 | H ^{γ2,3} 1.854/1.615, H ^{δ2,3} 3.244, H ^{ϵ} 7.646 |
| Met16 | 8.275 | 4.265 | 2.319/2.114 | H ^{γ2,3} 2.724/2.552, H ^{ϵ} 2.077 |
| Gln17 | 8.550 | 3.908 | 2.256/2.046 | H ^{γ2,3} 2.428/2.300, H ^{ϵ21,22} 7.261/6.869 |
| Glu18 | 8.159 | 4.125 | 2.204/2.140 | H ^{γ2,3} 2.471/2.321 |
| Met19 | 7.976 | 4.203 | 2.311/2.196 | H ^{γ2,3} 2.708/2.608, H ^{ϵ} 2.112 |
| Leu20 | 8.458 | 4.007 | 1.691/1.616 | H ^{γ} 1.665, H ^{δ1,2} 0.926/0.890 |
| His21 | 8.257 | 4.556 | 3.346 | H ^{ϵ1,2} 8.524/7.306 |
| Lys22 | 8.101 | 4.042 | 2.014/1.718 | H ^{γ2,3} 1.422, H ^{δ2,3} 1.647, H ^{ϵ2,3} 2.993 |
| Ile23 | 8.128 | 3.964 | 1.928 | H ^{γ12,13} 1.697/1.262, H ^{γ2} 0.986, H ^{δ1} 0.859 |
| Gln24 | 8.384 | 4.026 | 2.029 | H ^{γ2,3} 2.574/2.334, H ^{ϵ21,22} 7.295/6.876 |
| Lys25 | 7.895 | 4.072 | 1.920/1.848 | H ^{γ2,3} 1.476/1.389, H ^{δ2,3} 1.655, H ^{ϵ2,3} 2.975 |
| Gln26 | 7.931 | 4.137 | 2.203/2.153 | H ^{γ2,3} 2.500/2.383, H ^{ϵ21,22} 7.444/6.820 |
| Met27 | 8.212 | 4.249 | 2.165/2.127 | H ^{γ2,3} 2.702/2.582, H ^{ϵ} 2.076 |
| Lys28 | 7.881 | 4.205 | 1.940/1.891 | H ^{γ2,3} 1.522/1.459, H ^{δ2,3} 1.695, H ^{ϵ2,3} 2.986 |
| Glu29 | 8.182 | 4.203 | 2.069/2.014 | H ^{γ2,3} 2.391/2.286 |
| Asn30 | 8.159 | 4.664 | 2.869/2.792 | H ^{δ21,22} 7.623/6.968 |
| C-term amide | 7.346/7.197 | | | |

^a Acetylated N-terminal, amidated C-terminal peptide. Buffer used was 50 mM potassium phosphate buffer pH 5.0, 100 mM NaCl, 10% glycerol-d₈, 1 mM NaN₃, 50 μ M DSS, 5% D₂O. Peptide concentration, 3.8 mM.

Source: By the author.

Appendix J – ¹H chemical shifts of SEPT5CC at 298 K.^a

| Residue | δ (¹ H ^N) [ppm] | δ (¹ H ^{α}) [ppm] | δ (¹ H ^{β}) [ppm] | δ (side chain) [ppm] |
|-----------------|---|---|--|---|
| Glu1 | - ^b | 4.210 | 2.164 | H ^{γ2,3} 2.501/2.420 |
| Thr2 | 8.603 | 4.391 | 4.313 | H ^{γ2} 1.294 |
| Glu3 | 8.724 | 4.269 | 2.096/2.064 | H ^{γ2,3} 2.477 |
| Lys4 | 8.400 | 4.136 | 1.823 | H ^{γ2,3} 1.490/1.392, H ^{δ2,3} 1.701, H ^{ϵ2,3} 3.001 |
| Leu5 | 8.007 | 4.265 | 1.722/1.612 | H ^{γ} 1.822, H ^{δ1,2} 0.955/0.897 |
| Ile6 | 8.022 | 3.865 | 1.897 | H ^{γ12,13} 1.554/1.155, H ^{γ2} 0.901, H ^{δ1} 0.832 |
| Arg7 | 8.269 | 4.244 | 1.889/1.747 | H ^{γ2,3} 1.642, H ^{δ2,3} 3.226, H ^{ϵ} 7.282 |
| Met8 | 8.186 | 4.312 | 2.154 | H ^{γ2,3} 2.690/2.561, H ^{ϵ} 2.086 |
| Lys9 | 8.320 | 4.169 | 1.904 | H ^{γ2,3} 1.575/1.471, H ^{δ2,3} 1.714, H ^{ϵ2,3} 2.973 |
| Asp10 | 8.464 | 4.506 | 2.927/2.841 | |
| Glu11 | 8.347 | 4.139 | 2.211/2.151 | H ^{γ2,3} 2.518/2.487 |
| Glu12 | 8.155 | 4.112 | 2.280/2.156 | H ^{γ2,3} 2.572/2.486 |
| Leu13 | 8.007 | 4.115 | 1.826 | H ^{γ} 1.695, H ^{δ1,2} 0.952/0.912 |
| Arg14 | 8.006 | 4.128 | 1.937 | H ^{γ2,3} 1.761/1.633, H ^{δ2,3} 3.237, H ^{ϵ} 7.352 |
| Arg15 | 8.119 | 4.112 | 1.981/1.936 | H ^{γ2,3} 1.831/1.669, H ^{δ2,3} 3.242, H ^{ϵ} 7.382 |
| Met16 | 8.199 | 4.257 | 2.289/2.155 | H ^{γ2,3} 2.753/2.585, H ^{ϵ} 2.095 |
| Gln17 | 8.392 | 4.027 | 2.285/2.173 | H ^{γ2,3} 2.527/2.418, H ^{ϵ21,22} 7.385/6.853 |
| Gln18 | 8.216 | 4.124 | 2.277/2.153 | H ^{γ2,3} 2.620/2.477 |
| Met19 | 8.108 | 4.183 | 2.275/2.228 | H ^{γ2,3} 2.746/2.605, H ^{ϵ} 2.116 |
| Leu20 | 8.278 | 4.113 | 1.843/1.775 | H ^{γ} 1.668, H ^{δ1,2} 0.947/0.928 |
| Gln21 | 8.064 | 4.068 | 2.207/2.179 | H ^{γ2,3} 2.496/2.463, H ^{ϵ21,22} 7.464/6.890 |
| Arg22 | 8.012 | 4.172 | 1.970 | H ^{γ2,3} 1.810/1.674, H ^{δ2,3} 3.238, H ^{ϵ} 7.299 |
| Met23 | 8.159 | 4.245 | 2.160 | H ^{γ2,3} 2.740/2.588, H ^{ϵ} 2.092 |
| Lys24 | 8.146 | 4.056 | 1.924 | H ^{γ2,3} 1.566/1.423, H ^{δ2,3} 1.686, H ^{ϵ2,3} 2.966 |
| Gln25 | 8.011 | 4.126 | 2.177 | H ^{γ2,3} 2.501/2.422, H ^{ϵ21,22} 7.482/6.841 |
| Gln26 | 8.120 | 4.203 | 2.158 | H ^{γ2,3} 2.495/2.417, H ^{ϵ21,22} 7.509/6.861 |
| Met27 | 8.086 | 4.347 | 2.173/2.110 | H ^{γ2,3} 2.703/2.592, H ^{ϵ} 2.094 |
| Gln28 | 8.083 | 4.256 | 2.293/2.155 | H ^{γ2,3} 2.433 |
| Asp29 | 8.276 | 4.653 | 2.920/2.845 | |
| Gln30 | 8.175 | 4.285 | 2.196/2.017 | H ^{γ2,3} 2.416 |
| C-term amide | 7.505/7.149 | | | |

^a Free N-terminal, amidated C-terminal peptide. Buffer used was 50 mM potassium phosphate buffer pH 5.0, 150 mM NaCl, 1 mM NaN₃, 50 μ M DSS, 5% D₂O. Peptide concentration, 1.0 mM.

^b Peaks were unassignable due to exchange with solvent.

Source: By the author.

Appendix K – Swissprot-normalized profiles of 20 proteinogenic amino acids occupying the seven different positions of heptad repeats (*a, b, c, d, e, f, g*) for parallel and antiparallel coiled-coils.^a Most common occurrences are highlighted with darker backgrounds.

| | PARALLEL | | | | | | | ANTIPARALLEL | | | | | | |
|---|----------|----------|----------|----------|----------|----------|----------|--------------|----------|----------|----------|----------|----------|----------|
| | <i>a</i> | <i>b</i> | <i>c</i> | <i>d</i> | <i>e</i> | <i>f</i> | <i>g</i> | <i>a</i> | <i>b</i> | <i>c</i> | <i>d</i> | <i>e</i> | <i>f</i> | <i>g</i> |
| A | 0.71 | 1.59 | 1.08 | 1.25 | 0.66 | 1.43 | 0.77 | 0.80 | 1.10 | 0.98 | 0.92 | 0.93 | 1.31 | 0.95 |
| C | 0.58 | 0.36 | 0.09 | 1.08 | 0.09 | 0.37 | 0.27 | 0.60 | 0.00 | 0.44 | 1.41 | 0.00 | 0.22 | 0.67 |
| D | 0.05 | 1.78 | 1.53 | 0.12 | 0.54 | 1.52 | 0.77 | 0.22 | 1.98 | 0.56 | 0.06 | 1.25 | 1.19 | 0.69 |
| E | 0.22 | 2.66 | 2.94 | 0.56 | 3.27 | 2.37 | 3.73 | 0.49 | 2.54 | 2.50 | 0.45 | 3.10 | 2.55 | 3.10 |
| F | 0.47 | 0.34 | 0.48 | 0.47 | 0.31 | 0.28 | 0.14 | 0.30 | 0.08 | 0.84 | 0.92 | 0.34 | 0.34 | 0.34 |
| G | 0.04 | 0.33 | 0.15 | 0.02 | 0.12 | 0.43 | 0.08 | 0.13 | 0.81 | 0.19 | 0.09 | 0.24 | 0.24 | 0.10 |
| H | 0.48 | 0.82 | 1.58 | 0.22 | 0.48 | 1.07 | 0.24 | 0.52 | 0.58 | 1.45 | 1.44 | 1.01 | 0.58 | 0.29 |
| I | 2.12 | 0.23 | 0.39 | 0.45 | 0.49 | 0.47 | 0.63 | 3.47 | 0.51 | 0.57 | 1.90 | 0.62 | 0.23 | 0.91 |
| K | 0.97 | 1.86 | 1.73 | 0.72 | 2.18 | 1.81 | 2.00 | 1.32 | 1.62 | 1.92 | 0.15 | 1.75 | 1.69 | 1.64 |
| L | 3.10 | 0.46 | 0.44 | 5.28 | 0.71 | 0.44 | 0.74 | 2.38 | 0.79 | 0.76 | 4.42 | 0.97 | 0.52 | 1.10 |
| M | 0.94 | 0.51 | 0.79 | 1.04 | 0.75 | 0.46 | 0.86 | 1.00 | 0.28 | 0.28 | 1.26 | 0.42 | 0.28 | 0.70 |
| N | 2.69 | 0.95 | 1.08 | 0.30 | 1.13 | 1.40 | 0.33 | 0.36 | 1.37 | 1.30 | 0.07 | 0.89 | 1.46 | 1.05 |
| P | 0.00 | 0.06 | 0.06 | 0.00 | 0.00 | 0.00 | 0.00 | 0.06 | 0.00 | 0.00 | 0.00 | 0.00 | 0.00 | 0.00 |
| Q | 0.44 | 2.10 | 2.67 | 0.72 | 3.76 | 2.14 | 3.56 | 1.28 | 2.17 | 1.93 | 0.38 | 2.69 | 3.95 | 1.93 |
| R | 0.87 | 1.48 | 1.48 | 0.11 | 1.67 | 1.72 | 1.64 | 1.60 | 1.59 | 2.15 | 0.22 | 1.23 | 1.35 | 1.72 |
| S | 0.38 | 1.00 | 0.96 | 0.49 | 0.60 | 0.76 | 0.70 | 0.39 | 1.06 | 0.73 | 0.48 | 0.82 | 1.31 | 0.82 |
| T | 0.46 | 0.62 | 0.82 | 0.72 | 0.81 | 0.97 | 0.79 | 0.72 | 0.37 | 0.80 | 0.67 | 0.56 | 0.62 | 0.43 |
| V | 1.83 | 0.42 | 0.32 | 0.57 | 0.39 | 0.39 | 0.41 | 0.94 | 0.39 | 0.45 | 1.30 | 0.55 | 0.30 | 0.79 |
| W | 0.11 | 0.12 | 0.00 | 0.33 | 0.48 | 0.24 | 0.12 | 0.26 | 0.88 | 0.29 | 0.00 | 0.00 | 0.00 | 0.00 |
| Y | 0.99 | 0.58 | 0.40 | 1.32 | 0.36 | 0.46 | 0.36 | 0.30 | 0.00 | 1.11 | 0.80 | 0.22 | 0.11 | 0.55 |

^a Data were searched for coiled-coil sequences that were interchain, homodimeric, longer than 21 residues, with canonical heptameric repeats and had a low level of redundancy between them. Database used was CC+.²¹¹

Source: By the author.

Appendix L – Demonstration of the chemical shifts fitting equation (Equation 7, page 63).

The simplest case involves two states in exchange, 1 and 2 (Equation S1 and S2)

$$K_{12} = \frac{p_2}{p_1} = \exp\left(-\frac{\Delta G_{12}}{RT}\right) \quad (\text{S1})$$

$$p_1 + p_2 = p_1(1 + K_{12}) = p_1 \left[1 + \exp\left(-\frac{\Delta G_{12}}{RT}\right)\right] \quad \text{or} \quad (\text{S2a})$$

$$p_1 + p_2 = p_2(1 + K_{21}) = p_2 \left[1 + \exp\left(-\frac{\Delta G_{21}}{RT}\right)\right] \quad (\text{S2b})$$

Considering states 1 and 2 in fast exchange, the NMR chemical shift will be a population-weighted average (Equation S3)

$$\delta = \frac{\delta_1 p_1 + \delta_2 p_2}{p_1 + p_2} \quad (\text{S3})$$

Removing the dependency of the states populations, p_1 and p_2 (Equation S4)

$$\delta = \frac{\delta_1 + \delta_2 \exp\left(-\frac{\Delta G_{12}}{RT}\right)}{1 + \exp\left(-\frac{\Delta G_{12}}{RT}\right)} \quad (\text{S4})$$

Analogously, the same can be done for N states (1, 2, 3, ..., N) in fast exchange and written in the form of a finite sum (Equation S5)

$$\delta = \frac{\sum_{i=1}^N \delta_i \exp\left(-\frac{\Delta G_{1i}}{RT}\right)}{\sum_{i=1}^N \exp\left(-\frac{\Delta G_{1i}}{RT}\right)} \quad (\text{S5})$$

where $\Delta G_{11} = 0$.

Appendix M – Demonstration of the NMR cross-peaks intensities fitting equation (Equation 9, page 63).

The cross-peak volumes in NMR are directly proportional to the population of the state that gives rise to that respective peak (C is a proportionality constant in Equation S6)

$$V_i = Cp_i \quad (\text{S6})$$

Starting with two states (1 and 2) in slow exchange, we can rewrite Equation S1 to display the pressure-dependent cross-peak volumes arising from each individual state (Equation S7)

$$K_{12} = \frac{V_2(p)}{V_1(p)} = \exp\left(-\frac{\Delta G_{12}}{RT}\right) \quad (\text{S7})$$

The sum of all cross-peak volumes (V) is used to substitute $V_2(p)$ in Equation S7

$$V_2(p) = V(p) - V_1(p) \quad (\text{S8})$$

$$\frac{V(p) - V_1(p)}{V_1(p)} = \exp\left(-\frac{\Delta G_{12}}{RT}\right) \quad (\text{S9})$$

Isolating the peak volume from the native state (state 1) in Equation S9, we obtain (Equation S10)

$$V_1(p) = \frac{V(p)}{1 + \exp\left(-\frac{\Delta G_{12}}{RT}\right)} \quad (\text{S10})$$

Analogously, the same can be done for N states (1, 2, 3, ..., N) in slow exchange and written in the form of a finite sum (Equation S11)

$$V_1(p) = \frac{V(p)}{\sum_{i=1}^N \exp\left(-\frac{\Delta G_{1i}}{RT}\right)} \quad (\text{S11})$$

where $\Delta G_{11} = 0$.

Equation S11 applies only to pure slow exchange systems. In mixed systems with states exchanging with both fast and slow exchange rates, that expression cannot be applied. Next, we develop equations suitable to mixed systems. First, let us consider a system (Figure

below) with three states in fast exchange (states 1, 2 and 3) and three states in slow exchange (states 1, II and III).

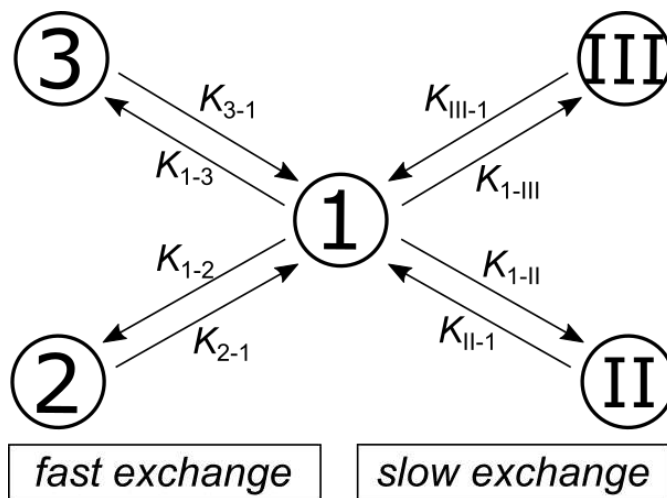


Figure S1 – Mixed exchanging-states system with three conformers in fast exchange (states 1, 2 and 3) and three conformers in slow exchange (1, II and III). The respective equilibrium constants are represented.

Source: By the author.

Since three states are in fast exchange (states 1, 2 and 3), their contribution to the sum of the peak volumes will be in the form V_{123} , given that only one peak from these three states can be seen in the spectrum. The total volume will be (Equation S12)

$$V(p) = V_I(p) + V_{II}(p) + V_{123}(p) \quad (S12)$$

In terms of state populations we have (Equation S13)

$$p_T = p_I + p_{II} + (p_1 + p_2 + p_3) \quad (S13)$$

Dividing Equation S13 by p_I and recognizing the population ratios as the respective equilibrium constants (using Equation S1), we derive (Equation S14)

$$\frac{p_T}{p_I} = \exp\left(-\frac{\Delta G_{1I}}{RT}\right) + \exp\left(-\frac{\Delta G_{1II}}{RT}\right) + \left[1 + \exp\left(-\frac{\Delta G_{12}}{RT}\right) + \exp\left(-\frac{\Delta G_{13}}{RT}\right)\right] \quad (S14)$$

There is also information about the $V_{123}(p)$ contribution of states in fast exchange (Equation S15, C is a constant)

$$V_{123}(p) = C(p_1 + p_2 + p_3) \quad (S15)$$

Making the same procedure previously done (dividing by p_1 and recognizing the population ratios as exponential functions), we can easily reach to (Equation S16)

$$\frac{V_{123}(p)}{p_1} = C \left[1 + \exp\left(-\frac{\Delta G_{12}}{RT}\right) + \exp\left(-\frac{\Delta G_{13}}{RT}\right) \right] \quad (\text{S16})$$

Isolating p_1 in Equation S16 and replacing it in Equation S14, the following is obtained (Equation S17)

$$p_T = \frac{V_T(p)}{C} = V_{123}(p) \frac{\exp\left(-\frac{\Delta G_{1I}}{RT}\right) + \exp\left(-\frac{\Delta G_{1II}}{RT}\right) + \left[1 + \exp\left(-\frac{\Delta G_{12}}{RT}\right) + \exp\left(-\frac{\Delta G_{13}}{RT}\right) \right]}{C \left[1 + \exp\left(-\frac{\Delta G_{12}}{RT}\right) + \exp\left(-\frac{\Delta G_{13}}{RT}\right) \right]} \quad (\text{S17})$$

The volume $V_{123}(p)$ is usually the quantity that can be extracted from the spectra – called from now on only as $V(p)$; the total volume $V_T(p)$ is unknown, but we can assume that it is constant given that the total concentration (c_T) is also constant with pressure (no aggregation/deaggregation).

$$V_T(p) = V_T(p_0) \quad (\text{S18})$$

After such assumption, we can write a expression for $V(p)$

$$V(p) = V_T(p_0) \frac{1 + \exp\left(-\frac{\Delta G_{12}}{RT}\right) + \exp\left(-\frac{\Delta G_{13}}{RT}\right)}{1 + \exp\left(-\frac{\Delta G_{1I}}{RT}\right) + \exp\left(-\frac{\Delta G_{1II}}{RT}\right) + \exp\left(-\frac{\Delta G_{12}}{RT}\right) + \exp\left(-\frac{\Delta G_{13}}{RT}\right)} \quad (\text{S19})$$

Notice that the dividend in Equation S19 involves only exponentials relative to the M states in fast exchange (in this example, states 1, 2 and 3) and the divisor includes information about all N states. Generalizing the model to M states in fast exchange and $N-M$ states in slow exchange (Equation S20)

$$V(p) = V_T(p_0) \frac{\sum_{i=1}^M \exp\left[-\frac{\Delta G_{1i}(p)}{RT}\right]}{\sum_{i=1}^N \exp\left[-\frac{\Delta G_{1i}(p)}{RT}\right]} \quad (\text{S20})$$

Volume NMR data can be analyzed relatively to $V(p_0)$; in this fashion, the quantity $V_T(p_0)$ can be removed by dividing $V(p)$ by $V(p_0)$ (Equation S21)

$$\frac{V(p)}{V(p_0)} = \frac{\sum_{i=1}^M \exp\left[-\frac{\Delta G_{1i}(p)}{RT}\right]}{\sum_{i=1}^N \exp\left[-\frac{\Delta G_{1i}(p)}{RT}\right]} \frac{\sum_{i=1}^N \exp\left[-\frac{\Delta G_{1i}(p_0)}{RT}\right]}{\sum_{i=1}^M \exp\left[-\frac{\Delta G_{1i}(p_0)}{RT}\right]} \quad (\text{S21})$$

However, in practice, cross-peak volumes are often normalized by the volume at the lowest pressure point $V(p_i)$, which can be different from p_0 (Equation S22)

$$V(p_0) = V(p_i) * a_i \quad (\text{S22})$$

where a_i is approximately unitary.

We can finally write the expression for a mixed system with M states in fast exchange and $N-M$ states in slow exchange (Equation S23)

$$\frac{V(p)}{V(p_i)} = a_i \frac{\sum_{i=1}^M \exp\left[-\frac{\Delta G_{1i}(p)}{RT}\right]}{\sum_{i=1}^N \exp\left[-\frac{\Delta G_{1i}(p)}{RT}\right]} \frac{\sum_{i=1}^N \exp\left[-\frac{\Delta G_{1i}(p_0)}{RT}\right]}{\sum_{i=1}^M \exp\left[-\frac{\Delta G_{1i}(p_0)}{RT}\right]} \quad (\text{S23})$$

where $\Delta G_{1i}(p)$ is usually represented only as ΔG_{1i} and $\Delta G_{1i}(p_0)$ is written as ΔG_{1i}^0 .

Assuming that no additional line broadening emerges with pressure, NMR cross-peak intensities can also be studied using Equation S23.

Appendix N – Demonstration of the polymerization equation (Equation 16, page 70).

The dissociation constant, K_D , is an important value to describe protein-protein and protein-ligand binding strength. It is measured in concentration (molar, M) and represents the inverse of the association constant, K_A . For a dimerization equilibrium process, the equilibrium constants can be written as (Equation S24)

$$m + m \xrightleftharpoons{K_A} d$$

$$K_D = \frac{1}{K_A} = \frac{c_1^2}{c_2} \quad (\text{S24})$$

with c_1 being the monomeric (m) concentration and c_2 the concentration of dimers (d).

Extrapolating the reasoning for the elongation of an n -mer polymer assuming that K_D does not depend on the polymer size, it is possible to isolate c_n , the concentration of n -mer polymers prior to the monomer elongation (Equation S25)

$$c_n = \left(\frac{c_1}{K_D}\right)^n K_D \quad (\text{S25})$$

The total protein concentration (c_T) expressed in monomeric units can be computed as a sum over all polymer concentrations (c_n) multiplied by their n -th order (Equation S26)

$$c_T = \sum_{n=1}^{\infty} n \cdot c_n \quad (\text{S26})$$

Rewriting Equation S26, replacing c_n as represented in Equation S25, we obtain (Equation S27)

$$c_T = K_D \sum_{n=1}^{\infty} n \left(\frac{c_1}{K_D}\right)^n \quad (\text{S27})$$

sum which can be approximated by the following result (Equation S28)

$$\sum_{n=1}^{\infty} na^n = \frac{a}{(1-a)^2}, \quad \text{for } a < 1 \quad (\text{S28})$$

Using $a = c_1/K_D$, we can easily solve the sum (Equation S29)

$$c_T = \frac{c_1}{\left(1 - \frac{c_1}{K_D}\right)^2} \quad (\text{S29})$$

Equation S29 can be interpreted as a quadratic equation for c_1 (Equation S30)

$$Ac_1^2 + Bc_1 + C = 0, \quad \text{with } A = 1$$

$$B = -K_D(2 + K_D/c_T) \quad (\text{S30})$$

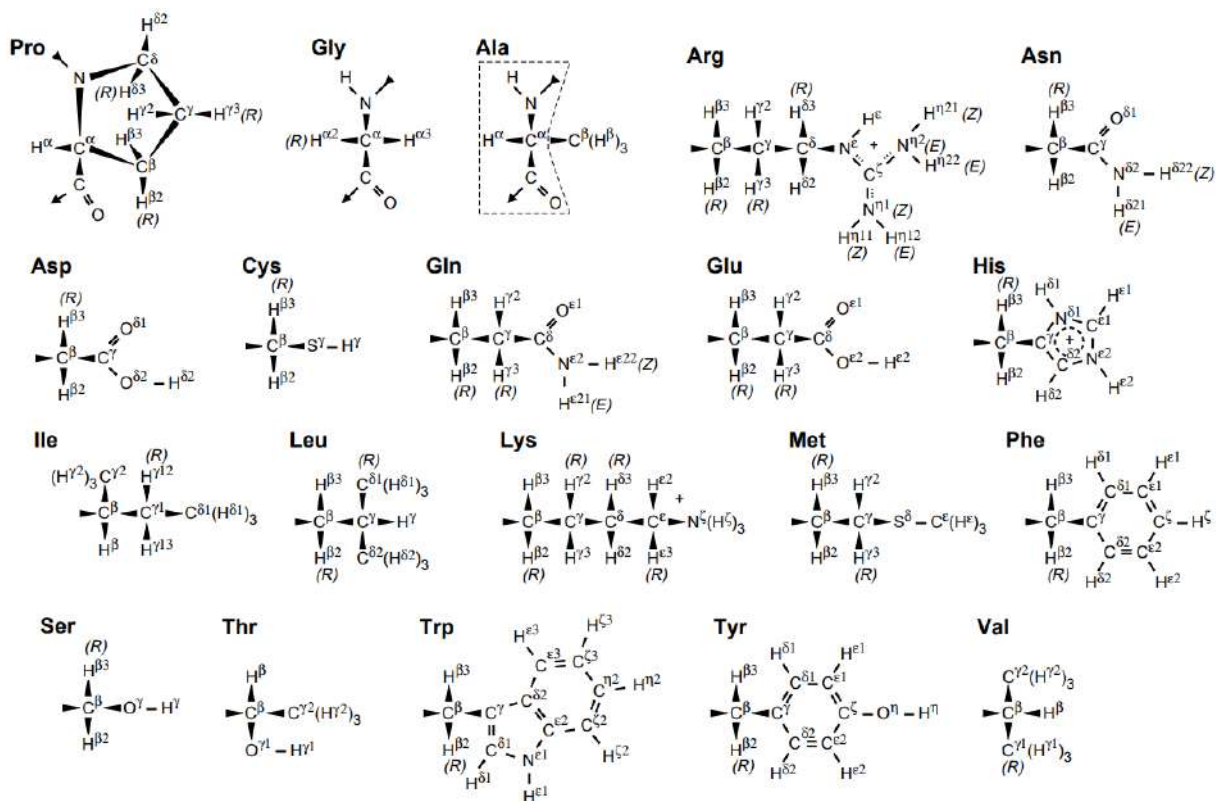
$$C = K_D^2$$

which has two solutions but only one is meaningful and physically relevant (Equation S31)

$$c_1 = K_D \left(1 + \frac{K_D}{2c_T} - \sqrt{\left(1 + \frac{K_D}{2c_T}\right)^2 - 1} \right) \quad (\text{S31})$$

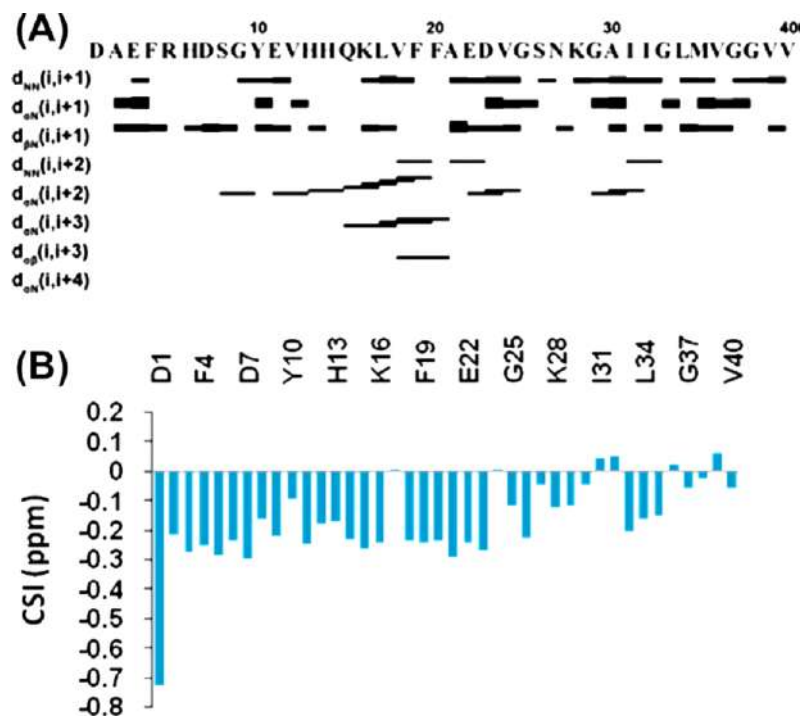
ANNEX

Annex A – Atom nomenclature recommendation for the presentation of NMR data.



Source: MARKLEY¹⁰⁵

Annex B – NOE pattern (A) and chemical shift index CSI (B) reported for A β 1-40 by Vivekanandan.



Source: VIVEKANANDAN³⁹